

# Galaxy Masses

Stéphane Courteau<sup>a</sup>, Michele Cappellari<sup>b</sup>, Roelof S. de Jong<sup>c</sup>, Aaron A. Dutton<sup>d</sup>, Eric Emsellem<sup>e</sup>,  
 Henk Hoekstra<sup>f</sup>, L.V.E. Koopmans<sup>g</sup>, Gary A. Mamon<sup>h</sup>, Claudia Maraston<sup>i</sup>, Tommaso Treu<sup>j</sup>,  
 Lawrence M. Widrow<sup>a</sup>

<sup>a</sup>Queen's University, Department of Physics, Engineering Physics and Astronomy, Kingston, Ontario, Canada

<sup>b</sup>Sub-department of Astrophysics, Department of Physics, University of Oxford, Denys Wilkinson Building, Keble Road, Oxford OX1 3RH, UK

<sup>c</sup>Leibniz-Institut für Astrophysik Potsdam (AIP), An der Sternwarte 16, 14482 Potsdam, Germany

<sup>d</sup>Max-Planck-Institut für Astronomie, Königstuhl 17, 69117 Heidelberg, Germany

<sup>e</sup>European Southern Observatory, Karl-Schwarzschild-Strasse 2, 85748, Germany and Université Lyon 1, Observatoire de Lyon, Centre de Recherche Astrophysique de Lyon and Ecole Normale Supérieure de Lyon, 9 avenue Charles André, F-69230 Saint-Genis Laval, France

<sup>f</sup>Leiden Observatory, Leiden University, P.O. Box 9513, NL-2300 RA Leiden, The Netherlands

<sup>g</sup>University of Groningen, Kapteyn Astronomical Institute, P.O.Box 800, 9700 AV, Groningen, The Netherlands

<sup>h</sup>Institut d'Astrophysique de Paris (UMR 7095: CNRS & UPMC), 98 bis Bd Arago, F-75014 Paris, France

<sup>i</sup>University of Portsmouth, Institute of Cosmology and Gravitation, Dennis Sciama Building, Burnaby Road, Portsmouth, UK

<sup>j</sup>University of California, Santa Barbara, Department of Physics, Santa Barbara, CA

## Abstract

Galaxy masses play a fundamental role in our understanding of structure formation models. This review addresses the variety and reliability of mass estimators that pertain to stars, gas, and dark matter. The different sections on masses from stellar populations, dynamical masses of gas-rich and gas-poor galaxies, with some attention paid to our Milky Way, and masses from weak and strong lensing methods, all provide review material on galaxy masses in a self-consistent manner.

*Keywords:* galaxies: dark matter — galaxies: evolution — galaxies: formation

## Contents

<b>1</b>	<b>Introduction</b>	<b>4</b>
<b>2</b>	<b>From light to mass: modelling the stellar <math>M^*/L</math> ratio</b>	<b>6</b>
2.1	Modelling galaxies and their Stellar Populations, a Historical Introduction . . . . .	6
2.2	Basics of Stellar Population Models . . . . .	8
2.3	Stellar Mass from $M^*/L$ vs Colour Diagnostics . . . . .	13
2.3.1	Effect of Star Formation History . . . . .	15
2.3.2	Stellar Initial Mass Function . . . . .	20
2.3.3	Model ingredients . . . . .	21
2.4	Data Fitting Techniques . . . . .	23
2.5	Robustness of Stellar Mass Derivations . . . . .	24
2.6	Future Prospects . . . . .	26

<b>3</b>	<b>Dynamical Masses of Gas-Rich Galaxies</b>	<b>27</b>
3.1	Mass Estimates from Rotation Curves . . . . .	28
3.2	Inner Parts . . . . .	31
3.3	Mass Modeling . . . . .	33
3.3.1	Mass Modeling Limitations . . . . .	35
3.4	Other Galaxy Mass Constraints . . . . .	36
3.4.1	Maximal and Sub-maximal Disks . . . . .	37
3.4.2	Velocity Dispersion Measurements . . . . .	38
3.4.3	Scaling Relations Residuals . . . . .	39
3.4.4	Fluid Dynamical Modeling . . . . .	39
3.4.5	Gravitational Lensing . . . . .	39
3.4.6	Two-body Interactions and the Mass of the Local Group . . . . .	40
3.5	Future Prospects . . . . .	41
<b>4</b>	<b>Dark Matter and Mass Models of the Milky Way</b>	<b>42</b>
4.1	Introduction . . . . .	42
4.2	Multicomponent Models for the Milky Way . . . . .	42
4.3	Further Observational Constraints on the Milky Way Potential . . . . .	47
4.3.1	Circular Speed at the Sun's Position in the Galaxy . . . . .	47
4.3.2	Local Escape Speed . . . . .	47
4.3.3	Kinematic Tracers . . . . .	48
4.3.4	Vertical Force and Surface Density in the Solar Neighborhood . . . . .	49
4.4	Future Prospects . . . . .	51
<b>5</b>	<b>Dynamical Masses of Gas-Poor Galaxies</b>	<b>52</b>
5.1	Introduction . . . . .	52
5.2	Simple Mass Estimators . . . . .	53
5.3	Methods based on Dynamical Modelling . . . . .	56
5.3.1	Jeans Analysis . . . . .	57
5.3.2	Spherical Modelling . . . . .	58
5.3.3	Axisymmetric Modelling . . . . .	59
5.4	Distribution Function Analysis . . . . .	61
5.4.1	Spherical Distribution Function Modelling . . . . .	61
5.4.2	Towards Flattened Systems . . . . .	62
5.4.3	General Orbit-based Modelling . . . . .	63
5.5	Results . . . . .	64
5.5.1	Integrated Stellar Light: the Inner Regions and the IMF . . . . .	64
5.5.2	Globular Clusters and Planetary Nebulae: the Outer Regions . . . . .	66
5.5.3	Other Tracers and Combined Approaches . . . . .	67
5.5.4	The Mass-Anisotropy Degeneracy . . . . .	68
5.5.5	Discrete Star Velocities for Dwarf Spheroidal Galaxies . . . . .	68
5.6	Future Prospects . . . . .	72

<b>6 Weak Lensing by Galaxies</b>	<b>73</b>
6.1 Introduction . . . . .	73
6.2 Theory of Weak Lensing . . . . .	74
6.3 Shear . . . . .	75
6.4 Magnification . . . . .	76
6.5 Galaxy-Mass Cross-Correlation Function . . . . .	77
6.6 Properties of Dark Matter Halos . . . . .	79
6.7 Halo Shapes . . . . .	81
6.8 Future Prospects . . . . .	82
<b>7 The Dark and Luminous Mass Distribution of Early-type Galaxies using Strong Gravitational Lensing</b>	<b>84</b>
7.1 Introduction . . . . .	84
7.2 Basic Lensing Theory . . . . .	84
7.2.1 The Thin-Lens Approximation . . . . .	85
7.2.2 The Lens Equation . . . . .	86
7.2.3 Axisymmetric Lenses . . . . .	87
7.2.4 Lensing & Stellar Dynamics . . . . .	88
7.3 Observational Results . . . . .	90
7.3.1 Sloan Lens ACS Survey (SLACS) . . . . .	90
7.3.2 The Density Profiles of Early-Type Galaxies (ETGs) . . . . .	93
7.3.3 The Stellar IMF and Dark Matter Fraction in ETGs . . . . .	94
7.3.4 Mass Substructure in ETGs . . . . .	95
7.3.5 Luminous Dwarf Galaxies . . . . .	96
7.3.6 Dark Substructures . . . . .	97
7.4 Future Prospects . . . . .	101
<b>8 Acknowledgments</b>	<b>102</b>

## 1. Introduction

The distribution of matter in cosmological structures is a fundamental property of nature as the mass of a system is likely the major driver of its evolution. This is especially true for stars whose evolution depend almost fully on their initial mass (and chemical composition) on the main sequence, as embodied by the (idealistic) Vogt-Russell theorem. Mass also plays a fundamental role in galaxy evolution. Galaxies have largely been shaped through mergers and galaxy interactions in hierarchical fashion whereby small systems merged into bigger ones. At early times, star formation was most effective in massive galaxies but as the Universe aged, star formation was likely quenched in those massive systems but continued in smaller galaxies, a phenomenon now called “downsizing”. Oldest stars are thus found in the most massive systems. The complex interplay between star formation efficiency and quenching is likely modulated by a galaxy’s total mass.

Measurements of the distribution of matter in the Universe enable a variety of tests of structure formation models on different scales. For instance, the distribution of galaxy masses on all scales enables the closest possible, though not direct, comparison of predicted mass functions for baryonic and non-baryonic matter in the Universe. The relative fraction of baryonic to non-baryonic matter is also indicative of fundamental, yet poorly understood, processes in galaxy formation which typically give rise to tight scaling relations based on the stellar and dynamical masses of galaxies.

Because galaxy masses play such a critical role in our understanding of the formation and evolution of cosmic structures, we wish to review the variety and reliability of mass estimators for gas-poor and gas-rich galaxies and discuss our ability to derive from those estimators meaningful constraints of theoretical galaxy formation models. While certain techniques enable only the measurement of galaxy masses on large scales, others allow the decomposition of individual mass components such as gas, stars and dark matter at different galactocentric radii. The latter methods probe the gravitational potential through the dynamics of visible tracers where baryons are (sub-)dominant. Although many galaxies may be safely assumed to be virialized, uncertainties in their mass estimates remain, for instance due to anisotropies in the velocity distributions. Furthermore, baryon-dominated regions remain poorly understood, which complicates a direct comparison of galaxy formation models to observational data.

Many techniques exist for the determination of galaxy masses. The most popular involves the measurement of Doppler shifts of nebular and/or stellar atomic lines due to internal dynamics. Stellar motions can also be resolved in the closest galaxies, such as our The Milky Way, Andromeda, and other Local Group stellar systems; galaxy masses of more distant systems otherwise rely on integrated spectra. Another mass estimator consists of converting the galaxy light profile into a mass profile using a suitable stellar mass-to-light ratio (usually derived from stellar population models). A more global approach has also involved the mapping of gravitational lensing effects, both strong and weak. This list is not meant to be complete, as we review below. However, in all cases, galaxy mass estimates account for matter encompassed within a specified radius and are thus always a lower limit to the total galaxy mass.

This review has evolved from discussions which took place during the celebrations of Vera Rubin’s career at Queen’s University in June 2009<sup>1</sup>. All the authors of this review were indeed present at that conference. While each section of this review was initially written by separate teammates, the final product reflects the full team’s imprimatur. This review was inspired by, and

---

<sup>1</sup>See <http://www.astro.queensu.ca/GalaxyMasses09> for workshop presentations and photographs.

is meant as a modern revision of, early treatises on the masses and mass-to-light ratios of galaxies by Burbidge & Burbidge (1975) and Faber & Gallagher (1979), respectively.

The review is organized as follows: we first present in §2 the central topic of stellar  $M/L$  determinations from stellar population models. This is followed by a discussion of the mass estimates for gas-rich galaxies in §3, including the special (resolved) case of the Milky Way in §4. Gas-poor galaxies are addressed in §5 and weak and strong lensing techniques are presented in §6 and §7, respectively. Conclusions, with a view towards future developments, are presented at the end of each section.

This review is naturally incomplete; conspicuously missing topics include the measurement of stellar and dynamical masses of high redshift galaxies (e.g. Förster Schreiber et al. 2006; Bezanson et al. 2011; Alaghband-Zadeh et al. 2012), the direct comparison of stellar and dynamical mass estimates (e.g. de Jong & Bell 2007; Taylor et al. 2010), mass function determinations (e.g. stellar mass functions: Bundy et al. 2006; Pozzetti et al. 2010; Maraston et al. 2012) (e.g. dynamical mass functions: Trujillo-Gomez et al. 2011; Papastergis et al. 2011, 2012), constraints on halo masses by statistical techniques such as those involving satellite kinematics (More et al. 2011a; Wojtak & Mamon 2013), group catalogs (Yang et al. 2009), and abundance matching (Behroozi et al. 2013), to name a few.

Furthermore, this review is restricted to mass analyses based on Newtonian dynamics. Alternatives exist, the most popular being MOND (e.g. Milgrom 1983), but a proper treatment of them is beyond the scope of this review. Readers interested in alternative models, MOND or others, are referred to the review by Famaey & McGaugh (2012).

## 2. From light to mass: modelling the stellar $M^*/L$ ratio

### 2.1. Modelling galaxies and their Stellar Populations, a Historical Introduction.

The stellar mass  $M^*$  of a galaxy is a key physical parameter of galaxy formation and evolution studies as it traces the galaxy formation process. The stellar mass of a galaxy grows through processes such as the internal conversion of gas and dust into stars via star formation, or external events like major interactions with other galaxies and subsequent merging which may induce further star formation, as well as minor events such as accretion of satellites. Moreover, knowledge of the galaxy stellar mass is crucial in order to decompose the contributions from stars and dark matter to the dynamics of galaxies. Modern galaxy formation models embedded in a  $\Lambda$ -Cold Dark Matter universe can also predict the evolution of the galaxy mass assembly over cosmic time (e.g. De Lucia et al. 2007).

Galaxies shine because their stars radiate the energy they produced via nuclear reactions in their cores. The theory of stellar evolution describes the amount of energy released by a star given its initial mass. Hence, by modelling the light emitted by all the stars in a galaxy over all wavelengths - the so-called “integrated spectral energy distribution (SED)” - one can in principle derive the stellar mass that is responsible for such radiation. However, a certain fraction of evolved stars no longer shine yet still contribute to the galaxy mass budget in the form of stellar remnants such as white dwarfs, neutron stars and black holes. The sum of *living* stars plus remnants makes up the “stellar mass”,  $M^*$ , of a galaxy.

Despite our detailed knowledge of stellar evolution, the modelling of a galaxy spectrum - which is the superposition of all spectra from individual stars - is a challenging exercise since the exact stellar composition of a galaxy and its overall stellar generations are unknown *a priori*. These depend on the history of star formation, chemical enrichment, accretion and interaction. Unlike stellar clusters whose vast majority of stars are coeval and share the same chemical composition, galaxies are a complicated ensemble of stellar generations. Recent extensive reviews of SED modelling of galaxies have appeared in Walcher et al. (2011) and Conroy (2013).

As recognised early on by Oort (1926) and Baade (1944), our own Milky Way is composed of various populations of stars, each featuring different dynamics, chemical properties, and formation epochs. Thus, from a stellar content viewpoint, galaxies can be broken into *stellar populations* with shared definable properties. The “simple stellar population” (SSP) is defined as a group of coeval stars with homogeneous chemistry (at birth) and similar orbits/kinematics. A recent, comprehensive text book on stellar populations in galaxies is due to Greggio & Renzini (2011).

Star clusters, either open or globular, are the closest realisation of SSPs in nature. The main unknown of an SSP is the Stellar Initial Mass Function (IMF), which gives the mass spectrum of the stellar generation at birth. The latter is not known from first principles. Empirical determinations of the IMF based on solar neighborhood data were first modeled by Salpeter (1955) as a power-law with exponent of  $\sim -2.35$ . An IMF must be assumed when calculating the properties of population models. While galaxies are not SSPs, they can be viewed as a sum of all present SSPs: that is, Galaxies =  $\sum_j SSP_j$ . The distribution of stellar generations in time and chemical enrichment is called the “Star Formation History” (SFH). Several analytical laws describe plausible SFHs which depend on the timescale of the Star Formation Rate (SFR), such as exponentially-declining models, or  $\tau$ -models, models with constant star formation, models with time-increasing star formation, etc. Examples of such SFHs are shown in Figure 1.

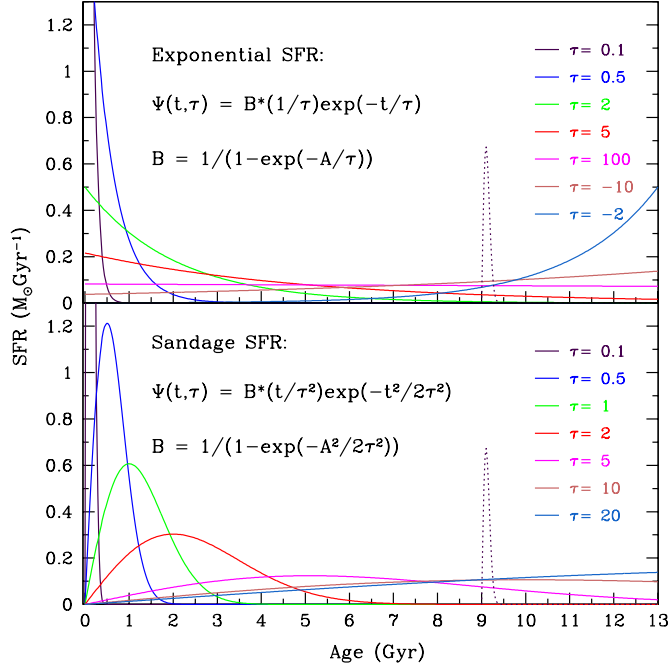


Figure 1: Time evolution of the exponential (upper panel) and Sandage (1986a) (lower panel) star formation histories (solid curves). The dotted curve is a Sandage-style burst of star formation in which 10% of the total mass of stars are formed. From MacArthur et al. (2004).

Ultimately, the stellar content of a galaxy over time,  $t$ , may be thought of as:

$$\text{Galaxy} = \sum_{\text{time}} \text{SFR}(t) \times \text{SSP}(t, Y, Z, \text{IMF}), \quad (1)$$

with  $Y$  the Helium abundance and  $Z$  the abundance of heavier elements (metallicity). Note that  $Y$ ,  $Z$ , and the IMF may vary between different stellar generations, i.e. amongst different SSPs, but they do not vary within an SSP by definition.

It is useful to note that little is known about the physical processes that drive the rate of star formation and the emerging mass spectrum (the IMF). We know that stars form from dense, cold gas in gas that is shock compressed (e.g. in disks, during galaxy interactions or dynamical instabilities), but a theory which predicts the SFR and the IMF in different galaxies and as a function of time has yet to be written. For these reasons, these two physical quantities are parametrized in population models and observations to guide ongoing developments. Indeed, our limited knowledge about the SFR and IMF is a major problem in the precise determination of a galaxy's stellar mass.

Historically, the problem of modelling a galaxy spectrum has been approached in two ways. In the so-called “optimised population synthesis” (Spinrad & Taylor 1971; Faber 1972; O’Connell 1976; Pickles 1985; Bica & Alloin 1986), empirical stellar spectra are combined in proportions such that the resulting composite spectrum can best reproduce the galaxy spectrum. These proportions can be ad hoc, hence neither necessarily obeying stellar evolution timescales nor a realistic stellar IMF. The obtained best-fit model can provide an excellent representation of the galaxy spectrum,

but it cannot be evolved with time. Hence the optimised spectral fitting does not allow to study galaxy evolution in a cosmological context. Still, it can provide important insights on the types of stars which are effectively present in a stellar system (e.g. MacArthur et al. 2009). Optimised synthesis can also be used to obtain an instantaneous description of a galaxy spectrum in order to achieve accurate estimates of broadening of absorption lines for velocity dispersion measurements (see §5).

The alternative approach makes use of stellar evolutionary models, which describe the detailed time evolution of the luminosity and temperature of stars of different mass. Integrated spectra for galaxies are calculated by adding up the contributions of the individual model stars after assuming an IMF and a SFH. These so-called “evolutionary population synthesis models”, based on stellar evolution theory, can be evolved in time back and forth and galaxy evolution can be studied at arbitrary cosmic distances with the same underlying theory. The comparison between these models and observational data provides estimates for the average formation epoch, metallicity and SFH of a galaxy, thus enabling an evaluation of the stellar mass through the model mass-to-light, or  $M^*/L$ , ratio. These models, pioneered by Tinsley (1972), Tinsley & Gunn (1976), Renzini & Voli (1981), and Bruzual (1983), from which galaxy stellar masses are derived, will be described extensively in the next section (§2.2), focusing on the quantities that affect directly the stellar mass derivation, using various models available in the literature. We also address the impact of different model fitting techniques on extracted results and conclude with an assessment of the accuracy of galaxy stellar mass estimates.

## 2.2. Basics of Stellar Population Models

Evolutionary Population Synthesis (EPS) models provide the expected spectral energy distribution (SED) of a stellar population as a function of key parameters, such as:

1. the formation epoch, or the time elapsed since the beginning of star formation, normally referred to as the *age*,  $t$ , of the population, measured in years;
2. the star formation history (SFH), often parametrized with analytic functions, e.g.  $SFR \propto e^{-t/\tau}$  (see Figure 1);
3. the chemical composition, often referred to as metallicity and expressed as the fractional abundance  $Z$  of elements heavier than He and H ( $[Z/H]$ ), or as the fractional abundance of iron ( $[Fe/H]$ );
4. the chemical abundance ratios, or the ratios of all key elements with respect to those values measured in the Sun: e.g. the ratio of Magnesium to Iron  $[Mg/Fe]$ , the ratio of Oxygen to Iron  $[O/Fe]$ ; etc.;
5. the Initial Mass Function (IMF).

These are the main parameters controlling the time evolution of the population. Further assumptions need to be made for stars evolving over specific evolutionary phases, which will be mentioned below.

The model ingredients are: the stellar evolutionary tracks and/or isochrones, the stellar spectral libraries, the parametrization for the mass-loss which affects several late stages of evolution such as the Thermally-Pulsing Asymptotic Giant Branch (TP-AGB), the Red Giant Branch (RGB), the Horizontal Branch (HB), and also the Main Sequence (MS) in young populations.

A further model feature is the computational procedure, which may be an integration by mass of the luminosity contributions (so-called isochrone synthesis technique, Bruzual & Charlot 1993) or a technique based on Renzini’s *fuel consumption theorem* (Renzini 1981; Buzzoni 1989; Maraston

1998, 2005). This theorem states that the number of stars at each burning stage is proportional to the time it takes to exhaust the nuclear fuel burnt at that stage. This can be interpreted as the conservation of energy for stellar populations. In population synthesis models, it is a useful tool to quantify the contribution of rapid, and very luminous, stellar phases as found at the tip of the RGB, the AGB and the RGB bump (cf. discussion in Maraston 2005). Numerical experiments have shown that calculations based on the fuel consumption theorem and isochrone synthesis agree well (Charlot & Bruzual 1991), provided the mass bin of the mass integration in the isochrone synthesis case is small (Maraston 1998 finds  $10^{-6}M_{\odot}$  for the tip of the RGB). Moreover, the fuel consumption theorem is useful for including in synthetic integrated models those stellar phases for which a complete isochrone may not be available, such as the AGB, the Horizontal Branch with different morphologies, and the hot stars responsible for producing the UV-upturn in ellipticals.

A detailed description of the individual population models can be found in the corresponding papers, e.g. Vazdekis et al. (1996, hereafter, Vazdekis models), Fioc & Rocca-Volmerange (1997, PEGASE models), Bruzual & Charlot (2003, BC03), Maraston (2005, Maraston) and Conroy et al. (2009, FSPS), in addition to the reviews cited in the previous section.

The basic model EPS unit is the SSP. In the following SSPs are first used to illustrate the fundamental dependencies of  $M^*/L$  on age and metallicity, with composite models treated later on.

The most important driver of an SSP's luminosity evolution is its *age*, since the most massive stars live quickly but are orders of magnitude more luminous than smaller mass stars. For most IMFs the mass of a stellar population is dominated by the faintest stars and changes relatively little with time after the first Gyr of age (see Figure 2), but the luminosity of a population is dominated by its brightest stars showing large changes over time. Besides the Main Sequence, which provides a substantial contribution to the light at virtually every age, the brightest stars are found in different post-Main Sequence (PMS) evolutionary phases. Which phase dominates depends upon the age of the stellar population and the wavelength of observation. In young populations ( $t \lesssim 200$  Myr), Helium burning stars dominate the light, while at intermediate-age ( $200 \text{ Myr} < t \lesssim 2 \text{ Gyr}$ ), the Thermally-Pulsing Asymptotic Giant Branch (TP-AGB) stars take over (in some models, see below); at old ages, Red Giant Branch (RGB) stars outshine all other stars. AGB and RGB phases are mostly bright in the near-IR (NIR), while MS stars contribute mostly to optical bands (see Fig. 11 in Maraston 1998).

The luminosity of an SSP is therefore a strong function of time. This rate varies with wavelength given the contributions from different evolutionary phases. The overall luminosity evolution is more significant in the blue/optical spectral range where MS stars dominate, scaling roughly logarithmically with time (Tinsley 1972), as compared to the NIR light of old populations ( $t \gtrsim 2 - 3 \text{ Gyr}$ ), where the slowly evolving RGB stars dominate. The rate of luminosity change at NIR wavelengths is large near 0.3-1 Gyr in models including the TP-AGB phase (e.g. Maraston 1998, 2005; Marigo et al. 2008), since the onset of this phase implies a rapid increase of the NIR luminosity due to the cool and luminous TP-AGB stars. This effect is model-dependent. Global age and metallicity effects on the  $M^*/L$  in various bands for SSP models is shown in Figure 2.

The stellar population's metallicity also affects stellar evolution time scales and mostly the stellar SEDs. Metal-rich stars are cooler (because of a higher opacity in their stellar envelopes) and fainter (because the turnoff mass is smaller and most outgoing photons are trapped into their envelope), hence the higher  $M^*/L$  of a metal-rich population due to a lower luminosity (while  $M^*$  changes little). This trend is visible in Figure 2. Metallicity effects are significantly milder at NIR bandpasses; at very high metallicity (see the 3.5 solar metallicity track in Figure 2, long dashed line), the trend reverses in NIR bands, since the luminosity of such a metal-enriched population is

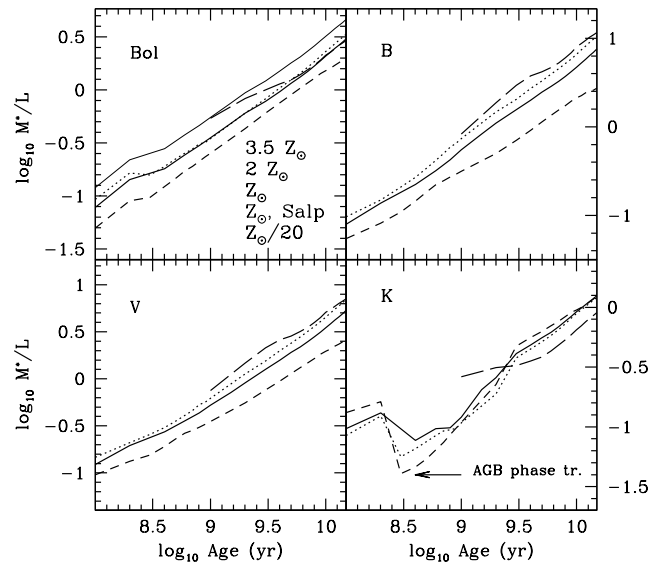


Figure 2: The stellar bolometric  $M^*/L$  and  $M^*/L$  in various bands ( $B$ ,  $V$ ,  $K$ ) as function of age for SSPs (single burst models) and the different indicated metallicities. All models for Kroupa IMF, except for the thin solid line in the top left diagram for a Salpeter IMF. The stellar mass  $M^*$  in this figure accounts for stellar mass losses, as in Maraston (1998; 2005). See also text for details. From Maraston (2005).

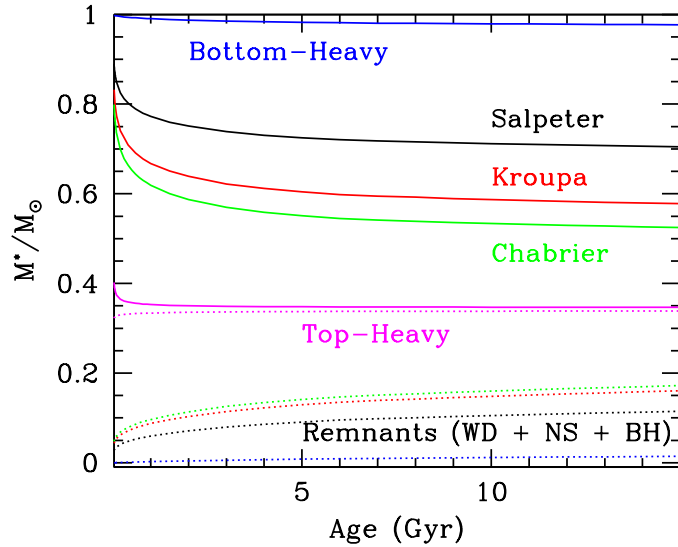


Figure 3: Evolution of the stellar mass fractions for stellar populations with the same total initial mass (normalized to  $1M_{\odot}$ ) and different initial mass functions. “Bottom-Heavy” and “Top-Heavy” are extreme cases of single-sloped IMFs with exponents 3.5 and 1 in the notation in which the Salpeter slope is 2.35.  $M^*$  evolves because stars die progressively and leave remnants with mass lower than the initial mass. Also shown are the fractions of  $M^*$  in remnants, namely White Dwarfs (WD), Neutron Stars (NS) and Black Holes (BH). Based on Maraston (2005) models.

concentrated at longer wavelengths (see Maraston 2005, for a full discussion). As is well known, ageing of a stellar population has the same effect as increasing metals since, as the most massive stars die out, the temperature distribution skews towards cooler values. The combined age and metallicity effects on dwarf and giant stars result in the so-called “age-metallicity (A/Z) degeneracy” in the optical region of their spectrum (e.g. Faber 1972; Renzini & Buzzoni 1986; Worthey 1994; Maraston & Thomas 2000). At optical wavelengths, the effect is such that a population of stars that is three times more metal rich mimics a population twice its age; this is the “3/2 rule” of Worthey (1994). This A/Z degeneracy at optical wavelengths obviously holds for  $M^*/L$  ratios as well. The optical A/Z degeneracy can be lifted by including data at longer wavelengths where giants dominate the spectrum and increasing metallicity results in redder colors, with a small dependence on age (with the exception of the AGB time). Worthey (1994) proposed that the spectral region around 1 micron (i.e. between the  $I, J$  bandpasses, depending slightly on age and IMF) is the most insensitive to metallicity. This notion has been exploited with color-color diagrams involving optical and at least one NIR passbands to analyse the stellar populations of integrated stellar systems (e.g. de Jong 1996; Bell & de Jong 2000; Maraston et al. 2001; MacArthur et al. 2004; Roediger et al. 2011). This concept of using an extended wavelength range has also been exploited for the study of high-redshift galaxies where the time spanned since the Big Bang is short and the age dependencies can be disregarded. In particular, the TP-AGB phase appears in galaxy spectra and the inclusion of the NIR allows galaxy ages to be better constrained (Maraston et al. 2006).

The total stellar mass  $M^*$  of an SSP also evolves with time. It typically decreases with time since the most massive stars progressively die leaving stellar remnants with mass smaller than the

initial ones.  $M^*$  is a strong function of the IMF. Figure 3 shows the evolution of  $M^*$  for several widely-used empirically-based IMFs, namely Salpeter (1955, black), Kroupa (2001, red), Chabrier (2003, green). These IMFs follow the same Salpeter power law slope for stellar masses larger than  $0.6 M_\odot$ , but have, to varying degrees, less stars than predicted by this Salpeter law slope below this mass limit (hence bottom-light). It should be reminded that Salpeter (1955, black), Kroupa (2001, red), Chabrier (2003, green) were all based on solar neighborhood data.

Also shown are two additional, not empirically-based IMFs meant to illustrate extreme cases of a dwarf-dominated (labeled “bottom-heavy”) and a giant-dominated (labeled “top-heavy”) IMF. These are single-sloped IMFs with exponents 3.5 and 1 in the notation in which the Salpeter’s one is 2.35, and are meant to illustrate galaxies dominated by low-mass and high-mass stars, respectively. Evidence for these extreme IMFs has been advocated in the literature. For example, van Dokkum & Conroy (2012) suggest a dwarf-dominated IMF in massive early-type galaxies (hereafter ETGs) to explain the strength of near-IR lines. Similarly, dynamical modeling studies (Cappellari et al. 2012, see also §5) and gravitational lensing studies (Treu et al. 2010; Auger et al. 2010b; Brewer et al. 2012, see also §7) of ETGs find evidence for the same type of IMF, with larger mass-to-light ratios than those predicted by Chabrier-like IMFs.

At the other end of the mass spectrum, Baugh et al. (2007) find that a top-heavy IMF in high-redshift bursts helps in explaining the colours of massive dusty and bursty distant galaxies (so-called “sub-millimiter” galaxies).

For the same total initial mass, the stellar masses of top-heavy IMFs evolve faster with time because of their larger proportion of massive stars. Most of the evolution occurs within the first Gyr, following the much faster evolution timescales of stars more massive than roughly  $2 M_\odot$ . Over a Hubble time, the amount of mass loss averages 30 to 40% of the initial mass. For composite population models with ongoing star formation, the decrement is reduced to  $\sim 20\%$  (see Maraston et al. 2006). In the Maraston models, the total remnant mass is budgeted amongst white dwarfs, neutron stars and black holes, following the analytical prescription of Renzini & Ciotti (1993). Maraston (1998) has explored IMFs with various exponents to show that  $M^*$  is maximally large for both dwarf-dominated as well as top-heavy IMFs, while the minimum  $M^*$  is achieved with a bottom-light<sup>2</sup>. IMFs such as the Scalo (1986), Kroupa (2001) or Chabrier (2003)-type IMFs (see Figs 16, 17 in Maraston 1998). A population born with a dwarf-dominated (or “bottom-heavy”) IMF has a large  $M^*$  since most stars have a small mass hence their extended lifetime and they contribute their total mass to  $M^*$ . A giant-dominated (or “top-heavy”) IMF has a large  $M^*$  given by the large number of massive remnants left by the evolved massive stars. These considerations are important as the value of  $M^*$  and the assumptions regarding the IMF impact directly the evaluation of the total stellar mass and the dark matter content in galaxies.

It should be noted that the predicted  $M^*$  may differ amongst different population synthesis models (see model comparisons between Bruzual & Charlot (2003) and Maraston (2005) in Fig. 3 of MacArthur et al. (2010)). This discrepancy may reflect a different accounting of stellar remnants. Hence, in comparing stellar masses obtained with different EPS models, one should also consider if and how the remnant masses are accounted for. For example, the Worthey (1994) models consider the mass contribution of the sole living stars, while Bruzual & Charlot (1993) consider a constant  $M^*$ , etc.

---

<sup>2</sup>Note that bottom-light refers to an IMF that is not as rich in dwarf stars as the Salpeter one, namely has a different slope above  $0.6 M_\odot$ . This is different from a top-heavy IMF, which is strongly dominated by giant stars due to a smaller exponent value all over the mass range

Other factors may complicate the broad-brush stellar evolution picture painted above. For example, stars in exotic evolutionary phases - such as Hot Horizontal Branch (HHB) at high metallicity and Blue Straggler (BS) stars - may alter the luminosity in the blue spectral range. These events probably affect mostly globular cluster studies, as the relative contribution of these phases to the total light of a galaxy should not be very significant. Also, one should not rely on a single band - especially a blue band - to determine stellar masses. The reddest side of the spectrum is equally challenging with the evolution along the TP-AGB being woefully uncertain due to the unknown mass loss. A lively debate pertaining to the reliability of optical/NIR stellar mass estimates is currently ongoing (e.g., Bruzual (2007), Marigo et al. (2008), Conroy et al. (2009), Zibetti et al. (2009), MacArthur et al. (2010), Conroy & Gunn (2010), Lyubenova et al. (2012), and Conroy (2013)).

A resolution of the significance of the TP-AGB phase to stellar mass estimates cannot be achieved in this review. However, a sound estimate of the stellar mass appears to be provided by the  $g - r$  color (Zibetti et al. 2009; Taylor et al. 2011). The effect of the TP-AGB phase on stellar mass derivations stemming from the use of models with and without a substantial TP-AGB contribution is highlighted when appropriate.

Extinction from dust also affects broadband luminosities hence  $M^*/L$  ratios and stellar population colors. However, in optical passbands the expected dust effects on  $M^*/L$  and population color run parallel to the expected stellar population color- $M^*/L$  relations and the mass estimates are only weakly affected (e.g. Bell & de Jong 2001). Likewise, line indices are only slightly affected by dust (MacArthur 2005) and can help disentangle extinction from population effects. For full stellar mass estimation dust extinction should be included in analyses, but dust is here not further addressed. Finally, most stellar systems will not be approximated by single-burst or SSP models, rather by composite populations with multiple ages and metallicities. The unknown galaxy star formation histories complicate the interpretation of integrated light observations and will be discussed in §2.3.1).

In the following we focus on mass determinations in relation to fitting of the broad-band spectrum, as this situation is common to both low as well as high-redshift studies, where high resolution spectral fitting is presently unfeasible. It should also be noticed that comparison of galaxy mass determinations obtained via broad-band or spectral fitting agree well when the signal-to-noise of the spectrum is high (Chen et al. 2012).

### 2.3. Stellar Mass from $M^*/L$ vs Colour Diagnostics

The list at the beginning of §2.2 makes clear that the "Big 4" variables that stand between the observed photometric distribution of star-light and our interpretation in terms of stellar mass are: (i) the correctness of stellar evolution models along stellar phases; (ii) the SFH; (iii) the chemical enrichment history; and (iv) the IMF. These are all inter-connected astrophysically and phenomenologically. Part of this interconnection could be labeled the 5th variable of "environment". In most cases when analysing galaxies, little information is available on the big 4, with perhaps the exclusion of (i) which can be calibrated and tested in local stars. Hence, usually a variety of models are assumed including different formalizations for (ii), (iii) and (iv). The significance of these assumptions is shown below.

Following Bell & de Jong (2001), we illustrate how  $M^*/L$  ratios in the  $B$  and the  $K$ -band correlate with ( $B-R$ ) and ( $I-K$ ) colors (as tracers of age and/or metallicity), and the mostly age sensitive  $H\delta_A$  index. Figure 2 shows that  $M^*/L$  values in other optical passbands behave similarly as the  $M/L_B$  plots, just with a slightly different slope.

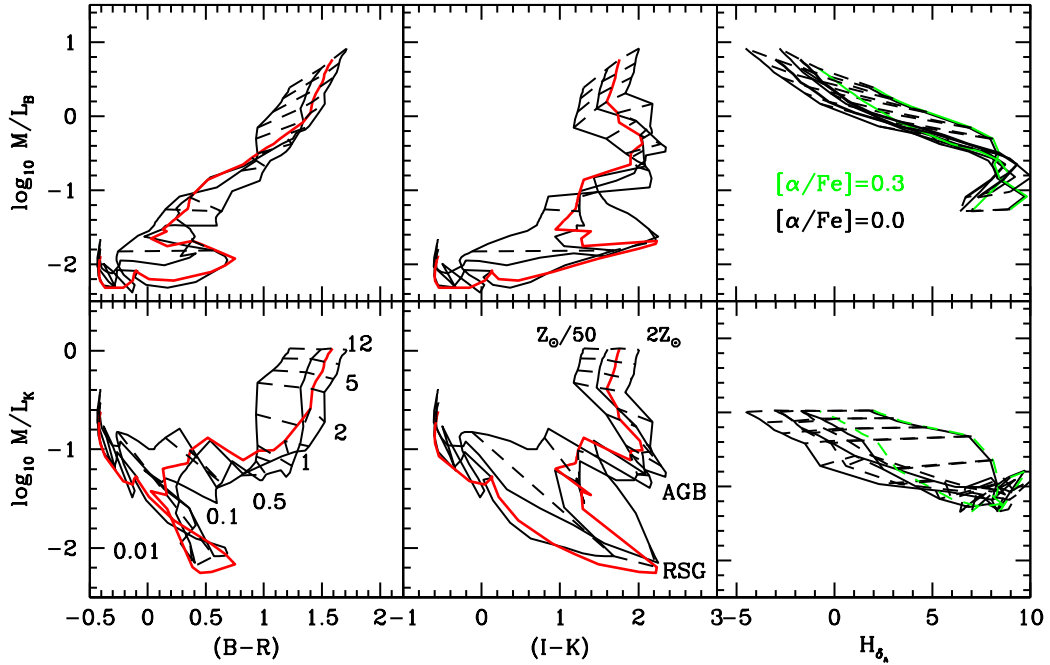


Figure 4: Trends of Maraston (2005) SSP models with various ages and metallicities, and a Salpeter IMF.  $M^*/L$  values in  $B$  and  $K$ -band (top-to-bottom) are shown versus  $(B-R)$ ,  $(I-K)$ , and the  $H\delta_A$  line index (left-to-right). The latter models are from Thomas et al. (2011a); green lines connect models for  $[\alpha/\text{Fe}]$  ratio of +0.3, black lines connect solar-scaled models. Models with a same age (in Gyr) are connected with dashed lines, models with a same metallicity with solid lines ( $Z=0.001, 0.01, 0.02, 0.04$ ). Red lines highlight solar metallicity ( $Z=0.02$ ).

Figure 4 shows grids of model colors,  $M^*/L$  and a spectroscopic index for SSPs of various ages and metallicities. Once a population is older than about 0.1 Gyr,  $M^*/L_B$  versus  $(B-R)$  displays a good correlation, which is fairly independent of metallicity. The  $M^*/L_K$  versus  $(B-R)$  is more ambiguous with age as  $M^*/L_K$  evolves slowly after the TP-AGB phase-transition (meaning, after some Gyr of age). The relations of  $M^*/L$  with  $(I-K)$  color cannot be used alone to derive  $M^*$  because the model loci are nearly vertical after 0.1 Gyr, meaning that at a given metallicity  $M^*/L$  is nearly independent of color. As mentioned earlier, the luminosity in the NIR after a few 100 Myr is dominated by evolved (AGB and later RGB) stars. The lower NIR  $M^*/L$  at early ages ( $\sim 10$  Myr) is due to short-lived, bright red supergiants. Note that this caveat is only relevant for very recent star formation, basically from HII regions.

Perhaps the best approach to measuring  $M^*/L$  is to fit SEDs simultaneously in at least three passbands, with one in the NIR, hence breaking the age-metallicity degeneracy. Modulo model uncertainties as detailed in the following sections, convergence to the right  $M^*/L$  value may be achieved (as shown by Zibetti et al. (2009) or by Maraston et al. (2001) for massive star clusters and Maraston et al. (2006) for high-redshift galaxies).

Finally, the rightmost column of Figure 4 shows an example of  $M^*/L$  trends with an absorption line index. The  $H\delta_A$  Balmer line index (Worley & Ottaviani 1997) was chosen as it has been used specifically for the estimation of  $M^*$  for the SDSS galaxies (e.g. Kauffmann et al. 2003). This index is sensitive to the age of the stellar population, being the strongest around 0.3–0.5 Gyr (depending on metallicity) when A-type stars dominate the spectrum, and smaller at both older and younger ages (see Fig. 8 in Maraston et al. 2001). This degeneracy for  $H\delta_A$  can obviously be broken (for a single burst population) by using an extra spectral indicator with a monotonic behavior with age. Two further complications should be noted. Because of its temperature dependence, the index is also affected by old, though hot, stars such as metal-poor blue HB stars (Maraston et al. 2003). Moreover, the index has been shown to be sensitive to the  $[\alpha/\text{Fe}]$  ratio, because of strong Fe lines present in the pseudo-continua (Thomas et al. 2004a). For instance, the index is stronger in  $[\alpha/\text{Fe}]$ -enhanced populations (such as those of massive ETGs) than in solar-scaled ones. The trend with abundance ratios is shown in Figure 4, where the grid in green displays models for the same total metallicity  $Z$ , but enhanced  $[\alpha/\text{Fe}]=0.3$ . The consideration of these effects when dealing with massive galaxies is important, as a strong index can otherwise only be explained by a lower age, which in turn would induce a mismatch in the derivation of the  $M^*/L$  ratio. Ideally in the future it should be possible to complete the last panel of Figure 4 by considering the abundance-ratio effects on colors and mass-to-light. Broadbrush, the model grid distribution shown in  $H\delta_A$  versus  $M^*/L$  is similar to the  $(B-R)$  versus  $M^*/L$  distributions, except for the very youngest ages. The same degeneracies are therefore also present in composite age models and we will no longer show the  $H\delta_A$  models separately.

Single burst models are ideal cases that apply well to star clusters, but not to galaxies, where a prolonged star formation is in general more appropriate. The determination of  $M^*$  in these cases is much more difficult, as the latest generations dominate the light and drive down the  $M^*/L$  hence  $M^*$ , which leads to underestimate of the stellar mass (Bell & de Jong 2001; MacArthur et al. 2009; Maraston et al. 2010). These issues are discussed in the next section.

### 2.3.1. Effect of Star Formation History

Stellar systems like galaxies are expected to have a wide range of SFHs. The effect of prolonged star formation history on the model grids is visualised in Figure 5 by using exponentially declining SFR models or  $\tau$ -models (as introduced by Bruzual 1983), with  $\text{SFR}(t) \propto \exp(-t/\tau)$ , where  $\tau$

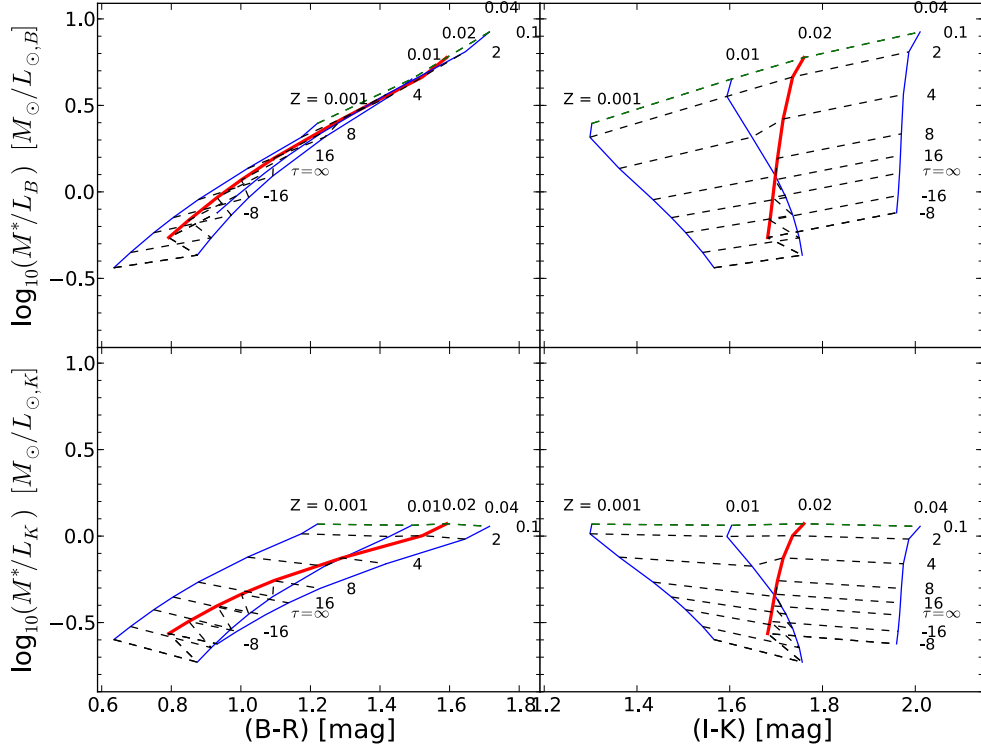


Figure 5: Trends in  $M^*/L$  ratios using exponentially declining star formation rate models. The models are the same as in Figure 4, except that instead of a single burst an exponentially declining star formation rate is used observed at age 12 Gyr after star formation began. Models with the same  $e$ -folding timescale  $\tau$  are connected with dashed lines, where positive  $\tau$  stands for decreasing star formation rate with time, negative  $\tau$  for increasing star formation rate, and  $\tau = \infty$  is a constant star formation rate model. Solid lines connect models with equal indicated metallicity, where the red line highlights solar metallicity. Based on Maraston (2005) models.

indicates the  $e$ -folding timescale of star formation and can be both positive and negative. This model is a reasonable first approximation of the star formation history of a spiral galaxy or, for very low  $\tau$ 's, of a passive system. Negative  $\tau$  values represent galaxies which have increasing SFRs, especially galaxies with recent star bursts (e.g. Bell & de Jong 2000).

The model  $M^*/L$  ratios in the optical are nearly degenerate versus  $(B-R)$  in Figure 5. This degeneracy is somewhat broken in  $(B-R)$  versus the near-IR  $M^*/L_K$ , especially for the lowest metallicities ( $Z < 0.004$ ). However, realizing that chemical evolution caused by modest amounts of star formation raises the system metallicity rapidly to at least 0.1 solar (or  $Z=0.002$ ; in a closed box, conversion of  $\sim 20\%$  of gas mass into stars raises the average metallicity to over 0.1 solar), the range of relevant metallicities becomes narrower in most applications, making the color- $M^*/L_K$  relation tighter.

Tracing mainly evolved stellar populations,  $(I-K)$  is largely metallicity sensitive, weakly sensitive on age, and  $(I-K)$  on its own (without any other passbands) is not useful for mass estimation as Figure 5 clearly shows. Moreover, the details of evolved stellar evolution stages are still relatively poorly modeled and the exact shapes of these  $(I-K)$  diagrams are highly dependent on models used, as shown in §2.3.3.

Not all stellar systems are  $\sim 12$  Gyr old, either because they are observed at higher redshift when the Universe was much younger or because they may have had their major epoch of star formation significantly delayed. The effect of a younger final age on exponential SFR models is shown in Figure 6. This figure shows the same range of  $\tau$  values as in Figure 5, though now after 12, 8.5, 6, 3, and 2 Gyr (and for clarity only for solar and 1/20 solar models). For concordance cosmology, this corresponds to roughly redshifts  $z=0, 0.3, 0.7, 1.5$ , and 2 when starting star formation 12 Gyr ago. Model colors are shown in rest-frame.

The main conclusion from the color- $M^*/L$  diagrams in Figure 6 is that a final age change mainly results in a simple offset since the slope of the relation stays nearly constant especially for solar metallicities. The age-metallicity degeneracy stays intact in the optical relations. Only at the youngest ages and lowest metallicities, and predominantly in  $M^*/L_K$ , does the slope of the relation change.

So far only smooth SFHs have been considered in this section, but star formation will be more bursty in nature for especially smaller systems. A recent burst of star formation will dramatically lower the  $M^*/L$  of a total stellar system as well as change its SED to make it look much younger, because a young population is so much more luminous. The size of the effect will depend on the size of the star burst relative to the underlying population and the age difference between the populations. This effect may be most relevant for small galaxies, where any burst of stars is significant, and for stellar masses dominated by an old population, where any trickle of young stars will dramatically alter their properties. For instance, the rejuvenation caused by a “frosting” of young stars has been used to explain the apparent line indices based young ages of morphological ETGs that are thought to be mostly old (de Jong & Davies 1997; Trager et al. 2000), though hot horizontal branch stars produce the same effect on the observed line strengths (Maraston & Thomas 2000).

Figure 7 shows the effect of adding 10% of the final mass of the system in a star burst of 0.2 Gyr duration. The models start with the canonical set of 12 Gyr old exponential SFR models of Figure 5 to which 1, 2, 3, 4, or 6 Gyr old star bursts are added. For clarity, only the solar and 1/20 solar results are shown.

A number of features are apparent from Figure 7. Firstly, the effects of starbursts are largest in both color and  $M^*/L$  when starting with an old, small  $\tau$  population (independent of metallicity).

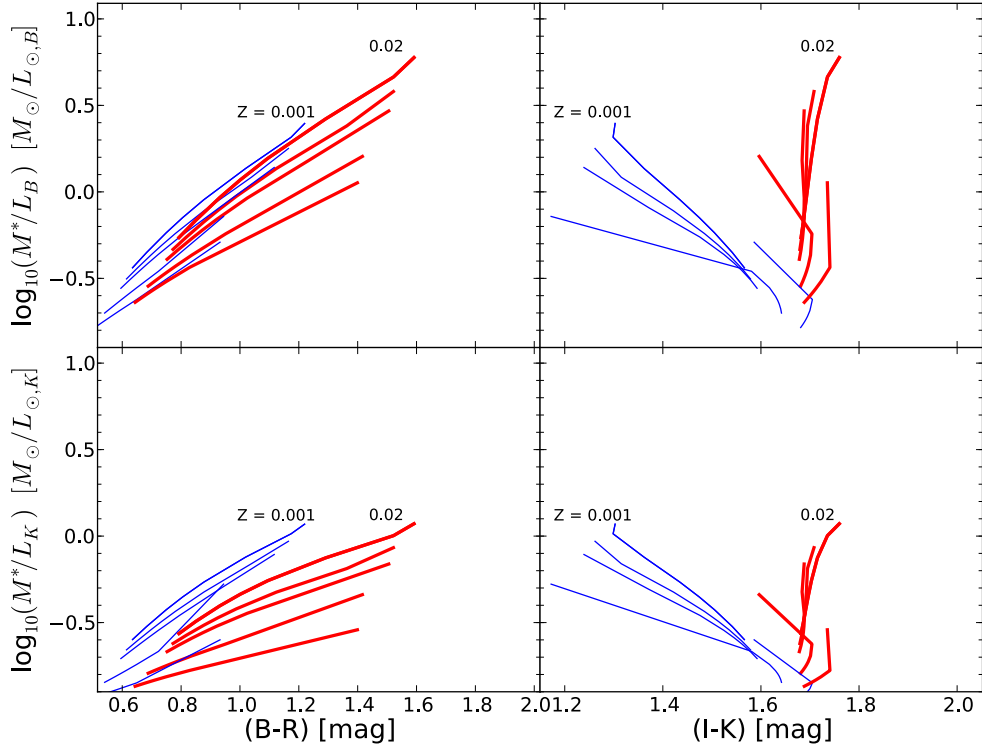


Figure 6:  $M^*/L$  ratios for exponentially declining star formation rate models with different final age. The models are the same as in Figure 5, except that the populations are now observed 12, 8.5, 6, 3, 2 Gyr (top-to-bottom) after star formation commenced. The top ends of the lines are the ends with the smallest positive  $\tau$  values, i.e. the oldest average age. For clarity, only the solar metallicity ( $Z=0.02$ ; thick red lines) and the 1/20th solar metallicity ( $Z=0.001$ ; thin blue lines) are plotted and the dashed lines connecting the same  $\tau$  values are not shown as in Figure 5. In principle these models form similar grids with different offsets. Based on Maraston (2005) models.

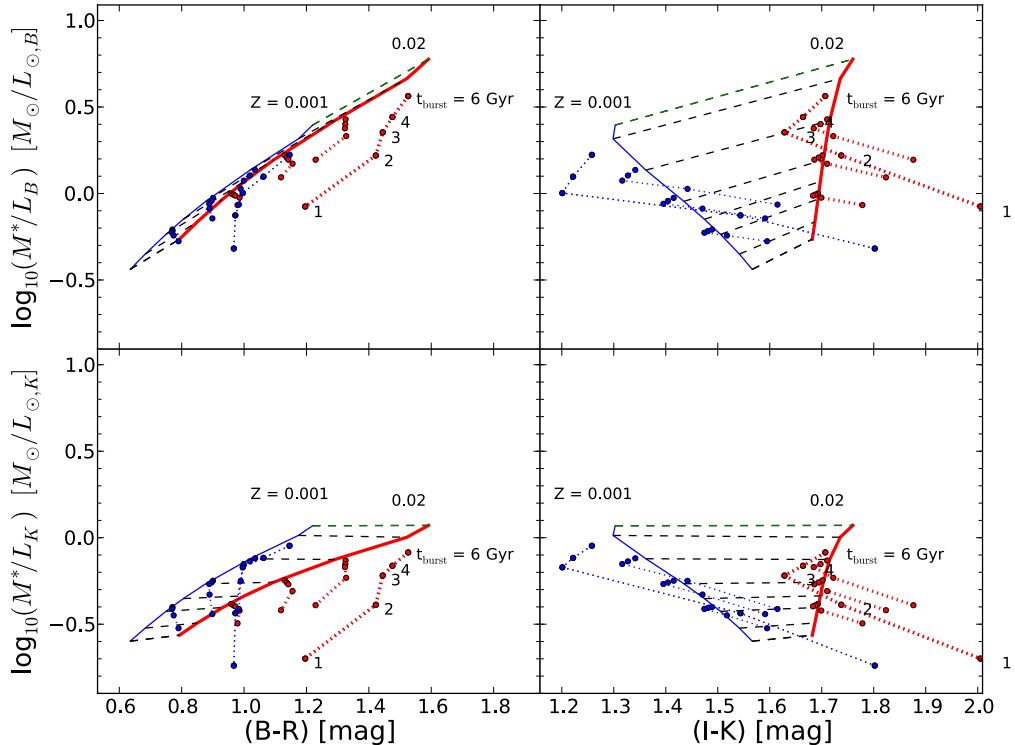


Figure 7:  $M^*/L$  ratios for exponentially declining star formation rate models with an additional star burst. The starting models without starburst are the same 12 Gyr old exponentially decaying SFR models as in Figure 5, except that for clarity only the solar metallicity ( $Z=0.02$ ; thick red) and the 1/20 solar ( $Z=0.001$ ; thin blue) are plotted. For  $\tau$  values  $\infty, 8, 4, 1$  a 10% final mass fraction starburst of 0.2 Gyr duration is added that occurred 1, 2, 3, 4, 6 Gyr ago (solid circles connected with dotted lines). Based on Maraston (2005) models.

Secondly, almost any burst of star formation will bias models towards lower  $M^*/L$  values at a given color compared to smooth star formation models. At a given  $(B-R)$  color, the maximum offset from a smooth SFH due to a late starburst is less than 0.5 dex, but in most combinations it is less than 0.3 dex. This effect is stronger for higher metallicities. Finally, when starting off from a fairly young underlying population ( $\tau > 5$  Gyr) the effects of modeled starbursts are only larger than 0.1 dex in  $M^*/L$  for bursts younger than 1–2 Gyr. In this case the population may actually become redder than the underlying population in  $(B-R)$  after a few Gyr after the burst, because the starburst will increase the luminosity weighted average age of the total population. When starting from mostly old populations ( $\tau < 5$  Gyr), the effect of a starburst on the  $M^*/L$  may be long-lived (4–6 Gyr).

If most galaxies had irregular star formation in their last 2–5 Gyr with variations in star formation rate of factors greater than two, most galaxies are expected to lie below the smooth exponential SFR model SED- $M^*/L$  relations. One can calculate this offset and increase in scatter by using models that include a varying amount of star formation and incorporate this in the derived SED- $M^*/L$  relations. Alternatively, one can reduce the scatter induced by these recent star burst by including an SED tracer of a stellar population younger than 2–3 Gyr when fitting the SED. One has to choose a tracer that is not degenerate in age and metallicity with the other SED tracers used. Some options include a  $(U-B)$  color or a higher order Balmer line. The combination of such recent star formation indicators and SED templates with an irregular SFR should yield a scatter reduction in  $M^*/L$  by  $\sim 0.1$  dex if many objects with irregular SFR are contained in the sample.

More bandpasses (at least four) can provide additional degeneracy lift. For example, in the Maraston models a very red  $(I-K)$  color only corresponds to the TP-AGB dominated ages of  $\sim 1$  Gyr, which is more pronounced in a small tau-model. Most models behave similarly in the optical bands, while the NIR is driven by the treatment of evolved phases, for which there is a strong variance within existing models (see also §2.3.3).

### 2.3.2. Stellar Initial Mass Function

As noted in §2.1, the IMF is a major uncertainty in SP modelling and  $M^*/L$  ratios are strongly dependent on it. The IMF of external galaxies is in principle unknown (though see Tortora et al. 2013), but most IMFs determined for the Milky Way in the Solar neighborhood show a very similar behavior, namely a turnover in their logarithmic slope at about 0.6 Solar mass. The exact details of this turnover in IMF slope around this mass scale are poorly constrained (see discussions in e.g. Scalo 1986; Kroupa 2001; Chabrier 2003), but critically determine the total mass of the system. Figure 8 visualises the solar metallicity  $M^*/L$  versus color relation using different IMFs, specifically the same as in Figure 3. The predicted relations are clearly very similar in shape for exponential SFR models and the plausible Salpeter or Kroupa IMF (the Chabrier and Kroupa IMF’s behave very similarly). These different IMFs result primarily in offsets in zero-point of the  $M^*/L$  versus color relations. These offsets are independent of metallicity and nearly the same whether one measures  $M^*/L_B$  or  $M^*/L_K$ .

The  $M^*/L$  ratio versus color slope remains unchanged even assuming a rather extreme bottom-light IMF, but the offset is much larger (a factor of  $\sim 10$ ) for the latter (Figure 8). However, this IMF is ruled out by strong gravitational lensing and stellar dynamics which only permit  $M^*/L$  ratios up to a factor of  $\sim 2$  higher than that predicted for a Salpeter IMF (e.g. Brewer et al. 2012; Cappellari et al. 2012).

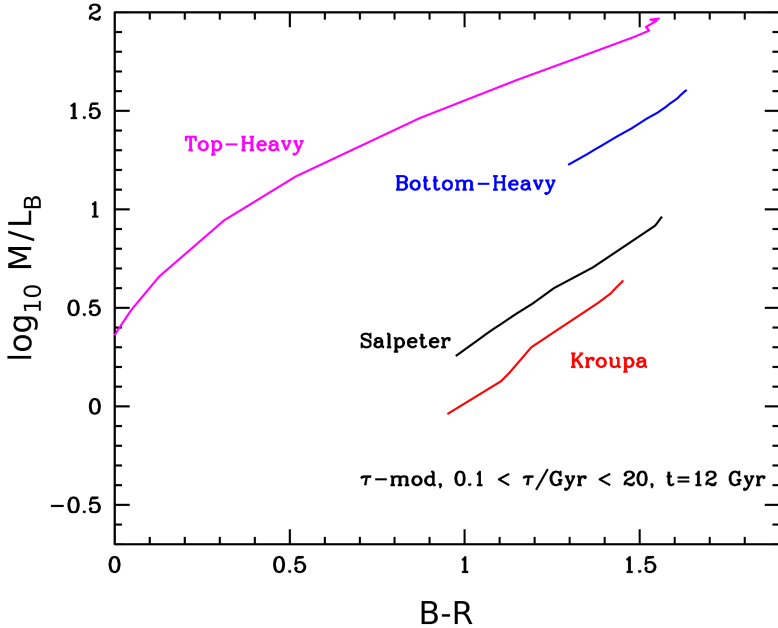


Figure 8:  $M^*/L$  ratios vs  $(B-R)$  for exponentially declining star formation rate models of age 12 Gyr and solar metallicity, with a Salpeter, Kroupa and the same top-heavy and bottom-heavy IMFs as in Figure 3.

### 2.3.3. Model ingredients

As noticed in §2.1, EPS models include several ingredients and assumptions (stellar evolutionary tracks, stellar spectral libraries, IMF, etc.), which may be treated differently in different models. It is beyond the scope of this review to investigate the effects of each ingredient and its uncertainty on the models (for reviews see, e.g. Charlot et al. 1996; Maraston 2005; Conroy et al. 2009; Leitherer & Ekström 2012). Rather,  $M^*/L$  versus color relations for the different EPS are compared here using exponential SFR models. The GALAXEV, PEGASE and FSPS models are used with a Chabrier IMF, while the Maraston models use a Kroupa IMF.

Not surprisingly, the GALAXEV (BC03) and PEGASE results are very similar in all color- $M^*/L$  diagrams, since they use the same Padova stellar evolutionary tracks and similar spectral libraries. At optical wavelengths, nearly all models agree to within 0.1 dex in  $(B-R)$  versus an  $M^*/L$  measured in an optical band.

As discussed in Charlot et al. (1996) and Maraston (2005), the treatment of TP-AGB and RGB stars lead to the largest discrepancies in the NIR which is rehashed here with the  $(I-K)$  versus  $M^*/L$  diagram. The  $(I-K)$  colors of old (small  $\tau$ ) populations with the same metallicity can differ by 0.2 mag, and up to 0.5 mag for young populations. The reason for this discrepancy is two-fold. Firstly, they are due to a different treatment of the (uncertain) late stages of stellar evolution (red supergiant, AGB, RGB). In these late stages, stars suffer mass loss that cannot be connected to the basic stellar parameters from first principles and must be parametrized and calibrated with data. This uncertainty involves energetics, stellar temperatures and stellar spectra for the AGB, and mostly stellar temperatures and spectra for the RGB. The importance of the TP-AGB phase of stellar evolution became clear, when it was shown that the BC03/Pegase/Starburst99 and Maraston

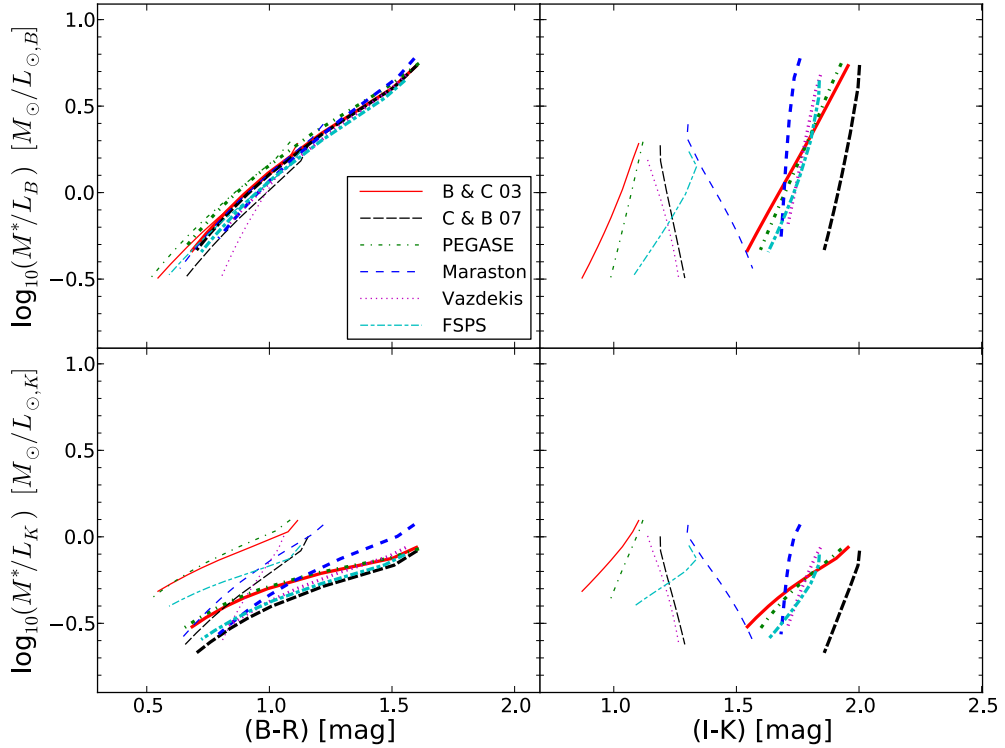


Figure 9:  $M^*/L$  for exponential SFR models of age 12 Gyr using SSPs from different authors. The models compared are GALAXEV 2003 (Bruzual & Charlot 2003) with Padova 1994 tracks, GALEXEV (2007, an updated version of (Bruzual & Charlot 2003) with different treatment of the TP-AGB phase), PEGASE 2.0 (Fioc & Rocca-Volmerange 1997), and the FSPS models (Conroy et al. 2009) all based on Padova stellar models and a Chabrier (2003) IMF, and the Maraston (2005) and the Vazdekis et al. (1996) models using a Kroupa (2001). Solar metallicity ( $Z=0.02$ ; thick lines) and  $1/5$  solar metallicity ( $Z=0.004$ ; thin lines) models are used, except for the Maraston models, where this metallicity is not available and a lower metallicity model of  $Z=0.001$  is plotted. The Chabrier and Kroupa IMFs give essentially the same results for broadband colors, hence by using these IMFs all the model sets can be compared even though some models are only available with either Chabrier or Kroupa IMFs.

(2005) models yielded systematic differences of several tenths of magnitudes in the NIR at intermediate ages of 0.2 to 2 Gyr (Maraston 2005; Maraston et al. 2006; Bruzual 2007), mostly attributable to differences in the treatment of TP-AGB stars. Secondly, numerical instabilities of luminosity integration along short-lived phases in the isochrone synthesis approach (see Maraston 1998, 2005) may explain why models based on the same stellar evolution tracks exhibit large fluctuations.

The models in Figure 9 with a small TP-AGB contribution (i.e. BC03, Pegase) display bluer values of  $(I-K)$  colors at young ages (low  $M^*/L$ ). The Vazdekis models would behave similarly, but they are redder only because they only include ages  $> 0.1$  Gyr. Models with a substantial TP-AGB contribution (Maraston 2005, GALEXEV 2007) display redder colors at young ages/large or negative  $\tau$ 's. At solar metallicity, old ages/small  $\tau$ 's (upper right corner of the diagram), models based on Padova tracks (B&C, FSPS, Pegase) are redder than the Maraston models based on the Cassisi et al. (1997) tracks because the former have a redder RGB (Fig. 9 in Maraston 2005, and discussion therein).

#### 2.4. Data Fitting Techniques

The variety of techniques to derive  $M^*/L$  values by fitting spectra has increased dramatically in the last decade (e.g. Walcher et al. 2011). Methods depend on the data available, ranging from two bandpasses (e.g. Bell & de Jong 2001), multiple broadband colors (e.g. Bell et al. 2003; Maraston et al. 2012), a few line indices (e.g. Kauffmann et al. 2003; Thomas et al. 2011b) to full spectral fitting (e.g. Blanton & Roweis 2007; Tojeiro et al. 2009; Chen et al. 2012). Broadband imaging is often preferred over spectroscopy when large numbers of galaxies are required, when 2D stellar maps are created (Zibetti et al. 2009), or in low S/N situations as in high-redshift studies (e.g. Daddi et al. 2005; Shapley et al. 2005; Maraston et al. 2006; Cimatti et al. 2008). While more data points should in theory increase the accuracy of the  $M^*/L$  estimation, this may not always be true in practice due to two reasons. Firstly, EPS models have larger systematic uncertainties at certain wavelengths (Figure 9). Such intrinsic model uncertainties should be taken into account while fitting the data, however this is rarely done (as it is not easy to quantify) and typically only the error in the measurement is used when weighing the different data points in the fit. Secondly, using more data points can also lead to systematic biases if the set of model templates is too limited to fit the complexity of the data. For example, long-ward  $K$  the SED is dominated by dust re-emission which is very difficult to model. Without a good description of dust re-emission, the fitting of far-IR data is meaningless and can even impede a proper understanding of shorter wavelength data. Another case is when smooth (e.g. exponentially declining) SFHs are used with data sets that include indicators very sensitive to recent star formation. In such cases, templates should include at least a combination of a smooth SFH and a late starburst.

Methods furthermore vary according to the number of templates fitted to the data, namely the range and type of SFHs and metallicity distributions (single burst, multiple burst, exponential SFH, etc.). This can lead to significant offsets whether one assumes that the most significant SF burst occurred 12 Gyr ago (e.g. Bell & de Jong 2001) or more recently (e.g. Trager et al. 2000). Integrated light SEDs rarely contain enough information to discriminate between burst timescales 8–13 Gyr ago, which can lead to offsets as high as 0.2 dex in  $M^*$ .

Finally, many mathematically different techniques have been used to fit models to data, ranging from simple minimum  $\chi^2$  fitting (e.g. Bell et al. 2003), to maximum-likelihood (e.g. Kauffmann et al. 2003; Taylor et al. 2011), and Bayesian methods (e.g. Auger et al. 2009). For large data samples, information compression techniques are often used to reduce computational time, such as principle component analysis (Chen et al. 2012), non-negative matrix factorization (Blanton &

Roweis 2007), and the linear compression technique used in MOPED (Panter et al. 2007). The optimum amount of reduction allowed while retaining all information available will depend on the data quality and model used and may be hard to determine (Tojeiro et al. 2007; Graff et al. 2011).

### 2.5. Robustness of Stellar Mass Derivations

Determining the accuracy and robustness of stellar mass estimation from SED fitting is non trivial since some of the intrinsic key properties of galaxies, most notably the SFH and the stellar IMF, are unknown. Nonetheless, estimates of uncertainties and systematic biases of a particular fitting method can be obtained by testing the results on mock galaxies. These mock galaxies are often based on semi-analytic galaxy formation models, providing hundreds of thousands of test galaxies with a wide range of (hopefully realistic) SFHs. Such comparisons can also provide guidance on the minimal and optimal data sets to use when fitting real data (Pforr et al. 2012; Wilkins et al. 2013).

The sections above make clear that several parameters affect the accuracy and biases of stellar mass estimates, the most important being: the IMF, data quality, EPS model, SFHs and chemical evolution, dust, and redshift. More detailed analyses can be found in, e.g. Conroy et al. (2009), Gallazzi & Bell (2009), Pforr et al. (2012), Wilkins et al. (2013), and references therein.

Firstly, the IMF is the main systematic uncertainty in  $M^*/L$  estimation. However, as long as the IMF slope does not change for  $M > 1 M_\odot$ , as is the case for Salpeter (1955), Kennicutt (1983), Kroupa (2001), or Chabrier (2003) IMFs, the incognita from the Initial Mass Function only results in a constant offset in stellar mass as the luminosity does not vary and only the total mass of a stellar population changes. A significant change of the IMF slope above  $M > 1 M_\odot$  implies a non constant offset (e.g. Pforr et al. 2012).

Constraints on the IMF normalization can be derived by comparing stellar population mass estimates to dynamical or lensing mass estimates such as described in the remainder of this review, with the simple notion that the mass in stars should not exceed the total measured one. Such a comparison is done in Bell & de Jong (e.g. 2001) using disk galaxy rotation curves. However, only upper limits can be obtained, since a fraction of the luminous mass can always be traded off to a (smooth) dark matter component with a similar mass distribution as the light. Only when there is a dynamical substructure on scales smaller than those expected for dark matter one can hope to obtain lower limits to the stellar mass normalizations. Examples include the dynamics of bar and spiral structure in disk galaxies, the effect of bulges on galaxy rotation curves, and the vertical velocity dispersion in disk galaxies (see §3). de Jong & Bell (2007) performed such a comparison between dynamical and stellar population mass estimates and showed that the SED- $M^*/L$  relation normalization can be constrained to within  $\sim 0.2$  dex (66% confidence level). If the IMF varies amongst galaxy types, as argued for instance by Treu et al. (2010), Auger et al. (2010b), Cappellari et al. (2012) and Conroy & van Dokkum (2012) (see also §5.5.1 and §7.3.3), the IMF effect becomes much more complicated and unpredictable, let alone any evolution of the IMF with redshift (van Dokkum 2008).

Proceeding with random uncertainties, the accuracy of mass estimation depends on the quality of the data. For example, Gallazzi & Bell (2009) determine that a spectral signal-to-noise of  $S/N > 20$  is required to get an accuracy of 0.1 dex in  $M^*/L$  when using a few optical indices. Tojeiro et al. (2009) performing full spectral fitting derived a  $\sim 0.1$  dex uncertainty in  $M^*$  due to the quality of the data ( $S/N \sim 10 - 15$  per pixel). Chen et al. (2012) exploited low  $S/N$  high- $z$  spectra from the SDSS-III/BOSS survey to argue that spectral fitting relying on a principal component analysis can lead to reliable results also for  $S/N \sim 5$ , though the actual parameters of the populations may not

be well determined. Fitting the broad-band signal instead of the spectrum for the low S/N case may be the best choice Maraston et al. (2012), and the two methods converge at high S/N.

The use of different EPS models also affects stellar masses, with an uncertainty of  $\sim 0.2$  to  $0.3$  dex (on the logarithmic mass, Maraston et al. 2006; Conroy et al. 2009; Ilbert et al. 2010), reaching at most  $0.6$  dex at  $z \sim 2$  (Conroy et al. 2009) when TP-AGB stars dominate the spectrum and the models vary most (see §2.3.3).

The adopted SFH in the models significantly contributes to the uncertainty and biases in  $M^*/L$  values (e.g. Maraston et al. 2010) for high-redshift galaxies. The range in functional forms (if a function is used at all), the chosen oldest and youngest stars, and the inclusion and number of starbursts all affect the uncertainty and bias in the  $M^*/L$  determination.

For galaxies at low-redshift with late star formation, Gallazzi & Bell (2009) find that the  $M^*/L$  may be overestimated by  $0.1$  dex when using spectral indices. Nearly similar accuracies can be obtained using one optical color, the choice of which may vary with redshift (Wilkins et al. 2013). Using more than one color reduces the offsets slightly, but even more colors will not reduce the uncertainties and offsets (Gallazzi & Bell 2009; Zibetti et al. 2009). This is in apparent contrast with Pforr et al. (2012), who argue that more passbands further reduce uncertainties and stress the benefits of near-IR data. This may be related to the limited set of templates adopted by Pforr et al. compared to the star formation histories in their mock catalog (if the templates do not fully span the range of “observed” galaxy parameters, more data help getting closer to the correct result) and possibly due to their inclusion of dust effects. Pforr et al. (2012) also show that - when the template star formation history matches the real one - as is the case for positive tau models for high-redshift galaxies (Maraston et al. 2010), the mass recovery from spectral fit is excellent and mostly independent of the waveband used in the fit.

Indeed, from the point of view of the SFH, high-redshift galaxies have less uncertain  $M^*/L$  as long as the redshifted data capture all necessary rest-frame wavelengths. This stems from a decrease in the number of possible SFHs (less time has passed since the initial star formation). Most notably the age difference between any old, underlying population and a recent burst is smaller, and the “frosting” or outshining effect by young stars is decreased (Maraston et al. 2010). For similar quality multi-passband data, this can reduce biases for dusty galaxies from  $0.5$  dex at  $z = 0.5$  to  $0.1$  dex at  $z = 2$  and uncertainties from  $0.5$  dex at  $z = 0.5$  to  $0.2$  dex at  $z = 2$  (Pforr et al. 2012).

Finally, dust in galaxies significantly alters the SED (e.g. MacArthur 2005). In case of very dusty systems spectroscopy clearly becomes the favoured channel for  $M^*/L$  estimation. Access to both photometric and spectroscopic data would enable a derivation of extinction values by comparing SED expectations derived from the spectral features to the observed photometry (e.g. Kauffmann et al. 2003). Pforr et al. (2012) show that including dust prescription in the SED fit dramatically increases the uncertainties and biases in stellar  $M^*/L$  estimates especially at low redshifts, with offsets being as large  $0.5$  dex and similarly sized rms uncertainties. When focussing on mass estimation, the conservative choice of neglecting dust as an additional parameter in the spectral fitting may lead to a more robust determination of stellar mass (Maraston et al. 2012).

## 2.6. Future Prospects

The stellar mass of galaxies,  $M^*$ , is a key parameter in studying the formation and evolution of galaxies over the cosmic time, tracing galaxy dynamics, and disentangling the contribution from dark matter to the overall galaxy potential. In this Section, we have reviewed the basic physics entering the derivation of  $M^*$ . This exploits the theory of stellar evolution to calculate the mass in stars from the amount of stellar light that galaxies emit. The modelling of the integrated galaxy light requires several assumptions regarding the distribution of ages and chemical compositions of the component stars (i.e. the galaxy star formation history), the distribution of stellar masses at birth (the stellar initial mass function) and the attenuation of light from dust. The fundamental tool to perform such modelling is called a “Stellar Population model”. We have described such models, highlighting their main uncertainties and how these affect the derivation of  $M^*$ . Using models from various authors we visualised the basic relations between  $M^*$  and the integrated spectral energy distribution, including color and spectral indices. Furthermore, we discussed the part of  $M^*$  which is composed of stellar remnants, such as white dwarfs, neutron stars and black holes, which do not emit light but contribute to the total mass, and their dependence on the stellar initial mass function.

Finally, we briefly addressed the main techniques to calculate  $M^*$  found in the literature and discussed the typical uncertainties and biases of SED based on stellar mass estimates. While these depend on galaxy type, they are: (i) for star-forming galaxies, the unknown star formation history and the fact that a small fraction by mass of newly born stars can outshine the underlying older population dominating the mass, thus jeopardising the mass derivation; and (ii) for both star-forming and passively evolving galaxies, the unknown IMF. Spectro-photometric data are most crucial for treating star-forming galaxies whereas the near-IR bands help in constraining the older, outshined component of the stellar population (see Figure 3 in Maraston et al. 2010).

Despite many unknowns, and excluding extreme cases of very dusty galaxies or galaxies with complicated and bursty star formation histories, relative stellar masses between galaxies can be regarded robust within 0.2 – 0.3 dex. The still poorly constraint IMF normalisation will shift SED derived  $M^*/L$  values of all galaxies up or down by a few tenth of a dex, and if IMF variations occur across galaxy types and/or with redshift errors in SED,  $M^*/L$  estimation may be as large as 0.5 dex. Recent simulations have shown how fundamental model parameters such as the choice of SFH, adopted wavelength range, redshift, and inclusion of dust, contribute to the uncertainties and can be used as a quantitative guide to assess uncertainties in  $M^*$  (Maraston et al. 2010, 2012; Pforr et al. 2012; Wilkins et al. 2013).

The most urgently required model improvements include constraining residual uncertainties in stellar evolution, specifically regarding the temperature of the RGB and the energetics of the TP-AGB stars, and the effect of non-solar abundance ratios on spectra. An improved understanding of star formation history effects for low- $z$  galaxies would also be beneficial.

This review section is by no means complete, but it provides the necessary background to understand several statements made in forthcoming sections. Other comprehensive reviews which address stellar mass estimates in galaxies include Conroy et al. (2009), Gregg & Renzini (2011), Walcher et al. (2011), and Conroy (2013).

### 3. Dynamical Masses of Gas-Rich Galaxies

Galaxy masses were first inferred from spiral galaxy rotation curves, which were themselves first measured in the early 1900's (Scheiner 1899; Slipher 1914; Pease 1918). The nebular lines from which velocity curves were derived already showed some evidence of a "tilt", indicative of rotation, even though these early spectra only sampled the inner parts of the galaxy. In his most original 1922 paper and using Pease's (1918) velocity curve of the Andromeda galaxy, Opik inferred a mass of  $4.5 \times 10^9 M_\odot$  within  $150''$  ( $\sim 0.6$  kpc) for M31. He did so by requiring that the M31 disk have a mass-to-light (hereafter M/L) ratio comparable to that of the solar neighborhood. This is the first reported measurement of galaxy mass. That same year, Kapteyn (1922) remarked in his study of the Milky Way's local mass density that "We have the means of estimating the mass of dark matter in the universe." This appears to be the very first reference to the concept of "dark matter" in astrophysics. His dynamical analysis and determination of the density in the solar neighborhood is also the first of its kind. However, Kapteyn failed to find the elusive dark matter given the limitations of his data and preliminary method, as reviewed by Oort (1932). The latter can be credited for the first discovery of dark matter in galaxies (see Zwicky 1933 for a similar discovery of dark matter in clusters of galaxies). In his 1940 study of NGC 3115, Oort remarks: "the distribution of mass in the system appears to bear almost no relation to that of the light". This is yet another pioneering report of large mass-to-light ratios in galaxies.

About our own Galaxy, Rubin et al. (1962) remarked "For  $R > 8.5$  kpc, the stellar [rotation] curve is flat, and does not decrease as is expected for Keplerian orbits." Indeed, by the late 1960's, improved detectors at optical and radio frequencies yielded routine detections of flat galaxy rotation curves. Using a then-state-of-the-art image-tube spectrograph at the KPNO 84 inch telescope, Vera Rubin and Kent Ford (1970) obtained the first extended rotation curve of a galaxy (M31) out to  $120'$  ( $\sim 27$  kpc). Roberts & Whitehurst (1975) confirmed the flatness of the M31 rotation curve observed by Rubin and Ford with 21cm velocities extending to  $170'$  ( $\sim 38$  kpc). Roberts & Whitehurst however contended that dwarf M stars are adequate to explain the required mass and mass-to-light ratio. They, as well as most astronomers then, seem to have missed Freeman (1970)'s note that the HI rotation curves that were available at the time did not turn over at the radius expected from their surface photometry. Freeman's 1970 paper, commonly cited for its study of exponential disks in galaxies (rather than the note about), was likely the very first to quantify the mismatch at large galactocentric radii between the observed rotation curve and the rotation curve expected from the light distribution and constant M/L.

The flatness of observed rotation curves in all galaxy types is now a well-established fact (Faber & Gallagher 1979; Rubin et al. 1985; Sofue & Rubin 2001) but it is not by itself proof of dark matter in galaxies (see the prophetic contribution by Kalnajs in the 1982 Besancon conference proceedings Athanassoula (1983)). Despite notable efforts by the likes of Kapteyn, Oort, Babcock, Mayall, de Vaucouleurs, Schwarzschild, the Burbidge's, Roberts, Rubin, and others, and the realization that luminous galaxies are not a simple Keplerian environment, the firm manifestation of dark matter through galaxy rotation curves would await extended dynamical measurements at radio wavelengths (21cm line of neutral hydrogen), especially with the Westerbork Synthesis Radio Telescope (WSRT) (e.g. Rogstad & Shostak 1972; Bosma 1978; van der Kruit & Allen 1978), and the ability to place upper limits on the contribution of the baryonic component to the total observed rotation curve (Bosma 1978; Carignan & Freeman 1985; van Albada et al. 1985; Kent 1986, 1987).

The first detailed and unambiguous demonstration of unseen mass in galaxy disks from the mass modeling of galaxy rotation curves came with Albert Bosma's outstanding PhD thesis in 1978. Using early disk analysis methods by Toomre (1963), Shu et al. (1971), and Nordsieck (1973), Bosma was

able to decompose the extended rotation curves of 25 spiral galaxies to show for the first time that the total M/L ratio of galaxies grows with radius. To our knowledge, Faber & Gallagher (1979) were the first to link measurements for the local mass density (Oort 1932, 1965), the velocity dispersion in galaxy clusters (Zwicky 1933), and the notion of flat extended galaxy rotation curves (Bosma 1978), into a coherent picture of missing mass on global galactic and extragalactic scales.

While measurements of gas and stellar motions for mass estimates of gas-rich galaxies are now fairly straightforward, it is of relevance to discuss the applicability and accuracy of their related mass estimators. Modern mass modeling of galaxy rotation curves, and the ability to disentangle baryonic and non-baryonic components, are being reviewed below.

A modern review of the structure of galaxy disks can also be found in van der Kruit & Freeman (2011, hereafter vdKF11). We shall defer to that review in some cases below for more detailed discussions and/or derivations than can be provided here.

In their 2001 ARAA article, Sofue and Rubin write “*Babcock and Oort share credit for uncovering the dark matter problem in individual spiral galaxies*” for their work in the 1930’s. The pioneering contributions in the 1960’s-80’s of Toomre, Kalnajs, Shu, Freeman, Bosma, Carignan, Kent, van Albada, van der Kruit, Sancisi, and others to the problem of galaxy mass models should also be underscored.

### 3.1. Mass Estimates from Rotation Curves

The mass distribution in disk galaxies is typically determined from resolved rotation curves or integrated line profiles extracted from emission lines such as H $\alpha$ , CO, and HI lines. With the current generation of detectors, the H $\alpha$  and CO lines yield high spectral resolution spectra over most of the optical disk; greater spatial coverage (often at the expense of spectral resolution) is usually obtained with resolved HI velocity curves. Integrated line widths only yield an estimate of a total mass within some (uncertain) isophotal radius. A more accurate assessment of the extended galaxy mass profile is obtained from 2D resolved HI velocity fields but the prohibitive exposure times constrain sample sizes (e.g. de Blok et al. 2008). For nearby disks, H $\alpha$  velocity fields (with, e.g., SparsePak, DensePak, PPAK) and CO velocity fields (with, e.g. CARMA) are just as slow to obtain. The extent of the neutral gas in spiral galaxies, as traced by rotation curves, can often exceed twice that of the stars.

There is good agreement between resolved rotation curves extracted from H $\alpha$ , HI and CO lines (Sofue & Rubin 2001; Simon et al. 2003, 2005; Spekkens & Sellwood 2007) and from [OII], [OIII], H $\beta$ , [NII], and [SII] lines (Courteau & Sohn 2003) within the optical disk of galaxies.

It is often assumed that HI line widths sample the disk to large galactocentric radii, by analogy to resolved HI rotation curves; however, HI line widths are a convolution of gas dynamics and exponentially declining gas surface densities (e.g. Cayatte et al. 1994) such that the effective depth of integrated line widths is likely representative of the gas distribution within the optical disk of a galaxy. This is in line with the many linear transformations that exist between H $\alpha$  rotation measures and HI line widths (Mathewson et al. 1992; Courteau 1997; Catinella et al. 2007, to name a few).

The circular velocity of a spherical system in a potential  $\Phi$  is given by

$$V_{\text{circ}}^2(r) = r \frac{d\Phi}{dr} = G \frac{M(r)}{r} \quad (2)$$

where  $M(r)$  is the enclosed mass within a sphere of radius  $r$ . For a flattened disk, as in most spiral galaxies, the right hand side of eq. (2) must to be replaced by the more exact expression derived

by Freeman (1970). In the absence of dark matter or bulge, it should be stated that the exact expression for the rotation curve of a self-gravitating exponential disk is described by (Freeman 1970):

$$V_{\text{circ}}^2(R) = 4\pi G \Sigma_0 R_d y^2 [I_0(y) K_0(y) - I_1(y) K_1(y)], \quad (3)$$

where,  $G$  is the gravitational constant,  $\Sigma_0$  the central surface brightness,  $R_d$  the disk exponential scale length,  $y \equiv R/2R_d$ , and  $I_i(y)$  and  $K_i(y)$  are the modified Bessel functions of the first and second kind (Freeman 1970, see also vdKF11 and Fig 2.17 of Binney & Tremaine 2008a). The rotation curve of a pure exponential, infinitesimally thin, disk peaks at  $V_{2.2} \equiv V(R = 2.15R_d)$ . For disks of finite thickness (say,  $z_0/R_d = 0.2$ , where  $z_0$  is the disk scale height), the rotation curve will have a very similar shape but a  $\sim 5\%$  lower peak (e.g. Casertano 1983); this will slightly affect the “shape” term in the square brackets in eq. (3), but leave the subsequent scalings untouched.

The reliability of  $M(r)$  depends on how the rotational velocities,  $V_{\text{rot}}$ , reflect the assumed circular velocities. Several factors which involve corrections for observational and physical effects come into play. First, the observed line-of-sight velocity,  $V_{\text{los}}$ , must be corrected for projection via:

$$V_{\text{rot}} = V_{\text{los}} / \sin i. \quad (4)$$

where  $i$  is the inclination of the galaxy disk (or a ring along that disk, for tilted ring solutions; Teuben 2002). The above equation applies for velocities along the major axis; for the general case along any other projection, see Teuben (2002).

The spatially-resolved rotation curve or integrated line width of a rotating system is obtained via the Doppler equation:

$$V_{\text{los}}(r) = c[\lambda(r) - \lambda_0]/\lambda_0, \quad (5)$$

where  $\lambda_0$  is the observed wavelength of the galaxy center and  $r$  is the position along the slit. A line width  $W$ , usually equal to  $2V_{\text{obs}}$ , must also be corrected for internal turbulence and other effects (e.g. Haynes & Giovanelli 1984; Catinella et al. 2007).

The inclination angle,  $i$ , for an oblate spheroid is given by the formula (Holmberg 1946):

$$i = \cos^{-1} \sqrt{\frac{(b/a)^2 - q_0^2}{1 - q_0^2}}, \quad (6)$$

where the semi-major ( $a$ ) and semi-minor ( $b$ ) axes are determined from isophotal fitting of the galaxy image, and  $q_0$  is the axial ratio of a galaxy viewed edge-on (for late-type disks,  $q_0 \simeq 0.13$  (Hall et al. 2012, and references therein)).

Inclination uncertainties in Eq. (2) can be most significant for systems with  $i < 30^\circ$  or for distant galaxies whose disk is poorly resolved (in such cases, space-based observations or adaptive optics are needed to overcome the effect of atmospheric blur). Inclination estimates vary as a function of wavelength and are clearly affected by warps beyond the optical disks (Briggs 1990). Tilt uncertainty, such as due to warps, can account for a significant fraction of the mass budget in the outer parts of the disk. This is illustrated in Figure 10 for the mass profiles of NGC 45, M31, and M33 obtained assuming a kinematical model with constant inclination and major axis position angle (red open squares) or a full tilted ring model (blue filled squares). The ratio of these curves is shown on the right side of Figure 10 as a function of radius normalized by the disk exponential scale length,  $h$ . While the value of  $h$  depends on the assumed distance to the galaxy and details of surface brightness profile fitting (Courteau et al. 2011), Figure 10 makes clear that tilted ring models are required for rotation curves extending beyond 5-6 optical disk scale lengths.

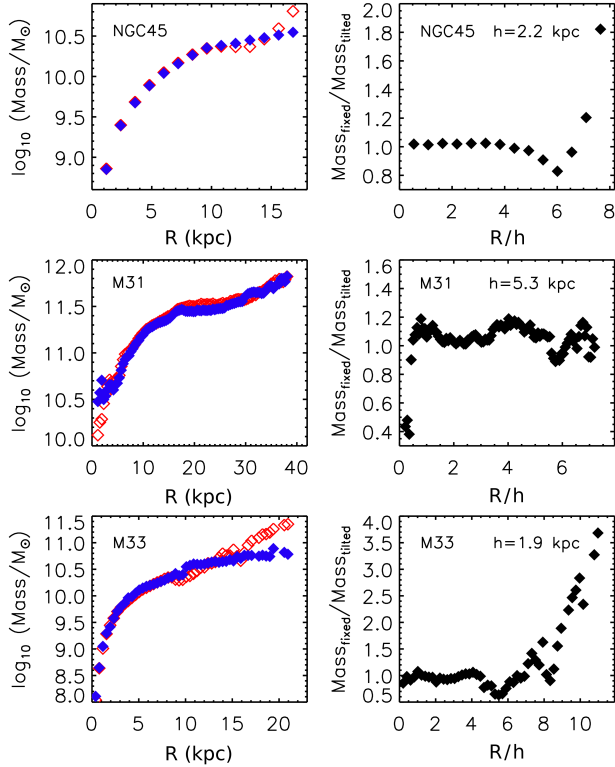


Figure 10: Mass profiles from HI rotation curves of NGC 45 (Chemin et al. 2006b), M31 (Chemin et al. 2009), and M33 (Chemin et al., in prep.). Mass profiles on the left were obtained from rotation curves assuming a kinematical model with constant inclination and constant position angle of the major axis (red open squares) or a full tilted ring model (blue filled squares). The adopted distances are NGC 45 ( $D = 5.9$  Mpc), M31 ( $D = 785$  kpc), M33 ( $D = 800$  kpc). The ratio of these mass profiles is shown on the right side where the radial scale has been normalized by the optical exponential disk scale length,  $h$ .

The effects of slit misalignment (erroneous position angles) for long-slit spectra on mass estimates are also addressed in Rhee et al. (2004), Spekkens et al. (2005), and Chemin et al. (2006a).

Ideally, a total enclosed galaxy mass should be determined using the most extended rotation curve and probing a regime where the RC is flat. Velocity curves can be modeled using a fitting function (Courteau 1997; Giovanelli & Haynes 2002). This is especially useful for low mass systems whose observed rotation curves rarely reach a plateau (caution is advised against extrapolations) or for noisy rotation curves with spiral structure wiggles. The reliability of mass estimates depends greatly on the stability of the velocity measure. For instance,  $V_{\text{obs}}$  is typically measured for one-sided resolved rotation curves at a fiducial marker such as  $V(R_{\text{max}})$ , where  $R_{\text{max}}$  is the radius at which  $V_{\text{obs}}$  reaches its peak value or  $V_{23.5}$ , the velocity measured at the 23.5 mag arcsec $^{-2}$  I-band isophote (Courteau 1997), or at half of a suitably chosen width of an integrated line profile (Haynes & Giovanelli 1984; Springob et al. 2005). Different definitions of rotational velocities or line widths can yield tighter galaxy scaling relations. For example, measurements of  $V_{\text{obs}}$  either at  $V_{2.2}$  or  $V_{23.5}$  yield the tightest scatter in various galaxy scaling relations for bright galaxies (Courteau 1997).

For the rising rotation curves of lower surface brightness systems, Catinella et al. (2007) note that the  $V_{2.2}$  values may not probe the RC deeply enough and that these may therefore show a surface brightness dependence.  $V_{23.5}$  would thus be a safer mass tracer, provided that the rotation curve is sampled that far.

Optical (typically H $\alpha$ ) rotation curves for bright galaxies may show extended flattening out to 4-5 disk scale lengths (Courteau 1997), such that a maximum  $V_{\max} = V(R_{\max})$  may be estimated. HI rotation curves routinely extend to that radius, making the measurement of  $V_{\max}$  straightforward from these data.

Beyond galaxy disks, little is known about the mass profiles of individual galaxies. By stacking galaxies of similar masses or luminosities, it is possible to use weak gravitational lensing (see §6) or satellite kinematics (e.g. More et al. 2011a) to measure total masses within the virial radius of the dark matter halo. This mass can be trivially converted into the circular velocity at the virial radius,  $V_{200}$ . By comparing with the rotation velocities within the optical disk,  $V_{\text{opt}}$ , one finds that on average for late-type galaxies  $V_{\text{opt}}/V_{200} \simeq 1.2$  (Dutton et al. 2010; Reyes et al. 2011). Thus, the dark matter near the virial radius may have slightly lower circular velocity than that of the inner baryons, and extended rotation curves are best decomposed into their major components (bar, bulge, disk, halo) rather than extrapolated. We discuss such decompositions in §3.3.

The velocity function (or the number of galaxies per unit circular velocity per volume) of spiral galaxies has been measured directly for the Virgo cluster by Papastergis et al. (2011). The full spectrum of (projected) line widths ranges from  $20 \text{ km s}^{-1}$ , where corrections for turbulence dominate measurement uncertainty, to more than  $400 \text{ km s}^{-1}$ .<sup>3</sup>

For a spherically symmetric system, the total mass enclosed within a radius  $R$  can be written in solar units as:

$$M(R) = 2.33 \times 10^5 R V_{\text{obs}}^2 / \sin^2(i) M_{\odot} \quad (7)$$

where  $R$  is the radius along the major axis in kpc and  $V_{\text{obs}}$  is the observed rotation velocity in  $\text{km s}^{-1}$ . Galaxy masses are thus best measured for systems with accurate distances; galaxies in unvirialized clusters or close enough ( $cz \lesssim 5000 \text{ km s}^{-1}$ ) to experience substantial deviations from the Hubble flow clearly suffer (linearly) from significant distance estimate errors.

Note that while the total enclosed mass,  $M(R)$ , is corrected for projection through Eq. (7), the complete deprojection of a rotation curve into a radial mass profile requires a tilted-ring analysis of the light distribution to account for the combined effects of a bulge, bar and disk (and sometimes a stellar halo) and isophotal warps Figure 10. Other physical effects discussed below in §3.2 make this endeavor, especially in the inner parts of a galaxy, a rather challenging and uncertain one. To probe the total galaxy potential in its outskirts would require other tracers such as planetary nebulae, globular clusters and satellites.

### 3.2. Inner Parts

In addition to errors introduced by deprojection effects and distance uncertainty, fundamental physical complications thwart the direct interpretation of galaxy rotation curves via Eq. (7) in their

---

<sup>3</sup>The fastest reported galaxy “disk” is that of UGC 12591, an S0/Sa galaxy rotating at  $500 \text{ km s}^{-1}$  and having a total mass within  $R_{25}$  equal to  $1.4 \times 10^{12} M_{\odot}$  ( $H_0 = 70 \text{ km s}^{-1} \text{Mpc}^{-1}$ ) (Giovanelli et al. 1986). Considering its X-ray emission and surprisingly low baryon mass fraction (3-5%; Dai et al. 2012), this galaxy is likely a massive spheroid that has accreted its, now rotating, neutral gas after assembling most of its stellar mass. The late merger/accretion event that formed the disk of UGC 12591 may have also turned on a massive outflow to drive its gas halo out to very large radii. As such, UGC 12591 should clearly not be compared against normal spiral galaxies.

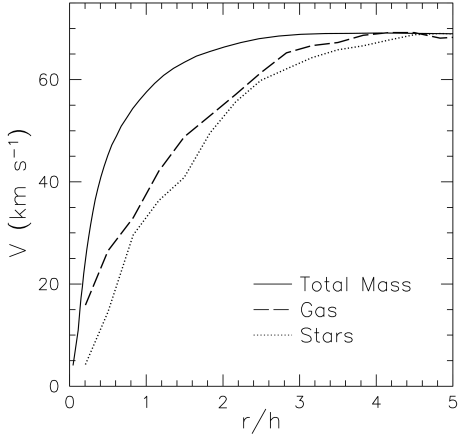


Figure 11: Simulated velocity curves for a dwarf galaxy from Valenzuela et al. (2007). The solid curve shows the spherical averaged circular velocity  $(GM_{\text{tot}}/r)^{1/2}$ . The long-dashed curve is for the azimuthally-averaged rotation velocity of gas particles. The stellar rotation velocity is shown by the dotted curve. Curves for the gas and stars are substantially below the circular velocity for  $r < 3h$ , where  $h$  is the disk scale length.

inner parts. These include deviations from circular orbits due to bar-like perturbations, differential dust opacity in the bulge and inner disk, density profile variations due to a triaxial halo, and more. We address these briefly below.

Because a large fraction of gas-rich galaxies have non-axisymmetric inner parts, non-circular velocities are often observed within the corotation radius of gas-rich galaxies (Lindblad et al. 1996; Weiner et al. 2001; Courteau et al. 2003; Valenzuela et al. 2007; Spekkens & Sellwood 2007; Sellwood & Sánchez 2010). Once identified, correcting for non-circular motions is a daunting task. To relate those motions with a photometric bar requires detailed, model-dependent fluid dynamical simulations (see §3.4.4). Beyond the self-consistent treatment of the bar in these fluid-dynamical models, the correlation between the observed photometric bar strength (or length) and the amplitude of bar-like non-circular motions has not been widely explored (Spekkens & Sellwood 2007; Sellwood & Sánchez 2010; Kuzio de Naray et al. 2012); the latter requires high-quality 2D velocity fields and an empirical means to measure bar-like flows. Furthermore, the contribution of a bar or oval distortion to non-circular motions depends on the angle between the bar axis and the major axis. The amplitude of a rotation curve will be biased high/low if a bar close to the minor/major axis is neglected (Spekkens & Sellwood 2007; Sellwood & Sánchez 2010).

As an example for the phenomenological description of the influence of a bar on measured rotation curves, we show in Figure 11 a diagram adapted from Valenzuela et al. (2007). These authors used N-body simulations to show that non-circular motions, combined with gas pressure support and projection effects, can result in a large underestimation of the circular velocity in the central  $\sim 1$  kpc region of a gas-rich dwarf galaxy. While those highlighted effects are stronger in barred systems, they are also present in axisymmetric disks. Their simulations show that  $V_{\text{obs}} \simeq V_{\text{circ}}$  only beyond 3 disk scale lengths.

The differential opacity in spiral disks (Bosma et al. 1992; Giovanelli & Haynes 2002) also cautions for a careful interpretation of optical rotation curves. The effects of dust extinction on velocity curves, which tend to mimic solid-body rotation, can be significant at high tilt ( $> 80^\circ$ ) and

for wavelengths bluer than H $\alpha$  (Courteau 1992; Bosma et al. 1992) within one disk scale length. This “tapering” effect is also luminosity dependent, being stronger for the most luminous systems (Giovanelli & Haynes 2002). This problem is mostly overcome by measuring rotation curves at near-infrared wavelengths (e.g. through the Pa  $\alpha$  and Br  $\gamma$  hydrogen recombination lines) where extinction is minimised<sup>4</sup>. Radio observations nearly alleviate this concern, though lower resolution at HI may affect the rise of the rotation curve in the central regions (Bosma 1978; van den Bosch & Swaters 2001), and the HI optical depth and related self-absorption effects are not negligible in more inclined galaxies (Rupen 1991). The high-spatial resolution kinematics of galaxies’ inner regions from high- $J$  CO line spectroscopy using the Atacama Large Millimeter Array will soon lessen these issues, though similar concerns as above for more inclined galaxies apply. Effects due to triaxiality and flattening of the disk have been discussed in Dutton et al. (2005) and Binney & Tremaine (2008, Fig. 2.13).

For distant galaxies, the inner rise of the rotation curve is also critically damped by both resolution effects and enhanced central galaxy activity which contributes more dust per unit area at early times. Both dust extinction and resolution yield observed rotation curves that are shallower than the true velocity profile (Förster Schreiber et al. 2006).

Due to the complex and somewhat uncertain modeling involved in correcting for non-circular motions and internal extinction, masses for nearby galaxies are often extracted beyond corotation or, equivalently, beyond two to three disk scale lengths (Kranz et al. 2003; Valenzuela et al. 2007).

### 3.3. Mass Modeling

An ultimate goal of galaxy mass studies is the decomposition of a mass profile into its main components – the bulge, disk and dark matter halo – *at all radii*. Unlike gas-poor systems (§5) whose spectral features are faint beyond one effective radius, mass modeling decompositions can be attempted for spiral galaxies since dynamical tracers are conspicuous from the center to the optical edge. Pioneering mass models have been derived by Casertano (1983), Wevers (1984), Carignan & Freeman (1985), van Albada et al. (1985) and others.

Mass modeling is possible because the gas particles and stars are sensitive to the full potential contributed by the baryons and dark matter. If the matter distribution is axially symmetric and in centrifugal equilibrium, then the total circular velocity is given by,

$$V_{\text{circ}} \simeq \sqrt{V_{\text{gas}}^2 + V_*^2 + V_{\text{halo}}^2}, \quad (8)$$

at each radius  $R$  in the plane of the galaxy, where  $V_{\text{gas}}$ ,  $V_*$ , and  $V_{\text{halo}}$  are the observed rotation curves of the gas, stars, and halo components respectively. The latter accounts for the baryons and presumed dark matter particles in the halo.  $V_{\text{halo}}$  is usually inferred once the gas and stellar component have been subtracted from the observed overall rotation curve.

The velocity curves for the stars and gas found in the galaxy bulge and disk can be obtained by inverting their respective light (emission) profiles into mass profiles using suitable potentials and stellar  $M/L_*$  ratios. For instance, the stellar rotation curve is obtained by multiplying the light profile, ideally in a band where dust extinction effects are minimised, with an optimized  $M/L_*$  consistent with stellar population models (§2).

---

<sup>4</sup>Clearly, the issue of extinction is less conspicuous in nearly face-on systems (Andersen et al. 2006).

The neutral atomic gas,  $M_{HI}$ , can be estimated from the total HI flux density,  $S_{21}$ , measured from the 21-cm line in absorption and emission:

$$M_{HI} = 2.33 \times 10^5 S_{21} (D/\text{Mpc})^2 M_\odot \quad (9)$$

where  $D$  is the physical distance to the source in Mpc and  $S_{21}$  is the integrated flux density of the source in  $\text{Jy km s}^{-1}$ . The total gas mass which accounts for helium and other metals is given by:

$$M_{\text{gas}} = 1.33 M_{HI} \quad (10)$$

for an optically thin gas. An estimate of the molecular gas mass is more challenging since  $H_2$ , the most abundant molecule in the Universe by far, has no permanent electric dipole moment and thus cannot emit in the state in which it is typically found. Consequently, the second most abundant molecule, the CO molecule which has an electric dipole and is often optically thick, can be used since it is collisionally excited by  $H_2$ . However, the conversion from CO intensity to  $H_2$  mass, via some “ $X_{CO}$ ” factor, is notoriously uncertain (e.g. Bolatto et al. 2008). Still, Braine et al. (1993) have estimated the mass contribution of molecular gas to  $\sim 20\%$  of the HI mass, and this fraction decreases in later-type systems. For these reasons, we do not consider the molecular mass content further.

Detailed mass models of spiral galaxies, including the equations for the density profiles and associated rotation curves for the bulge, disk and halo profiles can be found in, e.g., Dutton et al. (2005), de Blok et al. (2008), Tamm et al. (2012) and Section 11.1 of Mo et al. (2010). Disks are often modeled as idealized infinitesimally thin, radially exponential, collections of dust, gas and stars with surface density distributions (Freeman 1970):

$$\Sigma(R) = \Sigma_0 \exp(-R/R_d), \quad (11)$$

where  $R_d$  is the scale length of the specific disk component. The total mass of the disk is  $M_d = 2\pi\Sigma_0 R_d^2$ . Dutton et al. (2011b) show that disk scale lengths of the gas are on average 1.5 times greater than disk scale lengths measured in the R-band light. The case of a thicker disk (Casertano 1983) adds only a small effect to the overall rotation curve (Mo et al. 2010). Real disks, however, often show spiral arm features, truncations, anti-truncations, and other deviations from a pure exponential surface density distribution (see e.g. van der Kruit & Freeman 2011) that are best modeled through a free form reconstruction of the stellar mass by inversion of the light profile as discussed above after Eq. (8).

The halo profile is obtained as the difference (in quadrature) between the observed rotation curve and the inferred baryonic components (eq. (8)). The halo is typically modeled as a pseudo-isothermal profile (Burkert 1995), a cosmologically-motivated dark profile (Navarro et al. 1996b, 1997, hereafter NFW), or an Einasto fitting function (Einasto 1965, 1969). The halo profile can be conveniently parameterized via the following function (Kravtsov et al. 1998):

$$\rho_{\text{halo}}(r) = \frac{\rho_0}{(r/r_s)^\alpha (1+r/r_s)^{3-\alpha}}, \quad (12)$$

where  $\rho_0$  is a central density,  $r_s$  is a scale radius, and  $\alpha$  is a shape index. This density profile has an inner logarithmic slope of  $-\alpha$ . For  $\alpha = 1$  this reduces to the NFW profile, and at the scale radius,  $r_s$ , the slope of the density profile is  $-2$  (isothermal). At large radii, the logarithmic slope is  $-3$ .

### 3.3.1. Mass Modeling Limitations

The greatest source of uncertainty in mass modeling is the assessment of realistic stellar  $M/L_*$  ratios, followed by ill-constrained covariances amongst halo parameters as well as between halo and disk parameters, as we discuss below.

The computation of mass models through Eq. (8) usually involves four fundamental parameters: one for the stellar  $M/L_*$ , and three for the halo component (as in eq. (12)). In the language of NFW, those three quantities are the dark matter halo shape index,  $\alpha$ , a velocity normalization,  $V_{200}$ , and a concentration,  $c$ .

Figure 12 highlights many of the challenges inherent to mass modeling such as the intrinsic degeneracy of current mass model solutions due to strong covariances between the disk and halo model parameters (see also van Albada et al. 1985). Figure 12 shows examples of modeled rotation curves for galaxies in three different mass range. The purple and black points are H $\alpha$  and HI velocity data from Blais-Ouellette (2000). The fitted components are shown for the gas (green), disk (blue) and halo models (red). In each panel, one model parameter is held fixed while the others can adjust to achieve a best fit solution (by minimizing the global data-model  $\chi^2$  statistic). In all cases, the model decompositions (two per galaxy) in a given column have the same overall  $\chi^2$  statistic. Variations in the fitting parameters can result in the same data-model residuals ( $dV$ , shown in the smaller horizontal windows) thus yielding non-unique solutions. The two right-side panels highlight the well-known disk-halo degeneracy between the stellar disk  $M/L_*$ , here expressed as  $\Upsilon_R$  in the R-band, and the halo inner slope  $\alpha$  (a cusp has  $\alpha = 1$ , a core has  $\alpha = 0$ ; see Eq. (12)). The two central panels show another facet of the disk-halo degeneracy assuming that all dark matter halos are cuspy. The range of acceptable parameters is large. Finally, the left panels show that model degeneracies exist even amongst halo parameters, assuming a common best-fitting stellar  $M/L_*$  ratio (in agreement with stellar population models). Thus, in order to achieve realistic mass models, both accurate stellar  $M/L_*$  and well-constrained cosmological models are needed. Stellar  $M/L_*$  are only accurate to factors of two (§2) and the current range of allowed halo parameters,  $c$ ,  $V_{200}$  and  $\alpha$  is still too broad to provide tight (unique) mass model solutions (e.g. Macciò et al. 2008). The inner shape parameter,  $\alpha$ , is especially difficult to constrain observationally due to the added complication that only a small number of rotation curve points constrain this value; see (Dutton et al. 2005) and (de Blok 2010) for reviews.

An additional complication to the mass modeling exercise is whether the *initial* distribution of dark matter particles is affected by the gradual cooling of the baryons as a galaxy forms. If the potential variations due to the dissipating baryons occur slowly compared to the orbital period of a dark matter particle in circular orbit, then the end state of the system is independent of the path taken (Blumenthal et al. 1986; Gnedin et al. 2004; Abadi et al. 2010). Thus, contraction of the dark matter occurs when baryons collapse and come to the central region; if the gravitational potential increases, matter naturally follows. This “adiabatic” contraction of the halo due to the cooling baryons can be modeled as

$$r_f V_f(r_f) = r_i V_i(r_i), \quad (13)$$

where  $V_i(r_i)$  and  $V_f(r_f)$  are the initial and final rotation curves, respectively, and  $rV(r)$  is the adiabatic invariant (Mo et al. 2010)<sup>5</sup>. The example of a modeled rotation curve with and without

---

<sup>5</sup>These authors advocate using  $rV(r)$  as the adiabatic invariant, instead of the usual  $rM(r)$  invariant, since disks are not spherical. Note also that the algorithm for compression due to adiabatic infall in a spherical halo model may take a different form when random motions are accounted for (Sellwood & McGaugh 2005).

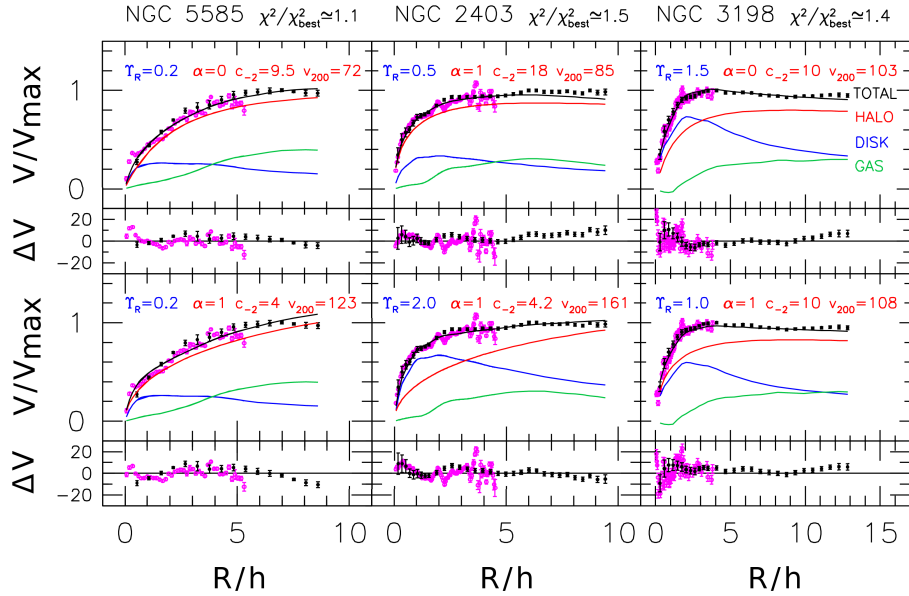


Figure 12: Mass models for three spiral galaxies with a range of peak circular velocity. The X-axis is in units of the optical disk scale length,  $h$ . The velocity on the Y-axis is normalized by the maximum observed orbital velocity. There are four free fitting parameters:  $T_R$ , is the stellar  $M/L_*$  (here in the R-band) and  $\alpha$ ,  $c$ , and  $V_{200}$  describe the NFW dark matter halo (see Dutton et al. 2005, for details). Variations in the fitting parameter can result in the same data-model residuals, as gauged by the model residuals  $dV$  (shown in the lower windows) and the overall  $\chi^2$ -square statistic. The model decompositions in each column (two per galaxy) have the same overall  $\chi^2$ -square statistic, shown at the top. Mass models are thus non-unique. See text for details.

adiabatic contraction (hereafter AC) is shown in Figure 13. This model has a fixed stellar  $M/L_* = 1$  and halo  $\alpha = 1$ . The ratio of dark to baryonic mass within the optical disk of a galaxy can increase by almost 40% if AC is invoked. In more extreme cases, AC can transform an initial  $\rho \propto r^{-1}$  NFW-type halo into a  $\rho \propto r^{-2}$  isothermal halo.

While AC is undoubtedly at play in all forming galaxies, it has been known for many years that baryonic effects such as supernova feedback and dynamical fraction can, in principle, result in reduced halo contraction or even halo expansion (e.g. Navarro et al. 1996a; El-Zant et al. 2001). Only recently have these effects been demonstrated in fully cosmological simulations of galaxy formation (Johansson et al. 2009; Abadi et al. 2010; Duffy et al. 2010; Macciò et al. 2012; Martizzi et al. 2012; Governato et al. 2012). Despite recent progress, cosmological simulations have not yet provided unique predictions for the response of dark matter halos to galaxy formation. A wide range of possibilities (from adiabatic contraction to expansion, from cuspy to cored halos) should thus be accounted for when attempting mass models of galaxies.

### 3.4. Other Galaxy Mass Constraints

Besides mass modeling of individual galaxies, with all the limitations that this entails as we saw above, potentially tighter constraints for the mass of baryonic and dark matter in disk galaxies may

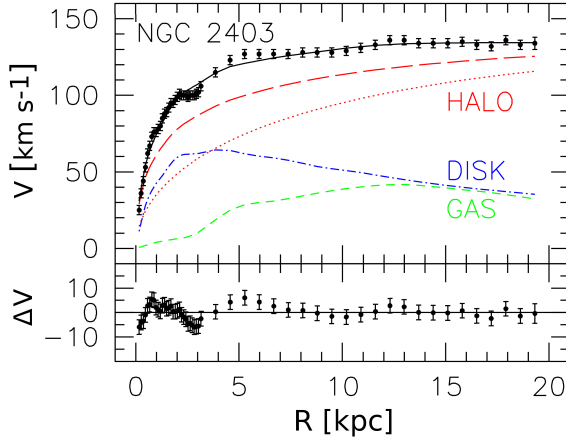


Figure 13: Mass model for the bright spiral galaxy NGC 2403 with an adiabatically contracted halo model (long dashed red line) or not (initial model shown with red dotted line). The disk and gas profiles correspond to the contracted final model. The data-fit residuals,  $\Delta V$ , are shown in the lower part of the figure. The ratio of dark to baryonic mass within the optical disk of a galaxy can increase by almost 40% within  $V_{2.2}$  if AC is invoked. The observed velocity data (black points) are from Blais-Ouellette (2000). See text for details about the modeling technique.

be achieved through dynamical or statistical arguments. As a way of introduction, we first present various methods to constrain the stellar  $M/L_*$ , independently of stellar population models.

#### 3.4.1. Maximal and Sub-maximal Disks

The hypothesis that the bulge and disk could contribute “maximally” to the rotation curve was introduced by Carignan & Freeman (1985) and van Albada et al. (1985) in order to overcome the intrinsic uncertainties of stellar  $M/L_*$  ratios. A maximal disk obeys

$$\mathcal{F} \equiv V_{\text{disk}}(R_{\text{max}})/V_{\text{tot}}(R_{\text{max}}) > 0.85,$$

where  $V_{\text{disk}}$  is the inferred velocity of the disk (stars and gas),  $V_{\text{tot}}$  is the total observed velocity, and  $R_{\text{max}}$  is the radius at which  $V_{\text{disk}}$  reaches its peak value (Sackett 1997). For a pure exponential disk, this is  $V_{2.2}$  (see §3.1). In other words, for a maximal disk galaxy,  $V_{\text{disk}}^2(R_{\text{max}})/V_{\text{tot}}^2(R_{\text{max}}) \gtrsim 0.72$  and the disk contributes at least 72% of the total rotational support at  $R_{\text{max}}$ . Note that this is just an arbitrary convention following Sackett (1997). A lesser contribution of the disk to the overall rotation curve at  $R_{\text{max}}$  is deemed “sub-maximal”. Since a galaxy with a sub-maximal disk with a significant bar or bulge component can still be baryon-dominated within  $R_{\text{max}}$ , we define a galaxy to be maximal at  $R_{\text{max}}$  if  $\mathcal{F} > 0.85$ , where  $V_{\text{disk}}$  is the inferred velocity of the baryons (bulge and disk). Even in the presence of a maximal disk, rare are the galaxies that do not require a halo component to match fully extended rotation curves. For dwarf galaxies, maximal disks often involve stellar  $M/L_*$  ratios that are physically implausible (Swaters et al. 2011).

The central panel of Figure 12 provides a good example of a sub-maximal (top) versus a maximal (bottom) disk fit. Both fits are equally valid numerically (see also Kassin et al. 2006; Noordermeer et al. 2007). Thus, without further constraints and especially extended HI rotation curves, the choice of a (sub-)maximal disk solution remains ill-constrained. Fortunately, arguments about the dynamical structure of disks and the existence of velocity-luminosity ( $VL$ , aka “Tully-Fisher”)

relation of spiral galaxies allow for new constraints to be implemented as we discuss in §3.4.3 (see also lucid discussions on this topic by vdKF11). In general, those other techniques listed below point to galaxy disks whose stellar masses are significantly below the so-called maximal value.

### 3.4.2. Velocity Dispersion Measurements

For a self-gravitating, radially exponential disk with vertical profile of the form  $\rho(R, z) = \rho(R, 0)\text{sech}^2(z/z_0)$ , van der Kruit (1988) and Bottema (1993) showed that the peak circular velocity of the stellar disk,  $V_{\text{disk}}$ , measured at  $R = 2.2R_d$  can be related to the vertical velocity dispersion,  $V_z$ , and the intrinsic thickness (or scale height) of the disk,  $z_0$ , via:

$$V_{\text{disk}}(R_{\text{max}}) = c_{\text{max}} \langle V_z^2 \rangle_{R=0}^{1/2} \sqrt{\frac{R_d}{z_0}}. \quad (14)$$

where  $c_{\text{max}} \simeq 0.88(1 - 0.28z_0/R_d)$  (Bershady et al. 2011). A more detailed discussion of eq. (14) is presented in vdKF11 (see their Section 3.2.4).

The power of Eq. (14) is that the disk  $M/L_*$ , derived via  $V_{\text{disk}}(R_{\text{max}})$ , can be determined independently of the dark matter halo. However, the measurements involved are difficult since the scale height,  $z_0$ , and the vertical component of the velocity dispersion,  $V_z$ , cannot be measured simultaneously. Thus this method is statistical in nature, at least for nearly edge-on (Kregel et al. 2005) and nearly face-on (Andersen et al. 2006; Andersen & Bershady 2013) systems. Indeed, for face-on systems,  $V_z$  can be measured but  $z_0$  must be inferred; and vice versa for edge-ons. The tightness of the statistical correlations used to infer  $z_0$  and  $V_z$  for face-on and edge-on galaxies, respectively, is reviewed by Bershady et al. (2010b). Furthermore, Bershady et al. (2011) showed that the edge-on sample of Kregel et al. (2005) and the face-on sample (so-called “DiskMass Survey”) of Bershady et al. (2010a) yield similar distributions of  $V_{\text{disk}}$  versus  $V_z$ . Systematic errors in  $M/L_*$  estimates based on Eq. (14) are thus relatively small.

Kregel et al. (2005) painstakingly determined the intrinsic stellar disk kinematics through Eq. (14) for 15 intermediate and late-type edge-on spiral galaxies using a dynamical modelling technique and assuming that  $\sigma_z/\sigma_r = 0.6 \pm 0.1$  (based on various plausible arguments). For 12 of their 15 spirals, they find on average  $\mathcal{F} = 0.53 \pm 0.04$ . They also find that the contribution of the disk to  $V_{2.2}$  is independent of barredness, in agreement with the “Tully-Fisher” (VL) analysis of barred galaxies<sup>6</sup> by Courteau et al. (2003) and Sheth et al. (2012) and the  $N$ -body simulations of Valenzuela & Klypin (2003).

More recently, Bershady et al. (2010a) applied the velocity dispersion method on a sample of 46 nearly face-on (inclinations  $\simeq 30$  degrees) galaxies. This survey uses integral-field spectroscopy to measure stellar and gas kinematics using the custom-built SparsePak and PPAK instruments. For the high-surface-brightness galaxy UGC 463, Westfall et al. (2011) find the galaxy to be sub-maximal at 2.2 disk scale lengths with  $\mathcal{F} = 0.61_{-0.09}^{+0.07}(\text{ran})_{-0.18}^{+0.12}(\text{sys})$ . The ratio  $\mathcal{F}$  could be much smaller for lower surface brightness systems. In fact, Bershady et al. (2011) confirm for 30 DiskMass systems covering a range of structural properties that the fraction  $\mathcal{F}$  ranges from 0.25 to 0.65 and increases with luminosity, rotation speed, and redder color. The DiskMass project does not include a dark matter component in their analysis since their data in the plane of the disk is largely baryon

---

<sup>6</sup>The fact that barred and unbarred galaxies share the same Tully-Fisher relation (Courteau et al. 2003) reflects that the angular momentum transferred from the bar to the halo is relatively small and easily absorbed by the halo. Thus, bars of all strengths belong to the same Tully-Fisher relation, as found in Sheth et al. (2012).

dominated (even in areas where dark matter dominates the enclosed mass). The impact of the dark halo is to make the disks less maximal (as advocated by Bottema 1993) at the 20% level.

### 3.4.3. Scaling Relations Residuals

Courteau & Rix (1999) suggested that sub-maximal disks provide a solution to the surface brightness independence of the  $VL$  relation (see also Zwaan et al. 1995). Courteau & Rix found that, *on average*, high-surface brightness spiral galaxies have  $\mathcal{F} \lesssim 0.6 \pm 0.1$ , as recently verified by Bershady et al. (2011, see §3.4.2). Their argument relies on the assumption that the scatter in the  $VL$  relation and the size-luminosity relation is largely controlled by the disk scale length, that spiral galaxies have self-similar  $M/L$  profiles (different than having constant  $M/L$  ratios), and that dark matter halos are adiabatically contracted. Dutton et al. (2007) revisited the Courteau & Rix method using a more detailed account of baryonic physics to find that  $\mathcal{F} \lesssim 0.72 \pm 0.05$  if AC is ignored or compensated for by other mechanisms which may result from non-spherical, clumpy gas accretion, coupled with dynamical friction transfer of energy from the gas to the dark matter. Dutton et al. (2007) reproduced the Courteau & Rix (1999) result if AC is invoked. Either way, most spiral disks obey the sub-maximal disk constraints.

### 3.4.4. Fluid Dynamical Modeling

Dynamical friction between a stellar bar and a dark matter halo is believed to slow down the pattern speed of the bar, and therefore fast bars should imply maximal disks (Weinberg 1985). A compilation of 17 barred galaxies analysed via the “Tremaine–Weinberg” method was presented by Corsini (2011); the overall impression from these analyses favors maximal disks. Likewise, slow bars might imply maximal halos (e.g., for UGC 628, Chemin & Hernandez 2009). However, some of these claims have been challenged on account of numerical artifacts yielding e.g. over-efficient bar slow down (Valenzuela & Klypin 2003). Indeed, Athanassoula (2003) and Athanassoula et al. (2013) have argued that the decrease in the pattern speed does not depend only on the mass of the dark matter halo, but also also on other galaxy properties such as gas fraction, or halo shape. Thus they argue that, on its own, the pattern speed decrease cannot set constraint to the halo mass.

Based on detailed fluid dynamic modeling, a maximal disk solution was found by Englmaier & Gerhard (1999) for the Milky Way and by Weiner et al. (2001) for the NGC 4123. Both galaxies are barred (see Sellwood & Sánchez 2010, for other examples). Conversely, the hydrodynamic gas simulations used by Kranz et al. (2003) to model the spiral arm structure of five grand design non-barred galaxies yield a wide range of  $\mathcal{F}$ , from closely maximal to 0.6. Galaxy disks appear to be maximal if  $V_{\max} > 200 \text{ km s}^{-1}$ , sub-maximal otherwise. Although detailed comparisons of observed galaxy velocity fields with hydrodynamic gas simulations are challenging, future galaxy masses review ought to include more analyses of this kind.

### 3.4.5. Gravitational Lensing

In the rare cases where a distant galaxy or quasar is lensed by a foreground galaxy, gravitational lensing can be used to place constraints on the projected ellipticity and mass within the Einstein radius. For disk-dominated lenses, this extra information coupled with spatially resolved kinematics can be used to break the disk-halo degeneracy (Dutton et al. 2011a). Until recently, only a handful of spiral galaxy lenses were known. The best studied being B1600+434 (Jaunsen & Hjorth 1997; Koopmans et al. 1998; Maller et al. 2000) and the “Einstein Cross” 2237+0305 (Huchra et al. 1985; Trott & Webster 2002; Trott et al. 2010). However, since these lenses are bulge-dominated, they are not ideally suited to constrain disk masses.

A number of recent searches for spiral lens galaxies (Féron et al. 2009; Sygnet et al. 2010; Treu et al. 2011) have uncovered several new disk-dominated spiral lenses. A joint strong lensing and dynamics analysis of the disk-dominated gravitational lens SDSSJ2141-0001, discovered as part of the SLACS survey (Bolton et al. 2008a), yields a best fit  $\mathcal{F} = 0.87_{-0.09}^{+0.05}$  (Barnabè et al. 2012), where  $\mathcal{F}$  includes both disk and bulge. Since the bulge contributes  $\sim 30\%$  of the stellar mass within 2.2 disk scale lengths, the *disk* is actually consistent (at the  $1\sigma$  level) with being sub-maximal.

### 3.4.6. Two-body Interactions and the Mass of the Local Group

The relative motions of two orbiting bodies, and assumptions about their angular momentum and total energy, may also be used to infer the total mass of that system.

Looking at our own Local Group (LG) of galaxies, the Milky Way and M31 galaxies display largely unperturbed disks suggesting that they are likely on their first passage since having formed. Based on that observation, Kahn & Woltjer (1959) were able to compute the relative motion of the Milky Way and M31 as a two-body problem assuming purely radial infall (zero angular momentum). This method, referred to as the “Kahn-Woltjer timing argument” (TA; see also Binney & Tremaine 2008), led Kahn & Woltjer to measure a total mass for the LG in excess of the reduced mass of M31 and the Milky Way by a factor greater than six, thus calling for a sizeable amount of hitherto undetected intergalactic matter. Sandage (1986b), using a similar argument for the deceleration of nearby galaxies caused by the LG, found a lower value for the maximum mass for the LG,  $M_{LG} = 5 \times 10^{12} M_\odot$ , with a best-fit value of  $4 \times 10^{11} M_\odot$ . Courteau & van den Bergh (1999) also used various mass estimators to compute  $M_{LG} = (2.3 \pm 0.6) \times 10^{12} M_\odot$  within 1.2 Mpc. More recently, Partridge et al. (2013) revised the TA for the LG by accounting for a Dark Energy component and finding a total  $M_{LG} = (6.19 \pm 0.56[\text{obs}] \pm 0.99[\text{sys}]) \times 10^{12} M_\odot$ . The systematic error is obtained by testing the TA model against LG-like objects selected from a cosmological simulation. The effect of dark energy is to make the value of  $M_{LG}$  roughly 12% larger than similar TA mass estimates that neglect it.

A major limitation of the TA is its reliance on single-galaxy interactions with the Milky Way and assumptions about virialization of the LG (Phelps et al. 2013). The latter implemented a numerical action method, originally developed by Peebles (1989), which takes into account the peculiar motions of a large subset of LG galaxies whilst eliminating the mass degeneracy in the two-body TA. Their method yields estimates of  $2.5 - 5.0 \times 10^{12} M_\odot$  for the Milky Way and  $1.0 - 5.0 \times 10^{12} M_\odot$  for M31. If the putative transverse velocity of M31 (van der Marel et al. 2012) is taken into account, the lower bound for the mass of the Milky Way drops from  $2.5 \times 10^{12} M_\odot$  to  $1.5 \times 10^{12} M_\odot$  in the 95% confidence region. The transverse velocity of M31 remains somewhat tentative owing to the uncertainty in our own orbit around the Milky Way center.

While the above figures seem high, the action method effectively measures a maximal possible mass for each bound system. Smaller mass estimates will thus be obtained on smaller scales. For instance, independent estimates for the dynamical mass of the Milky Way within 100 kpc range from  $M_{MW} = (4 - 1.4) \times 10^{12} M_\odot$  (see §4, Table 1); likewise for M31 with  $M_{M31} = (0.8 - 1.1) \pm 10^{12} M_\odot$  within the virial radius  $R_{200} = 189 - 213$  kpc, depending on the modeled dark matter distribution (Tamm et al. 2012).

Since this review is mostly concerned with mass estimators for individual galaxies, we do not investigate the mass of the LG further. The TA should however be noted as a method to estimate the mass of the Local Group and/or that of the Milky Way or M31 if one of the other masses is known independently. For more details on modern applications of the TA, see Phelps et al. (2013) and references therein. We review independent mass estimates of the Milky Way in §4.

### 3.5. Future Prospects

Mass modeling methods will require new constraints to break the disk-halo degeneracies as well as those internal to the halo model. Those may come from other mass estimators (not considered here due to space limits) based on e.g. external tracers such as planetary nebulae, globular clusters, and satellites (e.g. Yegorova et al. 2011). Nonetheless, various independent methods outlined in §3 present evidence for the prevalence of sub-maximal disks in most spiral galaxies with:

$$V_{\text{disk}}/V_{2.2} \simeq 0.6 \pm 0.1. \quad (15)$$

However, galaxies do come with a range in disk-to-halo masses, with the most massive ( $V_{\text{max}} > 200 \text{ km s}^{-1}$ ), high surface brightness spirals being close to having maximal disks. Almost all other galaxies, 90% of them being of dwarf type, are likely sub-maximal.

The dark matter near the virial radius likely has circular velocity at slightly lower speeds than the inner baryons. By comparing with the rotation velocities within the optical disk,  $V_{\text{opt}}$ , one finds from satellite kinematics and weak lensing that on average for late-type galaxies  $V_{\text{opt}}/V_{200} \simeq 1.2$  (Dutton et al. 2010; Reyes et al. 2011).

Looking ahead, very large kinematical surveys of spiral galaxies will enable a global characterization of rotation curve shapes for thousands of galaxies; e.g. MaNGA (“Mapping Nearby Galaxies at APO”; PI: Kevin Bundy) is a project to collect IFU velocity maps at Apache Point Observatory from 2014-2020 for  $\sim 10,000$  northern galaxies with stellar masses above  $10^9 M_{\odot}$  over a full range of gas contents, environments, and orientations. It will cover the range 360-1000 nm at a resolution of about 2500, with an emphasis on spectrophotometric calibration at all wavelengths. On shorter timescales, the Calar Alto Legacy Integral Field Area Survey (CALIFA) will already provide 2D PPAK IFU maps for  $\sim 600$  nearby galaxies (Sánchez et al. 2012). However, a short-coming of the large IFU surveys in progress and planned is their low spectral resolution. This will not enable measurements of disk velocity dispersions except in the inner regions where disentangling effects of the bulge kinematics will make interpretation difficult without more sophisticated analysis methods. One such method is the “Jeans Anisotropic Multi-Gaussian Expansion” described in detail in §5.3.3, although it will need to be augmented to consider the effects of dust extinction. CALIFA, and particularly MaNGA, will still truly refine our definition of velocity fields and the stellar populations in galaxies. Large samples of interferometric data will also be needed to extract velocity fields homogeneously for comparisons with optical velocity fields. This will be addressed by upcoming HI surveys with SKA pathfinders, notably WALLABY on ASKAP and its northern counterpart on WSRT. These projects may span  $\sim 5$  years or more.

Despite the extensive new galaxy dynamics data bases, the rigorous separation of baryonic and dark matter profiles in galaxies will require accurate stellar  $M/L_*$ ’s from stellar population models and/or dynamical measurements (e.g. Eq. 14) *as well as* precise constraints from  $\Lambda$ CDM structure formation models to resolve the many degeneracies between the luminous and dark matter components.

## 4. Dark Matter and Mass Models of the Milky Way

### 4.1. Introduction

As we saw in §3, Galactic rotation curves are one piece of the multifaceted dark matter puzzle. Around the time of Rubin & Ford (1970), cosmologists began to understand that relics from the early Universe, in the form of subatomic particles, could contribute significantly to the present-day mass density of the Universe. Today, the leading dark matter candidate is a stable, electrically neutral, supersymmetric particle with a mass between 1 GeV and 1 TeV. This weakly interacting massive particle or WIMP, would have been non-relativistic during the formation of large scale structure and hence, represents an example of cold dark matter (CDM; see, for example, Bertone et al. (2005)). WIMPs naturally form halos with roughly the right structure to explain flat rotation curves (Blumenthal et al. 1984; Dubinski & Carlberg 1991; Navarro et al. 1996b). Moreover, the halo mass function that is predicted by the standard CDM theory of structure formation is consistent with the observed hierarchy of virialized systems from dwarf galaxies to clusters (Press & Schechter 1974; Bardeen et al. 1986; Tinker et al. 2008).

In the mid-80's, several researchers pointed out that WIMPs might be detected in the laboratory (Drukier & Stodolsky 1984; Goodman & Witten 1985). At present over a dozen groups have deployed or are building terrestrial dark matter detectors (Bertone et al. 2005; Feng 2010). These experiments have the potential to probe the local density and velocity dispersion of dark matter at the position of the Earth. By the same token, the interpretation of these experiments, and in particular, the constraints inferred on the mass and scattering cross section of dark matter candidates, depend on astrophysical estimates of the local dark matter distribution function. Thus, there is a direct link between mass models of the Milky Way and dark matter detection in the laboratory.

Apart from the dark matter question, the Milky Way presents an opportunity to observe a "typical" (barred SBc) spiral galaxy from a unique vantage point. Thus, observations of the Milky Way hold a special place in our attempt to understand the formation and structure of spiral galaxies. The remainder of this section focuses on what we know about the distribution of baryons and dark matter in the Galaxy.

Studies of the Milky Way are invariably challenged by our position within it and by our frame of reference, which orbits about the Galactic center. In particular, our distance to the Galactic center and the circular speed at the position of the Sun remain uncertain at the 5% level (Ghez et al. 2008; Gillessen et al. 2009; Reid et al. 2009; Bovy et al. 2009; Brunthaler et al. 2011; Schönrich 2012). These uncertainties enter our interpretation of various observations and our determination of the mass of the Galaxy. On the other hand, the Milky Way offers a unique opportunity to probe the distribution of both visible and dark matter relatively close to the Galactic center. By contrast, for external disk galaxies, rotation curves provide evidence for dark matter only in the outermost regions where dark matter dominates. Estimates of the density of dark matter in the inner regions of large spiral galaxies require assumptions about the shape of the dark halo density profile.

The Milky Way is also unique in that there exist extensive catalogs of halo stars, globular clusters, and satellite galaxies with reliable Galactocentric distances and velocities. These tracers provide important constraints on the Galactic potential. Moreover, numerous stellar streams, such as the Sagittarius and Monoceros streams, may provide another handle on the Galactic potential.

### 4.2. Multicomponent Models for the Milky Way

The literature is replete with models of the Milky Way. An important early example can be found in Bahcall et al. (1982, hereafter BSS). Their model comprised a double-exponential disk, a

(deprojected) de Vaucouleurs stellar halo, a cuspy bulge, and a dark matter halo. The parameters that described the disk and stellar halo were taken from the earlier work by Bahcall & Soneira (1980), which, in turn, were based on star counts. The BSS model for the dark halo assumed a constant density core and a  $r^{-2.7}$  power-law fall-off at large radii. Notably, BSS showed that the different components of the Galaxy could “conspire” to produce a flat rotation curve for a wide range of model parameters, particularly the disk mass-to-light ratio and the structural parameters of the halo (see also Bahcall & Casertano 1985; van Albada et al. 1985). Blumenthal et al. (1984) argued that adiabatic contraction, the response of dark matter to the baryonic component as it condenses and forms the disk and bulge, could “explain” the apparent conspiracy that leads to flat rotation curves. Nevertheless, the disk-halo *conspiracy* in the context of a  $\Lambda$ CDM universe remains an outstanding problem in galactic astronomy while the disk-halo *degeneracy* continues to plague attempts to pin down the structural parameters of dark matter halos (Dutton et al. 2005).

Sellwood (1985) took the BSS model a step further by realizing it as an N-body distribution and numerically evolving it forward in time. He found that the BSS model was stable against bar formation though it did develop a two-armed spiral. Recall that a self-gravitating disk is generally unstable to the formation of a bar while a disk of particles on circular orbits in a background potential is stable. Disk galaxies lie somewhere between these extremes with the gravitational force felt by the disk particles coming from both the disk itself and the other components. In the BSS model, the bulge plays the key role in stabilizing the disk<sup>7</sup>.

Another influential model, especially for its focus on the Galactic bulge, was devised by Kent (1992). Kent et al. (1991) constructed a luminosity model for the bulge based on the 2.4  $\mu\text{m}$  map of the Galactic plane from the Spacelab Infrared Telescope. Kent (1992) combined this model with velocity dispersion data to determine the mass-to-light ratio for the Galactic bulge. He then constructed disk-bulge-halo mass models designed to fit the rotation curve. The results hinted at the existence of a supermassive black hole in the Galactic center. (For an earlier discussion of the existence of a central supermassive black hole, see Lacy et al. (1982)). Moreover, Kent’s model requires that one allow for non-circular motions in the gas, as in Gerhard & Vietri (1986). The Milky Way is now known to be a barred spiral galaxy (Blitz & Spergel (1991); Binney et al. (1997)) and mass models that incorporate a bar include Fux (1997, 1999) and Englmaier & Gerhard (2006).

Dehnen & Binney (1998) constructed a suite of disk-bulge-halo Galactic mass models. The observational constraints for their work included the circular speed curve, the velocity dispersion toward the bulge, the Oort constants, the local velocity dispersion tensor, and the force and surface density in the solar neighborhood. Dehnen & Binney (1998) surveyed the 10-dimensional parameter space of models using a restricted maximum likelihood analysis in that they considered 25 examples wherein some parameters were held fixed while the remaining parameters are allowed to vary so as to minimize the likelihood function.

Widrow et al. (2008, hereafter WPD) constructed dynamical models for the Galaxy using observational constraints similar to those considered by Dehnen & Binney (1998). WPD deployed Bayesian inference and a Markov Chain Monte Carlo (hereafter MCMC) algorithm to construct the full probability distribution function (PDF) over the model parameter space. The PDF is found

---

<sup>7</sup>Ostriker & Peebles (1973) suggested that a dark matter halo also could stabilize the disk against bar formation, but more modern simulations, including a live halo whose resonances are adequately described, have shown that the halo has a more complex role. During the bar formation phase, a more massive halo slows down the bar formation, but in the later, secular evolution phases, the halo actually helps the bar grow stronger by absorbing a considerable part of the angular momentum emitted by the bar region (Athanassoula 2002, 2003). See also §3.4.4.

to include regions of parameter space in which the model is highly unstable to the formation of a strong bar, so much that the models are almost certainly unphysical. In other regions of parameter space, the models are found to be mildly unstable to the formation of a weak bar and therefore may well represent an axisymmetric, idealized approximation to the Milky Way. Binney (2010a), Binney & McMillan (2011) and McMillan & Binney (2012) have continued to develop observationally-motivated models for the Milky Way along similar lines.

As mentioned above, both Dehnen & Binney (1998) and WPD use the Galactic circular speed curve as a model constraint. As with external galaxies, observations of neutral hydrogen provide a measure of the Galactic rotation curve, which translates to a circular speed curve provided the gas follows circular orbits. Inside the solar circle, HI observations are usually presented in terms of the so-called terminal velocity,  $v_{\text{term}}$ , which is defined as the peak velocity along a line of sight at Galactic coordinates  $b = 0$  and  $|l| < \pi/2$ . If one assumes axisymmetry, then the HI emission corresponding to the peak velocity originates from the galactocentric radius  $R = R_0 \sin l$  where  $R_0$  is our distance from the Galactic center. Thus  $v_c(R) = v_{\text{term}} + v_c(R_0) \sin l$  where  $v_c$  is the circular speed center. Malhotra (1995) for example, has determined the terminal velocity to the HI measurements of Weaver & Williams (1973); Bania & Lockman (1984); Kerr et al. (1986) and her measurements were used in both the Dehnen & Binney (1998) and WPD analyses.

The radial velocity of an object at Galactic coordinates  $(l, b)$  relative to the local standard of rest,  $v_{\text{LSR}}$  is related to the circurlar velocity via the expression

$$v_{\text{LSR}} = \left\{ \frac{R_0}{R} v_c(R) - v_c(R_0) \right\} \cos b \sin l . \quad (16)$$

Brand & Blitz (1993) consider a sample of HII regions/reflection nebulae with distances and radial velocities are available and use this method to infer the rotation of the Galaxy out to 17 kpc. Unlike the terminal velocity measurement,  $R$  must here be inferred from observations of the heliocentric distance  $D$  through the relation  $R = (D^2 \cos^2 b + R_0^2 - 2R_0 D \cos b \sin l)^{1/2}$ . Dehnen & Binney (1998) and Widrow & Dubinski (2005) present a statistical method for accomplishing this and incorporate the Brand & Blitz (1993) data into their Galactic model constraints. Note that both terminal velocity and outer rotation curve methods require  $R_0$  and  $v_c(R_0)$ , both of which are uncertain at the 5% level. A proper statistical analysis using these methods therefore requires a marginalization over  $R_0$  and  $v_c(R_0)$ , subject to prior probabilities for these parameters.

Xue et al. (2008) derived a Galactic rotation curve out to radius of 60 kpc. Their rotation curve is based on observations of blue horizontal branch (BHB) stars from the Sloan Digital Sky Survey (SDSS) which provided line-of-sight velocity distributions at different galactocentric radii. To construct the rotation curve, they compared these observations with mock observations of simulated Milky Way-like galaxies. Further investigations of halos stars are discussed below.

Figure 14 shows the inner rotation curve as inferred from HI observations by Malhotra (1995), the outer rotation curve inferred from observations of HII regions by Brand & Blitz (1993), and the Xue et al. (2008) rotation curve. The upper panel also shows the circular speed curve for one of two mass models from Xue et al. (2008). This model assumes a Hernquist bulge, a *sphericalized* exponential disk, and an NFW halo. The lower panel shows one of the more stable examples from the WPD Bayesian analysis. Note that the Xue et al. (2008) model was not constrained by Malhotra (1995) or Brand & Blitz (1993)'s data while the WPD model was constructed independent of the Xue et al. (2008) results.

Along rather different lines, Klypin et al. (2002) constructed mass models for both the Milky Way and M31 that were motivated by disk formation theory in the standard  $\Lambda$ CDM cosmology.

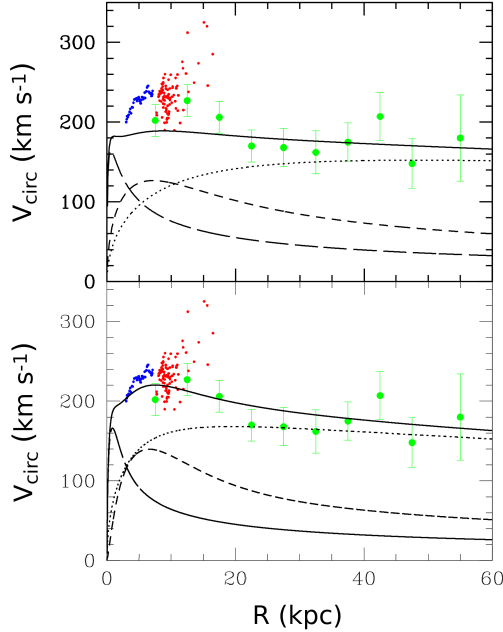


Figure 14: Rotation curve, as determined from the analysis of BHB stars by Xue et al. (2008) (green), the terminal velocity method by Malhotra (1995) (blue), and the analysis of Hii regions/reclection nebulae by Brand & Blitz (1993) (red). The upper panel shows the model predictions from Xue et al. (2011) for the total rotation curve (solid) and the contributions from the disk (dashed), bulge (long-dashed), and halo (dotted). The lower panel shows the WPD model.

To be precise, they assume that the proto-galaxy has a NFW halo with a concentration parameter in agreement with pure dark matter simulations. The present-day halo is derived by adiabatically contracting the early-time halo.

In Table 4.2, we present various structural parameters for the models described in this and the next section. We include, in addition to the disk, bulge and halo masses, the local dark matter density, the key quantity for terrestrial detection experiments. Note that the assumed canonical value for these experiments is  $0.0079 M_{\odot} \text{ pc}^{-3} = 0.3 \text{ GeV cm}^{-3}$  (Lewin & Smith 1996; Bertone et al. 2005). The local density of dark matter is of particular interest for direct detection experiments. A more complete discussion of this parameter can be found in Catena & Ullio (2010, 2012) and WPD.

As we saw in §3.4.1, a working definition for the maximal disk hypothesis is that

$$V_{\text{disk}}^2(R_{\max})/V_{\text{tot}}^2(R_{\max}) \gtrsim 0.72.$$

With the exception of a few of the Dehnen & Binney (1998) models and possibly the heavy disk model of Kent (1992), all models shown in Table 4.2 find (or assume) a submaximal disk for the Milky Way. Roughly speaking, systems with smaller values of  $V_{\text{disk}}^2/V_{\text{tot}}^2$  will be more stable against bar formation, though this ratio alone is an inadequate predictor of whether a bar will form (see, e.g. Debattista & Sellwood (2000) and WPD).

Table 1: Derived values for various models

model	$M_d$	$h$	$M_b$	$M_{100}$	$V_{\text{disk}}^2/V_{\text{tot}}^2$	$\rho_{DM,\odot}$
BSS	5.6	3.5	1.1	144	0.53	0.009
Kent (1992) – low $M_d$	3.7	2.8	1.2	125	0.4	0.013
Kent (1992) – high $M_d$	5.5	2.8	1.2	116	0.67	0.0097
Dehnen & Binney (1998)	0.36-1.5	2-3.4	3.3-5.1	40-75	0.33-0.83	0.009-0.012
Klypin et al. (2002)	4	3.5	0.8	55	0.37	0.007
Widrow et al. (2008: WPD)	4.1	2.8	0.96	$40^{+22}_{-19}$	0.5	$0.008 \pm 0.0014$
Smith et al. (2007)	5	4	1.5	55	0.4	0.011
Xue et al. (2008)	5	4	1.5	49	0.33	0.006
Gnedin et al. (2010)	5	3	0.5	89	0.33	0.014
McMillan et al. (2012)	5.7	2.9	0.9	83	0.63	0.0104
Moni Bidin et al. (2012)						$0 \pm 0.001$
Bovy & Tremaine (2012)						$0.008 \pm 0.003$

Table 1: Selected mass models of the Milky Way as presented in the text. The disk mass,  $M_d$ , bulge mass,  $M_b$ , and total mass within 100 kpc,  $M_{100}$ , are given in units of  $10^{10} M_\odot$ . The disk scale length,  $h$ , is given in units of kpc. Note that Smith et al. (2007) assume a Miyamoto-Nagai model (Miyamoto & Nagai 1975) for the disk where the peak in the contribution of the disk to the circular speed curve occurs at  $R_{\text{max}} \simeq 1.4h$ . Xue et al. (2008) assume a “spherical” disk potential where  $R_{\text{max}} \simeq 1.9h$ . All other models assume an exponential disk where  $R_{\text{max}} \simeq 2.2h$ . Column 6 gives the ratio  $V_{\text{disk}}^2/V_{\text{tot}}^2$  evaluated at  $R_{\text{max}}$  where  $V_{\text{tot}}$  and  $V_{\text{disk}}$  are the total observed velocity and contribution from the baryonic disk, respectively. The final column gives the density of dark matter in the solar neighborhood in units of  $M_\odot \text{pc}^{-3}$ .

### 4.3. Further Observational Constraints on the Milky Way Potential

#### 4.3.1. Circular Speed at the Sun's Position in the Galaxy

As mentioned above, our position within the Milky Way offers unique observational opportunities. Recently, Reid et al. (2009) (see also Brunthaler et al. (2011) reported VLBI measurements of trigonometric parallaxes and proper motions for 18 masers located in several of the Galaxy's spiral arms. These measurements yielded several structural parameters of Galaxy, most notably, the circular rotation speed at the position of the Sun. Their value  $V_c = 254 \pm 16 \text{ km s}^{-1}$ , is 15% higher than the standard IAU  $220 \text{ km s}^{-1}$ . (Brunthaler et al. (2011) analysed the same VLBI data but with updated values for the solar motion and found  $V_t = 239 \pm 7 \text{ km s}^{-1}$ .) By contrast, Koposov et al. (2010) found  $V_c = 221 \pm 18 \text{ km s}^{-1}$  by fitting an orbit to the GD-1 stellar stream. Naively, a 15% change in circular speed implies a 33% change in mass, though the implications for the bulge, disk, and halo masses would require an analysis that incorporates other constraints such as the ones carried out by Dehnen & Binney (1998) or WPD. Moreover, Bovy et al. (2009) reanalysed the maser data and found a somewhat lower value with  $V_c = 236 \pm 11$ . Their Bayesian analysis differed from that of Reid et al. (2009) by assuming a more general orbital distribution for the masers.

Recently, Schönrich (2012) described various ways to determine  $V_c$  based on stellar kinematics. The idea is to model the streaming motion of stars using the full phase space information available from the SDSS/SEGUE survey. The results are consistent with those described above and again suggest that  $V_c$  is  $\sim 10\%$  higher than the standard IAU value.

#### 4.3.2. Local Escape Speed

Smith et al. (2007) use a sample of high-velocity stars from the RAdial Velocity Experiment (RAVE; Steinmetz et al.) to infer that the local escape speed of the Galaxy is  $544_{-46}^{+64} \text{ km s}^{-1}$  (90% confidence interval). The fact that the escape speed is significantly higher than  $\sqrt{2}V_c$  provides compelling evidence that the Galaxy is embedded in a dark matter halo that extends well-beyond the solar circle. Smith et al. (2007) go on to combine their estimate for the escape speed with other kinematic constraints to derive (model-dependent) estimates for the virial radius, virial mass, and concentration of the Galactic dark halo. In particular, they consider a model for the Galaxy comprising a Miyamoto-Nagai (1975) disk, a Hernquist (1990) bulge, and an NFW halo. The halo potential can be written

$$\Phi_{\text{NFW}}(r) = \frac{GM_{\text{vir}}}{\ln(1+c) - c/(1+c)} \frac{1}{r} \ln\left(1 + \frac{r}{r_s}\right) \quad (17)$$

where  $r_s$  is the scale radius (see Equation 11),  $M_{\text{vir}} \equiv M(r = r_{\text{vir}})$  is the virial mass, and  $c = r_{\text{vir}}/r_s$  is the concentration parameter. The virial radius  $r_{\text{vir}}$  is defined such that the mean density within  $r_{\text{vir}}$  is  $\delta_{\text{th}}\rho_{\text{cr}}$  where  $\rho_{\text{cr}}$  is the background density (Navarro et al. (1996b)). The NFW potential has two free parameters. Thus, by combining the escape speed constraint

$$\Phi_{\text{total}} = -\frac{v_{\text{esc}}^2}{2} \quad (18)$$

with the constraint on the local circular speed, one can infer the parameters of the dark halo. Smith et al. (2007) assume  $M_d = 5 \times 10^{10} M_\odot$ ,  $M_b = 1.5 \times 10^{10} M_\odot$ ,  $\delta_{\text{th}} = 340$ , and  $V_c = 220 \text{ km s}^{-1}$  to obtain  $M_{\text{vir}} = 0.85_{-0.29}^{+0.55} \times 10^{12} M_\odot$ .

#### 4.3.3. Kinematic Tracers

Yet another route to constraining the mass distribution of the Galaxy, especially beyond the solar circle, is provided by kinematic tracers such as halo stars, globular clusters, and satellite galaxies. Line-of-sight velocities are naturally more easily measured than proper motions. For tracers in the outer parts of the Galaxy, these line-of-sight velocities are primarily radial (with respect to the Galactic center) whereas line-of-sight velocities of tracers in other galaxies will be a mixture of radial and tangential velocities. Thus, the analysis of Galactic tracers takes a different form to that for external galaxies.

Early work on dynamical tracers used simple mass estimators such as the following example due to Lynden-Bell et al. (1983).

$$M_{\text{est}} = \left( \frac{2}{\langle e^2 \rangle_s} \right) \left( \frac{1}{GN} \sum_{i=1}^N v_{ri}^2 r_i \right) \quad (19)$$

where the sum is over the  $N$  objects (satellites, globular clusters, etc.) of the sample. The quantity  $\langle e^2 \rangle_s$  is the mean orbital eccentricity ( $\langle e^2 \rangle_s = 1/2$  for an isotropic distribution) and encapsulates our ignorance of the orbit distribution. The above expression is suitable for a system of objects orbiting a point mass  $M$ . Recently, Watkins et al. (2010) carried out a detailed systematic study of mass estimators for both the Milky Way and Andromeda galaxies based on satellite kinematics. Their results illustrate just how sensitive mass estimates are to assumptions about the velocity structure of the satellite population. In particular, the mass estimates at 100 kpc range from  $1.8 \times 10^{11} M_\odot$  to  $2.3 \times 10^{12} M_\odot$  depending on the degree of radial velocity anisotropy. A detailed discussion of mass estimators as they might be applied to Gaia data can be found in An et al. (2012).

With enough kinematic tracers, one can determine a velocity dispersion profile. Battaglia et al. (2005) for example, derive a radial velocity dispersion profile for the Galaxy from a sample of 240 halo objects (mainly globular clusters and halo stars). The dispersion is roughly constant at  $120 \text{ km s}^{-1}$  within 30 kpc and then decreases to about  $50 \text{ km s}^{-1}$  at a Galactocentric distance of 120 kpc. These results are consistent with those from a sample of 2400 BHB stars by Xue et al. (2008), though that sample only extended to a Galactocentric radius of 60 kpc. As discussed above, Xue et al. (2008) use the kinematics of BHB stars to derive a rotation curve by comparing their data with mock observations of simulated galaxies. Alternatively, one can model the dispersion profile directly.

The decline in the dispersion profile beyond 30 kpc places constraints on the density profile of the dark halo. In particular, an isothermal halo, where the density is  $\propto r^{-2}$  is inconsistent with the data since the dispersion profile in this case is constant with radius. Battaglia et al. (2005) compare their dispersion profile with model profiles derived from the Jeans equation and find that the data are consistent an NFW halo that has a relatively high concentration ( $c = 18$ ) and  $M_{\text{vir}} \simeq 0.8 \times 10^{12} M_\odot$ .

Gnedin et al. (2010) also used halo stars to infer a rotation curve for the Milky Way. Their analysis was based on the spherical Jeans equation with the assumption that both the density and velocity dispersion profiles for the halo stars are described by power-law functions of radius. They find that the velocity dispersion declines very gradually out to 80 kpc and thus they infer a shallow slope for the dispersion profile. For this reason, they infer a larger mass for the virial radius and mass of the Galactic halo than Battaglia et al. (2005). Best-fit values for their three-component Galactic model (motivated, to a large extent, by the Klypin et al. (2002) cosmological model) are given in Table 4.2.

In principle, one can model the phase space DF for a set of tracers thereby taking full advantage of the data. This idea was discussed by Little & Tremaine (1987), who also introduced the use of

Bayesian statistics to the problem. One begins by calculating the likelihood function (the probability of the data (e.g., radial velocities and distances for a population of kinematic tracers) given a model for the tracer DF and gravitational potential. Bayes's theorem then allows one to calculate the corresponding probability of the model given the data. In general, one since on is interested in the potential, one marginalizes over those model parameters that describe the DF. More sophisticated models for the Milky Way potential were considered by Kochanek (1996) and Wilkinson & Evans (1999) who modelled the kinematics of the satellite galaxy population. Similarly, Deason et al. (2012) modelled the distribution function of BHB stars to obtain constraints on the Galactic potential from 15-40 kpc.

#### 4.3.4. Vertical Force and Surface Density in the Solar Neighborhood

The vertical structure of the Galactic potential provides a potentially powerful probe of the amount of dark matter in the solar neighborhood. The vertical force is approximately proportional to the surface density, which, in turn, can be compared to the total surface density from stars the interstellar medium. The classical means of determining the local vertical force requires a sample of stars with known vertical distances and velocities. The first detailed analysis of this type was carried out by Oort (1932) who built upon earlier and important work by Kapteyn (1922) and Jeans (1922). Attempts to understand the local vertical structure of the Galaxy from stellar kinematics have come to be known as the Oort problem.

Of course, in order to infer the local density of dark matter from the vertical structure of the Galaxy near the Sun, one requires a detailed model of the local distribution of visible matter. A detailed model of the visible components in the solar neighborhood can be found in Flynn et al. (2006). Note that the total estimated density in visible matter (their Table 2) is  $0.091 M_{\odot} \text{ pc}^{-3}$ , which is a factor of 6 – 10 times greater than the predicted local dark matter density. Flynn et al. (2006) also found the local mass-to-light ratios in the  $B$ ,  $V$ , and  $I$  bands to be  $(M^*/L)_B = 1.4 \pm 0.2$ ,  $(M^*/L)_V = 1.5 \pm 0.2$ , and  $(M^*/L)_I = 1.2 \pm 0.2$ , in good agreement with population synthesis predictions that use typical solar neighborhood IMFs.

In general, the kinematics of the stars in the disk of the galaxy can be described by a phase space distribution function (DF),  $f(\mathbf{r}, \mathbf{v}, t)$ , which obeys the collisionless Boltzmann equation

$$\frac{\partial f}{\partial t} + \mathbf{v} \cdot \frac{\partial f}{\partial \mathbf{r}} - \frac{\partial f}{\partial \mathbf{v}} \frac{\partial \Phi}{\partial \mathbf{r}} = 0 . \quad (20)$$

Typically, one assumes that the stars in the sample are in dynamical equilibrium ( $\partial f / \partial t = 0$ ) and that vertical motions decouple from motions in the disk plane. With these assumptions,  $f(\mathbf{r}, \mathbf{v}, t) \propto F(z, v_z)$  and

$$v_z \frac{\partial F}{\partial z} - \frac{\partial F}{\partial v_z} \frac{\partial \Phi}{\partial z} = 0 . \quad (21)$$

Finally, Jeans theorem implies  $F(z, v_z) = F(E_z)$  where  $E_z = v_z^2/2 + \Phi(R_0, z) - \Phi(R_0, 0)$ .

Formally, each star in the sample may be viewed as a  $\delta$ -function in  $z$  and  $v_z$  and therefore the data provide an estimate of  $F$ , which, in principle, may be used to infer  $\Phi$ . In general restrictive assumptions are required to extract  $\Phi$ . For example, the distribution may be assumed to be isothermal so that  $F \propto \exp(-E_z/\sigma_z^2)$  where  $\sigma_z$  is the vertical velocity dispersion. One then finds  $\Phi(z) = \ln(\nu(z)/\nu(0))$  where  $\nu(z) = \int F dv_z$  is the density run for the tracers. Variations of this method have been used by Oort (1932), Bahcall (1984), and Holmberg & Flynn (2000).

Kuijken & Gilmore (1989) proposed an alternative method which does not rely on the assumption of isothermality. The DF is related to the density and potential through an Abel transform:

$$F(E_z) = \frac{1}{2^{1/2}\pi} \int_{E_z}^{\infty} \frac{d\nu}{d\Phi} \frac{d\Phi}{(\Phi - E_z)^{1/2}} \quad (22)$$

In order to use this equation, Kuijken & Gilmore make an ansatz for the form of  $\Phi$ . For each choice of potential, they calculate  $F$  and then compare the velocity distribution of the model to that of the data. The best-fit over the space of potentials leads to an estimate for  $\Phi$ . In principle, the local density may be determined from  $\Phi$  through the Poisson equation. The difficulty is that one requires second derivatives of the potential. An alternative is to determine the local surface density, which is (approximately) proportional to the force. The dark matter distribution can then be assumed to be approximately constant close to the Galactic plane (i.e., dark matter is distributed in a halo and not a disk (but see Read et al. (2008) for an alternative viewpoint.)

Recently, Moni Bidin et al. (2012) argued that there is little or no dark matter in the solar neighborhood. Their analysis is based on an analysis of some 400 red giant branch stars found in the Two Micron All Sky Survey (Skrutskie et al. 2006). The stars in their sample lie in the direction of the South Galactic pole between 1.5 and 4.0 kpc from the Galactic midplane and are presumably mainly from the thick disk. Their analysis is based on the Poisson and Jeans equations under the assumptions that the stars in the solar neighborhood are in equilibrium and that the Galaxy has azimuthal symmetry. With these assumptions, the integrated surface density within a distance  $z$  of the Galactic midplane is

$$\Sigma(z) = -\frac{1}{4\pi G} \int_{-z}^z \frac{1}{R} \frac{\partial}{\partial R} (RF_R) dz - 2[F_z(z) - F_z(0)] \quad (23)$$

where  $F_R$  and  $F_z$  are the radial and vertical components of the force, respectively. They then use Jeans equation to write these components in terms of radial and vertical derivatives of the components of the velocity dispersion tensor and the density. While  $z$ -derivatives are estimated from the data, the data are too sparse to provide information about the radial derivatives. Rather, the authors assume that all second moments of the velocity dispersion tensor scale as  $\exp(-R/h)$  where  $h$  is the radial disk scale length for the surface density. Furthermore, they assume that the rotation curve is locally flat for all  $z$ .

With these assumptions, Moni Bidin et al. (2012) found that  $\Sigma(z = 1.5\text{kpc}) \simeq 55M_{\odot}\text{pc}^{-2}$  and is very nearly flat between 1.5 and 4.0 kpc. In fact, their  $\Sigma(z)$  curve is well-fit by the curve for visible mass. By contrast, the standard disk-halo model for the solar neighborhood has  $\Sigma(z = 1.5\text{kpc}) \simeq 75M_{\odot}\text{pc}^{-2}$  and rises to  $\sim 100M_{\odot}\text{pc}^{-2}$  by  $z = 4\text{kpc}$ . Moni Bidin et al. (2012) therefore conclude that there is little room for dark matter in the solar neighborhood.

These results have been called into question by Bovy & Tremaine (2012) who point out that while the circular speed ( $= \sqrt{-RF_R}$ ) may indeed be locally flat near the midplane, the mean velocity exhibits a significant lag with respect to the local standard of rest due to asymmetric drift. When this effect is taken into account, the data imply a local dark-matter density of  $0.008 \pm 0.002M_{\odot}\text{pc}^{-3}$ , a result that is consistent with the values shown in Table 4.2. As well Garbari et al. (2012) have analysed kinematic data for 2000 K dwarfs using a method that is also based on the Poisson-Jeans equations and found a relatively high value for the local dark matter density ( $\rho_{DM,\odot} = 0.022^{+0.015}_{-0.013}M_{\odot}\text{pc}^{-3}$ ).

Virtually all approaches to the Oort problem rely on the assumption that the stars in the solar neighborhood are in dynamical equilibrium. Widrow et al. (2012) found evidence that the disk near

the Sun has been perturbed. The results are based on their analysis of solar neighborhood stars from SDSS (Data Release 8; Aihara et al. 2011) and the SEGUE spectroscopic survey (Yanny et al. 2009). The evidence comes in the form of an asymmetry between the number density north and south of the Galactic midplane. The asymmetry function (difference between the number density to the North minus the number density to the South divided by the average) has the appearance of a wavelike perturbation. In addition, there appears to a gradual trend in the bulk velocity across the Galactic midplane. This result has also been observed in the RAVE survey (Williams et al. 2013). The perturbations are fairly small (10% or less in the density) and therefore the uncertainty in the surface density due to this effect is likely less than current observational uncertainties. Nevertheless, as the observational situation improves, it may become important to account for departures from equilibrium. In any case, the Widrow et al. (2012) result may well represent a new window into the interaction between the disk and halo. In particular, such perturbations may have arisen from a passing satellite or dark matter subhalo Widrow et al. (2012); Gómez et al. (2013).

A second issue concerns the assumption that  $E_z$  is an integral of motion, at least to a good approximation. Statler (1989) has stressed that, for  $|z| > 1\text{ kpc}$ , the approximation breaks down and has proposed the use of Stäckel potentials, which admit three exact integrals of motion. Unfortunately, the Stäckel potentials are a fairly restricted set and, to date, no realistic disk-bulge-halo model has yet used them.

#### 4.4. Future Prospects

The future for mass modelling of the Milky Way is undoubtedly promising with the anticipated explosion of data from observational programs such as Gaia (Perryman et al. 2001; Wilkinson et al. 2005) and LSST (Ivezic et al. 2008). Gaia will yield distances and proper motions for about one billion Milky Way stars to its faint limit of  $V \sim 20$  mag and also provide radial velocities for about 150 million stars as faint as  $V \sim 16$  mag. LSST has expected uncertainties in parallax and proper motions that are well matched to those expected for the faintest Gaia stars and will provide meaningful measurements down to  $r \sim 24$  mag. We can therefore expect direct parallax distances with accuracies better than 10% for turn-off stars to  $\sim 1$  kpc and for bright RGB stars to  $\sim 10$  kpc. Parallax distance accuracies of  $10 \text{ km s}^{-1}$  will be achieved for transverse velocities out to 10 kpc; similar accuracies for larger distances will require other (photometric) distance estimates to be folded in. Astronomers will then have an unprecedented description of the phase space distribution function for the stellar component of the Galaxy. Major achievable science goals with these data include the discovery of stellar streams from tidally disrupted satellites and new constraints on the local distribution of dark matter. Current Milky Way models may lack the richness and sophistication worthy of the data; several groups have indeed begun laying the groundwork for accurate Milky Way mass models in the era of Gaia and LSST (Binney 2010b; Sharma et al. 2011; An et al. 2012; McMillan & Binney 2013; Magorrian 2013, and the many articles in these proceedings).

## 5. Dynamical Masses of Gas-Poor Galaxies

### 5.1. Introduction

As we go from gas-rich spiral systems to early-type galaxies (ETGs) or dwarf spheroidals (dSphs), common practice is to abandon the systematic use of the extended neutral gas component of the former as a tracer to determine the mass distribution. However, many ETGs have a significant amount of gas, either ionised (e.g. Bertola et al. 1984; Fisher 1997; Sarzi et al. 2006), sometimes molecular (e.g. Sage et al. 2007; Young et al. 2011) or even neutral (Knapp et al. 1985; Morganti et al. 2006; di Serego Alighieri et al. 2007). In such cases, it is possible to conduct parallel approaches to constrain the overall mass profiles of the galaxies. This has been exploited in the context of, say, the search for supermassive black holes (see e.g. Neumayer 2010), the kinematics of the central regions (Corsini et al. 1999; Vega Beltrán et al. 2001; Pizzella et al. 2004; Sarzi et al. 2006, and references therein) or large-scale kinematics (Franx et al. 1994; Weijmans et al. 2008).

However, the scarcity and complexity of observed gaseous distributions and kinematics and the associated difficulty of properly modelling the dissipative content of galaxies with multi-component morphologies (though see e.g. Weiner et al. 2001) has led to further reliance on stellar dynamics: the interpretation of the large- (and small-) scale rotation curves revealed by the emitting gaseous content has thus generally been overtaken by state-of-the-art modelling of one of the existing dissipationless tracer, e.g. old stars, globular clusters, planetary nebulae. The associated side-products, i.e., constraints on the orbital structure of the galaxy under scrutiny, have the advantage of representing a rich source of information to establish its overall formation and evolution history.

In the following sub-sections, we will therefore restrict ourselves to briefly introducing the basic ingredients needed for the *kinematic modelling* of dissipationless systems, i.e., the determination of the total mass distribution, thus yielding the dark matter (DM) distribution after subtraction of the visible component. Determining the mass distribution requires extending beyond the simple use of the first velocity moment, the mean velocity  $V$ , as the centered second velocity moment, the stellar velocity dispersion  $\sigma$ , becomes a non-negligible actor. Orbital shapes also depart from the commonly-assumed circularity. Kinematic modelling is significantly more accurate through the measurement of the detailed shape of the velocity distribution, which is directly related to the orbital shapes, and thus allowing a better understanding of the formation of the galaxies under study.

We first provide some insights on the dependence of mass estimators based on the measurement of the line-of-sight (LOS) velocity dispersion on details of the probed aperture. We then describe the standard techniques of kinematic modelling, based upon either the Jeans equations of local dynamical equilibrium or the six-dimensional distribution functions and we highlight the recent improvements to these methods. We finally illustrate the power of these methods with recent analyses of observed gas-poor galaxies, often obtaining useful constraints on the compatibility of the DM profiles with those in  $\Lambda$ CDM halos. In several cases, one can also obtain useful constraints on the DM normalization, concentration, inner slope, as well as the orbital *velocity anisotropy* (hereafter anisotropy) in the inner and outer regions. This review does not specifically address the mass modelling of central supermassive black holes (see references in, e.g. Kormendy & Ho 2013), however most of the techniques that we discuss here also apply to that problem. The reader is also referred to Gerhard (2013) for another recent review on dark matter profiles determinations based on multiple tracers.

### 5.2. Simple Mass Estimators

Before engaging in the complexity of the mass modelling described in §5.3, we review simple mass estimators that have been proposed, all based on the scalar virial theorem (sVT).

The sVT states that for an isolated system in steady state

$$2K + W = 0, \quad (24)$$

where the total kinetic energy  $K = \frac{1}{2}M\langle v^2 \rangle$ ,  $M$  is the total galaxy mass and  $\langle v^2 \rangle$  is the mean square velocity of its stars, integrated over the entire galaxy, while  $W$  is the total potential energy, which depends on the distribution of the stars and the possible dark matter. This energy budget derives from a time average and depends on the isolation of the dynamical system (to ensure that the tracer is not affected by a neighboring system).

For a non-rotating spherical galaxy, the mean square velocity of the stars is related to the observed LOS velocity dispersion:  $\langle v^2 \rangle = 3\langle \sigma_{\text{LOS}}^2 \rangle$  (where both averages extend to infinity). Assuming finite mass, Eq. (24) gives

$$M = c \frac{r_r \langle \sigma_{\text{LOS}}^2 \rangle}{G}, \quad (25)$$

where  $r_r$  is a characteristic radius of the galaxy, while  $c = 6M^2/\{r_r \int_0^\infty [M(r)/r]^2 dr\}$ , in the self-consistent case. When the  $\langle \sigma_{\text{LOS}}^2 \rangle$  integral is extended over the *entire* galaxy, Eq. (25) is completely independent on the radial variation of the stellar anisotropy (Binney & Tremaine 2008, § 4.8.3). In the general case, the coefficient  $c$  depends uniquely on the total ( $\rho$ ) and tracer ( $\nu$ , i.e. stellar in galaxies) density profiles of the system.

The practical application of that formula has been the source of some confusion to be addressed before engaging into tentative interpretations. Firstly, the physical radius  $r_r$  is measured by the angular radius that it subtends; therefore, it depends directly on the assumed distance  $D$  of the object. Any uncertainty on  $D$  thus translates linearly into  $M$ . Secondly, there is an inherent uncertainty associated with  $r_r$ 's measurement: while it can be strictly defined as, for example, the radius at which half of the galaxy's total light is encompassed, the notion of total light itself is ill-defined (it often depends on a subjective extrapolation); the nature of the data also plays a role (e.g. bandpass and signal-to-noise effects). It is thus common to retrieve specific radii values differing by factors of two or more for the same well-studied systems (e.g. Kormendy et al. 2009; Chen et al. 2010). Both issues should be carefully addressed, especially when considering samples of galaxies for which distances and aperture radii emerge from heterogeneous sources and/or methods. Thirdly, when working at a finite radius  $r_r$ , one must add a non-negligible surface term into the virial theorem (The & White 1986).

The application of Eq. (25) as a robust mass estimator is further compounded by its limited applicability to real stellar systems: one can rarely observe the stellar  $\sigma_{\text{los}}$  for the entire galaxy, due to the rapid surface brightness drop with galactocentric radii. Therefore, the effect of using a finite aperture must be considered (Michard 1980; Bailey & MacDonald 1981; Tonry 1983). In early works, the coefficient  $c$  was only determined for specific galaxy surface brightness profiles (Poveda 1958; Spitzer 1969). Using Jeans models, it was realized that the coefficient  $c$  however depends significantly on the shape of galaxy surface brightness profile and on the dynamical structure of the galaxy (that is, its anisotropy, see e.g. Prugniel & Simien 1997; Bertin et al. 2002).

Moreover, galaxies contain unknown amounts of dark matter, making the total mass  $M$  an uncertain and ill-defined quantity. For these reasons, following Trujillo et al. (2004), we rewrite

Table 2: Structural constant  $c = GM(r_M)/[r_r \sigma_{\text{ap}}^2(R_\sigma)]$

	Spitzer	Cappellari	Wolf	3 $R_e$
$r_M$	$\infty$	$r_{1/2}^{\text{light}}$	$r_{1/2}^{\text{light}}$	$3 R_e$
$r_r$	$r_{1/2}$	$R_e$	$R_e$	$R_e$
$R_\sigma$	$\infty$	$R_e$	$r_{\text{vir}}$	$3 R_e$
<i>Predicted</i>	7.5	2.5	4.0	—
Hernquist	7.46	3.31	4.84	5.74
$n=2.0$ Sérsic	7.23	3.63	4.85	7.22
$n=4.0$ Sérsic	6.59	2.96	4.44	5.36
$n=5.5$ Sérsic	5.91	2.49	3.96	4.37
$n=2.0$ Sérsic + Einasto DM	112	3.74	4.96	8.38
$n=4.0$ Sérsic + Einasto DM	103	3.20	4.33	6.70
$n=5.5$ Sérsic + Einasto DM	94	2.76	3.95	5.70

Eq. (25) as

$$M(r_M) = c \frac{r_r \sigma_{\text{ap}}^2(R_\sigma)}{G}, \quad (26)$$

where the  $\sigma_{\text{los}}$  and mass integrals are restricted to finite radii, and where

$$\sigma_{\text{ap}}^2(R_\sigma) = \frac{\int_0^{R_\sigma} \Sigma(R) \sigma_{\text{LOS}}^2(R) R dR}{\int_0^{R_\sigma} \Sigma(R) R dR} \quad (27)$$

is the squared *aperture velocity dispersion* averaged over a cylindrical aperture on the sky of projected radius  $R_\sigma$ .

Cappellari et al. (2006) calibrated Eq. (26) using the observed surface distributions and integral-field kinematics within typically the *effective radius* containing half the projected luminosity,  $R_e$ , for a sample of ETGs, in combination with Schwarzschild's axisymmetric dynamical models. They found that the enclosed mass within the effective radius ( $r_r = R_e$ ) of ETGs can be robustly recovered using a best-fitting coefficient<sup>8</sup>  $c \approx 2.5$ , which varies little from galaxy to galaxy, with  $r_M = r_{1/2}^{\text{light}}$  (the radius of a sphere enclosing half of the galaxy light) and with  $r_r = R_\sigma = R_e$  (the radius of a cylinder enclosing half of the galaxy light). Using  $r_M = r_{1/2}^{\text{light}}$ ,  $r_r = R_e$  and  $R_\sigma \rightarrow \infty$ , Wolf et al. (2010) analytically derived  $c \approx 4.0$  for systems with  $\sigma_{\text{LOS}}(R) \approx \text{Cst}$  and proved that  $c$  depends very little on anisotropy (as expected given their infinite aperture for  $\sigma_{\text{ap}}$ ).<sup>9</sup>

Table 2 lists the values of  $c$  for some popular models of elliptical galaxies for comparison with different predictions (assuming isotropic velocities; anisotropic velocities are discussed later). The

<sup>8</sup>Their expression for  $(M/L)(r_M = R_e)$  was converted to enclosed mass assuming  $(M/L)(r_M = R_e) \approx (M/L)(r_M = r_{1/2})$ .

<sup>9</sup>Churazov et al. (2010) suggested a generalization of the approach of Wolf et al. (2010) by computing the mass at the radius where mass is least dependent on anisotropy, assuming the 3 cases of isotropic, radial and circular orbits.

values of  $c$  are computed by inserting the LOS velocity dispersion of Eq. (34) into Eq. (27), yielding

$$c = 3 \frac{M(r_M) M_p(R_\sigma)/(4\pi r_r)}{\int_0^\infty r \nu M dr - \int_{R_\sigma}^\infty (r^2 - R_\sigma^2)^{3/2} \nu M dr/r^2} \quad (28)$$

where  $\nu(r)$  and  $M_p(R)$  are the stellar mass density at  $r$  and stellar mass enclosed in the cylinder of radius  $R$ , and where the denominator is obtained, for isotropic orbits, by Mamon & Lokas (2005a, 2006).<sup>10</sup> Note that our models are idealized as they do not include realistic kinematics, galaxy rotation or multiple photometric components as in the real stellar systems on which the estimators were originally calibrated. The first three models (from Hernquist 1990 and Sersic 1968) assume no DM, while the last three include an  $m=6$  Einasto DM model (which Navarro et al. 2004 first found to fit best the halos in  $\Lambda$ CDM pure DM simulations), with radius of density slope  $-2$  equal to one tenth the quasi-virial radius,  $r_{200}$ ,<sup>11</sup> within which the DM accounts for 90% of the total.

For the Cappellari et al. and especially the Wolf et al. estimators, the mass within  $r_{1/2}$  depends little on the DM (the Spitzer relation, originally formulated for single-component polytropes, with  $r_M = r_{1/2}^{\text{light}}$ , matches that of Wolf et al., except for the Hernquist model, where  $c = 4.96$ ). Inclusion of velocity anisotropy, with  $\beta = r/2/(r + a_\beta)$  (Mamon & Lokas 2005b), where  $a_\beta = 2 R_e$  as found for ellipticals formed by mergers by Dekel et al. (2005), makes no difference when  $R_\sigma \rightarrow \infty$  (as theoretically expected) and decreases  $c$  by typically only 4% for finite  $R_\sigma$ .

In general, galaxies are not spherical and rotate. For this reason, Eq. (26) is not rigorously correct. However, for an aperture that extends to  $1R_e$ , Eq. (26) was empirically found to still provide a reliable enclosed-mass estimator (Cappellari et al. 2006, 2013b). In this case,  $\sigma_e$  is measured from a single ‘effective’ spectrum within an aperture, centered on the galaxy, enclosing half of the galaxy light. The spectrum can be obtained from integral-field observations for nearby galaxies, or from a single aperture for high-redshift ones. The resulting  $\sigma_e^2$  provides a good approximation to the luminosity-weighted velocity second moment  $\overline{v_{\text{LOS}}^2} \approx V^2 + \sigma^2$  inside the given aperture, where  $V$  is the observed mean stellar velocity at a given location and  $\sigma$  is the corresponding dispersion. For this reason,  $\sigma_e$  automatically includes contributions from both rotation and velocity dispersion and is only improperly called  $\sigma$ . The inclusion of rotation is essential for the reliability of the mass estimator.

The Spitzer (1969) and Wolf et al. (2010) formulae require kinematic measurements out to the virial radius<sup>12</sup>. Such data can currently be obtained only for dSph’s or globular clusters using individual stellar velocities. When those data are available, the latter formula is weakly sensitive to the differences in the input models. However, the Cappellari et al. (2006) formula should be used instead when only central kinematics (within  $\sim 1 R_e$ ) is available, as is currently the case for most ETGs. The data in Table 2 suggest that most of the difference in the coefficients  $c$  of Cappellari et al. and Wolf et al. is attributable to their use of different apertures to measure kinematics. Incidentally, both formulae provide formally correct results for a self-consistent Sérsic model with  $m = 5.5$ , where the difference in  $c$  is entirely explained by the different apertures.

Table 2 also illustrates that aperture averaged velocity dispersions out to  $3 R_e$  are insufficient

<sup>10</sup>The aperture velocity dispersions generally involve a triple integral. However, for simple anisotropic velocity models, one-third times the denominator of Eq. (28) becomes  $\int_0^{R_\sigma} R dR \int_R^\infty K_\beta(r/R, r_a/R) \nu(r) M(r) dr/r$ , where  $K_\beta$  is a dimensionless kernel given in Mamon & Lokas (2005b).

<sup>11</sup>At  $r_{200}$ , the mean mass density is defined to be 200 times the critical density of the Universe.

<sup>12</sup>The virial radius is defined to be that where the radial streaming motions are small, typically  $4/3$  of  $r_{200}$ .

to measure the DM fraction at that radius (which is determined more accurately using the radial profile  $\sigma_{\text{LOS}}(R)$  out to  $3 R_e$ ).

Below, we consider the more refined methods for determining the distribution of total mass of ETGs lacking a spatially extended gas tracer.

### 5.3. Methods based on Dynamical Modelling

The mass distribution in a gas-poor (and luminous) galaxy is expected to be generally dominated by baryons (mostly stars) in the inner parts and DM-dominated in the outskirts. The exact location and shape of the transition between these two regimes has been the subject of an active debate, with conclusions that seem to depend on the type (and mass) of the sampled galaxies.

The density profiles of DM halos in dissipationless  $\Lambda$ CDM simulations (hereafter  $\Lambda$ CDM halos) seem to converge (Navarro et al. 2004) to the “Einasto” model (e.g. Einasto & Haud 1989), which is mathematically “prettier” than the traditional Navarro et al. (1996b, hereafter NFW) model as its central density and total mass are both, unlike NFW, finite. These fits are now established from  $\simeq 10^{-3}$  (Navarro et al. 2010) to 2 or 3 (Prada et al. 2006) virial radii.

The inclusion of dissipative gas in cosmological simulations has the effect of concentrating the baryons in the centers of their structures, where they dominate the gravitational potential and drive the DM component deeper inside. On the scales of ETGs, this effect, commonly referred to as *adiabatic contraction* (Blumenthal et al. 1986; Gnedin et al. 2004) alters the DM density profile towards the singular isothermal ( $\rho \propto 1/r^2$ ) model. This result is, however, expected to be very sensitive to the details of the baryonic feedback processes, and orbit diffusion by the quickly varying potential could be an important agent in flattening of the DM halo cusp (e.g. Pontzen & Governato 2012). See more discussion on this issue in §3.3.1.

For all galaxy types, the dissipative nature of baryons leads them to accumulate in galaxy centers; indeed, if the baryons were negligible everywhere, the Einasto (or NFW) models found in  $\Lambda$ CDM halos would lead to much lower local stellar  $M/L$  and aperture velocity dispersion than observed (Mamon & Lokas 2005a). The dominance of baryons in the center and of DM in the envelopes of ETGs has been confirmed by X-ray measurements (Humphrey et al. 2006; Humphrey & Buote 2010) and dynamical modelling (e.g. Cappellari et al. 2006; Thomas et al. 2011b); see §5.5 below.

In the central region (within  $\sim 1 - 2 R_e$ ) of an ETG, we rely on a tracer that may generate the majority of the *local* potential, making the stars a nearly *self-consistent* component of the galaxy<sup>13</sup>. This would contrast with the galaxy’s outskirts, where the potential would be completely dominated by invisible matter, and our visible tracers are merely a set of orbiting entities.

The holy grail of dynamicists is the *distribution function* (hereafter DF), that is the density in phase space (the union of position and velocity spaces) of the *observed tracer* (luminosity for unresolved ETGs, numbers of stars for resolved dSphs). Its evolution is set by the collisionless Boltzmann equation (hereafter CBE), which states the incompressibility of the system in 6-dimensional phase space, or in simpler terms that the DF,  $f$ , is conserved along trajectories ( $df/dt = 0$ ). In vector notation, the CBE reads:

$$\frac{\partial f}{\partial t} + \mathbf{v} \cdot \nabla f - \nabla \Phi \cdot \frac{\partial f}{\partial \mathbf{v}} = 0 , \quad (\text{CBE})$$

---

<sup>13</sup>This should never be assumed but rather demonstrated.

where  $\Phi$  is the gravitational potential. In the last term,  $-\nabla\Phi$  is the force per unit mass acting on stars (and other bodies). The *total density*  $\rho$  is uniquely determined from  $\Phi$  through the Poisson equation:

$$\nabla^2\Phi = 4\pi G\rho . \quad (\text{Poisson})$$

Solving the CBE coupled with the Poisson equation is a challenging task, especially since  $f$  is a function of at least 6 variables (3 positions, 3 velocities, ignoring any time dependence), and one can rarely access the tracers representing the total density  $\rho$ . A way out of this conundrum is to consider *local variables*, to eliminate the direct dependence of  $f$  with respect to velocities, as detailed below.

### 5.3.1. Jeans Analysis

The traditional simpler approach to mass modeling involves writing the first velocity moments of the CBE, yielding the *Jeans equations*<sup>14</sup> that specify the local dynamical equilibrium

$$\frac{\partial \bar{\mathbf{v}}}{\partial t} + (\bar{\mathbf{v}} \cdot \nabla) \bar{\mathbf{v}} = -\nabla\Phi - \frac{1}{\nu} \nabla \cdot (\nu \boldsymbol{\sigma}^2) , \quad (29)$$

where  $\nu = \int f d^3\mathbf{v}$  is the space density of the tracer,  $\boldsymbol{\sigma}^2$  is the tracer's dispersion tensor, whose elements are  $\sigma_{ij}^2 = \bar{v}_i \bar{v}_j - \bar{v}_i \bar{v}_j$ , where  $\nu \bar{v}_i = \int v_i f d^3\mathbf{v}$  and  $\nu \bar{v}_i \bar{v}_j = \int v_i v_j f d^3\mathbf{v}$ . The product  $\nu \boldsymbol{\sigma}^2$  represents the *anisotropic dynamical pressure tensor* of the tracer.

The CBE and the Jeans equations (Eq. 29) apply to all systems, even out of dynamical equilibrium, as long as the tracers behave like test particles in the gravitational potential, hence do not interact (otherwise the right-hand-side of the CBE would be non-zero). In other words, the two-body relaxation time must be much longer than the age of the Universe, as is the case for ETGs, dEs (except in their nuclei) and dSphs. In particular (as mentioned above), in both the CBE and the Jeans equations, there is no requirement that the observed tracer density,  $\nu$ , be proportional to the total mass density,  $\rho$ .

With the simplifying assumptions of stationarity (ignoring any direct time dependence, i.e. removing the first term on the left-hand side of the CBE), these *stationary Jeans equations* specify the local dynamical equilibrium:

$$\nu (\bar{\mathbf{v}} \cdot \nabla) \bar{\mathbf{v}} + \nabla \cdot (\nu \boldsymbol{\sigma}^2) = -\nu \nabla\Phi . \quad (30)$$

Using the stationary Jeans equations (Eq. 30), one can relate the orbital properties, contained in the streaming (1st) and pressure (2nd) terms with the mass distribution contained in the potential (right-hand-side), through Poisson's equation. Such a *Jeans analysis* is fairly simple, as it circumvents the difficult problem of recovering the DF, by only considering its first few moments, which more directly relate to real astronomical observable quantities (depending on spatial coordinates). However, one is still left with a degeneracy between mass and the anisotropy of the pressure tensor, as we will discuss in the following subsections. Moreover, using moments does not guarantee that the DF is positive or null everywhere (Newton & Binney 1984).

---

<sup>14</sup>The Jeans equations are also called “equations of stellar hydrodynamics” or “hydrostatic equations”.

### 5.3.2. Spherical Modelling

The small departures from circular symmetry of many astrophysical systems observed in projection, such as globular clusters, dSphs and the rounder early-type galaxies as well as groups and clusters of galaxies, has encouraged dynamicists to often assume spherical symmetry in their kinematic modelling. The *stationary non-streaming spherical Jeans equation* can then be simply written

$$\frac{d(\nu \sigma_r^2)}{dr} + 2 \frac{\beta}{r} \nu \sigma_r^2 = -\nu(r) \frac{v_c^2}{r}, \quad (31)$$

where  $\nu \sigma_r^2$  is the *radial dynamical pressure* (hereafter *radial pressure*),  $v_c^2(r) = GM(r)/r = r d\Phi/dr$  is the squared circular velocity at radius  $r$ , while  $M(r)$  is the *total mass profile*, and where

$$\beta(r) = 1 - \frac{\sigma_\theta^2 + \sigma_\phi^2}{2 \sigma_r^2} = 1 - \frac{\sigma_\theta^2}{\sigma_r^2} \quad (32)$$

is the tracer's anisotropy profile with  $\sigma_r \equiv \sigma_{rr}$ , etc.,  $\sigma_\theta = \sigma_\phi$ , by spherical symmetry, and with  $\beta = 1, 0, \rightarrow -\infty$  for radial, isotropic and circular orbits, respectively. The stationary non-streaming spherical Jeans equation provides an excellent estimate of the mass profile, given all other 3D quantities, in slowly-evolving triaxial systems such as  $\Lambda$ CDM halos (Tormen, Bouchet, & White 1997) and for the stars in ETGs (e.g. formed by mergers of gas-rich spirals in dissipative  $N$ -body simulations; Mamon et al. 2006).

As one is left with two unknown quantities, the radial profiles of mass and anisotropy, linked by a single equation, one must contend with a nefarious *mass-anisotropy degeneracy* (MAD). The simplest and most popular approach to circumvent the MAD is to assume simply parameterized forms for both the mass and anisotropy profiles. One can then express the product of the observable quantities: the *surface density* profile,  $\Sigma(R)$ , and the *line of sight square velocity dispersion* profile,  $\sigma_{\text{LOS}}^2(R)$ , versus *projected radius*  $R$  through the *anisotropic kinematic projection equation* (Binney & Mamon 1982) expressing the observed quantity

$$\Sigma(R) \sigma_{\text{LOS}}^2(R) = 2 \int_R^\infty \left(1 - \beta \frac{R^2}{r^2}\right) \nu \sigma_r^2 \frac{r dr}{\sqrt{r^2 - R^2}}. \quad (33)$$

One can insert the radial pressure from the spherical stationary Jeans Eq. (31) into Eq. (33) to determine the line-of-sight (LOS) velocity dispersions through a double integration over  $\nu M dr$ . Mamon & Lokas (2005b, Appendix) have simplified the problem by writing the projected pressure as a single integral

$$\Sigma(R) \sigma_{\text{LOS}}^2(R) = 2 G \int_R^\infty K_\beta \left( \frac{r}{R}, \frac{r_\beta}{R} \right) \nu(r) M(r) \frac{dr}{r}, \quad (34)$$

where they determined simple analytical expressions for the dimensionless kernel  $K_\beta$  for several popular analytical formulations of  $\beta(r; r_\beta)$  (Tremaine et al. 1994 previously derived  $K_\beta(r, R) = \sqrt{1 - R^2/r^2}$  for  $\beta = 0$ ). The number density  $\nu$  is obtained by Abel inversion

$$\nu(r) = -(1/\pi) \int_r^\infty (\text{d}\Sigma_{\text{tot}}/\text{d}R) \text{d}R / \sqrt{R^2 - r^2}.$$

When both  $\rho(r)$  and  $\nu(r)$  are expanded as sums of spherical Gaussian functions (Bendinelli 1991), Eq. (34) can be applied to the individual Gaussians, which can have different  $\beta$  values. This leads to an expression involving a single quadrature for nearly general  $\beta(r)$  profiles (Cappellari 2008).

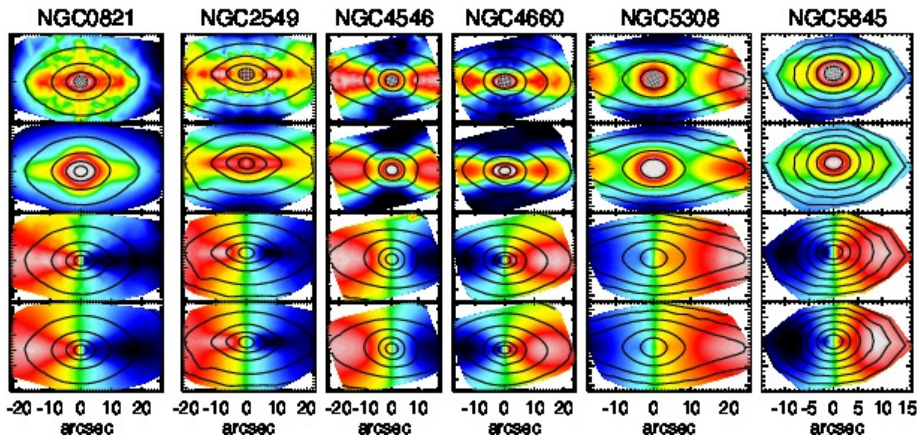


Figure 15: Data-model comparison of six fast rotator galaxies (previously classified as either E’s and S0’s) using the “Jeans Anisotropic MGE” (JAM) method (from Cappellari 2008). From *top* to *bottom*: bi-symmetrized observations of  $V_{\text{rms}} \equiv \sqrt{V^2 + \sigma^2}$ , model of same, bi-symmetrized observations of  $V$ , model of  $V$ . The *contours* show the isophotes. The models generally agree with the original non-symmetrized data within the statistical errors.

The next step in complexity is the non-parametric *mass inversion*, where  $\beta(r)$  is assumed, involving first the anisotropic kinematic deprojection by inverting Eq. (33) (Mamon & Boué 2010; Wolf et al. 2010) and then *directly* obtaining the mass profile by inserting the derived radial pressure into the Jeans Eq. (31). For simple  $\beta(r)$  models, the mass profile can be written as a single integral (Mamon & Boué 2010). Interestingly, for systems with roughly constant  $\sigma_{\text{LOS}}(R)$  (as is the case for most galaxies), the mass profile at the half-light radius  $r_{1/2} \simeq 1.3 R_e$  is almost independent of the assumed  $\beta(r)$ , as analytically derived by Wolf et al. (2010).

Alternatively, a mass profile is assumed and one directly determines the anisotropy profile through the non-parametric *anisotropy inversion*, first derived by Binney & Mamon (1982), with other algorithms by Tonry (1983), Bicknell et al. (1989), Dejonghe & Merritt (1992), and especially Solanes & Salvador-Solé (1990).

None of these approaches can lift the MAD. One promising alternative approach is to consider the variation with projected radius of the LOS velocity dispersion *and kurtosis* (Łokas 2002; Łokas & Mamon 2003). This method has been successfully tested (Sanchis et al. 2004) on  $\Lambda$ CDM halos viewed in projection, despite the fact that these halos are triaxial (Jing & Suto 2002a, and references therein), with anisotropy that increases with radius (Mamon & Łokas 2005b, and references therein), substructures and streaming motions. Unfortunately, the LOS projection of the 4th order Jeans equation, required in the dispersion-kurtosis method, is only possible when  $\beta = \text{Cst}$ , whereas ETGs formed by major mergers show rapidly increasing  $\beta(r)$  (Dekel et al. 2005). Nevertheless, Richardson & Fairbairn (2013a) recently generalized this approach for systems where the 4th order anisotropy is a function of the usual 2nd order one, as is indeed seen in  $\Lambda$ CDM halos (Wojtak et al. 2008).

### 5.3.3. Axisymmetric Modelling

Still, the large majority of the galaxies in the Universe are to first order axisymmetric (except for spiral arms and bars) and possess disks even for ETGs (McDonald et al. 2011; Krajnović et al. 2011). This includes fast-rotators (Emsellem et al. 2007; Cappellari et al. 2007; Emsellem et al. 2011) and spirals.

If we rewrite the stationary CBE in cylindrical coordinates  $(R, z, \phi)$  and assume *axial symmetry* and steady state, we obtain two non-trivial Jeans equations (Jeans 1922; Binney & Tremaine 2008, Eq. 4.222b,c) that are functions of four unknowns,  $\sigma_R^2$ ,  $\sigma_z^2$ ,  $\bar{v}_\phi^2$ , and  $\bar{v}_R v_z$  and do not uniquely specify a solution. By assuming that the velocity-ellipsoid is aligned with the cylindrical coordinates, we further simplify such equations as:

$$\frac{\nu\sigma_R^2 - \nu\bar{v}_\phi^2}{R} + \frac{\partial(\nu\sigma_R^2)}{\partial R} = -\nu \frac{\partial\Phi}{\partial R} \quad (35)$$

$$\frac{\partial(\nu\sigma_z^2)}{\partial z} = -\nu \frac{\partial\Phi}{\partial z}. \quad (36)$$

The two Eqs. (35) and (36) now depend only on  $\sigma_R^2$ ,  $\sigma_z^2$ ,  $\bar{v}_\phi^2$ , but one must still specify at least one function of  $(R, z)$  for a unique solution.

The generality of such equations can be maintained by writing a direct dependence between the two dispersions in the meridional plane via a function  $b$  such that  $\sigma_R^2 = b\sigma_z^2$ , with the boundary condition  $\nu\sigma_z^2 = 0$  as  $z \rightarrow \infty$ . This yields (e.g. Cappellari 2008)

$$\nu\sigma_z^2(R, z) = \int_z^\infty \nu \frac{\partial\Phi}{\partial z} dz \quad (37)$$

$$\nu\bar{v}_\phi^2(R, z) = b \left[ R \frac{\partial(\nu\sigma_z^2)}{\partial R} + \nu\sigma_z^2 \right] + R\nu \frac{\partial\Phi}{\partial R}. \quad (38)$$

For a given *observed* surface brightness and *assumed* total mass distribution, when Eqs. (37) and (38) are projected onto the plane of the sky and integrated along the LOS, they produce a *unique* prediction for the observed 2nd moment  $\bar{v}_{\text{LOS}}^2$ , as a function of  $b$  and the inclination  $i$ . The 2nd moment  $\bar{v}_{\text{LOS}}^2$  is empirically well approximated by  $v_{\text{rms}}^2 \equiv V^2 + \sigma^2$  (the squares of the centroid of a Gaussian fit to the LOS velocity profile and of its dispersion), which is easily observed in galaxies. This implies that  $V$  and  $\sigma$  do not provide separately any extra information on the galaxy mass that is not already contained in their quadratic sum. It also implies that, when galaxy rotation  $V$  is significant, one cannot neglect its contribution to the galaxy mass determination, and that one needs to know the inclination of the galaxy accurately. The dependence of the mass distribution on  $V_{\text{rms}}$  alone can be physically understood: for a given dynamical model, any star along a given orbit can have its sense of rotation reversed without altering  $\bar{v}_{\text{LOS}}^2$  (or the mass).

To predict galaxy rotations from the Jeans equations one must make an *extra* assumption on how the 2nd moments around the symmetry axis  $\bar{v}_\phi^2$  divides into ordered and random motions:  $\bar{v}_\phi^2 = \bar{v}_\phi^2 + \sigma_\phi^2$ . The simplest assumption to define this division is to adopt an *oblate velocity ellipsoid* (OVE), namely assume  $\sigma_\phi = \sigma_R > \sigma_z$  (Cappellari 2008). This OVE model has a streaming velocity uniquely defined by

$$\bar{v}_\phi^2 = \bar{v}_\phi^2 - b\sigma_z^2, \quad (39)$$

with  $\bar{v}_\phi^2$  and  $\sigma_z^2$  as given in Eqs. (37) and (38).

With  $b = 1$ , Eqs. (37) and (38) define a circular velocity-ellipsoid in the  $(v_R, v_z)$  plane: this is the historical *semi-isotropic* assumption that implies  $\sigma_R = \sigma_z$  (and  $\bar{v}_R v_z = 0$ ), and is sufficient to ‘close’ the set of equations to provide a unique solution for the remaining variables  $\sigma_z^2$  and  $\bar{v}_\phi^2$  (Nagai & Miyamoto 1976; Satoh 1980; Binney et al. 1990; van der Marel et al. 1990; Emsellem et al. 1994). If we consider Eq. (39), we retrieve the special case of the classic *isotropic rotator* (Binney 1978).

When the total mass and surface brightness are described via the *Multi-Gaussian Expansion* (MGE) method of Emsellem et al. (1994), the potential and Jeans Equations can be expressed in a simple form and  $\bar{v}_{\text{LOS}}^2$  only requires a single quadrature both for the semi-isotropic case (Emsellem et al. 1994, 1999). This is also true for the general case  $\sigma_R \neq \sigma_z \neq \sigma_\phi$ , and for all the six projected second moments, including radial velocities and proper motions, as demonstrated by Cappellari (2008). This flexibility can be more practically witnessed when using an implementation of the “Jeans Anisotropic MGE” (JAM) modelling method (see Cappellari 2008) augmented by the possibility to probe the parameter space within a Bayesian framework (e.g. §2.3.2). A key feature of the OVE rotator with constant  $b = (\sigma_R/\sigma_z)^2$  is that it maintains the simplicity of the isotropic (or semi-isotropic) rotator, but contrary to the latter, it provides a remarkably good description of the observations. In fact, these suggest that both fast-rotator ETGs (Cappellari et al. 2007; Thomas et al. 2009) and disk galaxies have a dynamical structure roughly characterized by a flattening of the velocity ellipsoid in the  $z$  direction parallel to the galaxy symmetry axis (Gerssen et al. 1997, 2000; Shapiro et al. 2003; Noordermeer et al. 2008). Indeed, once an accurate description of the surface brightness of the galaxies is provided via the MGE, the OVE rotator with constant  $b$  accurately predicts (Figure 15) both the first ( $V$ ) and 2nd ( $V_{\text{rms}} = \sqrt{V_{\text{rot}}^2 + \sigma^2}$ ) moment of the LOS velocity as inferred with state-of-the-art integral-field observations of the stellar kinematics of large samples of fast-rotator ETGs (Cappellari 2008; Scott et al. 2009; Cappellari et al. 2013b). The success of the cylindrical oriented approximation may be related to the disk-like nature of the majority of the galaxies in the Universe, where this particular alignment of the velocity ellipsoid appears natural (Richstone 1984).

Real galaxies need not have accurately cylindrically oriented velocity ellipsoids. In fact, theoretical arguments and numerical experiments suggest the velocity ellipsoid cannot be perfectly cylindrically oriented (e.g. Dehnen & Gerhard 1993). However, comparison with realistic  $N$ -body simulations of galaxies indicate that the cylindrically-oriented velocity ellipsoid approximation can be used to reliably measures the mean values of the internal anisotropy or to recover mean  $M/L$  even in realistic situations where the anisotropy is not constant (Lablanche et al. 2012).

#### 5.4. Distribution Function Analysis

Although the Jeans analysis is simple and fast, it has two disadvantages: firstly, the 2nd LOS velocity moment does not describe the full information of projected phase space (hereafter, PPS)  $(\alpha, \delta, v_{\text{LOS}})$ , where  $(\alpha, \delta)$  are the equatorial sky coordinates and  $v_{\text{LOS}}$  is the LOS velocity), and even the inclusion of the higher order moments (see e.g. Magorrian & Binney 1994; Magorrian 1995) is less informative than using the full PPS; Secondly, for spherically modeled galaxies, the solutions of the Jeans analysis depend on the required radial binning of the velocity moments. Moreover, the variation of the velocity moments with projected radius is often noisy, requiring smoothing of the data. We now describe a more general family of mass modelling methods, which solves for the gravitational potential and the DF, by fitting the PPS distribution predicted for combinations of gravitational potential and DF to the observed PPS distribution.

##### 5.4.1. Spherical Distribution Function Modelling

In spherical symmetry, the PPS is simply  $(R, v_{\text{LOS}})$ , where  $R$  is the projected radius, and the DF projects onto PPS as a triple integral (Dejonghe & Merritt 1992):

$$g(R, v_{\text{LOS}}) = 2 \int_R^\infty \frac{r \, dr}{\sqrt{r^2 - R^2}} \int_{-\infty}^{+\infty} dv_\perp \int_{-\infty}^{+\infty} f(r, \mathbf{v}) \, dv_\phi. \quad (40)$$

So, with the knowledge of the DF shape, one can fit its parameters to match the PPS.

In spherical systems with isotropic non-streaming velocities, the DF is a function of energy only, *i.e.*  $f = f(E)$ , while in anisotropic non-streaming (*e.g.*, non-rotating) spherical systems it is a function of energy and the modulus of the angular momentum. The PPS distribution in isotropic systems is (Strigari et al. 2010)

$$g(R, v_{\text{LOS}}) = 4\pi \int_R^\infty \frac{rdr}{\sqrt{r^2 - R^2}} \int_{\Phi(r) + v_{\text{LOS}}^2/2}^0 f(E) dE . \quad (41)$$

where the DF is given by the Eddington formula (Eddington 1916).

However,  $\Lambda$ CDM halos are anisotropic (*e.g.* Colín et al. 2000; Ascasibar & Gottlöber 2008). Wojtak et al. (2008) have recently shown that  $\Lambda$ CDM halos have DFs that are separable in energy and angular momentum, with  $f(E, L) = f_E(E) L^{2(\beta_\infty - \beta_0)} (1 + L^2/L_0^2)^{-\beta_0}$ , with  $\beta_0 = \beta(0)$  and  $\beta_\infty = \lim_{r \rightarrow \infty} \beta$ , and where  $L_0$  is a free parameter related to the “anisotropy radius” where  $\beta(r) = (\beta_0 + \beta_\infty)/2$ . Unfortunately, the energy part of the DF is non-analytical, though Wojtak et al. show how it can be efficiently evaluated numerically (they also provide an analytical approximation for  $f_E(E)$ ). This  $\Lambda$ CDM halo-based DF can then be applied to fit the distribution of objects in PPS using Eq. (40), as shown by Wojtak et al. (2009).

For quasi-spherical galaxies, where, in contrast to clusters and  $\Lambda$ CDM halos, dissipation ought to play an important role, it is not yet clear that the DF is separable in energy and angular momentum as Wojtak et al. (2008) have found for  $\Lambda$ CDM halos. Moreover, the triple integral in Eq. (40) makes the  $\Lambda$ CDM halo DF method computationally intensive. The simplest and popular alternative is to fit the PPS assuming a Gaussian distribution for the LOS velocities, and the radial profiles of mass and anisotropy (Battaglia et al. 2008; Strigari et al. 2008; Wolf et al. 2010). Unfortunately, this method provides very weak constraints on the anisotropy (Walker et al. 2009b).<sup>15</sup> One can assume instead a Gaussian shape for the 3D velocity distribution, as in the MAMPOSSt method of Mamon, Biviano, & Boué (2013), again adopting radial profiles of mass and anisotropy, and fitting the predicted distribution of particles in PPS. This operation only involves a single integral.

Both the  $\Lambda$ CDM halo DF and MAMPOSSt methods have been successfully tested on  $\Lambda$ CDM halos viewed in projection (Wojtak et al. 2009; Mamon et al. 2013, respectively). They both yield useful constraints on both the mass and anisotropy profiles: with  $\sim 500$  tracers, the mass  $M_{200}$  within the (quasi-virial) radius  $r_{200}$  and the outer anisotropy are recovered with  $\sim 30\%$  and  $\sim 20\%$  relative accuracy, while the scale radius of the DM is obtained to within a factor 1.5. The bias in the recovered  $M_{200}$  correlates with the ratio of LOS velocity dispersion measured within the virial sphere, estimated along the LOS to that measured in 3D (corrected by  $\sqrt{3}$ ) so that the limiting factor for accurate mass measurements is the triaxiality of  $\Lambda$ CDM halos (Mamon et al. 2013).

#### 5.4.2. Towards Flattened Systems

The majority of the gas-poor ETGs have important elongation in the plane of the sky. A number of methods have been developed and tested in an attempt to retrieve the full DF for flattened systems. In the case of the semi-isotropic approximation, Hunter & Qian (1993), expanding upon the Eddington formula for spherical systems, demonstrated that a direct inversion of the mass density  $\rho$  can be obtained analytically, which can then be applied to galaxies with complex morphologies

---

<sup>15</sup>Walker et al. (2009b) did not fit the PPS but  $\sigma_{\text{LOS}}(R)$ .

(see e.g. Emsellem et al. 1999). Besides the fact that this involves analytic extrapolations of functions into the complex plane, flattened systems do not seem consistent with the semi-isotropic hypothesis. It may therefore be worth re-examining this technique with the OVE assumption in mind.

Other techniques based on, for instance, the expansion of the DF into a set of basis functions (Dejonghe 1989), have enjoyed some success (Kuijken 1995; Gerhard et al. 1998; Emsellem et al. 1999). When the potential is of the Stäckel form, the DF can be readily expressed (de Zeeuw 1985; Arnold et al. 1994), and the orbital structure is then a simple function of basic building blocks corresponding to explicit integrals of motion (see applications in e.g. Hunter & de Zeeuw 1992; Statler 2001). For these specific cases, the general solution of the Jeans Equations providing the moments in terms of standard integrals has even been worked out by van de Ven et al. (2003). Unfortunately, the difficulty of choosing a relevant set of basis functions for the DF, or to design models that fit specific galaxies from the very centre to the outer parts, has led modelers to consider other more natural methods that treat a galaxy as the sum of well-chosen orbits: this is the subject of the following section.

#### 5.4.3. General Orbit-based Modelling

A popular approach to non-spherical potentials (as well as spherical ones) is that of *orbit modelling* (Schwarzschild 1979; Richstone & Tremaine 1984). In the axisymmetric case, one considers orbits of given  $E$ ,  $L_z$  and  $I_3$  (a non-classic integral of motion) in a given potential (i.e., the DF is made of delta functions in  $E$ ,  $L_z$  and  $I_3$ ). One searches for a linear combination of these orbits that minimizes the residuals between predicted and true observables, enforcing positive weights. These weights are obtained either by averaging the observables over an orbit (Schwarzschild) or by continuously updating them (Syer & Tremaine 1996; NMAGIC code of de Lorenzi et al. 2007; Dehnen 2009; Long & Mao 2010). Such a technique can also be generalized to triaxial systems (van den Bosch et al. 2008). Although more challenging to implement than Jeans analyses, orbit-based and particle-based methods constitute the state-of-the-art methods of kinematic modelling.

Due to its generality, Schwarzschild's method is more robust to the biases that may affect some of the other methods. It can also handle observable quantities more effectively, such as higher order Gauss-Hermite moments, while Jeans analyses are mostly concerned with the first two exact velocity moments. The robust measurement of the latter can be challenging given the complex LOS velocity distributions. Schwarzschild's method has been used extensively to measure masses of supermassive black holes in galaxies (e.g. van der Marel et al. 1998; Cretton & van den Bosch 1999; Verolme et al. 2002; Gebhardt & et al. 2003; Valluri et al. 2004), to measure  $M/L$  or DM profiles (e.g. Cappellari et al. 2006; Thomas et al. 2007; Weijmans et al. 2009) or to study the orbital anisotropy (e.g. Cappellari et al. 2007; van den Bosch et al. 2008; Thomas et al. 2009).

The generality of Schwarzschild's method is linked with the presence of degeneracies in the recovered parameters, and with the general need to regularize the sampling of the PPS by adding minimization constraints. Indeed, the unknown three-dimensional shape and using plane-of-sky velocities makes the dimension of the observable projected phase space too low. In fact, observations can at best provide a 3D quantity, namely the LOSVD at every projected location on the sky plane. This observable has the same dimension as the DF which, for Jeans's theorem, generally depends on the three isolating integrals of motion. The dimensionality equivalence between the observables and the DF explains why one can uniquely recover the DF from the data, when all other model parameters are known (Thomas et al. 2004b; Krajanović et al. 2005; van de Ven et al. 2008; Morganti & Gerhard 2012). However it is unlikely to robustly constrain additional quantities from the same

3D data (Valluri et al. 2004), namely the 3D total mass distribution and the angles at which it is observed. Important degeneracies are indeed found when trying to measure the galaxy shape (Krajnović et al. 2005; van den Bosch & van de Ven 2009) or mass distributions (de Lorenzi et al. 2009; see also Figure 17 below) with very general approaches.

### 5.5. Results

As emphasized above in §5.4.1, the CBE can be applied to any tracer, as long as the system is sufficiently isolated. The choice of tracers typically involves the (old) stellar population, the globular cluster or planetary nebula systems, satellite galaxies, or X-ray emission from hot gas when present.<sup>16</sup> Leaving the analysis of resolved dwarf spheroidal galaxies for §5.5.5, nearly all kinematic studies of ETGs have focused on the bright end of the luminosity function, as dwarf ellipticals are often too difficult to study.<sup>17</sup>

#### 5.5.1. Integrated Stellar Light: the Inner Regions and the IMF

The integrated stellar light component is the prime choice of tracer when considering regions within  $\simeq 1 - 2 R_e$  (see Figure 15), and relatively luminous galaxies. Most of the observations then generally extend beyond the first two velocity moments (van der Marel et al. 1994), which often helps to break the MAD (Gerhard et al. 1998; Napolitano et al. 2011). For galaxies that are intrinsically flattened or with complex morphologies, it is critical to make use of the two-dimensional kinematic maps provided by, for instance, integral-field spectroscopy as shown by Krajnović et al. (2005) and Cappellari & McDermid (2005). Progress can also be made by comparing dynamical and stellar population estimates to infer DM fractions and more generally the mass distribution in the central regions of galaxies (Gerhard et al. 2001; Cappellari et al. 2006; Napolitano et al. 2010; Thomas et al. 2011b; Wegner et al. 2012). Among others, these works confirm that the total  $M/L$  in the inner region of ETGs does not agree with the one predicted using stellar population models with a universal IMF. This can be interpreted as evidence for a variation in the dark matter fraction in the galaxies central regions, if the IMF is universal, or that the IMF is not universal and likely a function of total mass.

The most extensive set of detailed dynamical models to date, accurately reproducing both the galaxy photometry and the integral-field stellar kinematics, was constructed for the 260 ETGs of the ATLAS<sup>3D</sup> survey (Cappellari et al. 2013b). This study used axisymmetric anisotropic models based on the Jeans equations (JAM in §5.3.3) and includes a rather general dark halo, where both its slope and normalization are varied to reproduce the data within a Bayesian framework. The halo inner logarithmic slope is allowed to vary from the values predicted by halo contraction models (Abadi et al. 2010) to the nearly constant density profiles expected from halo expansion models (Pontzen & Governato 2012). The median fraction of dark matter inferred from the models, within a sphere of radius  $r = R_e$ , is just 10–20%. Cappellari et al. (2013b) find this dark matter fraction to be consistent with predictions for the same galaxies inferred by linking NFW halos to the real galaxies and assuming halo masses via the halo abundance matching technique (e.g. Behroozi et al. 2010). Using satellites as tracers of the gravitational potential, the NFW model

---

<sup>16</sup>See also the use of low-mass X-ray binaries as mass/dynamical tracers in dSph galaxies by Dehnen & King (2006).

<sup>17</sup>The more rapidly declining surface brightness profiles of dwarf ellipticals relative to their giant counterparts makes the spectroscopic measurements at several  $R_e$  especially challenging.

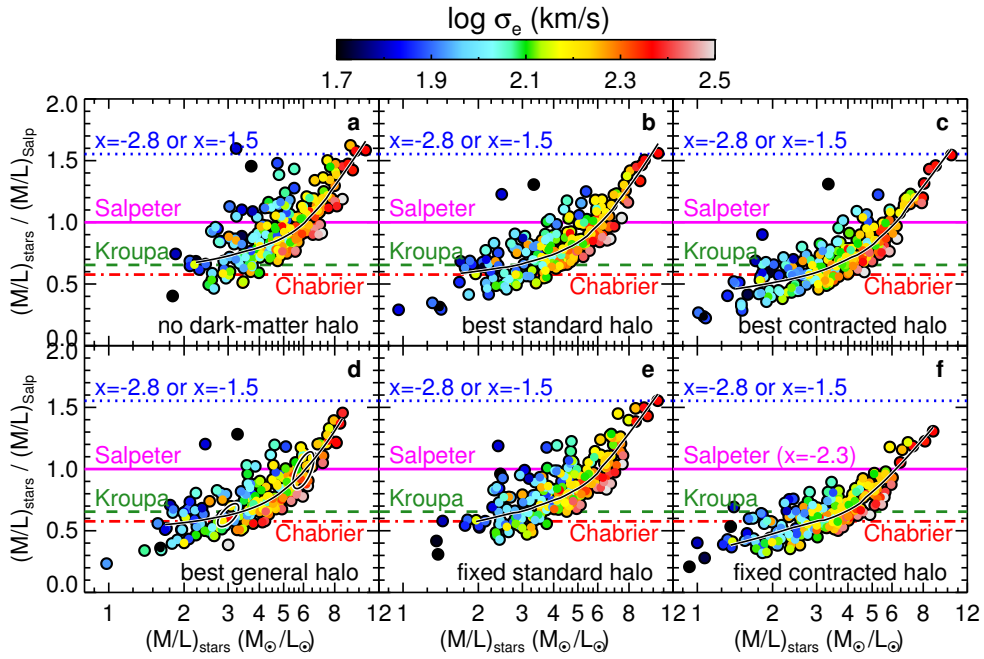


Figure 16: Systematic variation of the stellar IMF in ETGs. The six panels show the ratio between the  $(M/L)_{\text{stars}}$  of the stellar component, determined using dynamical models, and the  $(M/L)_{\text{Salp}}$  of the stellar population, measured via stellar population models with a Salpeter IMF, as a function of  $(M/L)_{\text{stars}}$ . The black solid line is a *LOESS* non-parametric regression to the data. Colours indicate the galaxies' stellar velocity dispersion,  $\sigma_e$ , which is related to the galaxy mass. The horizontal lines indicate the expected values for the ratio if the galaxy had (i) a Chabrier IMF (red dash-dotted line); (ii) a Kroupa IMF (green dashed line); (iii) a Salpeter IMF ( $x = -2.3$ , solid magenta line) and two additional power law IMFs with (iv)  $x = -2.8$  and (v)  $x = -1.5$  respectively (blue dotted line). Different panels correspond to different assumptions for the dark matter halos employed in the dynamical models as written in the black titles. A curved relation is clearly visible in all panels. From Cappellari et al. (2012).

of Wojtak & Mamon (2013) extrapolates<sup>18</sup> to a similar DM fraction within  $R_e$  for red galaxies of masses  $1.6 - 5 \times 10^{11} M_\odot$  (see Figure 17 below), but to much larger dark matter fractions for lower and higher mass red galaxies.

The study of Cappellari et al. (2012) finds that dark matter cannot explain the systematic increase in the total  $M/L$  with the galaxies velocity dispersion  $\sigma_e$ . This implies a systematic variation of the stellar IMF with  $\sigma_e$ , with the mass normalization changing by a factor up to 2–3, or from Chabrier (2003) or Kroupa (2001) to heavier than Salpeter (1955) over the full galaxy population (Figure 16; Cappellari et al. 2012). The Salpeter or heavier IMF for the most massive ETGs is consistent with recent findings from the analysis of IMF sensitive spectral features (van Dokkum & Conroy 2010; Spinelli et al. 2012; Conroy & van Dokkum 2012) and with strong lensing results (see, e.g., Treu et al. 2010; Auger et al. 2010b; Dutton et al. 2013, and discussion in §7), under the assumption of cosmologically motivated dark matter halos. This result also smoothly bridges the gap between the IMF inferred for massive ETGs and the lighter Chabrier/Kroupa inferred for

<sup>18</sup>The projected radii of the satellite galaxies analyzed by Wojtak & Mamon (2013) begin at  $5 R_e$ .

spiral galaxies (Bell & de Jong 2001, see §3).

Alternatives to a non-universal IMF do exist, to explain the dynamical or lensing results, but they require that (i) either all current stellar population models (§2) systematically and severely under predict the  $M/L$  for the galaxies with the largest  $\sigma$ , which are characterized by the largest metallicities, or (ii) the dark matter accurately follows the stellar distribution, contrary to what all simulations predict. Moreover the IMF trends inferred from spectral absorption features would need to be explained by a conspiracy of chemical abundance variation with galaxy  $\sigma$ . There is currently no evidence for any of these effects, but further investigations in these directions are still important.

Several recent studies have provided kinematic measurements of the integrated stellar light of ETGs beyond  $3 - 4 R_e$ , using long-slit (Thomas et al. 2007; Proctor et al. 2009; Coccato et al. 2010; Arnold et al. 2011) or two-dimensional spectroscopy (Weijmans et al. 2009). This, however, remains a rather challenging task, and as we probe outwards we must consider more discrete tracers such as globular clusters and planetary nebulae (see §5.5.2 below). The results obtained so far have provided a picture where ETGs are dominated by the stellar mass out to  $1 - 3 R_e$ , thus playing the counterpart of the *maximum disk* hypothesis in gas-rich systems (see §3.4.1) but for hotter stellar systems, while the outer halos are generally consistent with  $\Lambda$ CDM predictions.

### 5.5.2. Globular Clusters and Planetary Nebulae: the Outer Regions

In order to probe the distant radii beyond  $\simeq 4 R_e$ , observations from individual globular clusters (e.g. Foster et al. 2011) or planetary nebulae (Douglas et al. 2007; Romanowsky et al. 2009; Coccato et al. 2009; Napolitano et al. 2011) become essential, even though these populations are often scarce. See Gerhard (2013) for a recent review.

Globular clusters (GCs) have been used extensively to probe the mass distribution of the outer halos of ETGs (see e.g. Côté et al. 2003; Hwang et al. 2008; Lee et al. 2010, and references therein). There are three drawbacks to adopting GCs as dynamical tracers. 1) As most GCs are red and very old, they have orbited many times around their host galaxy, and the most adventurous ones with the smallest pericentres will have been progressively tidally stripped by the potential of the host galaxy. Therefore, for a given apocentre, the GCs with the largest pericentres will have survived, leading to a bias towards more circular orbits (in comparison with the underlying stellar population). 2) Their dynamics is thought to originate from rather violent physical processes (early collapse, gas-rich mergers) and may therefore not be strictly linked with the orbital structure of the old stellar population (Bournaud et al. 2008). 3) A bimodality in the colour distribution of GCs in bright ETGs is often observed (Brodie & Strader 2006), which may then call for several decoupled dynamical components in the final modelling. As for any tracer embedded in the outermost regions of a galaxy potential, it is sometimes difficult to assess the steady-state and dynamically relaxed nature of a certain tracer, and address whether or not the observations still probe the galaxy potential or lie beyond the boundary with the intra-cluster potential (Doherty et al. 2009).

One of the most thorough studies of a GC system by Schuberth et al. (2010) includes nearly 700 GCs for the central Fornax cluster massive early-type galaxy NGC 1399. Using a  $\beta = \text{Cst}$  Jeans analysis, these authors showed that the red GC population traces very well the field stellar population, while the blue one appears to be the superposition of several sub-populations including accreted or true cluster members. A similar study of the same galaxy with (4 times fewer) PNe by McNeil et al. (2010) illustrates the relative merits of using GCs and PNe as tracers of the gravitational potential.

It is fortunate that planetary nebulae (PNe) do not suffer from the three drawbacks affecting

GCs. PNe are generally thought to represent the distribution and dynamics of the galactic stellar halos with high fidelity (see, however, Méndez et al. 2001; Sambhus et al. 2006). Moreover, they are easy to observe, especially thanks to their very strong [OIII] emission line at 5007 Å. Henceforth, several dynamical studies have targeted PNe around bright ETGs using multi-slit or slit-less spectroscopy, or with the dedicated Planetary Nebulae Spectrograph (Douglas et al. 2002).

First analyses (Méndez et al. 2001; Romanowsky et al. 2003; Douglas et al. 2007) based on Jeans analysis and Schwarzschild modeling suggested that the host galaxies studied lacked DM, and were consistent with no DM (Romanowsky et al. 2003). However, recent results (e.g. Das et al. 2011) strongly confirm and quantify the discrepancy between the observed dynamics and that expected from the sole stellar light in giant ETGs such as NGC 4649. The extracted PNe luminosity distribution has also served to improve the distance estimated to that galaxy (Teodorescu et al. 2011). Although PN-based kinematic modeling is usually limited by the number of tracers (typically 100 to 200), the PN.S team has performed an ambitious observational program observing PNe in the outer regions of a dozen ETGs, with detailed results on a number of prototypical systems such as NGC 4374 in the Virgo cluster, reaching out to  $\simeq 5 R_e$  (Napolitano et al. 2011). This kinematic modeling usually assumes spherical symmetry, but there now exist several studies using axisymmetric models: e.g. NGC 4494 (Napolitano et al. 2009), NGC 3379 (de Lorenzi et al. 2009), NGC 4697 (Das et al. 2011).

The main limitation of such studies is the often assumed hypothesis of spherical symmetry for the mass distribution, but these results can still serve as strong guidelines to constrain the presence of dark matter in the outer halos of ETGs.

### 5.5.3. Other Tracers and Combined Approaches

At such large radii reached by the GC populations, as in NGC 1399, many studies take advantage of the presence of large X-ray halos around specific ETGs to constrain the corresponding radial mass, and make direct comparisons (Humphrey et al. 2006; Schuberth et al. 2010; Das et al. 2011; Gerhard 2013). A number of galaxies have been surveyed, mostly massive ETGs as they are more often embedded within such X-ray halos (Fukazawa et al. 2006; Nagino & Matsushita 2009). The assumed hypothesis of hydrostatic equilibrium for the hot gas may sometimes hamper the robustness of such conclusions, but these effects are generally thought to be small. This is convincingly confirmed by comparing several concomitant tracers (Churazov et al. 2008; Humphrey & Buote 2010; Humphrey et al. 2011) though some discrepancies have been reported, sometimes suggesting a transition from the galaxy halo to the cluster intergalactic medium Schuberth et al. (2010), or sometimes not yielding firm conclusions on their origins (Romanowsky et al. 2009).

As also mentioned above, even ETGs have sufficiently abundant (and well-behaved) gas components that can be used to constrain mass profiles out to large radii (Franx et al. 1994; Weijmans et al. 2008).

Orbits of individual satellites may further help constraining the potential around a galaxy (Geehan et al. 2006; van der Marel & Guhathakurta 2008). Prada et al. (2003) and Klypin & Prada (2009) used the SDSS to stack the PPS built from the satellites of thousands of otherwise fairly isolated galaxies and found it to be consistent with the predictions of  $\Lambda$ CDM simulations. Conroy et al. (2007) and More et al. (2011b) analysed galaxy satellites based on SDSS data, and derived the variation of virial mass with host galaxy luminosity, separating red and blue galaxies. They found both that red host galaxies of given blue luminosity have typically double the halo mass as their blue counterparts of same stellar mass. These two studies make assumptions that thwart the derivation of useful constraints on the anisotropy. Using the  $\Lambda$ CDM halo DF model (Wojtak et al.

2009) on a larger SDSS sample, Wojtak & Mamon (2013) are able to obtain more reliable relations between halo and stellar mass or luminosity, confirming to first order the results of Conroy et al. and More et al.. The stellar fractions within the virial radius of red galaxies with  $\log M_{\text{stars}} > 10$  exceed 1%, peaking at 2% for  $\log M_{\text{stars}} \approx 11.9$  and decreasing again to 1% at larger masses. However Wojtak & Mamon also find that red galaxies have more concentrated halos than blue galaxies of same stellar or halo mass, and that the orbits of satellites are marginally radial in the central regions, and increasingly radial with distance to the center. The reader may consult sections §6 and §7 on lensing for further details about the galaxy mass profiles at large radii.

As hinted above, a promising path toward robust mass profiles comes from the simultaneous use of all available tracers, hoping for a consistent picture to emerge. Many studies have been conducted towards this end, mostly targeting ETGs (Foster et al. 2011) and more specifically very massive ones (Woodley et al. 2010; Das et al. 2011; Arnold et al. 2011; Murphy et al. 2011). In agreement with results stated above, the overall impression from these studies calls for ETGs as being dominated by baryons within  $1 R_e$ , with DM representing about half of the mass within  $2 - 4 R_e$  and dominating at larger radii.

#### 5.5.4. The Mass-Anisotropy Degeneracy

The results presented in this section appear robust in a statistical sense. However, on an individual basis, measuring the mass profile in gas-poor galaxies is intrinsically difficult due to the degeneracy in the stellar dynamical models. The MAD is best broken by the joint use of several tracers, especially if they probe the same region of the potential. The use of tracers with very different orbital anisotropies can also be very useful to lift the MAD.

As an illustration of this MAD problem, Figure 17 shows the wide variety of solutions for the nearby (apparently) roundish ETG, NGC 3379, which had been the test-bed for the putative suggestion that ETGs are devoid of DM (Romanowsky et al. 2003; Douglas et al. 2007). One notices highly discrepant conclusions from various modeling attempts, in particular at the outer limit of spectroscopic observations ( $\sim 200''$  or  $\simeq 4 R_e$ ). The MAD is clearly present as the higher DM fractions indicate fairly radial orbits in the outer regions, while the lower ones come with isotropic orbits (e.g. de Lorenzi et al. 2009): this emphasizes the fact that specific tracers may constrain the mass distribution with uncertainties of different amplitude and nature. Moreover, there is a wide range of theoretical predictions. Also, some of the orbit solutions of Romanowsky et al. (2003) indicate ‘normal’ levels of DM at large radii (Mamon & Lokas 2005b). In fact, *all* recent observational modelling of NGC 3379 lead to an increased fraction of DM at increasing large radii. If NGC 3379, which has quasi-circular isophotes, were a nearly face-on S0 (Capaccioli et al. 1991), as suggested by its classification as a fast rotator (Emsellem et al. 2007), one would expect lower DM fractions (Magorrian & Ballantyne 2001).

#### 5.5.5. Discrete Star Velocities for Dwarf Spheroidal Galaxies

Relative to giant ETGs, dSphs constitute the other mass extreme. The study of such low luminosity objects and very faint galaxies relies mostly on very nearby (Local Group) galaxies, and largely in the context of resolved stellar populations (e.g. Gilmore et al. 2007). Mass modelling is feasible thanks to ambitious observational programs to measure the stellar kinematics of hundreds and sometimes several thousands of individual stars<sup>19</sup> (Tolstoy et al. 2004; Lokas et al. 2005; Simon

---

<sup>19</sup>Similar methods apply to the study of Milky Way stars; see §4.

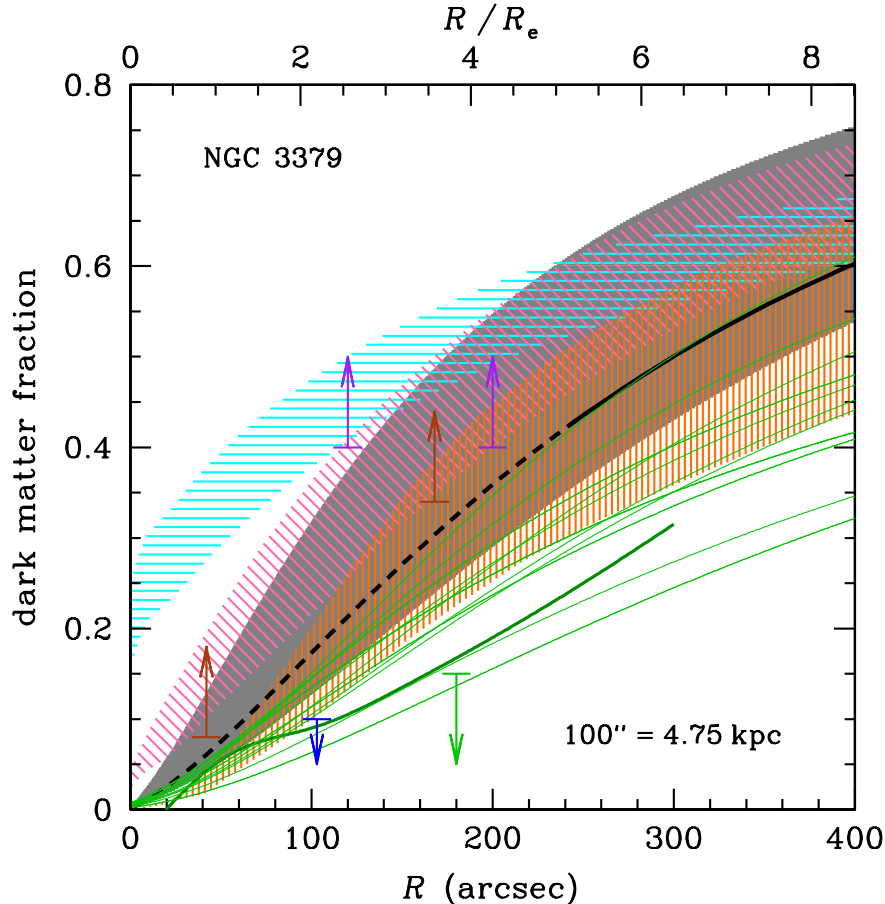


Figure 17: Dark matter fraction versus physical radius in NGC 3379 (assuming  $R_e=47''$  and Sérsic index  $n=4.74$ , following Douglas et al. 2007). The light green upper limit and light green curves respectively show the Jeans (PNe) and orbit-modelling solutions of Romanowsky et al. (2003) (stars+PNe), while the blue upper limit is the DF-modelling (stars) of Kronawitter et al. (2000). The medium-thickness dark green curve shows the spherical Jeans solution (stars+PNe) with double the number of PNe (Douglas et al. 2007). The orange vertically-shaded region gives the limits of NMAGIC orbit-modelling (stars+PNe) (de Lorenzi et al. 2009). The lower limits shows the orbit-modelling (stars) by Weijmans et al. (2009) (brown) and the isotropic Jeans analysis (globular clusters) of Pierce et al. (2006) (purple). The cyan horizontal- and magenta oblique-shaded regions give the predictions (see Dekel et al. 2005) from equal-mass merger SPH+cooling+feedback simulations (Cox et al. 2004), of respectively gas-poor and gas-rich spirals embedded in dark matter halos. The black curve is from the satellite kinematics study of Wojtak & Mamon (2013), adopting the mean of their 3rd and 4th stellar mass bins for red hosts (the stellar mass of NGC 3379 is in between), dashes for the extrapolation within the smallest satellite radii analyzed, while the grey shaded region represents the  $1\sigma$  confidence from the Monte Carlo Markov Chain analysis of Wojtak & Mamon.

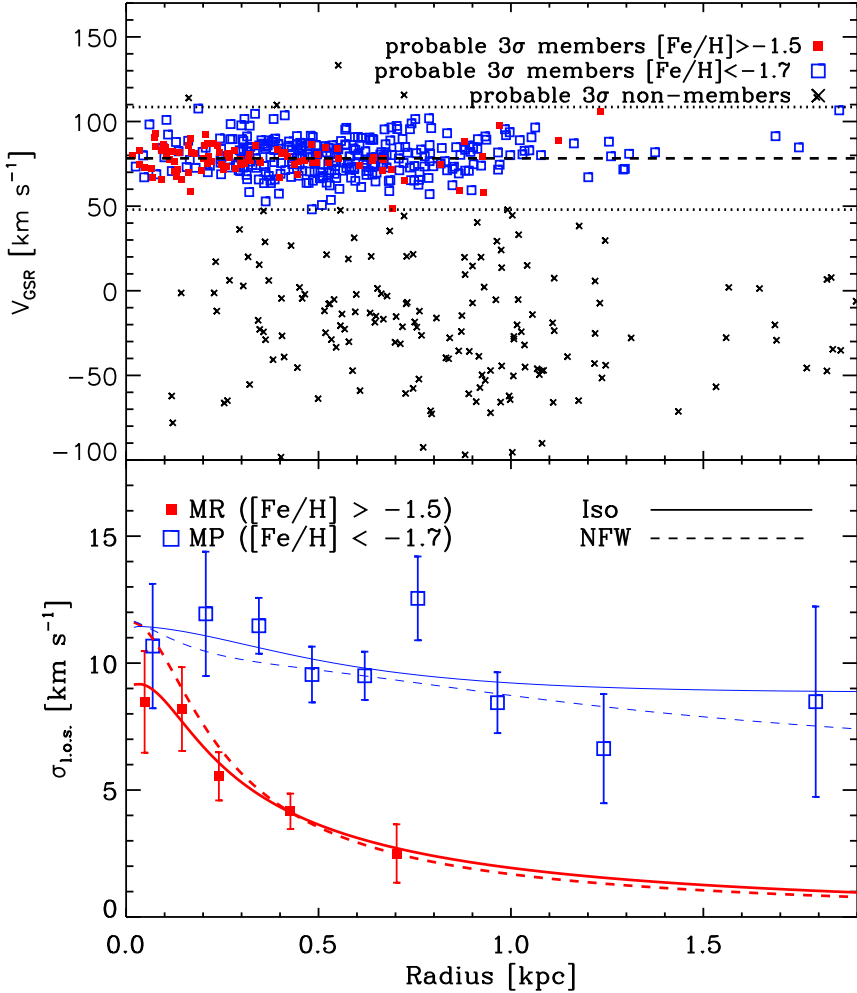


Figure 18: VLT/FLAMES velocity measurements for individual stars along the line-of-sight to the Sculptor dwarf spheroidal galaxy (dSph). *Top panel:* Line-of-sight velocities in the Galactic standard of rest versus projected radius for probable members to the Sculptor dSph (the *filled* and *open squares* show probable members with metallicity  $[\text{Fe}/\text{H}] > -1.5$  and  $< -1.7$ , respectively) and for probable non-members (*crosses*). The region of probable membership is indicated by the two *horizontal dotted lines*, while the *dashed line* indicates the systemic velocity of the galaxy. *Bottom panel:* Line-of-sight velocity dispersion profiles for the “metal-rich” ( $[\text{Fe}/\text{H}] > -1.5$ ) and “metal-poor” stars ( $[\text{Fe}/\text{H}] < -1.7$ ), as shown by the *filled* and *open squares with error-bars*, respectively. The *solid* and *dashed lines* show the L.o.s. velocity dispersion profiles for the best-fitting pseudo-isothermal (cored) and NFW (cusped) dark matter models. Figure adapted from results presented in Battaglia et al. (2008).

& Geha 2007; Walker et al. 2009a; Geha et al. 2010; Battaglia et al. 2011; Simon et al. 2011). We refer the reader to the detailed review by Battaglia et al. (2013).

An example of this method is shown in Figure 18 for the Sculptor dwarf spheroidal galaxy, studied in detail by Battaglia et al. (2008), who fit the PPS assuming Gaussian LOS velocity distributions (adding a component for contamination by our Milky Way). By disentangling the metal-poor and metal-rich stellar sub-populations, the authors were able to show that, if physically meaningful, these two sub-systems were compatible with the same potential (best fitted by an isothermal DM profile) but with different anisotropy, providing some clues about their origin, as the metal-rich sub-population appears to show a faster transition to radial orbits than the metal-poor one. The resulting dynamical mass-to-light ratio  $M/L$  reached values in excess of 150 inside  $\sim 2$  kpc, demonstrating the dominance of DM at all radii in such low surface brightness objects. Walker & Peñarrubia (2011) use a similar 2-population analysis to constrain the slopes of the mass profiles of the Fornax and Sculptor dSph galaxies, ruling out cusps as steep as  $-1$  (NFW) for both, and favoring inner slopes of  $-0.4 \pm 0.4$  (Fornax) and  $-0.5 \pm 0.5$  (Sculptor).

The DM core in Sculptor has been recently confirmed by Richardson & Fairbairn (2013b) using their new dispersion-kurtosis analysis with general anisotropy (Richardson & Fairbairn 2013a). Amorisco & Evans (2012) noted that Fornax has three distinct stellar populations (with different metallicities), and with this constraint, Amorisco et al. (2013) have shown that Fornax must indeed have a core of  $1_{-0.4}^{+0.8}$  kpc or else an NFW model with an unlikely very large scale radius. However, orbit modelling allows a cusp for Sculptor (Breddels et al. 2013) and Fornax (Jardel & Gebhardt 2012). Indeed, using orbit modelling, Breddels & Helmi (2013) conclude that while Fornax, Sculptor, Carina and Sextans can each accommodate either a cusp or a core, cores are unlikely when these 4 dSph galaxies are considered together. The debate between halo cusps and cores is thus still ongoing, largely because studies often group together different stellar populations that share different kinematics and neglect small but non-negligible rotation, and because non-spherical modelling increases the space of acceptable solutions.

Strigari et al. (2010) used an isotropic analysis (with Eq. (41) and Eddington's formula, and extracted the dispersion and kurtosis profiles from the former) to show that the classical dSph galaxies have LOS velocity dispersion, kurtosis and even distributions that are consistent with their surface density and with subhalos taken from the Aquarius  $\Lambda$ CDM simulation of the Milky Way (Springel et al. 2008), with dynamical masses between 2 and  $15 \times 10^8 M_\odot$ . More generally, it is believed (see Mateo 1998, , and references therein) that most dSphs have very high virial-theorem  $M/Ls$ . Recently, Walker et al. (2009b) and Wolf et al. (2010) have found that dSph  $M/Ls$  within the half-light radius increase towards lower masses down to the lowest mass *ultra-faint dwarfs* (UFDs). Although extrapolating these systems to their virial radii may be ill-advised, the data are consistent with all dSphs (including UFDs) having virial masses above  $10^8 M_\odot$  (Walker et al.; Wolf et al.).

However, the detailed modelling of dSphs is challenging because of Milky Way contamination (e.g. Lokas et al. 2005) and because their likely tidal tails are expected to lie very close to the LOS (Klimentowski et al. 2009), which could then lead to an overestimate of their mass (Klimentowski et al. 2007).

Furthermore, when the stellar velocity dispersion reaches extremely low values, additional ingredients such as the contribution of binary systems must be taken into account for proper dynamical modelling in particular for ultra-faint dwarf galaxies (see e.g. Martinez et al. 2011, and references therein).  $N$ -body models may be required for an accurate dynamical modelling of these objects.

### 5.6. Future Prospects

We have reviewed the basic methods to determine the distribution of total mass in gas-poor galaxies, whilst addressing a number of intrinsic degeneracies that may affect current determinations. We see two main directions for future applications of the discussed techniques:

One the one hand, for Local Group galaxies, the dynamical degeneracies can be alleviated by increasing the dimension of the observable space, namely by observing proper motions together with radial velocities of individual stars. At the present, this can be done for nearby star clusters by including plane-of-sky velocities from stellar proper motions in the dynamical models (e.g. van de Ven et al. 2006; van den Bosch et al. 2006; van der Marel & Anderson 2010).

The global space astrometry satellite GAIA (Perryman et al. 2001) will provide proper motions with unprecedented accuracy. Unfortunately, the classical dSph galaxies are so distant that the error on proper motions from GAIA will be of the order of their internal velocity dispersions e.g. Battaglia et al. 2013, so the gain from proper motions with GAIA may only be significant for the closest dSph galaxies. However, the future generation of 30–40m telescopes should roughly double the GAIA precision on proper motions (with a 5-year baseline, Davies & Genzel 2010), and lead to much more accurate mass and orbital modeling (as first suggested by Leonard & Merritt 1989).

These data will require and exploit the full generality and sophistication of the models. However, it is likely that such a wealth of data will also reveal new degeneracies associated with the sub-populations of stars in galaxies, themselves reflecting their complex formation and evolution history.

Meanwhile, if the increase in computing power grows at the current rate, one should be able to increasingly resort to  $N$ -body modelling (or associated techniques) to determine the distribution of mass in ETGs and dSphs that are not in perfect dynamical equilibrium and possibly address such models in some restricted cosmological context.

On the other hand, the same simpler techniques that are being applied today to relatively small samples of nearby galaxies will be used to study much larger samples of galaxies with two-dimensional stellar (and gaseous) kinematics and at increasingly larger redshift. The current state of the art is defined by the ATLAS<sup>3D</sup> (Cappellari et al. 2011) and CALIFA surveys (Sánchez et al. 2012), which have mapped a few hundred galaxies via integral-field spectroscopy. Ongoing surveys, such as the SAMI (PI: Scott Croom) and MaNGA (PI: Kevin Bundy), will extend the sample size by about two orders of magnitude, using multi-object two-dimensional spectrographs on dedicated telescopes. Accurate masses, which themselves rely on accurate distances, will still be a critical ingredient to study galaxy formation from these larger samples. Finally, the next frontier will involve constructing dynamical models of galaxies at significant redshift, to trace the assembly of galaxy masses over time. This will also make use of multi-object spectrographs, optimized for near-infrared wavelengths, to effectively reduce the exposure times by orders of magnitude, mounted on future generation very large telescopes. Within the next ten years (i.e.  $\sim 2024$ ), we may be able to approach the quality of the stellar kinematics of galaxies obtainable today in the Virgo cluster, up to the key redshift  $z \sim 2$ , when the Universe was just a quarter of its current age and much of the galaxy mass was being assembled.

## 6. Weak Lensing by Galaxies

### 6.1. Introduction

Most methods to constrain or measure the masses of galaxies are limited to relatively small radii, where baryons are dominant. This is, because these methods probe the gravitational potential through the dynamics of visible tracers. Although it is safe to assume that galaxies are virialized, uncertainties in the mass estimates remain, for instance due to anisotropies in the velocity distributions. Furthermore, these baryon dominated regions are not yet fully understood, which complicates a direct comparison of the models of galaxy formation to observational data. We note, however, that predictions from cosmological numerical simulations keep improving. Nonetheless, it would be advantageous to have observational constraints that can be robustly measured from numerical simulations. The virial mass of the galaxy is an obvious choice, but it is difficult to measure using dynamical methods. To date, only satellite galaxies have provided some information using data from large redshift surveys such as the SDSS (e.g. McKay et al. 2002; Prada et al. 2003).

In this section we focus on a direct probe of the matter distribution in the universe, which provides us with a unique opportunity to probe the outer regions of galaxies. It makes use of the fact that inhomogeneities in the matter distribution, such as the halos around galaxies, perturb the paths of photons emitted by distant sources: it is as if we are viewing these sources with a spatially varying index of refraction. As a result, the images of the distant galaxies typically appear slightly distorted (and magnified), an effect that is known as weak gravitational lensing. The amplitude of the distortion provides us with a direct measurement of the gravitational tidal field, which in turn can be used to “image” the distribution of dark matter *directly* (e.g. Kaiser & Squires 1993). If the distortion is large enough, multiple images of the source can be observed. This strong lensing provides accurate constraints on the mass distribution on small scales and its applications are discussed in §7.

The applications of weak lensing are not limited to galaxy-galaxy lensing, which is the study of the properties of galaxy dark matter halos. In fact the first detections were made by searching for the lensing-induced alignments of galaxies behind massive clusters of galaxies where the lensing signal is larger (Tyson et al. 1990; Fahlman et al. 1994). In recent years the focus has shifted to the measurement of the statistical properties of the large-scale structure: this cosmic shear is a promising probe of dark energy and has been detected with high significance (Fu et al. 2008). This application is driving much of the developments in improving measurement techniques, but also in terms of survey requirements. Consequently, galaxy-galaxy lensing studies benefit as well, because the data requirements are rather similar: we need to survey large areas of the sky, preferably in multiple bands in order to derive photometric redshifts. Such data sets are becoming available, and significant progress is expected in the coming years as the analyses of the first multi-color cosmic shear surveys are completed.

The first attempt to measure the weak lensing signal around galaxies<sup>20</sup> was made by Tyson et al. (1984) using data from photographic plates with fairly poor image quality. As discussed in more detail below, the determination of the lensing signal requires careful measurements of the shapes of faint galaxies which benefit greatly from good image quality. Consequently, the first detection was reported over a decade later by Brainerd et al. (1996) using deep ground-based CCD images. Soon after Hudson et al. (1998) exploited the combination of deep HST imaging and photometric redshifts in the Northern Hubble Deep Field.

---

<sup>20</sup>In fact, it was the first attempt ever to measure a weak lensing signal.

An accurate determination of the galaxy-galaxy lensing does not only require good image quality. As explained below, the signal around an individual galaxy is too low to be detected. Instead we stack the signals for a large ensemble of lenses to improve the signal-to-noise ratio of the measurement. The early studies were all based on small survey areas, thus yielding small numbers of lens-source pairs. This changed with the start of the Sloan Digital Sky Survey (SDSS): Fischer et al. (2000) used only 225 deg<sup>2</sup> of commissioning data and detected a significant galaxy-galaxy lensing signal out to 1 Mpc. The SDSS data are relatively shallow, but the large survey area provides the large number of lens-source pairs to measure the lensing signal with high accuracy. Another important feature of the SDSS is the availability of redshifts for the lenses (spectroscopic as well as photometric), which has been used by McKay et al. (2001), Guzik & Seljak (2002) and Mandelbaum et al. (2006b).

In the case of deep observations the reduction in the number of lenses (due to smaller survey area) is compensated by the increase in the number of sources, which are also more distant. Hence, even by imaging tens of square degrees the galaxy-galaxy lensing signal can be measured accurately (Hoekstra et al. 2004; Parker et al. 2007). Such surveys typically lack spectroscopic redshift information for the lenses and use photometric redshifts instead (but see van Uitert et al. 2011, for an example that combines SDSS spectroscopy with deeper imaging).

Below we provide a brief introduction to weak galaxy-galaxy lensing and present a number of highlights, demonstrating the potential of this technique. However, it is important to stress that this is a field that is still developing, and many exciting results are expected from the next generations of surveys.

### 6.2. Theory of Weak Lensing

Due to space limitations, we can only provide the most basic discussion of weak gravitational lensing. We refer the interested reader to a recent review by Hoekstra & Jain (2008) or the thorough introductions by Bartelmann & Schneider (2001) or Schneider (2006b).

Inhomogeneities along the line-of-sight deflect photons originating from distant galaxies. As these sources are typically small, the resulting effect is a remapping of  $f^s$ , the surface brightness distribution of the source:

$$f^{\text{obs}}(x_i) = f^s(\mathcal{A}_{ij}x_j), \quad (42)$$

where  $\mathbf{x}$  is the position on the sky and  $\mathcal{A}$  is the distortion matrix (i.e., the Jacobian of the transformation), which is specified by the projected surface density of the lens and the redshifts of the lens and the source. It is convenient to introduce the deflection potential  $\Psi$

$$\Psi(\mathbf{x}) = \frac{1}{\pi} \int d^2\mathbf{x}' \kappa(\mathbf{x}') \ln |\mathbf{x} - \mathbf{x}'|, \quad (43)$$

where the convergence  $\kappa$  is the ratio of the projected surface density  $\Sigma(\mathbf{x})$  and the critical surface density  $\Sigma_{\text{crit}}$ :

$$\kappa(\mathbf{x}) = \frac{\Sigma(\mathbf{x})}{\Sigma_{\text{crit}}}, \quad (44)$$

with  $\Sigma_{\text{crit}}$  defined as

$$\Sigma_{\text{crit}} = \frac{c^2}{4\pi G} \frac{D_s}{D_l D_{ls}}. \quad (45)$$

Here  $D_s$ ,  $D_l$ , and  $D_{ls}$  correspond to the angular diameter distances between the observer and the source, observer and the lens, and the lens and the source. Hence, the lensing signal depends on both the redshifts of the lenses and the sources. Note that (in particular) the sources are too faint to determine spectroscopic redshifts, and photometric redshifts are used instead. Early galaxy-galaxy lensing studies lacked redshift information for both lenses and sources and average redshift distributions were used to infer masses (e.g. Hoekstra et al. 2004; Parker et al. 2007)). Redshift information is particularly useful for the lenses, as it allows one to study the lensing signal as a function of baryonic content and environment. Often photometric redshifts are also used for the lenses (Hoekstra et al. 2005; Kleinheinrich et al. 2006), with the notable exception of the SDSS (Mandelbaum et al. 2006b; van Uitert et al. 2011).

Redshifts for individual sources are not critical, provided their redshift distribution is known. However, if such information is lacking, faint satellite galaxies associated with the lens will dilute the lensing signal, if left unaccounted for. Furthermore, if these galaxies align their major axis towards the host galaxies, they will bias the signal (Agustsson & Brainerd 2006).

The distortion matrix  $\mathcal{A}$  can be written in terms of the second derivatives of the deflection potential  $\Psi$

$$\mathcal{A} = \delta_{ij} - \frac{\partial^2 \Psi}{\partial \theta_i \partial \theta_j} = \begin{pmatrix} 1 - \kappa - \gamma_1 & -\gamma_2 \\ -\gamma_2 & 1 - \kappa + \gamma_1 \end{pmatrix}, \quad (46)$$

where we used that  $\kappa = \frac{1}{2} \nabla^2 \Psi$  and introduced the complex shear  $\gamma \equiv \gamma_1 + i\gamma_2$ , which are related to the deflection potential through

$$\gamma_1 = \frac{1}{2}(\Psi_{,11} - \Psi_{,22}) \quad \text{and} \quad \gamma_2 = \Psi_{,12}, \quad (47)$$

If  $\kappa$  and  $\gamma \ll 1$  (i.e., the weak lensing regime), the effect of the remapping by  $\mathcal{A}$  is to transform a circular source into an ellipse, with axis ratio  $\sim (1 - |\gamma|)/(1 + |\gamma|)$  and position angle  $\alpha = \arctan(\gamma_2/\gamma_1)/2$ . In addition, the source is magnified by a factor

$$\mu = \frac{1}{\det \mathcal{A}} = \frac{1}{(1 - \kappa)^2 - |\gamma|^2}, \quad (48)$$

boosting the flux by the same amount. To first order, the magnification depends on the convergence only. Both the shearing and magnification of sources are observable effects, although both are quite different in terms of techniques and systematics.

### 6.3. Shear

To study the dark matter distribution in the universe, the measurement of the shearing of background galaxies is most commonly used, because of the better signal-to-noise that can be achieved per lens-source pair when compared to the effect of magnification. It involves the measurement of the shapes of the faint background galaxies. Under the assumption that galaxies are randomly oriented in the absence of lensing, the strength of the tidal gravitational field can be inferred from the measured ellipticities of an ensemble of sources.

If we consider an isolated lens, the effect of weak lensing is a systematic (purely) tangential alignment of the images of the background galaxies with respect to the lens galaxy. The average tangential distortion, defined as

$$\gamma_T = -(\gamma_1 \cos 2\phi + \gamma_2 \sin 2\phi), \quad (49)$$

can then be used to quantify the lensing signal. Here  $\phi$  is the azimuthal angle with respect to the lensing galaxy. For any mass distribution the azimuthally averaged tangential shear can be interpreted as a mass contrast:

$$\langle \gamma_T \rangle(r) = \bar{\kappa}(< r) - \bar{\kappa}(r). \quad (50)$$

A simple model to compare to the data is the singular isothermal sphere (SIS) with  $\rho(r) = \sigma^2/(2\pi G r^2)$ , where  $\sigma$  is the line-of-sight velocity dispersion. For this mass distribution we obtain

$$\gamma_T(r) = \kappa(r) = \frac{r_E}{2r}, \quad (51)$$

where  $r_E$  is the Einstein radius, which can be expressed in terms of  $\sigma$  and  $\beta = \langle D_{ls}/D_s \rangle$ :

$$r_E = \beta \left( \frac{\sigma}{186 \text{ km/s}} \right)^2 \text{ arcsec}. \quad (52)$$

If we fit the model to the data from  $R_0$  to  $R$ , the corresponding error is

$$\sigma_{r_E} = \sqrt{\frac{1}{\pi \bar{n} \ln(R/R_0)}} \sigma_{\text{gal}}, \quad (53)$$

where  $\bar{n}$  is the number density of sources and  $\sigma_{\text{gal}}$  their intrinsic ellipticity ( $\sigma_{\text{gal}} \sim 0.3$ ). For deep ground based observations  $\bar{n} \sim 10 - 20 \text{ arcmin}^{-2}$ . As discussed below, we should only consider the signal at  $R < 120''$  and  $R > 5''$  (because the lens light should not interfere with our shape measurement). For a galaxy with a velocity dispersion of 150 km/s, we obtain a typical signal-to-noise ratio of  $r_E/\sigma_{r_E} \sim 0.39/1.4 \sim 0.26$  (adopting a typical value of  $\beta = 0.6$ ). Even with the much higher source density in HST observations the best we can achieve is  $S/N \sim 1$ . Hence the signal of an individual lens galaxy is by far too small to be detected. Instead we have to average the signals for an ensemble of lenses to improve the signal-to-noise ratio.

Furthermore, the induced lensing signal is tiny, much smaller than the typical observational distortions that affect the observed shapes of the galaxies. The most relevant ones are the circularisation by the PSF (seeing) and PSF anisotropy. The former lowers the signal (if uncorrected for) and the latter can mimic a lensing signal. Much effort has been spent on understanding and correcting these sources of systematics. A major driver has been the study of lensing by large-scale structure, a.k.a. cosmic shear, which is an important way to study dark energy (see Hoekstra & Jain (2008) for a review) and extremely sensitive to residual systematics. In galaxy-galaxy lensing, however, one averages the signal perpendicular to lines connecting many lens-source pairs, which are randomly oriented with respect to the direction of PSF anisotropy. As a result any residual systematics are suppressed. The measurement of halo shapes is somewhat more sensitive, but as shown in Hoekstra et al. (2004) current results are not affected and it is possible to reduce the impact further, albeit at the expense of increasing the noise (Mandelbaum et al. 2006a; van Uitert et al. 2012).

#### 6.4. Magnification

The measurement of the magnification provides a complementary way to study the mass distribution. The actual magnification cannot be measured because the intrinsic fluxes of the sources are unknown. Instead, the signal can be inferred from the change in the source number counts. Such a change arises from the balance between two competing effects. On the one hand the actual volume

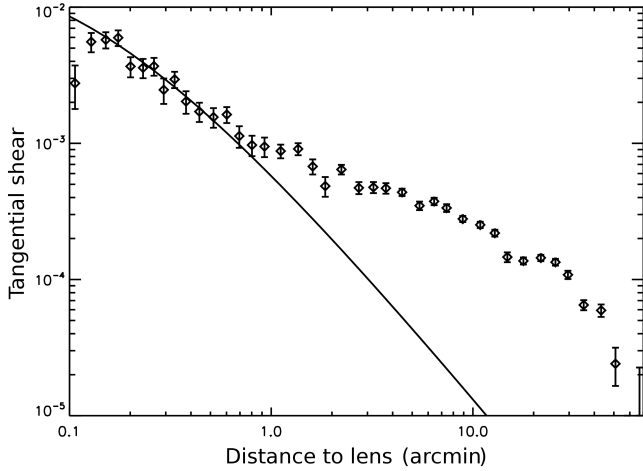


Figure 19: Plot of the ensemble averaged tangential shear as a function of distance from the lens using  $334 \text{ deg}^2$  of  $r'$  data from the RCS2 (van Uitert et al. 2011). The lenses are selected to have apparent magnitudes  $19.5 < m_r < 21.5$  and the sources  $22 < m_r < 24$ . For reference the best fit NFW profile is also drawn, which shows that on scales beyond  $1'$  ( $\sim 300 \text{ kpc}$ ) the clustering of the lenses becomes important.

that is surveyed is reduced, because the solid angle behind the cluster is enlarged. However, the fluxes of the sources in this smaller volume are boosted, thus increasing the limiting magnitude. As a consequence, the net change in source surface density depends not only on the mass of the lens, but also on the steepness of the intrinsic luminosity function of the sources. If it is steep, the increase in limiting magnitude wins over the reduction in solid angle, and an excess of sources is observed. If the number counts are shallow a reduction in the source number density is observed.

The uncertainty in the measurement is determined by variations in the number density (i.e., a combination of Poisson noise and the clustering of the sources). A correct interpretation of the results only requires accurate photometry and knowledge of the (unlensed) luminosity function. Therefore the requirements on the PSF are much less stringent compared to the shear-based approach.

The magnification has been measured for quasars in the SDSS (Scranton et al. (2005); Ménard et al. (2008)) and Lyman-break galaxies in the CFHT Legacy Survey by Hildebrandt et al. (2009). The latter study is of particular interest, because these drop-out galaxies are readily identified in deep wide-field imaging surveys. Furthermore, as the sources are all at high redshift, this approach provides a unique way to study the masses of high redshift ( $z \sim 1$ ) galaxies using ground-based data.

### 6.5. Galaxy-Mass Cross-Correlation Function

If galaxies are well separated, or randomly distributed, the observed lensing signal can be directly related to the ensemble averaged dark matter distribution. In the real universe, however, galaxies are clustered. This complicates such a simple interpretation of the data. On sufficiently small scales the lensing signal is dominated by individual halos, but on larger scales we measure the combined signals from many halos. An example is shown in Figure 19, which shows results from the analysis of  $334 \text{ deg}^2$  of data from the RCS2 (van Uitert et al. (2011); also see e.g., Fischer et al. (2000);

Hoekstra et al. (2004); Sheldon et al. (2004)). A significant signal is measured out to  $30'$  from the lenses, which corresponds to  $\sim 9$  Mpc. Figure 19 also shows the best fit NFW profile (to data between 0.2 and 0.6 arcmin), which drops below the observations for scales larger than  $1'$  ( $\sim 300$  kpc). Hence on these larger scales the clustering of the lenses is important to interpret the data. van Uitert et al. (2011) also compared the data to a SIS model and found that it also fits the data well out to  $\sim 300$  kpc, indicating that it is typically difficult to distinguish between profiles. We note that Gavazzi et al. (2007) used a combination of strong and weak lensing measurements around massive ellipticals and found that a SIS model provides a good fit to the data. As discussed below, this does not imply that the density profile is isothermal. Rather, it is believed to be the result of the clustering of galaxies, which themselves have NFW density profiles.

It is therefore more appropriate to think of the galaxy-galaxy lensing signal as a measurement of the cross-correlation between the galaxy and mass distribution: the galaxy-mass cross-correlation function. This observable provides additional constraints for models of galaxy formation and can be used to study the bias parameter as a function of scale (e.g. van Waerbeke 1998). In particular, it allows us to study whether the (small scale) bias is non-linear and/or stochastic (e.g. Pen 1998; Dekel & Lahav 1999).

The galaxy-mass cross-correlation function is closely related to the galaxy two-point correlation function and the cosmic shear signal, as they all provide ways to study the growth of structures via gravitational instability. On large scales the biasing is (close to) linear and the galaxy and dark matter distributions are well correlated. In this situation the galaxy power spectrum is  $b^2$  times the matter power spectrum,  $P(k)$  which can be measured through cosmic shear studies (Hoekstra & Jain 2008; Fu et al. 2008)). The value of the bias parameter  $b$  is not known a priori. Similarly, the galaxy-mass cross-power spectrum will be  $b \times r \times P(k)$ , where  $r$  is the cross-correlation coefficient. The observed tangential shear measurement can be expressed as a integral over the power spectrum multiplied by a filter (see Guzik & Seljak 2001; Hoekstra et al. 2002, for more details).

The combination of the galaxy two-point correlation function and the galaxy-galaxy lensing signal provides a direct measurement of the ratio  $b/r$  as a function of scale. This ratio was first measured by Hoekstra et al. (2001), who later extended the analysis to the full RCS data in Hoekstra et al. (2002). They found that  $b/r$  is constant out to  $\sim 7$  Mpc with an average value of  $1.09 \pm 0.035$  for  $\sim L_*$  galaxies. Sheldon et al. (2004) found similar results using SDSS data. Hoekstra et al. (2002) also included cosmic shear measurements from the VIRMOS-Descart survey (Van Waerbeke et al. 2002) to study the scale dependence of  $b$  and  $r$  separately. Although, Hoekstra et al. (2002) found tentative evidence for a variation of  $b$  and  $r$  with scale, this results needs to be confirmed as residual systematics in the cosmic shear signal may have affected the results (Van Waerbeke et al. 2005).

Finally, Reyes et al. (2010) recently showed how General Relativity can be tested by combining the observed galaxy-galaxy lensing signal with measurements of redshift-space distortions and the clustering of galaxies. This measurement combines three probes of large-scale structure to compare the two scalar potentials in the gravitational metric ( $\psi$  and  $\phi$ ). In  $\Lambda$ CDM and GR, both scalar potentials are equal. The lensing signal is sensitive to the sum of these, whereas the clustering measurements are only sensitive to the Newtonian potential  $\phi$ . Although each of the observational probes depends on the value of the bias and the normalization of the power spectrum, the combination of these probes does not. Reyes et al. (2010) used data from the SDSS and found good agreement with GR on scales ranging from  $\sim 2 - 40$  Mpc. The results cannot yet rule out  $f(R)$  gravity models, but do disfavor some TeVeS models.

### 6.6. Properties of Dark Matter Halos

Although the study of the galaxy-mass cross-correlation function can provide useful constraints for models of galaxy formation, one would also like to learn more about the properties of the galaxy dark matter halos themselves. This requires us to “separate” the contributions from individual halos from the clustering of the lenses. There are a number of ways this can be done. For instance, we can use the actual positions of the lenses and make the simplifying assumption that the observed signal arises only from the dark matter halos associated with those lenses. Hence this approach does not describe well the situation in clusters or the large-scale structure. Furthermore, it is computationally expensive, in particular if the model is extended to include more parameters. An advantage, however, is that it uses the two-dimensional shear field around the lenses, which is compared to the observations in a maximum likelihood fashion. The maximum likelihood method, however, has not been studied in detail using numerical simulations and it is currently unclear to what extent the simplifying assumptions bias the results. Such tests are needed before this approach can be applied to modern, large data sets.

The maximum likelihood method was used by Hoekstra et al. (2004) to examine the extent of dark matter halos around galaxies (also see e.g. Brainerd et al. 1996; Hudson et al. 1998). The lack of color information limited the analysis, but Hoekstra et al. (2004) was able to constrain for the first time the sizes of the dark matter halos. Figure 20 shows the result when an NFW model is assumed (Navarro et al. 1997). The mass and scale radius  $r_s$  are free parameters in the model, which are well constrained. Numerical simulations of cold dark matter (e.g. Navarro et al. 1997)) predict a correlation between these parameters and the dashed line shows this prediction, which is in excellent agreement with these measurements. However, the mass-concentration relation depends on cosmology (in particular the normalization of the matter power spectrum  $\sigma_8$ ), which has changed over the years. Furthermore, larger numerical simulations have been used to examine the relations between halo properties and their evolution. The original results presented in Hoekstra et al. (2004) used  $\sigma_8 = 0.85$ , but updated results with both lower and higher figures both yield larger values for  $r_s$ . We therefore also show in Figure 20 the expectations for Neto et al. (2007) who used  $\sigma_8 = 0.9$  and Duffy et al. (2008) who used  $\sigma_8 = 0.8$ ; given the limited investigations on the merits of the maximum likelihood method, it is unclear whether or not there is tension between the data and the predictions. It does suggest that this is an avenue worth pursuing.

In high density regions, such as clusters of galaxies, the galaxy dark matter halos are expected to be tidally stripped due to the interaction with the tidal field of the smooth cluster mass distribution. Galaxy-galaxy lensing studies provide the only way to examine the sizes of the dark matter halos as a function of cluster-centric radius (Natarajan & Kneib 1997; Natarajan et al. 1998). A complication is that the signal arises from a combination of the stripped halos and the global cluster mass distribution. The various components can be modelled by a maximum likelihood method<sup>21</sup>). To minimize contamination by field galaxies, with their much more extended halos, early work has been confined to early type galaxies (Natarajan et al. 1998; Limousin et al. 2007), but recently Natarajan et al. (2009) were able to study late type galaxies as well. These studies have shown that dark matter halos of cluster galaxies are tidally truncated (Limousin et al. 2007; Natarajan et al. 2009), which is also observed in strong lensing studies Halkola et al. (2007).

The clustering of dark matter halos as a function of mass is well-understood. This knowledge can be used to predict the galaxy-mass cross-correlation function, by relating the dark matter

---

<sup>21</sup>Which can also include strong lensing features to constrain the model further.

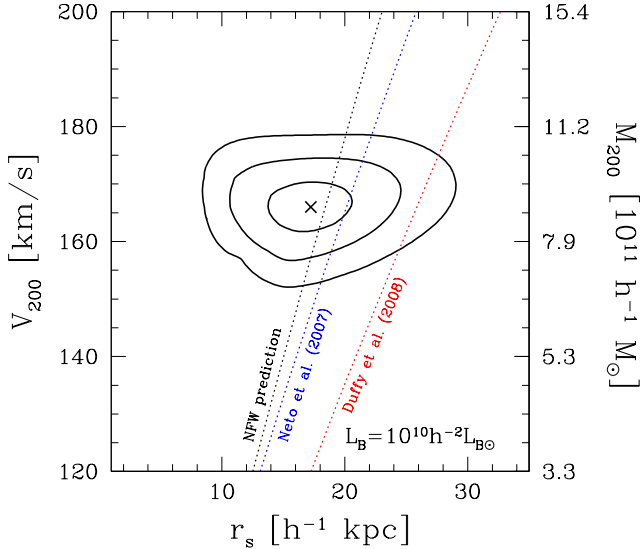


Figure 20: Joint constraints on the scale radius  $r_s$  and mass  $M_{200}$  (and corresponding rotation velocity  $V_{200}$ ) for a galaxy with an NFW profile and a fiducial luminosity  $L_B = 10^{10} h^{-2} L_{B\odot}$ . The contours indicate the 68%, 95% and 99.7% confidence on two parameters jointly. The dotted line indicates the prediction from the numerical simulations by NFW (from Hoekstra et al. 2004). Our updated version of this figure shows expectations from works by Neto et al. (2007) and Duffy et al. (2008).

distribution statistically to the observable galaxies through a halo occupation distribution (HOD; Seljak (2000); for a review see Cooray & Sheth (2002)). This halo model approach is a powerful (and natural) way to interpret the data as it provides a natural way to account for the fact that the clustering depends on mass and that more massive halos host more than one galaxy (i.e., groups and clusters of galaxies). A minor drawback is that it only uses the tangential component of the shear. For isolated lenses the signal is indeed purely tangential, but this is no longer the case for an ensemble of lenses. The halo model was used by Guzik & Seljak (2002) and Mandelbaum et al. (2006b) to interpret the results from the SDSS and constrain the fraction of satellite galaxies. A similar study was carried out by van Uitert et al. (2011) who complemented the SDSS spectroscopic data with deep imaging data from the second Red-sequence Cluster Survey (RCS2). This improved constraints for the massive galaxies, which on average are at higher redshifts.

The former studies focus only on the galaxy-mass cross-correlation function, but a consistent model for galaxy formation also makes predictions for the clustering of galaxies and the luminosity and/or stellar mass functions. Combining the information of these complementary probes can improve the constraints on the halo model parameters (Leauthaud et al. 2011). Such a joint analysis was performed recently by Leauthaud et al. (2012) using data from the COSMOS survey. The high quality lensing data, in combination with unprecedented wavelength coverage, allowed Leauthaud et al. (2012) to study the evolution of the stellar-to-halo mass relation from  $z = 0.2$

out to  $z = 1$ . They found that the halo mass scales with stellar mass  $\propto M_*^{0.46}$  for galaxies with  $M_* < 5 \times 10^{10} M_\odot$  over the redshift range studied, whereas the slope of the relation steepens for higher masses.

One can also attempt to 'avoid' the complication caused by the clustering of the lenses by considering only relatively 'isolated' lenses. In this case the observed lensing signal is dominated by only a single galaxy. Such a selection, which requires (photometric) redshift information, was used in Hoekstra et al. (2005) to study the relation between the virial mass and the luminosity. They limited the sample to galaxies that are more than  $30''$  away from a brighter galaxy. For these galaxies Hoekstra et al. (2005) found that the virial mass scales with luminosity as  $\propto L^{1.5}$ , in agreement with the results from Guzik & Seljak (2002); Mandelbaum et al. (2006b) who used the halo model to interpret the SDSS data. For a galaxy with fiducial luminosity of  $L_B = 10^{10} h^{-2} L_B \odot$  Hoekstra et al. (2005) obtained a virial mass  $M_{\text{vir}} = 9.9_{-1.3}^{+1.5} \times 10^{11} M_\odot$ , also in good agreement with Mandelbaum et al. (2006b).

If we assume that baryons do not escape the dark matter overdensity they are associated with, the ratio of  $M_b$ , the mass in baryons, to the virial total mass of the halo is  $M_b/M_{\text{vir}} = \Omega_b/\Omega_m$ . Furthermore, the amount of cold gas is negligible for massive galaxies. Therefore, by comparing the stellar mass of the lenses to the virial mass determined by weak lensing, the efficiency with which baryons are converted into stars can be constrained. Hoekstra et al. (2005) found that late types convert a  $\sim 2$  times larger fraction of baryons into stars compared to early-type galaxies. The measurement of Hoekstra et al. (2005) is mostly constrained by relatively luminous galaxies. Mandelbaum et al. (2006b) find that the conversion efficiencies are independent of morphological type for stellar masses less than  $\sim 7 \times 10^{10} M_\odot$ , but also find that later type galaxies appear more efficient for higher stellar masses. Heymans et al. (2006) used GEMS data to study the mean virial to stellar mass ratio for a complete sample of massive galaxies out to  $z \sim 0.8$ . The results, which agreed well with Hoekstra et al. (2005) and Mandelbaum et al. (2006b) showed little evidence for evolution. Leauthaud et al. (2012) also study the stellar mass fraction as a function of mass finding a minimum at a halo mass of  $\sim 1.2 \times 10^{12} M_\odot$ .

These studies demonstrate the potential of weak lensing results for the study of galaxy evolution. We note, however, the accuracy of the halo model is limited, and that measurements soon will be limited by this.

### 6.7. Halo Shapes

The average shape of dark matter halos can provide another way to learn more about the nature of dark matter (and the interaction with baryons). Numerical simulations of CDM have shown that the resulting dark matter halos are triaxial with a typical ellipticity of  $\sim 0.3$  (e.g. Dubinski & Carlberg 1991; Jing & Suto 2002b; Hayashi et al. 2007). In the case of self-interacting dark matter, the predicted halos are more spherical, although this difference is more pronounced on small scales (Davé et al. 2001). We also note that hydrodynamic simulations suggest that baryonic effects cause dark matter halos to evolve more oblate configurations at all radii, even if the effect of baryons is most prominent in the inner parts (e.g. Kazantzidis et al. 2004, 2010).

The small scales, which are baryon-dominated, are best probed by strong lensing studies or dynamical studies. The latter approach has been extended to larger scales through the study of streams of stars in the Milky Way (Helmi 2004; Koposov et al. 2010). On large scales, which are best constrained by numerical simulations, only weak lensing studies can provide observational constraints on the shapes of dark matter halos. The measurement, however, is difficult: we now need to measure an azimuthal variation in the, already small, galaxy-galaxy lensing signal. The

azimuthal variation is measured with respect to the major axis of the light distribution, i.e. we assume that the halos are aligned with the lens. If halos are flattened, but not aligned with the light distribution, the resulting lensing signal will be isotropic. Hence, any misalignment will reduce the amplitude of the azimuthal variation and the weak lensing constraints are in effect lower limits on the shapes. Such misalignments might result from baryonic effects. For instance Bailin et al. (2005) found in their hydrodynamic simulations of disk galaxies that the outer part of the halo is not well aligned with the inner regions, which do show a good alignment between disk and inner halo (also see e.g. Abadi et al. 2010).

Weak lensing studies of dark matter halo shapes are more sensitive to systematic effects/errors compared to the measurement of the galaxy-mass cross-correlation function. For instance, residual PSF anisotropy leads to correlations between the lenses and sources, biasing the dark matter halo shape determination (Hoekstra et al. 2004; Mandelbaum et al. 2006a, e.g.)). However, even in the absence of residual systematics, lensing by lower redshift structures can align the lens and the source, reducing the signature of an anisotropic halo. This cosmic shear contribution is described in detail in Mandelbaum et al. (2006a) (also see Brainerd (2010) and Howell & Brainerd (2010) who also discuss this problem). This source of bias becomes more prominent with increasing lens redshift and will need to be taken into account when interpreting the current generation of surveys. Fortunately, Mandelbaum et al. (2006a) provide a method to suppress this signal, although this can only be applied reliably on relatively small scales and with limited accuracy (van Uitert et al. 2012).

A successful measurement of the halo shapes requires a much larger number of lens-source pairs, as the signal-to-noise ratio is about a tenth of that of the tangential shear signal, and limited to small scales (van Uitert et al. 2012). In recent years a number of pioneering studies have been carried out, but the results are still inconclusive. The first claim of elliptical dark matter halos using weak lensing was presented in Hoekstra et al. (2004) using  $42 \text{ deg}^2$  of data from the RCS. The lenses were selected based on their apparent magnitude and early type galaxies contribute most of the signal. Hoekstra et al. (2004) found that the halos are aligned with the light distribution and estimated an ellipticity of  $\langle e_{\text{halo}} \rangle = 0.33^{+0.07}_{-0.09}$ . These results are in fair agreement with the results from Parker et al. (2007), who used  $22 \text{ deg}^2$  of deep  $i'$  data from the CFHT Legacy Survey and also inferred an ellipticity  $\sim 0.3$ .

The analysis of SDSS data by Mandelbaum et al. (2006a) did not detect an azimuthal variation in the lensing signal when considering the full sample of lens galaxies. However, when restricting the sample to bright early type galaxies, the results of Mandelbaum et al. (2006a) do suggest that the halos are aligned with the light. Recently, van Uitert et al. (2012) completed the analysis of  $800 \text{ deg}^2$  of RCS2 data, but did not detect a significant anisotropy signal. Part of the loss of precision is caused by a careful accounting for possible systematic effects.

An interesting, still open question, is whether the alignments are the same for different types of galaxies. The possible differences between the various analyses needs to be investigated further, but it is clear that significant progress will only be possible with the next generation of deep, multi-color surveys which provide redshift information for the lenses. The latter is important because of the scale dependence of the anisotropy signal (Mandelbaum et al. 2006a; van Uitert et al. 2012).

### 6.8. Future Prospects

Early weak galaxy-galaxy studies have already provided unique constraints on the properties of dark matter halos, such as constraints on their extent and shapes, as well as masses. The SDSS results have demonstrated the usefulness of multi-color data and redshift information for the lenses.

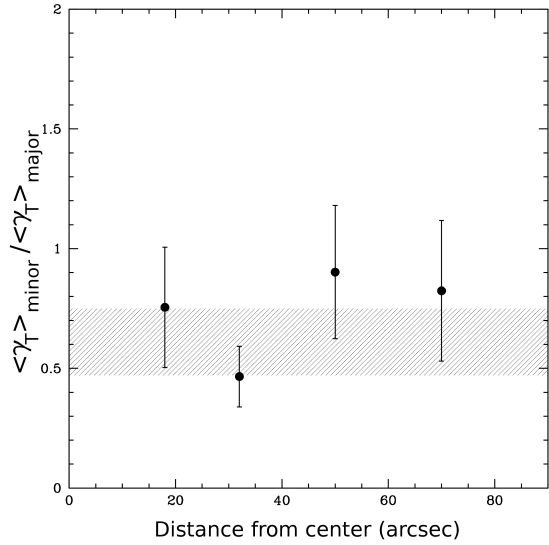


Figure 21: Ratio of the mean shear experienced by sources closest to the minor axes of a foreground lens to that of sources closest to the major axes for lenses with axis ratios  $b/a$  between 0.5 and 0.8. This criterion preferentially selects early type galaxies. The results are taken from Parker et al. (2007) who analysed  $22 \text{ deg}^2$  of  $i'$  data from the CFHTLS. The weighted average shear ratio is  $0.61 \pm 0.14$ .

Of particular interest would be studies that complement the SDSS with deeper imaging. The precision of photometric redshifts limits their usefulness at low redshifts, but for the study of lenses with  $z > 0.3$  the excellent statistics that can be achieved from the next generation surveys are expected to outweigh the limitations. For instance the KiloDegree Survey (KiDS) which started observations in the fall of 2011 will cover  $1500 \text{ deg}^2$  in nine filters. The extensive wavelength coverage will yield accurate photometric redshifts for the lenses. As a result statistical errors will be reduced by a factor  $\sim 4$  over current results and provide a first opportunity to study in detail the properties of dark matter halos as a function of density and baryon contents. The Dark Energy Survey, which recently started taking data, will image  $5000 \text{ deg}^2$ .

Another major step forward will come from the Large Synoptic Survey Telescope (LSST) which plans to start surveying  $\sim 20,000 \text{ deg}^2$  around the turn of this decade and space-based dark energy projects, such as the recently approved Euclid mission Laureijs et al. (2011), which is scheduled for launch in 2020. The excellent statistics provided by the latter projects will allow for the study the galaxy lensing signal over a wide range in physical properties and redshift. Thanks to these developments galaxy-galaxy lensing will continue to develop into an important tool to study galaxy masses as a function of their (observable) baryonic properties.

## 7. The Dark and Luminous Mass Distribution of Early-type Galaxies using Strong Gravitational Lensing

### 7.1. Introduction

Despite being a fundamental parameter required to test galaxy formation models (White & Rees 1978; Blumenthal et al. 1984), the measurement of galaxy masses with few percent accuracy on any scale is notoriously difficult. This is particularly the case for early-type galaxies (ETGs) which are not rotationally supported and generally lack gas-dynamical tracers. As we have seen in previous sections, a wide range of methods, or their combinations, have been employed to measure galaxy total masses on very different scales: e.g. stellar and gas dynamics, hydrostatic equilibrium of X-ray emitting gas and weak gravitational lensing. Whereas each of these methodologies have their own advantages and limitations, they also all have varying levels of precision and varying scales within which a mass can be measured.

In general, however, none of these methods reach the percent-level precision which is often required to accurately measure, for instance, the contribution of dark matter to the inner regions of galaxies where both baryons and dark matter interact and possibly play equal partners in galaxy formation models (e.g. Saglia et al. 1992; Bertin et al. 1992; Loewenstein & White 1999; Keeton 2001; Padmanabhan et al. 2004). In addition to degeneracies, some methods also become problematic beyond the local universe considering the limited signal-to-noise ratio of observations with present-day telescopes.

In this section, we focus on strong gravitational lensing (plus stellar dynamics) as a probe of the mass of galaxies out to tens of kpc scales, covering their inner regions to several effective radii (and beyond in combination with weak lensing). In addition, we shortly discuss the use of gravitational lensing to quantify the level of mass substructure in the dark matter haloes (e.g. CDM substructure or dwarf satellites). The basics of strong lensing theory and the ability to measure galaxy masses to percent level accuracy on different scales are shortly introduced. This is exemplified with several recent highlights, mostly based on the largest strong lensing survey to date: the Sloan Lens ACS (SLACS) Survey Bolton et al. (2006a). This section is neither complete nor unbiased and we refer to Schneider (2006a) or Treu (2010) for more thorough theoretical and observational overviews.

### 7.2. Basic Lensing Theory

Strong gravitational lensing can, to very good approximation, be regarded as geometric optics in curved space-time (Schneider et al. 1992; Kochanek 2006), with the usual conservation of surface brightness. We can also assume in nearly all astrophysical circumstances that the gravitational field that causes lensing (weak or strong) satisfies  $|\phi|/c^2 \ll 1$  and that perturbations from the FRW metric of the Universe are small. As in geometric optics, curved space-time can heuristically be associated with a refractive index  $n = 1 + 2|\phi|/c^2$  for each point in space. A change in refractive index leads to a deflection of the light-ray by

$$\vec{\alpha} = \int \vec{\nabla}_\perp n \, dl = \frac{2}{c^2} \int \vec{\nabla}_\perp \phi \, dl. \quad (54)$$

Hence an observer sees the light ray from a different direction than where it originated. In summary, two parallel rays of light (or wavefronts; Kayser & Refsdal 1983) originating from slightly different positions will in general not remain parallel and can either diverge or converge. Similarly, rays of light being emitted in different directions from a single source can sometimes end up crossing each other again. If an observer (e.g. on Earth) happens to be at that crossing point, the emitting source

will be seen multiple times. The deflection can be used to learn more about the mass distribution of the deflector (e.g. galaxy, cluster, stars, etc). It is worth noting that the concepts of time-delay and deflection can be unified in the generalization of the concept of “Fermat’s principle” (Schneider 1985; Blandford & Narayan 1986), where lensed images form on extrema of a so-called time-delay surface.

### 7.2.1. The Thin-Lens Approximation

Before coming up with a general equation for (strong) lensing, we illustrate some of these aspects in case of a point-mass (e.g. a star or stellar remnant) with gravitational potential

$$\phi(\xi, z) = \frac{GM}{\sqrt{\xi^2 + z^2}}, \quad (55)$$

where  $\xi$  and  $z$  are the distances perpendicular and parallel to the line-of-sight from the point mass to the observer, respectively, and  $G$  and  $M$  are the gravitational constant and mass of the lens. One finds (note that  $\xi^2 = \vec{\xi} \cdot \vec{\xi}$  and then the gradient is carried out w.r.t.  $\vec{\xi}$ ):

$$\vec{\nabla}_\perp \phi = \frac{GM\vec{\xi}}{(\xi^2 + z^2)^{3/2}}. \quad (56)$$

Integrating this along the l.o.s., assuming  $z$  goes from minus to plus infinity, the deflection angle for a point mass is

$$\hat{\alpha} = \frac{4GM}{c^2\xi} = \frac{2R_s}{\xi}, \quad (57)$$

where  $R_s = 2GM/c^2$  is the Schwarzschild radius. In general the impact parameter  $b \gg R_s$ , hence the deflection angles are far smaller than unity (weak deflection), justifying the approximations that were made so far.

We now also note that in general the distance  $\Delta z$  over which light is substantially deflected is much smaller than the distance of the lensed source of light to the deflector and the deflector to the source. In that case, we can approximate any extended lens by the “thin lens approximation”, where the density distribution ( $\rho$ ) is collapsed along the line of sight in to a surface density  $\Sigma(\vec{\xi}) = \int \rho(\vec{\xi}, z) dz$ . The latter is often the only mass-related quantity that can be determined. Deflection is assumed to occur (effectively) instantaneously in the lens plane of the deflector. The thin lens approximation is practically always justified for describing the main deflector. However, whenever very high accuracy is required it should be kept in mind that the universe is not exactly homogeneous and isotropic on large scales and therefore describing the intervening space between the source and the deflector and between the deflector and the observer with a standard Robertson-Walker metric is only an approximation. In reality, photons will propagate through over and under-densities, resulting effectively in additional distortion (shear) and focus/defocus in addition to the one provided by the main deflector (see §6). This effect is usually accounted for as external shear and convergence and result in typical corrections of order a few percent to the strong lensing inference (e.g. Keeton et al. 1997; Treu et al. 2009; Suyu et al. 2010, 2013).

Extending now from the point-source deflector to a general (surface) mass distribution, using  $M \rightarrow \Sigma(\vec{\xi}) d^2\vec{\xi}$ , one readily finds that

$$\vec{\alpha}(\vec{\xi}) = \frac{4G}{c^2} \iint \frac{\Sigma(\vec{\xi})(\vec{\xi} - \vec{\xi}')}{|\vec{\xi} - \vec{\xi}'|^2} d^2\vec{\xi}'. \quad (58)$$

For circularly symmetric lenses with  $\xi = |\vec{\xi}|$  we have

$$\vec{\alpha}(\xi) = \frac{4GM(\leq \xi)\vec{\xi}}{c^2\xi^2} \quad (59)$$

with

$$M(\leq \xi) = 2\pi \int_0^\xi \Sigma(\xi')\xi' d\xi'. \quad (60)$$

We are now ready to introduce the lens equation which forms the basis of lensing theory.

### 7.2.2. The Lens Equation

Now that the deflection for any general and circularly symmetric mass distribution can be calculated, we can relate any point in plane (at a distance  $D_s$ ) where the emitting source is, to a point at  $\vec{\theta} = \vec{\xi}/D_d$  in the plane of the deflector (at a distance  $D_d$ ) as seen by the observer. We also assume that the distance from the deflector to the source is  $D_{ds}$ , which in GR is not necessarily equal to  $D_s - D_d$ . In that case (Figure 22), we readily find in scalar notation  $\theta D_s = \beta D_s + \hat{\alpha} D_{ds}$ , assuming the small-angle approximation, or equivalently

$$\vec{\beta} = \vec{\theta} - \frac{D_{ds}}{D_s} \vec{\alpha}, \quad (61)$$

where  $\vec{\beta}$  is the vector angle to the source as it would be seen (w.r.t. some arbitrary coordinate origin, usually chosen to the deflector centroid) if not lensed and  $\vec{\theta}$  is the vector angle of the lensed image(s) as observed. Defining the reduced deflection angle as  $\vec{\alpha} \equiv \frac{D_{ds}}{D_s} \vec{\alpha}$ , we arrive at the standard non-linear lens equation

$$\vec{\beta}(\vec{\theta}) = \vec{\theta} - \vec{\alpha}(\vec{\theta}). \quad (62)$$

We note here that the non-linearity of  $\vec{\alpha}(\vec{\theta})$  can lead to multiple solutions of  $\vec{\theta}$  of the lens equation for a given source position  $\vec{\beta}$ , hence multiple imaging (strong lensing) occurs (note that this equation holds for each position of an extended source and that image surface brightness for each solution  $\vec{\theta}$  is identical to that of the source at  $\vec{\beta}$ ). The extreme case of multiple imaging is the creation of the “Einstein Ring” for circularly symmetric lenses, for which

$$\beta = \theta - \frac{4GM(\theta)D_{ds}}{c^2 D_d D_s} \frac{1}{\theta}. \quad (63)$$

Defining the Einstein radius

$$\theta_E \equiv \left[ \frac{4GM(\theta)D_{ds}}{c^2 D_d D_s} \right]^{1/2}, \quad (64)$$

the lens equation for  $\beta = 0$  has the solution  $\theta = \pm\theta_E$ . Because of symmetry, a source aligned with the source-deflector line will be imaged into a perfect Einstein ring.

We can take one more step to simplify the equations. We do this assuming the deflector has constant density (a “mass-sheet”). In that case

$$\alpha(\theta) = \left[ \frac{4\pi G \Sigma D_d D_{ds}}{c^2 D_s} \right] \theta = \left[ \frac{\Sigma}{\Sigma_{\text{crit}}} \right] \theta, \quad (65)$$

with  $\Sigma_{\text{crit}} \equiv c^2 D_s / (4\pi G D_d D_{ds})$ . We further define the so called ‘‘convergence’’  $\kappa \equiv \Sigma / \Sigma_{\text{crit}}$ . Hence, the deflection angle is linear and  $\beta = (1 - \kappa)\theta$ . For  $\kappa = 1$ , parallel rays converge to a single focus, making the transition from  $\kappa < 1$  to  $\kappa > 1$  special. The mass-sheet with  $\kappa = 1$  is a perfect focusing lens. Whereas this is not the case for general lenses, it turns out that lenses with  $\kappa > 1$  at any point, can (do not have to though) create multiple images because of over-focusing. With this definition the deflection angle becomes

$$\vec{\alpha}(\vec{\theta}) = \frac{1}{\pi} \iint \frac{\kappa(\vec{\theta})(\vec{\theta} - \vec{\theta}')}{|\vec{\theta} - \vec{\theta}'|^2} d^2\vec{\theta}'. \quad (66)$$

It can be shown that the average convergence inside the Einstein radius of any circularly symmetric deflector is exactly equal to one. Thus for lens systems with a (near) Einstein ring, the mass inside the Einstein radius is  $M_E \equiv \pi(D_d\theta_E)\Sigma_{\text{crit}}$  independent of the density profile of the deflector. In fact, deviations from symmetry are only secondary effects. Hence the masses of strong lenses can be determined to rather exquisite accuracy if a reasonable Einstein radius can be defined.

### 7.2.3. Axisymmetric Lenses

Whereas lens modeling can be rather complex, in general axisymmetric (in 2D) lenses give good insight into the processes that are important in lensing. This is because many lenses are ETGs, which generally have round mass distributions (and potential) with small ellipticities. It is therefore useful to derive some properties for these types of lenses, giving first-order results for other lenses as well.

We thus assume  $\kappa(\theta) = \kappa(|\vec{\theta}|)$  and  $\alpha(\theta) = |\vec{\alpha}(|\vec{\theta}|)|$ . It is then easy to show that

$$\alpha(\theta) = \frac{M(<\theta)}{\theta} = \langle \kappa \rangle(\theta)\theta, \quad (67)$$

with

$$M(<\theta) \equiv 2 \int_0^\theta d\theta' \theta' \kappa(\theta') \quad (68)$$

and

$$\langle \kappa \rangle(\theta) = \frac{M(<\theta)}{\theta^2}. \quad (69)$$

Hence the deflection angle then reduces to

$$\beta = (1 - \langle \kappa \rangle(\theta))\theta. \quad (70)$$

This immediately shows that for an Einstein ring with  $\beta = 0$ , that  $\langle \kappa \rangle(\theta) = 1$ . Hence for any axisymmetric lens the average convergence inside the Einstein radius is unity. The enclosed mass can thus be inferred independent of the density profile. In physical units

$$M_E = \pi \theta_E^2 D_d^2 \Sigma_{\text{crit}}, \quad (71)$$

or conversely

$$\theta_E = \left( \frac{4GM_E D_{ds}}{c^2 D_d D_s} \right)^{1/2}. \quad (72)$$

Thence if the Einstein radius can be determined, the mass can be determined.

#### 7.2.4. Lensing & Stellar Dynamics

A powerful complementary constraint that is worth mentioning at this point is the combination of the precise total mass measurement using strong gravitational lensing with stellar kinematic measurements. Whereas this combinations can becomes rather complex for two or three integral (non-spherical) models, here we illustrate the basic idea assuming spherical symmetry and power-law density and luminosity density models Treu & Koopmans (2002a); Koopmans (2004); Bolton et al. (2006b). Despite these simplifications, these toy-models give rather robust results for the density slopes of ETGs.

Let us suppose that the stellar component has a luminosity density  $\nu_l(r) = \nu_{l,o}r^{-\delta}$  and is a trace component embedded in a total (i.e. luminous plus dark-matter) mass distribution with a density  $\nu_\rho(r) = \nu_{\rho,o}r^{-\gamma'}$ . In addition, let us assume that the anisotropy of the stellar component  $\beta = 1 - (\sigma_\theta^2/\sigma_r^2)$  is constant with radius. For a lens galaxy with a projected mass  $M_E$  inside the Einstein radius  $R_E$ , the luminosity weighted average line-of-sight velocity dispersion inside an aperture  $R_A$  is given, after solving the spherical Jeans equations, by

$$\langle \sigma_{||}^2 \rangle(\leq R_A) = \frac{1}{\pi} \left[ \frac{GM_E}{R_E} \right] f(\gamma', \delta, \beta) \times \left( \frac{R_A}{R_E} \right)^{2-\gamma'} \quad (73)$$

with

$$f(\gamma', \delta, \beta) = 2\sqrt{\pi} \left( \frac{\delta - 3}{(\xi - 3)(\xi - 2\beta)} \right) \times \quad (74)$$

$$\left\{ \frac{\Gamma[(\xi - 1)/2]}{\Gamma[\xi/2]} - \beta \frac{\Gamma[(\xi + 1)/2]}{\Gamma[(\xi + 2)/2]} \right\} \times \\ \left\{ \frac{\Gamma[\delta/2]\Gamma[\gamma'/2]}{\Gamma[(\delta - 1)/2]\Gamma[(\gamma' - 1)/2]} \right\} \quad (75)$$

with  $\xi = \gamma' + \delta - 2$ . Similarly,

$$\sigma_{||}^2(R) = \frac{1}{\pi} \left[ \frac{GM_E}{R_E} \right] \left( \frac{\xi - 3}{\delta - 3} \right) f(\gamma', \delta, \beta) \times \left( \frac{R}{R_E} \right)^{2-\gamma'}. \quad (76)$$

In the simple case of a SIS with  $\gamma' = \delta = \xi = 2$  and  $\beta = 0$ , we recover the well-known result

$$\sigma_{||}^2(R) = \frac{1}{\pi} \left[ \frac{GM_E}{R_E} \right] \quad (\text{SIS}). \quad (77)$$

From Eq. (73), one sees that the radial dependence of the stellar velocity dispersion depends on  $\gamma'$  only. All other parameters (i.e.  $\delta$ ,  $\beta$ , etc.) only enter into the normalization. Since the luminosity density (i.e.  $\delta$ ) and  $M_E$  are measured with little uncertainty, the measurement of  $\langle \sigma_{||}^2 \rangle(\leq R_A \neq R_E)$  immediately gives the density slope  $\gamma'(\beta)$  (where  $\beta$  in general plays only a minor role). This is the basis of combining stellar dynamics with gravitational lensing to obtain not only the mass but also the density-slope of ETGs.

Figure 22: A sub-sample of SLACS lenses (credit: Adam Bolton; see [www.slacs.org](http://www.slacs.org)) in false-color. Each panels shows the data on the left and a model of the system on the right.

**Figure “hugeslacsmosaic.eps” to be shown here, using the full page.**

We can estimate the change  $\delta\gamma'$  from the observables. One finds to first order (assuming fixed values of  $\beta$  and  $\delta$ ):

$$\begin{aligned}\frac{\delta\sigma_{||}}{\sigma_{||}}(\leq R_A) &= \frac{1}{2} \frac{\delta M_E}{M_E} + \frac{1}{2} \left( \frac{\partial \log f}{\partial \log \gamma'} - \gamma' \log \left[ \frac{R_A}{R_E} \right] \right) \\ &\times \frac{\delta\gamma'}{\gamma'} \equiv \frac{1}{2} \left( \frac{\delta M_E}{M_E} + \alpha_g \frac{\delta\gamma'}{\gamma'} \right).\end{aligned}\quad (78)$$

The second term in this equation was already derived by Treu & Koopmans (2002a). If we further assume the errors on  $M_E$  and  $\sigma_{||}$  to be independent,

$$\langle \delta_{\gamma'}^2 \rangle \approx \alpha_g^{-2} \left\{ \langle \delta_{M_E}^2 \rangle + 4 \langle \delta_{\sigma_{||}}^2 \rangle \right\}, \quad (79)$$

where  $\delta_{...}$  indicate fractional errors. Since in general  $\delta_{M_E} \ll \delta_{\sigma_{||}}$ , one finds the simple rule of thumb that the error  $\delta_{\gamma'} \sim \delta_{\sigma_{||}}$  for close-to-isothermal mass models, since  $\alpha_g \sim 2$ . This estimate is in very good agreement with the results from properly solving the Jeans equations for two-component mass models and justifies neglecting the mass errors (Treu & Koopmans 2004).

### 7.3. Observational Results

In this section we highlight some recent results on the study of early-type galaxies using strong gravitational lensing.

We focus on two aspects of strong gravitational lensing that have recently progressed rapidly and that we think have great promise in future galaxy structure and evolutions studies: (i) The combination of strong lensing, stellar kinematics and stellar populations to constrain the inner stellar and dark-matter mass profiles of ETGs as function of their mass and redshift and (ii) the use of simply-parameterized and grid-based modeling of strong lenses to constrain the level mass substructure in the inner regions of ETGs. We illustrate how lensing can address these two science drivers based mostly on recent results from the Sloan Lens ACS Survey (SLACS).

#### 7.3.1. Sloan Lens ACS Survey (SLACS)

The SLACS gravitational lenses (Bolton et al. 2006a; Treu et al. 2006; Koopmans et al. 2006; Gavazzi et al. 2007; Bolton et al. 2008a; Gavazzi et al. 2008; Bolton et al. 2008b; Auger et al. 2009; Treu et al. 2009; Auger et al. 2010a; Newton et al. 2011) were selected from the spectroscopic database of the SDSS based on the presence of absorption-dominated galaxy continuum at one redshift and nebular emission lines (Balmer series, [OII] 3727, or [OIII] 5007) at a higher redshift. The spectroscopic lens survey technique was first envisioned by Warren et al. (1998); Hewett et al. (2000) following the serendipitous discovery of the gravitational lens 0047–2808 through the presence of high-redshift Lyman- $\alpha$  emission in the spectrum of the targeted lower redshift elliptical galaxy. Further details of the SLACS approach are provided in Bolton et al. (2005, 2004). The SLACS Survey includes candidates from the SDSS MAIN galaxy sample Strauss et al. (2002) in addition to candidates from the SDSS luminous red galaxy (LRG) sample Eisenstein et al. (2001). Most candidates were selected on the basis of multiple emission lines, though several lens candidates were observed on the basis of secure [OII] 3727 line detections alone. By virtue of this spectroscopic selection method, all SLACS lenses and lens candidates have secure foreground (“lens”) and background (“source”) redshifts from the outset. Accurate redshifts such as these are essential for most quantitative scientific applications of strong lensing, as they are required to convert angles into physical lengths.

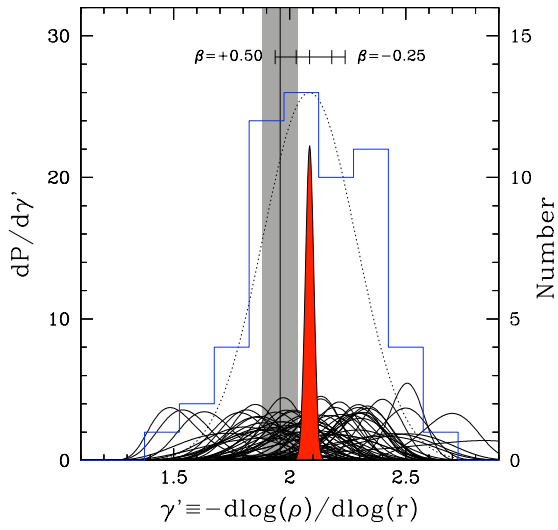


Figure 23: The logarithmic density slopes of 58 SLACS early-type galaxies (thin solid curves). The filled red curve is the joint posterior probability distribution of the average density slope of the sample. The histogram indicates the distribution of median values of the density slopes. The dotted Gaussian curve indicates the intrinsic scatter in  $\gamma'_{LD}$  (see text). We assume a Hernquist luminosity-density profile and no anisotropy (i.e.  $\beta_r = 0$ ). The small dashes indicate the shift in average density slope for  $\beta_r = +0.50, +0.25, -0.50, -0.25$  (left to right), respectively. Note the reversal of the  $\beta_r = -0.50$  and  $-0.25$  dashes. The vertical solid line and gray region indicates the best-fit value and 68% CL interval, respectively, of the average density derived from scaling relations.

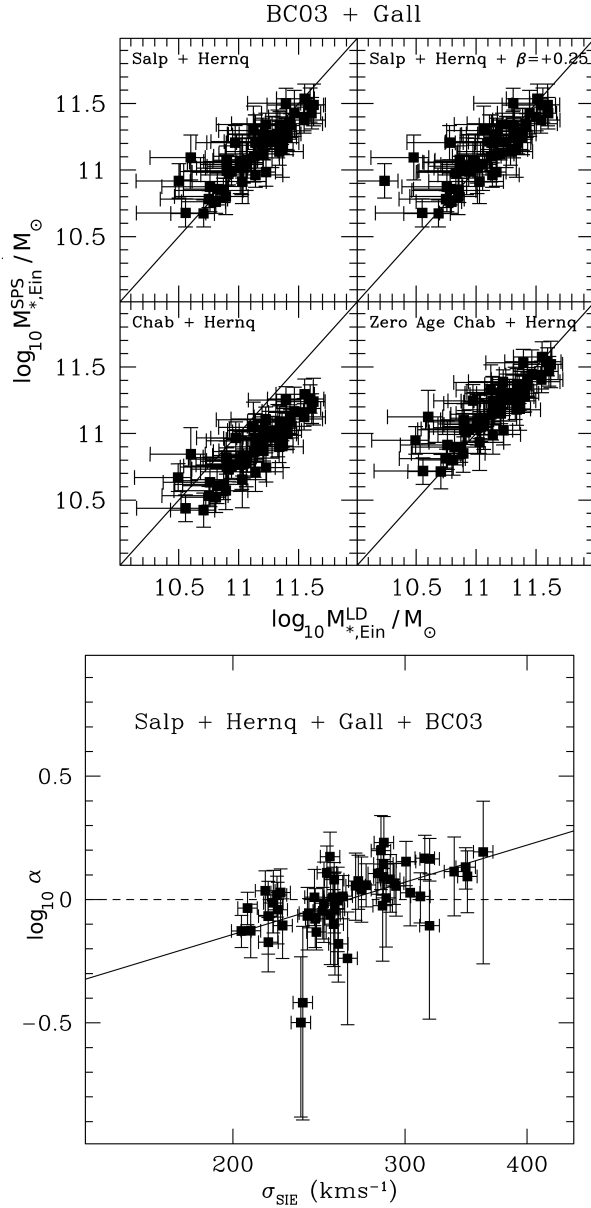


Figure 24: *Top figure:* Comparison between stellar mass in the cylinder of radius equal to the Einstein Radius as inferred from lensing and dynamical models (x-axis) and that inferred from fitting stellar populations synthesis models to the observed spectral energy distribution (y-axis). The solid line indicates the identity. Stellar populations synthesis models by Bruzual & Charlot (2003) are assumed together with an informative metallicity prior Gallazzi et al. (2005). *Bottom figure:* Template mismatch parameter  $\alpha \equiv M_{*,\text{Ein}}^{\text{LD}} / M_{*,\text{Ein}}^{\text{SPS}}$  for Salpeter IMF as a function of lensing velocity dispersion (left), stellar velocity dispersion (center) and V-band luminosity corrected to  $z = 0.2$ . A tentative positive trend with velocity dispersion is observed (solid line). The dashed line represents the trend expected for a universal Salpeter IMF.

### 7.3.2. The Density Profiles of Early-Type Galaxies (ETGs)

When combining the total mass inside the Einstein radius given by detailed lensing modeling, usually accurate to a few percent (Kochanek 1991), with measurements of stellar kinematics (either inside an aperture, along a slit or through 2D IFU measurement), a powerful constraint can be set on the average (kinematically weighted) density profile of ETGs inside the Einstein radius (or effective radius which ever is larger). This methodology, shortly outlined in the previous section, has been successfully applied initially by the Lenses Structure & Dynamics (LSD) survey (e.g. Koopmans & Treu 2002; Treu & Koopmans 2002a,b; Koopmans & Treu 2003; Treu & Koopmans 2004) and more recently by the SLACS survey, the BELLS Survey (Bolton et al. 2012; Brownstein et al. 2012), the SL2S Survey (Ruff et al. 2011; Gavazzi et al. 2012), and the SWELLS Survey (Treu et al. 2011) for the case of spiral deflectors. Whereas the quality of the kinematic profiles in general can not compete with that obtained for local ETGs (§5), the combination of these data with strong lensing at higher redshifts has several major advantages.

First, even “low quality” lensing information combined with a single measurement of the stellar velocity dispersion can often be obtained out to  $z \sim 1$  without major telescope investment. This allows their inner mass profiles to be determined even at half the age of the Universe. Hence, evolution (in the ensemble average properties) of ETGs can be studied (e.g. Ruff et al. 2011; Bolton et al. 2012). Second, the additional use of strong lensing masses (plus constraints on its density slope near the Einstein radius) helps break the mass-sheet and mass-anisotropy degeneracies.

The results of the SLACS survey based on the combination of lensing and kinematic constraints for  $\sim 60$  ETGs lenses are described in a number of papers (Koopmans et al. 2006; Czoske et al. 2008; Koopmans et al. 2009; Barnabè et al. 2009, 2010; Auger et al. 2010b). Regarding the total mass density profile, Koopmans et al. (2009) and Auger et al. (2010b) found that inside one effective radius massive elliptical galaxies with  $M_{\text{eff}} \geq 3 \cdot 10^{10} M_{\odot}$  are well-approximated by a power-law ellipsoid with an average logarithmic density slope of  $\langle \gamma'_{\text{LD}} \rangle \equiv -d \log(\rho_{\text{tot}})/d \log(r) = 2.078 \pm 0.027$  (random error on mean) with an intrinsic scatter of  $0.16 \pm 0.02$  (for isotropic orbits; results change as shown in Figure 23 for reasonable amounts of anisotropy). Whereas this result is based on a separate analysis of the lensing and stellar kinematics and assumes spherical symmetry (or simple scaling relations), it has been confirmed by more sophisticated joint and self consistent lensing and dynamical analysis methods based on axisymmetric mass distributions and two integral Schwarzschild modeling of the full lensing data and two dimensional velocity fields (Czoske et al. 2008; Barnabè et al. 2009). Based on a subset of 16 lens ETGs with deep integral field spectroscopy Barnabè et al. (2011) find  $\langle \gamma' \rangle = 2.074^{+0.043}_{-0.041}$  with an intrinsic scatter of  $0.143^{+0.054}_{-0.014}$ . Overall the internal structure of the SLACS ETGs at  $z = 0.1 - 0.4$  is found to be perfectly consistent with that found for their nearby counterparts, as described in §5 of this review.

The addition of weak gravitational lensing data to the strong lensing and dynamics analysis allows one to extend the measurement of the total mass density profile well beyond the effective radii in an ensemble sense. With exquisite HST data, the weak lensing signal is measurable for sample of just a few tens of ETGs in the redshift range  $z = 0.1 - 0.8$  (Gavazzi et al. 2007; Lagattuta et al. 2010; Auger et al. 2010b). The two main results of the combined weak, strong and dynamics analyses are that SLACS lenses have average virial mass  $\sim 2 \cdot 10^{13} M_{\odot}$  and that their *total* mass density profile is well described by a single isothermal sphere  $\gamma' \approx 2$  out to  $\sim 100$  effective radii. This result is remarkable because neither the stellar component nor the dark matter halo are well described by single power laws, and yet their sum is. This total mass profile is well reproduced by the combination of a stellar component and a standard NFW halo (Gavazzi et al. 2007) for sensible values of stellar mass to light ratio. This is very different with what is found at higher and lower

masses (clusters and dwarfs) where typically a single isothermal sphere is not a good description of the total mass density profile. The simplicity of the total mass density profiles of ETGs has been sometimes called the “bulge-halo” conspiracy (Dutton & Treu 2013), and it provides important constraints on theoretical models of ETGs formation, especially on parameters that drive the star formation efficiency like supernovae and nuclear feedback (Remus et al. 2013; Dubois et al. 2013).

The conclusion that can be drawn from these analyses is that ETGs on average have density profiles that are close to isothermal. However, one needs to keep in mind that there is an intrinsic scatter of  $\sim 10\%$  in the logarithmic density slope between galaxies (i.e. they do not all have similar density profiles), which could be due to their formation history. This intrinsic scatter is comparable to studies of nearby galaxies (e.g. Gerhard et al. 2001) based on stellar kinematics alone. The only dependence on third parameters identified so far is that between the slope and the stellar mass density inside the effective radius, where higher stellar mass-density ETGs have steeper density slopes (Dutton & Treu 2013). This tantalizing result is confirmed by the self-consistent axisymmetric modeling technique (Barnabè & Koopmans 2007; Barnabè et al. 2012), and proves that ETGs are at least a two parameter family even when it comes to their internal mass structure.

### 7.3.3. The Stellar IMF and Dark Matter Fraction in ETGs

Strong lensing can constrain the mass inside the Einstein radius very accurately. In combination with the luminosity inside the Einstein radius this yields a firm upper limit on the stellar mass-to-light ratio inside that radius (e.g. Brewer et al. 2012). As discussed in Chapter 2, given an optical infrared spectral energy distribution, modern stellar population synthesis models are believed to provide estimates of the stellar mass to light ratio that are accurate to within roughly for old stellar populations like the one found in massive ETGs. In this case, the main source of uncertainty is the shape of the stellar initial mass function, which is needed to convert the observed luminosity - dominated by a small range of stellar masses - to the total mass in stars and stellar remnants. Thus, by combining gravitational lensing, stellar kinematics and stellar population synthesis modeling, powerful new constraints can be set on the stellar IMF and the fraction of dark matter in the inner regions of ETGs. By means of additional information, like spatially resolved kinematics and/or simple assumptions on the functional form of the dark matter density profile, one can break in part the degeneracy between the stellar IMF and the dark matter fraction and derive very realistic limits on the either one (e.g. Treu & Koopmans 2004, for limits on the dark matter fraction inside the Einstein Radius out to  $z \sim 1$ ).

Treu et al. (2010) studied the stellar initial mass function of ETGs by comparing the stellar mass fraction inside one effective radius determined solely from lensing and stellar dynamics with that inferred from stellar population synthesis models. Whereas these limits are rather weak on a system-to-system basis, the combination of 56 SLACS ETGs allows a rather detailed comparison. The main result is that bottom-heavy IMFs such as that measured by Salpeter (1955) are strongly preferred over light-weight IMFs such as that proposed by Chabrier (2003), assuming standard NFW dark matter density profiles. This result is further strengthened by Auger et al. (2010b) who modeled these systems in detail, including adiabatic contraction and weak-lensing constraints, and found that only heavy Salpeter-type IMF are consistent with the observed properties of ETGs. In combination with standard results based on spiral galaxy rotation curves (see §3) and dynamical measurements of early-type galaxies (see §5), these results indicated the stellar initial mass function cannot be universal.

The lensing and kinematic studies by themselves (Treu et al. 2010) also suggest that the IMF normalization varies with galaxy mass Figure 24 within the sample of SLACS lenses, if NFW halos

are allowed. However, the mass dependency within the SLACS sample becomes insignificant if the halos are allowed to contract in response to baryonic physics (Auger et al. 2010b).

Several subsequent studies, discussed elsewhere in his review, also point toward non-universal IMFs using independent techniques. For example, based on detailed modeling of weak stellar absorption features van Dokkum & Conroy (2010), confirmed the lensing result that the IMF of massive early-type galaxies are inconsistent with Chabrier. In addition, they provide the crucial suggestion that the extra mass is to be attributed to low mass stars, with overall IMF shape similar to Salpeter's. Detailed stellar dynamical modeling of spatially resolved velocity fields of ETGs also adds important information. First, it provides an independent confirmation of the initial lensing results that Chabrier-like IMFs are disfavored for massive ETGs. Second, the local galaxy samples cover a large enough range in stellar mass to detect a trend in stellar mass-to-light normalization within ETGs themselves, assuming the inner mass density profiles of their dark matter halos can be modelled as power laws which are allowed to vary within a fixed range across the sample (Cappellari et al. 2012, 2013a).

Overall there is good agreement between the dynamical, lensing and stellar population probes (Dutton et al. 2013). Given its broad implications, it is reassuring that many independent lines of evidence (e.g. Zaritsky et al. 2012) contradict the simple hypothesis of a universal IMF, which has been a central tenet of extragalactic astronomy for the few past decades. Much work is currently under way to determine the exact form of the IMF, clarify systematic uncertainties, and investigate possible variations with morphology or other parameters (e.g. Dutton et al. 2012; Conroy & van Dokkum 2012; Conroy et al. 2013; Sonnenfeld et al. 2012; Spinelli et al. 2011, 2012, 2013; Smith & Lucey 2013; Ferreras et al. 2013; Goudfrooij & Kruijssen 2013, and elsewhere in this review).

#### 7.3.4. Mass Substructure in ETGs

Whereas the results described above are concerned with the smooth mass distributions of ETGs, gravitational lensing can also measure the level of mass-density fluctuations, and in particular on the amount of substructure in their inner regions. Thus, gravitational lensing provides an opportunity to measure directly the mass function of subhalos, irrespective of their stellar content. This is a stringent test of the nature of dark matter, since cold dark matter predicts that the subhalo mass function should go as  $dN/nM \propto M^{-1.9}$  down to very small masses (Springel et al. 2008).

The first lensing studies of this topic, based on the so-called flux-ratio anomalies Mao & Schneider (1998); Metcalf & Madau (2001) of radio-loud lenses quasars from the CLASS survey (Dalal & Kochanek 2002) indicated a level of substructure broadly consistent with the expectations of CDM cosmology. In the following decade, much work has been devoted to understanding the systematic uncertainties associated with this method (e.g. Koopmans et al. 2003; Kochanek & Dalal 2004; Dobler & Keeton 2006; Shin & Evans 2008; Metcalf & Amara 2012), but overall progress has been limited mostly by the small number of known quadruply imaged radio loud quasars. Detailed comparisons with cosmological numerical simulations are challenging, owing to the need for high resolution and approximations related to the implementation of baryonic physics (e.g. Kochanek & Dalal 2004; Mao et al. 2004; Macciò et al. 2006; Xu et al. 2009, 2012). It also remains an open question whether some of these anomalies are caused by dark or luminous substructure (e.g. More et al. 2008, 2009; Jackson et al. 2010; Nierenberg et al. 2012).

To overcome some of the limitations of flux-ratio anomaly systems (e.g. the position and mass of the substructure are highly degenerate so only statistical constraints can really be placed currently), and exploit the large samples of galaxy-galaxy strong lens systems, Koopmans (2005) developed a new method based on the entire surface brightness distribution of the (extended) lens source. The

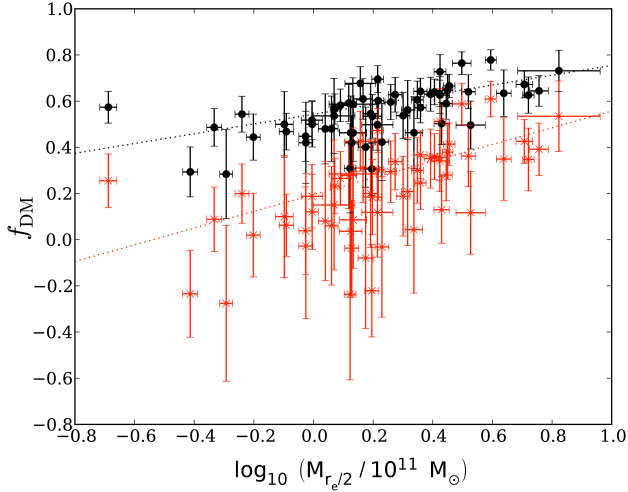


Figure 25: Relations between the projected dark matter fraction within half of the effective radius and  $M_*/r_e$ . Red points are for a Salpeter IMF and black points are for a Chabrier IMF.

information contained in thousands of pixels allows one to reconstruct the surface mass density of the deflector, pin-point the position of possible substructures, and determine their masses (see also (Vegetti & Koopmans 2009) for a complete Bayesian extension of this method). Alternative methods have been developed by other groups to reconstruct on a grid the surface mass density of gravitational lenses, or their gravitational potential, albeit mostly with the goal of studying cosmology from gravitational time delays. The method developed by Suyu et al. (2009) is very similar in spirit to that of Vegetti & Koopmans (2009), while the one developed and applied by Saha et al. (2006) differs substantially. In the latter method the mass distribution is reconstructed on a grid using only multiple image positions as a constraints. Thus the amount of freedom in the models is substantially larger and the choice of geometric priors becomes more important. Putting this class of model into a statistical framework is challenging although efforts are underway (Coles 2008).

### 7.3.5. Luminous Dwarf Galaxies

A nice demonstration of these methodologies is provided by known luminous substructures in gravitational lens systems. For example, the system shown in Figure 26 was discovered by Lin et al. (2009) and shows a bright arc with a dwarf galaxy (G4) splitting the giant arc on sun-arcsec scale. Whereas this anomaly of the arc is caused by the dwarf galaxy, similar anomalies could in principle also be caused by dark substructure and be used to reconstruct their mass and position. Not all such cases however are as obvious as this case. The best reconstruction of the lensed arcs is shown in Figure 27 (a galaxy surface brightness model has been subtracted) and a grid-based reconstruction of the potential and surface density (lower-right panel) has been constructed (e.g. Vegetti et al. 2010a). A high over-density is clearly visible at the position of the anomaly. Replacing this object by a tidally-truncated pseudo-Jaffe mass model, a mass of mass of  $M_{\text{sub}} = (2.75 \pm 0.04) \times 10^{10} M_\odot$  inside its tidal radius of  $r_t = 0.68$  arcsec is found. This result is robust against changes in the lens model. The satellite luminosity is  $L_B = (1.6 \pm 0.8) \times 10^9 L_\odot$ , leading to a total mass-to-light

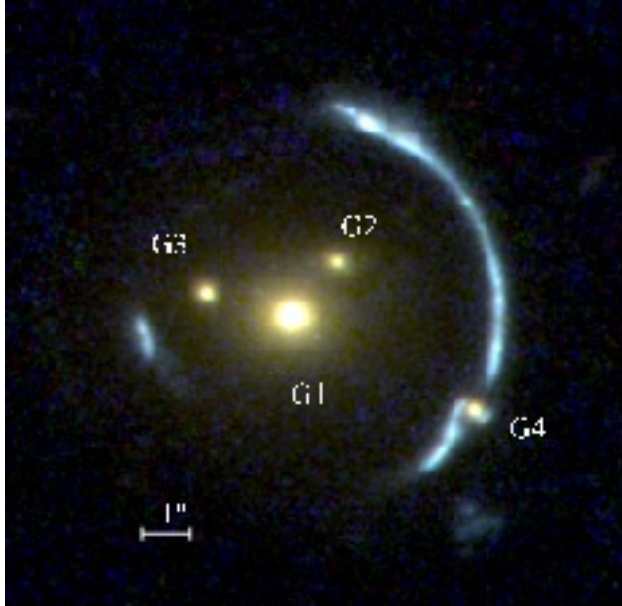


Figure 26: Overview of the lens system the “Clone”. This false-colour image was created from HST/WFPC2 images through filters F450W, F606W and F814W.

ratio within the tidal radius of  $(M/L)_B = (17.2 \pm 8.5) M/\text{L}_\odot/\text{L}_\odot$ . While this mass-to-light ratio is high compared to early-type dwarfs, it is also an upper limit since the extended emission is hard to measure due to the arc. Another demonstration of the power of this method is given by the analysis of the system SL2SJ08544-0121 by Suyu & Halkola (2010).

#### 7.3.6. Dark Substructures

The method is currently being applied to the SLACS lenses with the goal of quantifying the abundance of substructures independent of their luminosity. Two detections have been reported so far.

The first substructure detected via gravitational imaging is in the Jackpot system (Gavazzi et al. 2008), which shows two concentric rings of sources at two redshifts. The inner ring of this system, even though rather smooth, has a very high signal-to-noise ratio and is therefore quite suitable for the grid-based analysis method.

A simply-parameterized elliptical power-law density model plus external shear provides a good fit to the data, but for a rather structured source model (Vegetti et al. 2010b). Figure 28 shows a reconstruction of the system down to the noise level where the source is more smooth, but a perturbation of the lensing potential is required at 4.3 kpc projected distance from the lens center (the red feature in the upper-left of the lower-right panel shows the corresponding over density).

Whereas there is a tradeoff between the complexity of the source and that of the lens potential, this can objectively be assessed through the Bayesian evidence (i.e. the probability of the data when marginalizing over the full posterior probability function) and the smooth-source plus more complex lens model is preferred at a (rough) equivalent of  $16-\sigma$  significance (Vegetti et al. 2010b).

This detection is confirmed by modeling the substructure with a tidally truncated pseudo-Jaffe

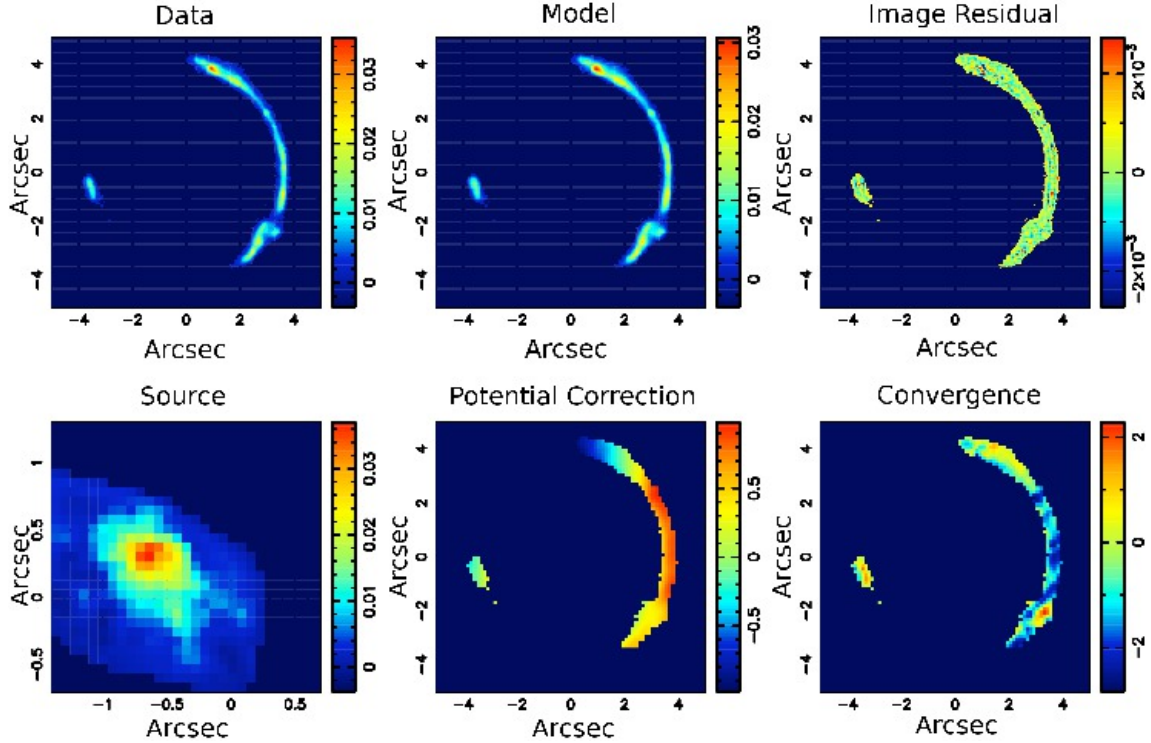


Figure 27: Illustration of pixelized reconstruction of the source surface brightness and lens potential corrections of the lens system shown in Figure 26 using the gravitational imaging technique. The top-left panel shows the data, consisting of the surface brightness of a highly distorted lensed source. The top-middle panel shows the model surface brightness, while the top-right one shows the image residuals (data-model). The bottom-left panel shows the source surface brightness distribution reconstructed in the source plane (i.e. after “delensing”; note the zoomed-in angular scale). The bottom-middle panel shows the corrections to the gravitational potential, with respect to a smooth simply parameterized mass distribution. The bottom-right panel shows the inferred convergence, i.e., the projected surface mass distribution. Note the peak at the lower right corner of the image corresponding to the satellite responsible for the curvature in the arc.

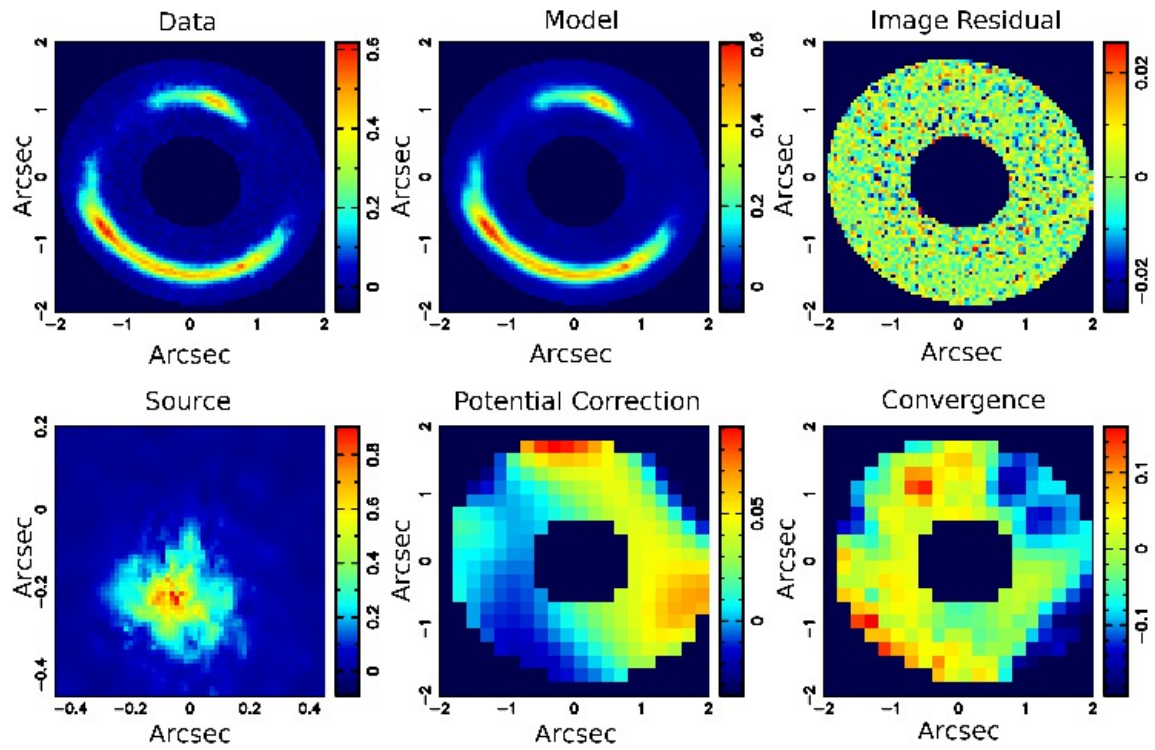


Figure 28: Gravitational imaging analysis of the Jackpot gravitational lens system. The panels are as in Figure 27. Note the convergence peak in the top right portion of the bottom-right panel, corresponding to the detected substructure.

density profile (Vegetti et al. 2010b). The substructure mass is  $M_{\text{sub}} = (3.51 \pm 0.15) \times 10^9 M_\odot$ . A lower limit of  $(M/L)_{V,\odot} \geq 120 M_\odot/\text{L}_V$  (3- $\sigma$ ) is set inside a sphere of 0.3 kpc centred on the substructure ( $r_{\text{tidal}}=1.1$  kpc). This implies a projected dark matter mass fraction in substructure at the radius of the inner Einstein ring of  $f = 2.15^{+2.05}_{-1.25}$  percent (68% C.L) in the mass range  $4 \times 10^6 M_\odot$  to  $4 \times 10^9 M_\odot$ , assuming  $\alpha = 1.9 \pm 0.1$  (with  $dN/dm \propto m^{-\alpha}$ ). Assuming a flat prior on  $\alpha$ , between 1.0 and 3.0, increases this to  $f = 2.56^{+3.26}_{-1.50}$  percent (68% C.L). The likelihood ratio is  $\sim 0.5$  between these fractions and that from simulations ( $f_{\text{N-body}} \approx 0.003$ ). More recently, a second detection has been reported in the CLASS gravitational lens system B1938+666 based on HST and Keck adaptive optics images (Vegetti et al. 2012). Remarkably the satellite mass is only  $2 \times 10^8 M_\odot$  and yet it is detected at redshift 0.881.

The inference on the substructure mass function based on just two systems are clearly very uncertain (Vegetti et al. 2012), but so far the results are broadly consistent with those expected from numerical simulations. Effort is under way to refine those measurements by applying the gravitational imaging technique to larger samples of lenses (Vegetti et al. 2013, in preparation). Proving that the substructure is inside the ETG and not along the line of sight is actually challenging (Chen et al. 2003, 2011). At the moment the level of line of sight contamination is ill-constrained.

#### *7.4. Future Prospects*

The method of strong gravitational lensing has progressed significantly in the past decade, proving to be fundamental tool for precision astrophysics and cosmology. Progress in the field has come from new observations of unprecedently large samples of lensed systems, a growing synergy with other techniques (stellar kinematic and stellar population studies), and the development of new methodologies such as self-consistent lensing and dynamics and grid-based strong lensing. Whereas this research area is just too extensive for an exhaustive review in this short a space, we have tried to illustrate the progress and potential of strong lensing by highlighting some recent results from the largest galaxy-scale strong lens survey to date, the SLACS survey. These examples demonstrate that valuable constraints can be set on the inner density profiles of ETGs as well as on their dark-matter mass fraction as function of galaxy mass and cosmic time, their stellar IMF and the level of mass substructure.

One obvious concern is that strong gravitational lenses are rare in the sky (approximately fewer than 1/100-1/1000 massive ETGs can be detected as strong lenses, depending on resolution and depth). However, even in an era when exquisite data can be gathered for much larger samples of non-lens galaxies, strong lensing still brings unique and extremely precise measurements of mass (typically to a few percent) which are independent of the standard assumptions and uncertainties of other more traditional methods, as discussed at some length in this review. By combining strong gravitational lensing information with that inferred from other methods one may break many of the traditional degeneracies (e.g. mass-anisotropy, IMF versus stellar mass) and achieve new insights into the formation and evolution of early-type galaxies. Furthermore strong lensing thrives at cosmological distances where other methods suffer from the inevitable loss in sensitivity and angular resolution. For example, as discussed in this review, only by using strong lensing information can one determine, as a function of cosmic time accurate mass profiles, the normalization of the stellar IMF and the abundance of dark substructures. Thus, strong lensing is an essential tool for any evolutionary study of the mass structure of ETGs.

Furthermore, the upcoming decade will see a revolution in the study of strong gravitational lens systems. At the moment, most strong lensing applications are limited by the number of known strong lens systems suitable for that particular application. The current samples, limited to only a few hundred galaxy-scale lenses, are insufficient to explore detailed trends in mass, redshifts, and other potentially illuminating parameters. However, the current and next generation of wide field sky surveys (e.g. from Herschel-ALMA, DES, LSST, PanSTARRS, LOFAR, Euclid, KiDS, SKA, etc.) will enable the discovery of  $10^3\text{-}10^5$  galaxy-scale lens systems thus removing the limitations stemming from sample size once and for all. With only limited resources for detailed follow-up of individual sources at present, strong lenses will clearly become a high-priority target given the high density of information that they provide.

## **8. Acknowledgments**

We are most grateful to Lia Athanassoula, Giuseppina Battaglia, Matt Bershady, James Bullock, Laurent Chemin, Enrico Maria Corsini, Nathan Deg, Ken Freeman, Dimitri Gadotti, Ortwin Gerhard, Stacy McGaugh, Kristine Spekkens, and Piet van der Kruit for useful discussions. Laurent Chemin, Octavio Valenzuela and Giuseppina Battaglia are also thanked for providing Figures 10, 11, and 18 respectively. Cory Wagner very kindly improved the presentation of various figures, and two diligent referees provided valuable comments that improved various parts of this review.

SC and LMW acknowledge the support of the Natural Sciences and Engineering Research Council of Canada through respective Discovery grants. MC acknowledges support from a Royal Society University Research Fellowship. AAD acknowledges support from the Canadian Institute for Theoretical Astrophysics (CITA) National Fellows program. HH and LVEK acknowledge support by NWO VIDI grants, while TT acknowledges support from the Packard Foundation through a Packard Research Fellowship.

## References

- Abadi, M.G., Navarro, J.F., Fardal, M., Babul, A., Steinmetz, M., 2010, Galaxy-induced transformation of dark matter haloes, MNRAS 407, 435
- Agustsson, I., Brainerd, T.G., 2006, The Orientation of Satellite Galaxies: Evidence of Elongation in the Direction of the Host, ApJ 644, L25
- Aihara, H., Allende Prieto, C., An, D.e., 2011, The Eighth Data Release of the Sloan Digital Sky Survey: First Data from SDSS-III, ApJS 193, 29
- Alaghband-Zadeh, S., Chapman, S.C., Swinbank, A.M., Smail, I., Harrison, C.M., Alexander, D.M., Casey, C.M., Davé, R., Narayanan, D., Tamura, Y., Umehata, H., 2012, Integral field spectroscopy of  $2.0 < z < 2.7$  submillimetre galaxies: gas morphologies and kinematics, MNRAS 424, 2232
- Amorisco, N.C., Agnello, A., Evans, N.W., 2013, The core size of the Fornax dwarf spheroidal, MNRAS 429, L89
- Amorisco, N.C., Evans, N.W., 2012, A Troublesome Past: Chemodynamics of the Fornax Dwarf Spheroidal, ApJ 756, L2
- An, J., Evans, N.W., Deason, A.J., 2012, Mass estimators in the Gaia era, MNRAS 420, 2562
- Andersen, D.R., Bershady, M.A., 2013, The Photometric and Kinematic Structure of Face-on Disk Galaxies. III. Kinematic Inclinations from  $\text{H}\alpha$  Velocity Fields, ApJ 768, 41
- Andersen, D.R., Bershady, M.A., Sparke, L.S., Gallagher, III, J.S., Wilcots, E.M., van Driel, W., Monnier-Ragaigne, D., 2006, The Photometric and Kinematic Structure of Face-on Disk Galaxies. I. Sample Definition,  $\text{H}\alpha$  Integral Field Spectroscopy, and H I Line Widths, ApJS 166, 505
- Arnold, J.A., Romanowsky, A.J., Brodie, J.P., Chomiuk, L., Spitler, L.R., Strader, J., Benson, A.J., Forbes, D.A., 2011, The Fossil Record of Two-phase Galaxy Assembly: Kinematics and Metallicities in the Nearest S0 Galaxy, ApJ 736, L26
- Arnold, R., de Zeeuw, P.T., Hunter, C., 1994, Orbital Content and Velocity Fields of Triaxial Galaxies, MNRAS 271, 924
- Ascasibar, Y., Gottlöber, S., 2008, The dynamical structure of dark matter haloes, MNRAS 386, 2022
- Athanassoula, E. (ed.), 1983, Internal kinematics and dynamics of galaxies; Proceedings of the Symposium, Université Franche-Comté, Besançon, France, August 9-13, 1982, vol. 100 of IAU Symposium
- Athanassoula, E., 2002, Bar-Halo Interaction and Bar Growth, ApJ 569, L83
- Athanassoula, E., 2003, What determines the strength and the slowdown rate of bars?, MNRAS 341, 1179
- Athanassoula, E., Machado, R.E.G., Rodionov, S.A., 2013, Bar formation and evolution in disc galaxies with gas and a triaxial halo: morphology, bar strength and halo properties, MNRAS 429, 1949

- Auger, M.W., Treu, T., Bolton, A.S., Gavazzi, R., Koopmans, L.V.E., Marshall, P.J., Bundy, K., Moustakas, L.A., 2009, The Sloan Lens ACS Survey. IX. Colors, Lensing, and Stellar Masses of Early-Type Galaxies, ApJ 705, 1099
- Auger, M.W., Treu, T., Bolton, A.S., Gavazzi, R., Koopmans, L.V.E., Marshall, P.J., Moustakas, L.A., Burles, S., 2010a, The Sloan Lens ACS Survey. X. Stellar, Dynamical, and Total Mass Correlations of Massive Early-type Galaxies, ApJ 724, 511
- Auger, M.W., Treu, T., Gavazzi, R., Bolton, A.S., Koopmans, L.V.E., Marshall, P.J., 2010b, Dark Matter Contraction and the Stellar Content of Massive Early-type Galaxies: Disfavoring "Light" Initial Mass Functions, ApJ 721, L163
- Baade, W., 1944, The Resolution of Messier 32, NGC 205, and the Central Region of the Andromeda Nebula., ApJ 100, 137
- Bahcall, J.N., 1984, K giants and the total amount of matter near the sun, ApJ 287, 926
- Bahcall, J.N., Casertano, S., 1985, Some possible regularities in the missing mass problem, ApJ 293, L7
- Bahcall, J.N., Schmidt, M., Soneira, R.M., 1982, On the interpretation of rotation curves measured at large galactocentric distances, ApJ 258, L23
- Bahcall, J.N., Soneira, R.M., 1980, The universe at faint magnitudes. I - Models for the galaxy and the predicted star counts, ApJS 44, 73
- Bailey, M.E., MacDonald, J., 1981, A comparison between velocity dispersion profiles of de Vaucouleurs and King galaxy models, MNRAS 194, 195
- Bailin, J., Kawata, D., Gibson, B.K., Steinmetz, M., Navarro, J.F., Brook, C.B., Gill, S.P.D., Ibata, R.A., Knebe, A., Lewis, G.F., Okamoto, T., 2005, Internal Alignment of the Halos of Disk Galaxies in Cosmological Hydrodynamic Simulations, ApJ 627, L17
- Bania, T.M., Lockman, F.J., 1984, A survey of the latitude structure of galactic H I on small angular scales, ApJS 54, 513
- Bardeen, J.M., Bond, J.R., Kaiser, N., Szalay, A.S., 1986, The statistics of peaks of Gaussian random fields, ApJ 304, 15
- Barnabè, M., Auger, M.W., Treu, T., Koopmans, L.V.E., Bolton, A.S., Czoske, O., Gavazzi, R., 2010, The non-evolving internal structure of early-type galaxies: the case study SDSSJ0728+3835 at  $z = 0.206$ , MNRAS 406, 2339
- Barnabè, M., Czoske, O., Koopmans, L.V.E., Treu, T., Bolton, A.S., 2011, Two-dimensional kinematics of SLACS lenses - III. Mass structure and dynamics of early-type lens galaxies beyond  $z \sim 0.1$ , MNRAS 415, 2215
- Barnabè, M., Czoske, O., Koopmans, L.V.E., Treu, T., Bolton, A.S., Gavazzi, R., 2009, Two-dimensional kinematics of SLACS lenses - II. Combined lensing and dynamics analysis of early-type galaxies at  $z = 0.08\text{--}0.33$ , MNRAS 399, 21

- Barnabè, M., Dutton, A.A., Marshall, P.J., Auger, M.W., Brewer, B.J., Treu, T., Bolton, A.S., Koo, D.C., Koopmans, L.V.E., 2012, The SWELLS survey - IV. Precision measurements of the stellar and dark matter distributions in a spiral lens galaxy, MNRAS p. 3040
- Barnabè, M., Koopmans, L.V.E., 2007, A Unifying Framework for Self-consistent Gravitational Lensing and Stellar Dynamics Analyses of Early-Type Galaxies, ApJ 666, 726
- Bartelmann, M., Schneider, P., 2001, Weak gravitational lensing, Physics Reports 340, 291
- Battaglia, G., Helmi, A., Breddels, M., 2013, Internal kinematics and dynamical models of dwarf spheroidal galaxies around the Milky Way, New Ast Rev , submitted, arXiv:1305.5965
- Battaglia, G., Helmi, A., Morrison, H., Harding, P., Olszewski, E.W., Mateo, M., Freeman, K.C., Norris, J., Shectman, S.A., 2005, The radial velocity dispersion profile of the Galactic halo: constraining the density profile of the dark halo of the Milky Way, MNRAS 364, 433
- Battaglia, G., Helmi, A., Tolstoy, E., Irwin, M., Hill, V., Jablonka, P., 2008, The Kinematic Status and Mass Content of the Sculptor Dwarf Spheroidal Galaxy, ApJ 681, L13
- Battaglia, G., Tolstoy, E., Helmi, A., Irwin, M., Parisi, P., Hill, V., Jablonka, P., 2011, Study of the Sextans dwarf spheroidal galaxy from the DART Ca II triplet survey, MNRAS 411, 1013
- Baugh, C.M., Lacey, C.G., Frenk, C.S., Granato, G.L., Silva, L., Bressan, A., Benson, A.J., Cole, S., 2007, The Nature of (Sub)millimeter Galaxies in Hierarchical Models, in: Baker, A.J., Glenn, J., Harris, A.I., Mangum, J.G., Yun, M.S. (eds.), , From Z-Machines to ALMA: (Sub)Millimeter Spectroscopy of Galaxies, vol. 375 of Astronomical Society of the Pacific Conference Series, p. 7
- Behroozi, P.S., Conroy, C., Wechsler, R.H., 2010, A Comprehensive Analysis of Uncertainties Affecting the Stellar Mass-Halo Mass Relation for  $0 < z < 4$ , ApJ 717, 379
- Behroozi, P.S., Wechsler, R.H., Conroy, C., 2013, The Average Star Formation Histories of Galaxies in Dark Matter Halos from  $z = 0\text{--}8$ , ApJ 770, 57
- Bell, E.F., de Jong, R.S., 2000, The stellar populations of spiral galaxies, MNRAS 312, 497
- Bell, E.F., de Jong, R.S., 2001, Stellar Mass-to-Light Ratios and the Tully-Fisher Relation, ApJ 550, 212
- Bell, E.F., McIntosh, D.H., Katz, N., Weinberg, M.D., 2003, The Optical and Near-Infrared Properties of Galaxies. I. Luminosity and Stellar Mass Functions, ApJS 149, 289
- Bendinelli, O., 1991, Abel integral equation inversion and deconvolution by multi-Gaussian approximation, ApJ 366, 599
- Bershady, M.A., Martinsson, T.P.K., Verheijen, M.A.W., Westfall, K.B., Andersen, D.R., Swaters, R.A., 2011, Galaxy Disks are Submaximal, ApJ 739, L47
- Bershady, M.A., Verheijen, M.A.W., Swaters, R.A., Andersen, D.R., Westfall, K.B., Martinsson, T., 2010a, The DiskMass Survey. I. Overview, ApJ 716, 198
- Bershady, M.A., Verheijen, M.A.W., Westfall, K.B., Andersen, D.R., Swaters, R.A., Martinsson, T., 2010b, The DiskMass Survey. II. Error Budget, ApJ 716, 234

- Bertin, G., Ciotti, L., Del Principe, M., 2002, Weak homology of elliptical galaxies., *A&A* 386, 149
- Bertin, G., Saglia, R.P., Stiavelli, M., 1992, Elliptical galaxies with dark matter. I - Self-consistent models. II - Optimal luminous-dark matter decomposition for a sample of bright objects, *ApJ* 384, 423
- Bertola, F., Bettoni, D., Rusconi, L., Sedmak, G., 1984, Stellar versus gaseous kinematics in E and SO galaxies, *AJ* 89, 356
- Bertone, G., Hooper, D., Silk, J., 2005, Particle dark matter: evidence, candidates and constraints, *Phys. Rep.* 405, 279
- Bezanson, R., van Dokkum, P.G., Franx, M., Brammer, G.B., Brinchmann, J., Kriek, M., Labbé, I., Quadri, R.F., Rix, H.W., van de Sande, J., Whitaker, K.E., Williams, R.J., 2011, Redshift Evolution of the Galaxy Velocity Dispersion Function, *ApJ* 737, L31
- Bica, E., Alloin, D., 1986, A base of star clusters for stellar population synthesis, *A&A* 162, 21
- Bicknell, G.V., Bruce, T.E.G., Carter, D., Killeen, N.E.B., 1989, The stellar dynamics of NGC 1399, *ApJ* 336, 639
- Binney, J., 1978, On the rotation of elliptical galaxies, *MNRAS* 183, 501
- Binney, J., 2010a, Distribution functions for the Milky Way, *MNRAS* 401, 2318
- Binney, J., Gerhard, O., Spergel, D., 1997, The photometric structure of the inner Galaxy, *MNRAS* 288, 365
- Binney, J., Mamon, G.A., 1982, M/L and velocity anisotropy from observations of spherical galaxies, or must M87 have a massive black hole?, *MNRAS* 200, 361
- Binney, J., McMillan, P., 2011, Models of our Galaxy - II, *MNRAS* 413, 1889
- Binney, J., Tremaine, S., 2008, *Galactic Dynamics: Second Edition*, Princeton University Press
- Binney, J.J., 2010b, Joint Discussion 5 Modelling the Milky Way in the Era of Gaia, *Highlights of Astronomy* 15, 173
- Binney, J.J., Davies, R.L., Illingworth, G.D., 1990, Velocity mapping and models of the elliptical galaxies NGC 720, NGC 1052, and NGC 4697, *ApJ* 361, 78
- Blais-Ouellette, S., 2000, Distribution de la matière sombre dans les galaxies spirales, PhD Thesis, Université de Montréal
- Blandford, R., Narayan, R., 1986, Fermat's principle, caustics, and the classification of gravitational lens images, *ApJ* 310, 568
- Blanton, M.R., Roweis, S., 2007, K-Corrections and Filter Transformations in the Ultraviolet, Optical, and Near-Infrared, *AJ* 133, 734
- Blitz, L., Spergel, D.N., 1991, Direct evidence for a bar at the Galactic center, *ApJ* 379, 631

- Blumenthal, G.R., Faber, S.M., Flores, R., Primack, J.R., 1986, Contraction of dark matter galactic halos due to baryonic infall, *ApJ* 301, 27
- Blumenthal, G.R., Faber, S.M., Primack, J.R., Rees, M.J., 1984, Formation of galaxies and large-scale structure with cold dark matter, *Nature* 311, 517
- Bolatto, A.D., Leroy, A.K., Rosolowsky, E., Walter, F., Blitz, L., 2008, The Resolved Properties of Extragalactic Giant Molecular Clouds, *ApJ* 686, 948
- Bolton, A.S., Brownstein, J.R., Kochanek, C.S., Shu, Y., Schlegel, D.J., Eisenstein, D.J., Wake, D.A., Connolly, N., Maraston, C., Arneson, R.A., Weaver, B.A., 2012, The BOSS Emission-Line Lens Survey. II. Investigating Mass-density Profile Evolution in the SLACS+BELLS Strong Gravitational Lens Sample, *ApJ* 757, 82
- Bolton, A.S., Burles, S., Koopmans, L.V.E., Treu, T., Gavazzi, R., Moustakas, L.A., Wayth, R., Schlegel, D.J., 2008a, The Sloan Lens ACS Survey. V. The Full ACS Strong-Lens Sample, *ApJ* 682, 964
- Bolton, A.S., Burles, S., Koopmans, L.V.E., Treu, T., Moustakas, L.A., 2005, SDSS J140228.22+632133.3: A New Spectroscopically Selected Gravitational Lens, *ApJ* 624, L21
- Bolton, A.S., Burles, S., Koopmans, L.V.E., Treu, T., Moustakas, L.A., 2006a, The Sloan Lens ACS Survey. I. A Large Spectroscopically Selected Sample of Massive Early-Type Lens Galaxies, *ApJ* 638, 703
- Bolton, A.S., Burles, S., Schlegel, D.J., Eisenstein, D.J., Brinkmann, J., 2004, Sloan Digital Sky Survey Spectroscopic Lens Search. I. Discovery of Intermediate-Redshift Star-forming Galaxies behind Foreground Luminous Red Galaxies, *AJ* 127, 1860
- Bolton, A.S., Rappaport, S., Burles, S., 2006b, Constraint on the post-Newtonian parameter  $\gamma$  on galactic size scales, *Phys. Rev. D* 74, 6, 061501
- Bolton, A.S., Treu, T., Koopmans, L.V.E., Gavazzi, R., Moustakas, L.A., Burles, S., Schlegel, D.J., Wayth, R., 2008b, The Sloan Lens ACS Survey. VII. Elliptical Galaxy Scaling Laws from Direct Observational Mass Measurements, *ApJ* 684, 248
- Bosma, A., 1978, The distribution and kinematics of neutral hydrogen in spiral galaxies of various morphological types, PhD Thesis, University of Groningen
- Bosma, A., Byun, Y., Freeman, K.C., Athanassoula, E., 1992, The opacity of spiral disks, *ApJ* 400, L21
- Bottema, R., 1993, The Stellar Kinematics of Galactic Disks, *A&A* 275, 16
- Bournaud, F., Duc, P.A., Emsellem, E., 2008, High-resolution simulations of galaxy mergers: resolving globular cluster formation, *MNRAS* 389, L8
- Bovy, J., Hogg, D.W., Rix, H.W., 2009, Galactic Masers and the Milky Way Circular Velocity, *ApJ* 704, 1704
- Bovy, J., Tremaine, S., 2012, On the Local Dark Matter Density, *ApJ* 756, 89

- Brainerd, T.G., 2010, Multiple Weak Deflections in Galaxy-Galaxy Lensing, *ApJ* 713, 603
- Brainerd, T.G., Blandford, R.D., Smail, I., 1996, Weak Gravitational Lensing by Galaxies, *ApJ* 466, 623
- Brand, J., Blitz, L., 1993, The Velocity Field of the Outer Galaxy, *A&A* 275, 67
- Breddels, M.A., Helmi, A., 2013, Model comparison of the dark matter profiles of Fornax, Sculptor, Carina and Sextans, *A&A*, submitted, arXiv:1304.2976
- Breddels, M.A., Helmi, A., van den Bosch, R.C.E., van de Ven, G., Battaglia, G., 2013, Orbit-based dynamical models of the Sculptor dSph galaxy, *MNRAS* 433, 3173
- Brewer, B.J., Dutton, A.A., Treu, T., Auger, M.W., Marshall, P.J., Barnabè, M., Bolton, A.S., Koo, D.C., Koopmans, L.V.E., 2012, The SWELLS survey - III. Disfavouring 'heavy' initial mass functions for spiral lens galaxies, *MNRAS* 422, 3574
- Briggs, F.H., 1990, Rules of behavior for galactic WARPS, *ApJ* 352, 15
- Brodie, J.P., Strader, J., 2006, Extragalactic Globular Clusters and Galaxy Formation, *ARA&A* 44, 193
- Brownstein, J.R., Bolton, A.S., Schlegel, D.J., Eisenstein, D.J., Kochanek, C.S., Connolly, N., Maraston, C., Pandey, P., Seitz, S., Wake, D.A., Wood-Vasey, W.M., Brinkmann, J., Schneider, D.P., Weaver, B.A., 2012, The BOSS Emission-Line Lens Survey (BELLS). I. A Large Spectroscopically Selected Sample of Lens Galaxies at Redshift  $\sim 0.5$ , *ApJ* 744, 41
- Brunthaler, A., Reid, M.J., Menten, K.M., Zheng, X.W., Bartkiewicz, A., Choi, Y.K., Dame, T., Hachisuka, K., Immer, K., Moellenbrock, G., Moscadelli, L., Rygl, K.L.J., Sanna, A., Sato, M., Wu, Y., Xu, Y., Zhang, B., 2011, The Bar and Spiral Structure Legacy (BeSSeL) survey: Mapping the Milky Way with VLBI astrometry, *Astronomische Nachrichten* 332, 461
- Bruzual, G., 1983, Spectral evolution of galaxies. I - Early-type systems, *ApJ* 273, 105
- Bruzual, G., 2007, Stellar Populations: High Spectral Resolution Libraries. Improved TP-AGB Treatment, in: A. Vallenari, R. Tantalo, L. Portinari, & A. Moretti (ed.), , From Stars to Galaxies: Building the Pieces to Build Up the Universe, vol. 374 of Astronomical Society of the Pacific Conference Series, p. 303
- Bruzual, G., Charlot, S., 1993, Spectral evolution of stellar populations using isochrone synthesis, *ApJ* 405, 538
- Bruzual, G., Charlot, S., 2003, Stellar population synthesis at the resolution of 2003, *MNRAS* 344, 1000
- Bundy, K., Ellis, R.S., Conselice, C.J., Taylor, J.E., Cooper, M.C., Willmer, C.N.A., Weiner, B.J., Coil, A.L., Noeske, K.G., Eisenhardt, P.R.M., 2006, The Mass Assembly History of Field Galaxies: Detection of an Evolving Mass Limit for Star-Forming Galaxies, *ApJ* 651, 120
- Burbidge, E.M., Burbidge, G.R., 1975, The Masses of Galaxies, the University of Chicago Press, p. 81

- Burkert, A., 1995, The Structure of Dark Matter Halos in Dwarf Galaxies, *ApJ* 447, L25
- Buzzoni, A., 1989, Evolutionary population synthesis in stellar systems. I - A global approach, *ApJS* 71, 817
- Capaccioli, M., Vietri, M., Held, E.V., Lorenz, H., 1991, Is the standard elliptical NGC 3379 a triaxial disk galaxy?, *ApJ* 371, 535
- Cappellari, M., 2008, Measuring the inclination and mass-to-light ratio of axisymmetric galaxies via anisotropic Jeans models of stellar kinematics, *MNRAS* 390, 71
- Cappellari, M., Bacon, R., Bureau, M., Damen, M.C., Davies, R.L., de Zeeuw, P.T., Emsellem, E., Falcón-Barroso, J., Krajnović, D., Kuntschner, H., McDermid, R.M., Peletier, R.F., Sarzi, M., van den Bosch, R.C.E., van de Ven, G., 2006, The SAURON project - IV. The mass-to-light ratio, the virial mass estimator and the Fundamental Plane of elliptical and lenticular galaxies, *MNRAS* 366, 1126
- Cappellari, M., Emsellem, E., Bacon, R., Bureau, M., Davies, R.L., de Zeeuw, P.T., Falcón-Barroso, J., Krajnović, D., Kuntschner, H., McDermid, R.M., Peletier, R.F., Sarzi, M., van den Bosch, R.C.E., van de Ven, G., 2007, The SAURON project - X. The orbital anisotropy of elliptical and lenticular galaxies: revisiting the  $(V/\sigma, \epsilon)$  diagram with integral-field stellar kinematics, *MNRAS* 379, 418
- Cappellari, M., Emsellem, E., Krajnović, D., McDermid, R.M., Scott, N., Verdoes Kleijn, G.A., Young, L.M., Alatalo, K., Bacon, R., Blitz, L., Bois, M., Bournaud, F., Bureau, M., Davies, R.L., Davis, T.A., de Zeeuw, P.T., Duc, P.A., Khochfar, S., Kuntschner, H., Lablanche, P.Y., Morganti, R., Naab, T., Oosterloo, T., Sarzi, M., Serra, P., Weijmans, A.M., 2011, The ATLAS<sup>3D</sup> project - I. A volume-limited sample of 260 nearby early-type galaxies: science goals and selection criteria, *MNRAS* 413, 813
- Cappellari, M., McDermid, R.M., 2005, The nuclear orbital distribution in galaxies as a fossil record of black hole formation from integral-field spectroscopy, *Classical and Quantum Gravity* 22, 347
- Cappellari, M., McDermid, R.M., Alatalo, K., Blitz, L., Bois, M., Bournaud, F., Bureau, M., Crocker, A.F., Davies, R.L., Davis, T.A., de Zeeuw, P.T., Duc, P.A., Emsellem, E., Khochfar, S., Krajnović, D., Kuntschner, H., Lablanche, P.Y., Morganti, R., Naab, T., Oosterloo, T., Sarzi, M., Scott, N., Serra, P., Weijmans, A.M., Young, L.M., 2012, Systematic variation of the stellar initial mass function in early-type galaxies, *Nature* 484, 485
- Cappellari, M., McDermid, R.M., Alatalo, K., Blitz, L., Bois, M., Bournaud, F., Bureau, M., Crocker, A.F., Davies, R.L., Davis, T.A., de Zeeuw, P.T., Duc, P.A., Emsellem, E., Khochfar, S., Krajnović, D., Kuntschner, H., Morganti, R., Naab, T., Oosterloo, T., Sarzi, M., Scott, N., Serra, P., Weijmans, A.M., Young, L.M., 2013a, The ATLAS<sup>3D</sup> project - XX. Mass-size and mass- $\sigma$  distributions of early-type galaxies: bulge fraction drives kinematics, mass-to-light ratio, molecular gas fraction and stellar initial mass function, *MNRAS* 432, 1862
- Cappellari, M., Scott, N., Alatalo, K., Blitz, L., Bois, M., Bournaud, F., Bureau, M., Crocker, A.F., Davies, R.L., Davis, T.A., de Zeeuw, P.T., Duc, P.A., Emsellem, E., Khochfar, S., Krajnović, D., Kuntschner, H., McDermid, R.M., Morganti, R., Naab, T., Oosterloo, T., Sarzi, M., Serra, P., Weijmans, A.M., Young, L.M., 2013b, The ATLAS<sup>3D</sup> project - XV. Benchmark for early-type

galaxies scaling relations from 260 dynamical models: mass-to-light ratio, dark matter, Fundamental Plane and Mass Plane, MNRAS 432, 1709

Carignan, C., Freeman, K.C., 1985, Basic parameters of dark halos in late-type spirals, ApJ 294, 494

Casertano, S., 1983, Rotation curve of the edge-on spiral galaxy NGC 5907: disc and halo masses, MNRAS 203, 735

Cassisi, S., Castellani, M., Castellani, V., 1997, Intermediate-age metal deficient stellar populations: the case of metallicity Z=0.00001., A&A 317, 108

Catena, R., Ullio, P., 2010, A novel determination of the local dark matter density, J. Cosmology and Astroparticle Phys. 8, 4

Catena, R., Ullio, P., 2012, The local dark matter phase-space density and impact on WIMP direct detection, J. Cosmology and Astroparticle Phys. 5, 5

Catinella, B., Haynes, M.P., Giovanelli, R., 2007, Rotational Widths for Use in the Tully-Fisher Relation. II. The Impact of Surface Brightness, AJ 134, 334

Cayatte, V., Kotanyi, C., Balkowski, C., van Gorkom, J.H., 1994, A very large array survey of neutral hydrogen in Virgo Cluster spirals. 3: Surface density profiles of the gas, AJ 107, 1003

Chabrier, G., 2003, Galactic Stellar and Substellar Initial Mass Function, pasp 115, 763

Charlot, S., Bruzual, A.G., 1991, Stellar population synthesis revisited, ApJ 367, 126

Charlot, S., Worthey, G., Bressan, A., 1996, Uncertainties in the Modeling of Old Stellar Populations, ApJ 457, 625

Chemin, L., Balkowski, C., Cayatte, V., Carignan, C., Amram, P., Garrido, O., Hernandez, O., Marcellin, M., Adami, C., Boselli, A., Boulesteix, J., 2006a, A Virgo high-resolution H $\alpha$  kinematical survey - II. The Atlas, MNRAS 366, 812

Chemin, L., Carignan, C., Drouin, N., Freeman, K.C., 2006b, H I Studies of the Sculptor Group Galaxies. VIII. The Background Galaxies: NGC 24 and NGC 45, AJ 132, 2527

Chemin, L., Carignan, C., Foster, T., 2009, H I Kinematics and Dynamics of Messier 31, ApJ 705, 1395

Chemin, L., Hernandez, O., 2009, A slow bar in a dark matter dominated galaxy, A&A 499, L25

Chen, C.W., Côté, P., West, A.A., Peng, E.W., Ferrarese, L., 2010, Homogeneous UGRIZ Photometry for ACS Virgo Cluster Survey Galaxies: A Non-parametric Analysis from SDSS Imaging, ApJS 191, 1

Chen, J., Koushiappas, S.M., Zentner, A.R., 2011, The Effects of Halo-to-halo Variation on Substructure Lensing, ApJ 741, 117

Chen, J., Kravtsov, A.V., Keeton, C.R., 2003, Lensing Optical Depths for Substructure and Isolated Dark Matter Halos, ApJ 592, 24

- Chen, Y.M., Kauffmann, G., Tremonti, C.A., White, S., Heckman, T.M., Kovač, K., Bundy, K., Chisholm, J., Maraston, C., Schneider, D.P., Bolton, A.S., Weaver, B.A., Brinkmann, J., 2012, Evolution of the most massive galaxies to  $z=0.6$  - I. A new method for physical parameter estimation, MNRAS 421, 314
- Churazov, E., Forman, W., Vikhlinin, A., Tremaine, S., Gerhard, O., Jones, C., 2008, Measuring the non-thermal pressure in early-type galaxy atmospheres: a comparison of X-ray and optical potential profiles in M87 and NGC 1399, MNRAS 388, 1062
- Churazov, E., Tremaine, S., Forman, W., Gerhard, O., Das, P., Vikhlinin, A., Jones, C., Böhringer, H., Gebhardt, K., 2010, Comparison of approximately isothermal gravitational potentials of elliptical galaxies based on X-ray and optical data, MNRAS 404, 1165
- Cimatti, A., Cassata, P., Pozzetti, L., Kurk, J., Mignoli, M., Renzini, A., Daddi, E., Bolzonella, M., Brusa, M., Rodighiero, G., Dickinson, M., Franceschini, A., Zamorani, G., Berta, S., Rosati, P., Halliday, C., 2008, GMASS ultradeep spectroscopy of galaxies at  $z\sim2$ . II. Superdense passive galaxies: how did they form and evolve?, A&A 482, 21
- Coccato, L., Arnaboldi, M., Gerhard, O., Freeman, K.C., Ventimiglia, G., Yasuda, N., 2010, Kinematics and line strength indices in the halos of the Coma brightest cluster galaxies NGC 4874 and NGC 4889, A&A 519, A95
- Coccato, L., Gerhard, O., Arnaboldi, M., Das, P., Douglas, N.G., Kuijken, K., Merrifield, M.R., Napolitano, N.R., Noordermeer, E., Romanowsky, A.J., Capaccioli, M., Cortesi, A., de Lorenzi, F., Freeman, K.C., 2009, Kinematic properties of early-type galaxy haloes using planetary nebulae, MNRAS 394, 1249
- Coles, J., 2008, A New Estimate of the Hubble Time with Improved Modeling of Gravitational Lenses, ApJ 679, 17
- Colín, P., Klypin, A.A., Kravtsov, A.V., 2000, Velocity Bias in a  $\Lambda$  Cold Dark Matter Model, ApJ 539, 561
- Conroy, C., 2013, Modeling the Panchromatic Spectral Energy Distributions of Galaxies, ARA&A 51, 393
- Conroy, C., Dutton, A.A., Graves, G.J., Mendel, J.T., van Dokkum, P.G., 2013, Dynamical Versus Stellar Masses in Compact Early-Type Galaxies: Further Evidence for Systematic Variation in the Stellar Initial Mass Function, arXiv:1306.2316
- Conroy, C., Gunn, J.E., 2010, The Propagation of Uncertainties in Stellar Population Synthesis Modeling. III. Model Calibration, Comparison, and Evaluation, ApJ 712, 833
- Conroy, C., Gunn, J.E., White, M., 2009, The Propagation of Uncertainties in Stellar Population Synthesis Modeling. I. The Relevance of Uncertain Aspects of Stellar Evolution and the Initial Mass Function to the Derived Physical Properties of Galaxies, ApJ 699, 486
- Conroy, C., Prada, F., Newman, J.A., Croton, D., Coil, A.L., Conselice, C.J., Cooper, M.C., Davis, M., Faber, S.M., Gerke, B.F., Guhathakurta, P., Klypin, A., Koo, D.C., Yan, R., 2007, Evolution in the Halo Masses of Isolated Galaxies between  $z \sim 1$  and  $z \sim 0$ : From DEEP2 to SDSS, ApJ 654, 153

- Conroy, C., van Dokkum, P.G., 2012, The Stellar Initial Mass Function in Early-type Galaxies From Absorption Line Spectroscopy. II. Results, *ApJ* 760, 71
- Cooray, A., Sheth, R., 2002, Halo models of large scale structure, *Physics Reports* 372, 1
- Corsini, E.M., 2011, Direct measurements of bar pattern speeds., *Memorie della Societa Astronomica Italiana Supplementi* 18, 23
- Corsini, E.M., Pizzella, A., Sarzi, M., Cinzano, P., Vega Beltrán, J.C., Funes, J.G., Bertola, F., Persic, M., Salucci, P., 1999, Dark matter in early-type spiral galaxies: the case of NGC 2179 and of NGC 2775, *A&A* 342, 671
- Côté, P., McLaughlin, D.E., Cohen, J.G., Blakeslee, J.P., 2003, Dynamics of the Globular Cluster System Associated with M49 (NGC 4472): Cluster Orbital Properties and the Distribution of Dark Matter, *ApJ* 591, 850
- Courteau, S., 1992, Tully-Fisher distances and motions in the northern sky, PhD Thesis, University of California, Santa Cruz
- Courteau, S., 1997, Optical Rotation Curves and Linewidths for Tully-Fisher Applications, *AJ* 114, 2402
- Courteau, S., Andersen, D.R., Bershady, M.A., MacArthur, L.A., Rix, H.W., 2003, The Tully-Fisher Relation of Barred Galaxies, *ApJ* 594, 208
- Courteau, S., Rix, H.W., 1999, Maximal Disks and the Tully-Fisher Relation, *ApJ* 513, 561
- Courteau, S., Sohn, Y.J., 2003, Galaxy Evolution from Emission Linewidths, in: R. Bender & A. Renzini (ed.), *The Mass of Galaxies at Low and High Redshift*, p. 204
- Courteau, S., van den Bergh, S., 1999, The Solar Motion Relative to the Local Group, *AJ* 118, 337
- Courteau, S., Widrow, L.M., McDonald, M., Guhathakurta, P., Gilbert, K.M., Zhu, Y., Beaton, R.L., Majewski, S.R., 2011, The Luminosity Profile and Structural Parameters of the Andromeda Galaxy, *ApJ* 739, 20
- Cox, T.J., Primack, J., Jonsson, P., Somerville, R.S., 2004, Generating Hot Gas in Simulations of Disk-Galaxy Major Mergers, *ApJ* 607, L87
- Cretton, N., van den Bosch, F.C., 1999, Evidence for a Massive Black Hole in the S0 Galaxy NGC 4342, *ApJ* 514, 704
- Czoske, O., Barnabè, M., Koopmans, L.V.E., Treu, T., Bolton, A.S., 2008, Two-dimensional kinematics of SLACS lenses - I. Phase-space analysis of the early-type galaxy SDSSJ2321-097 at  $z \sim 0.1$ , *MNRAS* 384, 987
- Daddi, E., Renzini, A., Pirzkal, N., Cimatti, A., Malhotra, S., Stiavelli, M., Xu, C., Pasquali, A., Rhoads, J.E., Brusa, M., di Serego Alighieri, S., Ferguson, H.C., Koekemoer, A.M., Moustakas, L.A., Panagia, N., Windhorst, R.A., 2005, Passively Evolving Early-Type Galaxies at  $1.4 < z < 2.5$  in the Hubble Ultra Deep Field, *ApJ* 626, 680
- Dai, X., Anderson, M.E., Bregman, J.N., Miller, J.M., 2012, XMM-Newton Detects a Hot Gaseous Halo in the Fastest Rotating Spiral Galaxy UGC 12591, *ApJ* 755, 107

- Dalal, N., Kochanek, C.S., 2002, Direct Detection of Cold Dark Matter Substructure, ApJ 572, 25
- Das, P., Gerhard, O., Mendez, R.H., Teodorescu, A.M., de Lorenzi, F., 2011, Using NMAGIC to probe the dark matter halo and orbital structure of the X-ray bright, massive elliptical galaxy, NGC 4649, MNRAS 415, 1244
- Davé, R., Spergel, D.N., Steinhardt, P.J., Wandelt, B.D., 2001, Halo Properties in Cosmological Simulations of Self-interacting Cold Dark Matter, ApJ 547, 574
- Davies, R., Genzel, R., 2010, MICADO: The Multi-adaptive Optics Imaging Camera for Deep Observations, The Messenger 140, 32
- de Blok, W.J.G., 2010, The Core-Cusp Problem, Advances in Astronomy 2010
- de Blok, W.J.G., Walter, F., Brinks, E., Trachternach, C., Oh, S.H., Kennicutt, Jr., R.C., 2008, High-Resolution Rotation Curves and Galaxy Mass Models from THINGS, AJ 136, 2648
- de Jong, R.S., 1996, Near-infrared and optical broadband surface photometry of 86 face-on disk dominated galaxies. II. A two-dimensional method to determine bulge and disk parameters., aaps 118, 557
- de Jong, R.S., Bell, E.F., 2007, Comparing Dynamical and Stellar Population Mass-To-Light Ratio Estimates, Island Universes - Structure and Evolution of Disk Galaxies, p. 107
- de Jong, R.S., Davies, R.L., 1997, The Shapes and Ages of Elliptical Galaxies, MNRAS 285, L1
- de Lorenzi, F., Debattista, V.P., Gerhard, O., Sambhus, N., 2007, NMAGIC: a fast parallel implementation of a  $\chi^2$ -made-to-measure algorithm for modelling observational data, MNRAS 376, 71
- de Lorenzi, F., Gerhard, O., Coccato, L., Arnaboldi, M., Capaccioli, M., Douglas, N.G., Freeman, K.C., Kuijken, K., Merrifield, M.R., Napolitano, N.R., Noordermeer, E., Romanowsky, A.J., Debattista, V.P., 2009, Dearth of dark matter or massive dark halo? Mass-shape-anisotropy degeneracies revealed by NMAGIC dynamical models of the elliptical galaxy NGC 3379, MNRAS 395, 76
- De Lucia, G., Poggianti, B.M., Aragón-Salamanca, A., White, S.D.M., Zaritsky, D., Clowe, D., Halliday, C., Jablonka, P., von der Linden, A., Milvang-Jensen, B., Pelló, R., Rudnick, G., Saglia, R.P., Simard, L., 2007, The build-up of the colour-magnitude relation in galaxy clusters since  $z \sim 0.8$ , MNRAS 374, 809
- de Zeeuw, T., 1985, Elliptical galaxies with separable potentials, MNRAS 216, 273
- Deason, A.J., Belokurov, V., Evans, N.W., An, J., 2012, Broken degeneracies: the rotation curve and velocity anisotropy of the Milky Way halo, MNRAS 424, L44
- Debattista, V.P., Sellwood, J.A., 2000, Constraints from Dynamical Friction on the Dark Matter Content of Barred Galaxies, ApJ 543, 704
- Dehnen, W., 2009, Tailoring triaxial N-body models via a novel made-to-measure method, MNRAS 395, 1079
- Dehnen, W., Binney, J., 1998, Mass models of the Milky Way, MNRAS 294, 429

- Dehnen, W., Gerhard, O.E., 1993, Three-integral models of oblate elliptical galaxies, MNRAS 261, 311
- Dehnen, W., King, A., 2006, Probing dark matter with X-ray binaries, MNRAS 367, L29
- Dejonghe, H., 1989, A quadratic programming technique for modeling gravitating systems, ApJ 343, 113
- Dejonghe, H., Merritt, D., 1992, Inferring the mass of spherical stellar systems from velocity moments, ApJ 391, 531
- Dekel, A., Lahav, O., 1999, Stochastic Nonlinear Galaxy Biasing, ApJ 520, 24
- Dekel, A., Stoehr, F., Mamon, G.A., Cox, T.J., Novak, G.S., Primack, J.R., 2005, Lost and found dark matter in elliptical galaxies, Nature 437, 707, arXiv:astro-ph/0501622
- di Serego Alighieri, S., Gavazzi, G., Giovanardi, C., Giovanelli, R., Grossi, M., Haynes, M.P., Kent, B.R., Koopmann, R.A., Pellegrini, S., Scodellaggio, M., Trinchieri, G., 2007, The HI content of early-type galaxies from the ALFALFA survey. I. Catalogued HI sources in the Virgo cluster, A&A 474, 851
- Dobler, G., Keeton, C.R., 2006, Finite source effects in strong lensing: implications for the substructure mass scale, MNRAS 365, 1243
- Doherty, M., Arnaboldi, M., Das, P., Gerhard, O., Aguerri, J.A.L., Ciardullo, R., Feldmeier, J.J., Freeman, K.C., Jacoby, G.H., Murante, G., 2009, The edge of the M 87 halo and the kinematics of the diffuse light in the Virgo cluster core, A&A 502, 771
- Douglas, N.G., Arnaboldi, M., Freeman, K.C., Kuijken, K., Merrifield, M.R., Romanowsky, A.J., Taylor, K., Capaccioli, M., Axelrod, T., Gilmozzi, R., Hart, J., Bloxham, G., Jones, D., 2002, The Planetary Nebula Spectrograph: The Green Light for Galaxy Kinematics, PASP 114, 1234
- Douglas, N.G., Napolitano, N.R., Romanowsky, A.J., Coccato, L., Kuijken, K., Merrifield, M.R., Arnaboldi, M., Gerhard, O., Freeman, K.C., Merrett, H.R., Noordermeer, E., Capaccioli, M., 2007, The PN.S Elliptical Galaxy Survey: Data reduction, planetary nebula catalog, and basic dynamics for NGC 3379, ApJ 664, 257
- Drukier, A., Stodolsky, L., 1984, Principles and applications of a neutral-current detector for neutrino physics and astronomy, Phys. Rev. D 30, 2295
- Dubinski, J., Carlberg, R.G., 1991, The structure of cold dark matter halos, ApJ 378, 496
- Dubois, Y., Gavazzi, R., Peirani, S., Silk, J., 2013, AGN-driven quenching of star formation: morphological and dynamical implications for early-type galaxies, MNRAS 433, 3297
- Duffy, A.R., Schaye, J., Kay, S.T., Dalla Vecchia, C., 2008, Dark matter halo concentrations in the Wilkinson Microwave Anisotropy Probe year 5 cosmology, MNRAS 390, L64
- Duffy, A.R., Schaye, J., Kay, S.T., Dalla Vecchia, C., Battye, R.A., Booth, C.M., 2010, Impact of baryon physics on dark matter structures: a detailed simulation study of halo density profiles, MNRAS 405, 2161

- Dutton, A.A., Brewer, B.J., Marshall, P.J., Auger, M.W., Treu, T., Koo, D.C., Bolton, A.S., Holden, B.P., Koopmans, L.V.E., 2011a, The SWELLS survey - II. Breaking the disc-halo degeneracy in the spiral galaxy gravitational lens SDSS J2141-0001, *MNRAS* 417, 1621
- Dutton, A.A., Conroy, C., van den Bosch, F.C., Prada, F., More, S., 2010, The kinematic connection between galaxies and dark matter haloes, *MNRAS* 407, 2
- Dutton, A.A., Conroy, C., van den Bosch, F.C., Simard, L., Mendel, J.T., Courteau, S., Dekel, A., More, S., Prada, F., 2011b, Dark halo response and the stellar initial mass function in early-type and late-type galaxies, *MNRAS* 416, 322
- Dutton, A.A., Courteau, S., de Jong, R., Carignan, C., 2005, Mass Modeling of Disk Galaxies: Degeneracies, Constraints, and Adiabatic Contraction, *ApJ* 619, 218
- Dutton, A.A., Macciò, A.V., Mendel, J.T., Simard, L., 2013, Universal IMF versus dark halo response in early-type galaxies: breaking the degeneracy with the Fundamental Plane, *MNRAS* 432, 2496
- Dutton, A.A., Mendel, J.T., Simard, L., 2012, Evidence for a non-universal stellar initial mass function in low-redshift high-density early-type galaxies, *MNRAS* 422, L33
- Dutton, A.A., Treu, T., 2013, The bulge-halo conspiracy in massive elliptical galaxies: implications for the stellar initial mass function and halo response to baryonic processes, *arXiv:1303.4389*
- Dutton, A.A., van den Bosch, F.C., Dekel, A., Courteau, S., 2007, A Revised Model for the Formation of Disk Galaxies: Low Spin and Dark Halo Expansion, *ApJ* 654, 27
- Eddington, A.S., 1916, The distribution of stars in globular clusters, *MNRAS* 76, 572
- Einasto, J., 1965, Trudy Inst. Astroz. Alma-Ata 51, 87
- Einasto, J., 1969, On Galactic Descriptive Functions, *Astronomische Nachrichten* 291, 97
- Einasto, J., Haud, U., 1989, Galactic models with massive corona. I - Method. II - Galaxy, *A&A* 223, 89
- Eisenstein, D.J., Annis, J., Gunn, J.E., Szalay, A.S., Connolly, A.J., Nichol, R.C., Bahcall, N.A., Bernardi, M., Burles, S., Castander, F.J., Fukugita, M., Hogg, D.W., Ivezić, Ž., Knapp, G.R., Lupton, R.H., Narayanan, V., Postman, M., Reichart, D.E., Richmond, M., Schneider, D.P., Schlegel, D.J., Strauss, M.A., SubbaRao, M., Tucker, D.L., Vanden Berk, D., Vogeley, M.S., Weinberg, D.H., Yanny, B., 2001, Spectroscopic Target Selection for the Sloan Digital Sky Survey: The Luminous Red Galaxy Sample, *AJ* 122, 2267
- El-Zant, A., Shlosman, I., Hoffman, Y., 2001, Dark Halos: The Flattening of the Density Cusp by Dynamical Friction, *ApJ* 560, 636
- Emsellem, E., Cappellari, M., Krajnović, D., Alatalo, K., Blitz, L., Bois, M., Bournaud, F., Bureau, M., Davies, R.L., Davis, T.A., de Zeeuw, P.T., Khochfar, S., Kuntschner, H., Lablanche, P.Y., McDermid, R.M., Morganti, R., Naab, T., Oosterloo, T., Sarzi, M., Scott, N., Serra, P., van de Ven, G., Weijmans, A.M., Young, L.M., 2011, The ATLAS<sup>3D</sup> project - III. A census of the stellar angular momentum within the effective radius of early-type galaxies: unveiling the distribution of fast and slow rotators, *MNRAS* 414, 888

- Emsellem, E., Cappellari, M., Krajnović, D., van de Ven, G., Bacon, R., Bureau, M., Davies, R.L., de Zeeuw, P.T., Falcón-Barroso, J., Kuntschner, H., McDermid, R., Peletier, R.F., Sarzi, M., 2007, The SAURON project - IX. A kinematic classification for early-type galaxies, MNRAS 379, 401
- Emsellem, E., Dejonghe, H., Bacon, R., 1999, Dynamical models of NGC 3115, MNRAS 303, 495
- Emsellem, E., Monnet, G., Bacon, R., 1994, The multi-gaussian expansion method: a tool for building realistic photometric and kinematical models of stellar systems I. The formalism, A&A 285, 723
- Englmaier, P., Gerhard, O., 1999, Gas dynamics and large-scale morphology of the Milky Way galaxy, MNRAS 304, 512
- Englmaier, P., Gerhard, O., 2006, Milky Way Gas Dynamics, Celestial Mechanics and Dynamical Astronomy 94, 369
- Faber, S.M., 1972, Quadratic programming applied to the problem of galaxy population synthesis., A&A 20, 361
- Faber, S.M., Gallagher, J.S., 1979, Masses and mass-to-light ratios of galaxies, ARA&A 17, 135
- Fahlman, G., Kaiser, N., Squires, G., Woods, D., 1994, Dark matter in MS 1224 from distortion of background galaxies, ApJ 437, 56
- Famaey, B., McGaugh, S.S., 2012, Modified Newtonian Dynamics (MOND): Observational Phenomenology and Relativistic Extensions, Living Reviews in Relativity 15, 10
- Feng, J.L., 2010, Dark Matter Candidates from Particle Physics and Methods of Detection, ARA&A 48, 495
- Féron, C., Hjorth, J., McKean, J.P., Samsing, J., 2009, A Search for Disk-Galaxy Lenses in the Sloan Digital Sky Survey, ApJ 696, 1319
- Ferreras, I., La Barbera, F., de la Rosa, I.G., Vazdekis, A., de Carvalho, R.R., Falcón-Barroso, J., Ricciardelli, E., 2013, Systematic variation of the stellar initial mass function with velocity dispersion in early-type galaxies, MNRAS 429, L15
- Fioc, M., Rocca-Volmerange, B., 1997, PEGASE: a UV to NIR spectral evolution model of galaxies. Application to the calibration of bright galaxy counts., A&A 326, 950
- Fischer, P., McKay, T.A., Sheldon, E., Connolly, A., Stebbins, A., Frieman, J.A., Jain, B., Joffre, M., Johnston, D., Bernstein, G., Annis, J., Bahcall, N.A., Brinkmann, J., Carr, M.A., Csabai, I., Gunn, J.E., Hennessy, G.S., Hindsley, R.B., Hull, C., Ivezić, Ž., Knapp, G.R., Limmongkol, S., Lupton, R.H., Munn, J.A., Nash, T., Newberg, H.J., Owen, R., Pier, J.R., Rockosi, C.M., Schneider, D.P., Smith, J.A., Stoughton, C., Szalay, A.S., Szokoly, G.P., Thakar, A.R., Vogeley, M.S., Waddell, P., Weinberg, D.H., York, D.G., The SDSS Collaboration, 2000, Weak Lensing with Sloan Digital Sky Survey Commissioning Data: The Galaxy-Mass Correlation Function to  $1\text{H}^{-1}\text{Mpc}$ , AJ 120, 1198
- Fisher, D., 1997, Kinematic Profiles of SO Galaxies, AJ 113, 950
- Flynn, C., Holmberg, J., Portinari, L., Fuchs, B., Jahreiß, H., 2006, On the mass-to-light ratio of the local Galactic disc and the optical luminosity of the Galaxy, MNRAS 372, 1149

- Förster Schreiber, N.M., Genzel, R., Lehnert, M.D., Bouché, N., Verma, A., Erb, D.K., Shapley, A.E., Steidel, C.C., Davies, R., Lutz, D., Nesvadba, N., Tacconi, L.J., Eisenhauer, F., Abuter, R., Gilbert, A., Gillessen, S., Sternberg, A., 2006, SINFONI Integral Field Spectroscopy of  $z \sim 2$  UV-selected Galaxies: Rotation Curves and Dynamical Evolution, *ApJ* 645, 1062
- Foster, C., Spitler, L.R., Romanowsky, A.J., Forbes, D.A., Pota, V., Bekki, K., Strader, J., Proctor, R.N., Arnold, J.A., Brodie, J.P., 2011, Global properties of 'ordinary' early-type galaxies: photometry and spectroscopy of stars and globular clusters in NGC 4494, *MNRAS* 415, 3393
- Franx, M., van Gorkom, J.H., de Zeeuw, T., 1994, Evidence for axisymmetric halos: The case of IC 2006, *ApJ* 436, 642
- Freeman, K.C., 1970, On the Disks of Spiral and S0 Galaxies, *ApJ* 160, 811
- Fu, L., Sembolini, E., Hoekstra, H., Kilbinger, M., van Waerbeke, L., Tereno, I., Mellier, Y., Heymans, C., Coupon, J., Benabed, K., Benjamin, J., Bertin, E., Doré, O., Hudson, M.J., Ilbert, O., Maoli, R., Marmo, C., McCracken, H.J., Ménard, B., 2008, Very weak lensing in the CFHTLS wide: cosmology from cosmic shear in the linear regime, *Astron. Astrophys.* 479, 9
- Fukazawa, Y., Botoya-Nonesa, J.G., Pu, J., Ohto, A., Kawano, N., 2006, Scaling Mass Profiles around Elliptical Galaxies Observed with Chandra and XMM-Newton, *ApJ* 636, 698
- Fux, R., 1997, 3D self-consistent N-body barred models of the Milky Way. I. Stellar dynamics, *A&A* 327, 983
- Fux, R., 1999, 3D self-consistent N-body barred models of the Milky Way. II. Gas dynamics, *A&A* 345, 787
- Gallazzi, A., Bell, E.F., 2009, Stellar Mass-to-Light Ratios from Galaxy Spectra: How Accurate Can They Be?, *ApJS* 185, 253
- Gallazzi, A., Charlot, S., Brinchmann, J., White, S.D.M., Tremonti, C.A., 2005, The ages and metallicities of galaxies in the local universe, *MNRAS* 362, 41
- Garbari, S., Liu, C., Read, J.I., Lake, G., 2012, A new determination of the local dark matter density from the kinematics of K dwarfs, *MNRAS* 425, 1445
- Gavazzi, R., Treu, T., Koopmans, L.V.E., Bolton, A.S., Moustakas, L.A., Burles, S., Marshall, P.J., 2008, The Sloan Lens ACS Survey. VI. Discovery and Analysis of a Double Einstein Ring, *ApJ* 677, 1046
- Gavazzi, R., Treu, T., Marshall, P.J., Brault, F., Ruff, A., 2012, The SL2S Galaxy-scale Gravitational Lens Sample. I. The Alignment of Mass and Light in Massive Early-type Galaxies at  $z = 0.2\text{--}0.9$ , *ApJ* 761, 170
- Gavazzi, R., Treu, T., Rhodes, J.D., Koopmans, L.V.E., Bolton, A.S., Burles, S., Massey, R.J., Moustakas, L.A., 2007, The Sloan Lens ACS Survey. IV. The Mass Density Profile of Early-Type Galaxies out to 100 Effective Radii, *ApJ* 667, 176
- Gebhardt, K., et al., 2003, Axisymmetric Dynamical Models of the Central Regions of Galaxies, *ApJ* 583, 92

- Geehan, J.J., Fardal, M.A., Babul, A., Guhathakurta, P., 2006, Investigating the Andromeda stream - I. Simple analytic bulge-disc-halo model for M31, MNRAS 366, 996
- Geha, M., van der Marel, R.P., Guhathakurta, P., Gilbert, K.M., Kalirai, J., Kirby, E.N., 2010, Local Group Dwarf Elliptical Galaxies. II. Stellar Kinematics to Large Radii in NGC 147 and NGC 185, ApJ 711, 361
- Gerhard, O., 2013, Dark matter in massive galaxies 295, 211
- Gerhard, O., Jeske, G., Saglia, R.P., Bender, R., 1998, Breaking the degeneracy between anisotropy and mass - The dark halo of the E0 galaxy NGC 6703, MNRAS 295, 197
- Gerhard, O., Kronawitter, A., Saglia, R.P., Bender, R., 2001, Dynamical Family Properties and Dark Halo Scaling Relations of Giant Elliptical Galaxies, AJ 121, 1936
- Gerhard, O.E., Vietri, M., 1986, The Peculiar Shape of the Inner Galactic Rotation Curve, MNRAS 223, 377
- Gerssen, J., Kuijken, K., Merrifield, M.R., 1997, The shape of the velocity ellipsoid in NGC 488, MNRAS 288, 618
- Gerssen, J., Kuijken, K., Merrifield, M.R., 2000, Disc heating in NGC 2985, MNRAS 317, 545
- Ghez, A.M., Salim, S., Weinberg, N.N., et al., 2008, Measuring Distance and Properties of the Milky Way's Central Supermassive Black Hole with Stellar Orbits, ApJ 689, 1044
- Gillessen, S., Eisenhauer, F., Trippe, S., et al., 2009, Monitoring Stellar Orbits Around the Massive Black Hole in the Galactic Center, ApJ 692, 1075
- Gilmore, G., Wilkinson, M.I., Wyse, R.F.G., Kleyna, J.T., Koch, A., Evans, N.W., Grebel, E.K., 2007, The Observed Properties of Dark Matter on Small Spatial Scales, ApJ 663, 948
- Giovanelli, R., Haynes, M.P., 2002, The Inner Scale Length of Spiral Galaxy Rotation Curves, ApJ 571, L107
- Giovanelli, R., Haynes, M.P., Rubin, V.C., Ford, Jr., W.K., 1986, UGC 12591 - The most rapidly rotating disk galaxy, ApJ 301, L7
- Gnedin, O.Y., Brown, W.R., Geller, M.J., Kenyon, S.J., 2010, The Mass Profile of the Galaxy to 80 kpc, ApJ 720, L108
- Gnedin, O.Y., Kravtsov, A.V., Klypin, A.A., Nagai, D., 2004, Response of Dark Matter Halos to Condensation of Baryons: Cosmological Simulations and Improved Adiabatic Contraction Model, ApJ 616, 16
- Gómez, F.A., Minchev, I., O'Shea, B.W., Beers, T.C., Bullock, J.S., Purcell, C.W., 2013, Vertical density waves in the Milky Way disc induced by the Sagittarius dwarf galaxy, MNRAS 429, 159
- Goodman, M.W., Witten, E., 1985, Detectability of certain dark-matter candidates, Phys. Rev. D 31, 3059
- Goudfrooij, P., Kruijssen, J.M.D., 2013, The Optical Colors of Giant Elliptical Galaxies and their Metal-Rich Globular Cluster s Indicate a Bottom-Heavy Initial Mass Function, ApJ 762, 107

- Governato, F., Zolotov, A., Pontzen, A., Christensen, C., Oh, S.H., Brooks, A.M., Quinn, T., Shen, S., Wadsley, J., 2012, Cuspy no more: how outflows affect the central dark matter and baryon distribution in  $\Lambda$  cold dark matter galaxies, MNRAS 422, 1231
- Graff, P., Hobson, M.P., Lasenby, A., 2011, An investigation into the Multiple Optimised Parameter Estimation and Data compression algorithm, MNRAS 413, L66
- Greggio, L., Renzini, A., 2011, Stellar Populations. A User Guide from Low to High Redshift
- Guzik, J., Seljak, U., 2001, Galaxy-dark matter correlations applied to galaxy-galaxy lensing: predictions from the semi-analytic galaxy formation models, MNRAS 321, 439
- Guzik, J., Seljak, U., 2002, Virial masses of galactic haloes from galaxy-galaxy lensing: theoretical modelling and application to Sloan Digital Sky Survey data, MNRAS 335, 311
- Halkola, A., Seitz, S., Pannella, M., 2007, The Sizes of Galaxy Halos in Galaxy Cluster Abell 1689, ApJ 656, 739
- Hall, M., Courteau, S., Dutton, A.A., McDonald, M., Zhu, Y., 2012, An investigation of Sloan Digital Sky Survey imaging data and multiband scaling relations of spiral galaxies, MNRAS 425, 2741
- Hayashi, E., Navarro, J.F., Springel, V., 2007, The shape of the gravitational potential in cold dark matter haloes, MNRAS 377, 50
- Haynes, M.P., Giovanelli, R., 1984, Neutral hydrogen in isolated galaxies. IV - Results for the Arecibo sample, AJ 89, 758
- Helmi, A., 2004, Is the dark halo of our Galaxy spherical?, MNRAS 351, 643
- Hernquist, L., 1990, An analytical model for spherical galaxies and bulges, ApJ 356, 359
- Hewett, P.C., Warren, S.J., Willis, J.P., Bland-Hawthorn, J., Lewis, G.F., 2000, High-Redshift Gravitationally Lensed Galaxies and Tunable Filter Imaging, in: W. van Breugel & J. Bland-Hawthorn (ed.), , Imaging the Universe in Three Dimensions, vol. 195 of Astronomical Society of the Pacific Conference Series, p. 94
- Heymans, C., Bell, E.F., Rix, H., Barden, M., Borch, A., Caldwell, J.A.R., McIntosh, D.H., Meisenheimer, K., Peng, C.Y., Wolf, C., Beckwith, S.V.W., Häußler, B., Jahnke, K., Jogee, S., Sánchez, S.F., Somerville, R., Wisotzki, L., 2006, A weak lensing estimate from GEMS of the virial to stellar mass ratio in massive galaxies to  $z \sim 0.8$ , MNRAS 371, L60
- Hildebrandt, H., van Waerbeke, L., Erben, T., 2009, CARS: The CFHTLS-Archive-Research Survey. III. First detection of cosmic magnification in samples of normal high- $z$  galaxies, Astron. Astrophys. 507, 683
- Hoekstra, H., Hsieh, B.C., Yee, H.K.C., Lin, H., Gladders, M.D., 2005, Virial Masses and the Baryon Fraction in Galaxies, ApJ 635, 73
- Hoekstra, H., Jain, B., 2008, Weak Gravitational Lensing and Its Cosmological Applications, Annual Review of Nuclear and Particle Science 58, 99

- Hoekstra, H., van Waerbeke, L., Gladders, M.D., Mellier, Y., Yee, H.K.C., 2002, Weak Lensing Study of Galaxy Biasing, *ApJ* 577, 604
- Hoekstra, H., Yee, H.K.C., Gladders, M.D., 2001, Measurement of the Bias Parameter from Weak Lensing, *ApJ* 558, L11
- Hoekstra, H., Yee, H.K.C., Gladders, M.D., 2004, Properties of Galaxy Dark Matter Halos from Weak Lensing, *ApJ* 606, 67
- Holmberg, J., Flynn, C., 2000, The local density of matter mapped by Hipparcos, *MNRAS* 313, 209
- Howell, P.J., Brainerd, T.G., 2010, Galaxy-galaxy lensing by non-spherical haloes - I. Theoretical considerations, *MNRAS* 407, 891
- Huchra, J., Gorenstein, M., Kent, S., Shapiro, I., Smith, G., Horine, E., Perley, R., 1985, 2237 + 0305: A new and unusual gravitational lens, *AJ* 90, 691
- Hudson, M.J., Gwyn, S.D.J., Dahle, H., Kaiser, N., 1998, Galaxy-Galaxy Lensing in the Hubble Deep Field: The Halo Tully-Fisher Relation at Intermediate Redshift, *ApJ* 503, 531
- Humphrey, P.J., Buote, D.A., 2010, The slope of the mass profile and the tilt of the Fundamental Plane in early-type galaxies, *MNRAS* 403, 2143
- Humphrey, P.J., Buote, D.A., Canizares, C.R., Fabian, A.C., Miller, J.M., 2011, A Census of Baryons and Dark Matter in an Isolated, Milky Way Sized Elliptical Galaxy, *ApJ* 729, 53
- Humphrey, P.J., Buote, D.A., Gastaldello, F., Zappacosta, L., Bullock, J.S., Brighenti, F., Mathews, W.G., 2006, A Chandra View of Dark Matter in Early-Type Galaxies, *ApJ* 646, 899
- Hunter, C., de Zeeuw, P.T., 1992, Triaxial galaxy models with thin tube orbits, *ApJ* 389, 79
- Hunter, C., Qian, E., 1993, Two-integral distribution functions for axisymmetric galaxies, *MNRAS* 262, 401
- Hwang, H.S., Lee, M.G., Park, H.S., Kim, S.C., Park, J.H., Sohn, Y.J., Lee, S.G., Rey, S.C., Lee, Y.W., Kim, H.I., 2008, The Globular Cluster System of M60 (NGC 4649). II. Kinematics of the Globular Cluster System, *ApJ* 674, 869
- Ilbert, O., Salvato, M., Le Floc'h, E., Aussel, H., Capak, P., McCracken, H.J., Mobasher, B., Kartaltepe, J., Scoville, N., Sanders, D.B., Arnouts, S., Bundy, K., Cassata, P., Kneib, J.P., Koekemoer, A., Le Fèvre, O., Lilly, S., Surace, J., Taniguchi, Y., Tasca, L., Thompson, D., Tresse, L., Zamorani, G., Zucca, E., 2010, Galaxy Stellar Mass Assembly Between  $0.2 < z < 2$  from the S-COSMOS Survey, *ApJ* 709, 644
- Ivezic, Z., Tyson, J.A., Acosta, E., for the LSST Collaboration, e., 2008, LSST: from Science Drivers to Reference Design and Anticipated Data Products, arXiv:0805.2366
- Jackson, N., Bryan, S.E., Mao, S., Li, C., 2010, Satellites in the field and lens galaxies: SDSS/COSMOS versus SLACS/CLASS, *MNRAS* 403, 826
- Jardel, J.R., Gebhardt, K., 2012, The Dark Matter Density Profile of the Fornax Dwarf, *ApJ* 746, 89

- Jaunsen, A.O., Hjorth, J., 1997, Detection of a spiral lens galaxy and optical variability in the gravitational lens system B1600+434., *A&A* 317, L39
- Jeans, J.H., 1922, The motions of stars in a Kapteyn universe, *MNRAS* 82, 122
- Jing, Y.P., Suto, Y., 2002a, Triaxial Modeling of Halo Density Profiles with High-Resolution N-Body Simulations, *ApJ* 574, 538
- Jing, Y.P., Suto, Y., 2002b, Triaxial Modeling of Halo Density Profiles with High-Resolution N-Body Simulations, *ApJ* 574, 538
- Johansson, P.H., Burkert, A., Naab, T., 2009, The Evolution of Black Hole Scaling Relations in Galaxy Mergers, *ApJ* 707, L184
- Kahn, F.D., Woltjer, L., 1959, Intergalactic Matter and the Galaxy., *ApJ* 130, 705
- Kaiser, N., Squires, G., 1993, Mapping the dark matter with weak gravitational lensing, *ApJ* 404, 441
- Kapteyn, J.C., 1922, First Attempt at a Theory of the Arrangement and Motion of the Sidereal System, *ApJ* 55, 302
- Kassin, S.A., de Jong, R.S., Weiner, B.J., 2006, Dark and Baryonic Matter in Bright Spiral Galaxies. II. Radial Distributions for 34 Galaxies, *ApJ* 643, 804
- Kauffmann, G., Heckman, T.M., Tremonti, C., Brinchmann, J., Charlot, S., White, S.D.M., Ridgway, S.E., Brinkmann, J., Fukugita, M., Hall, P.B., Ivezić, Ž., Richards, G.T., Schneider, D.P., 2003, The host galaxies of active galactic nuclei, *MNRAS* 346, 1055
- Kayser, R., Refsdal, S., 1983, The difference in light travel time between gravitational lens images. I - Generalization of the wavefront method to arbitrary deflectors and inhomogeneous universes, *A&A* 128, 156
- Kazantzidis, S., Abadi, M.G., Navarro, J.F., 2010, The Sphericalization of Dark Matter Halos by Galaxy Disks, *ApJ* 720, L62
- Kazantzidis, S., Kravtsov, A.V., Zentner, A.R., Allgood, B., Nagai, D., Moore, B., 2004, The Effect of Gas Cooling on the Shapes of Dark Matter Halos, *ApJ* 611, L73
- Keeton, C.R., 2001, Cold Dark Matter and Strong Gravitational Lensing: Concord or Conflict?, *ApJ* 561, 46
- Keeton, C.R., Kochanek, C.S., Seljak, U., 1997, Shear and Ellipticity in Gravitational Lenses, *ApJ* 482, 604
- Kennicutt, R.C., 1983, On the evolution of the spiral galaxies in the Virgo cluster, *AJ* 88, 483
- Kent, S.M., 1986, Dark matter in spiral galaxies. I - Galaxies with optical rotation curves, *AJ* 91, 1301
- Kent, S.M., 1987, Dark matter in spiral galaxies. II - Galaxies with H I rotation curves, *AJ* 93, 816
- Kent, S.M., 1992, Galactic structure from the spacelab infrared telescope. III - A dynamical model for the Milky Way bulge, *ApJ* 387, 181

- Kent, S.M., Dame, T.M., Fazio, G., 1991, Galactic structure from the Spacelab infrared telescope. II - Luminosity models of the Milky Way, *ApJ* 378, 131
- Kerr, F.J., Bowers, P.F., Jackson, P.D., Kerr, M., 1986, Fully sampled neutral hydrogen survey of the southern Milky Way, *A&AS* 66, 373
- Kleinheinrich, M., Schneider, P., Rix, H., Erben, T., Wolf, C., Schirmer, M., Meisenheimer, K., Borch, A., Dye, S., Kovacs, Z., Wisotzki, L., 2006, Weak lensing measurements of dark matter halos of galaxies from COMBO-17, *Astron. Astrophys.* 455, 441
- Klimentowski, J., Lokas, E.L., Kazantzidis, S., Mayer, L., Mamon, G.A., Prada, F., 2009, The orientation and kinematics of inner tidal tails around dwarf galaxies orbiting the Milky Way, *MNRAS* 400, 2162
- Klimentowski, J., Lokas, E.L., Kazantzidis, S., Prada, F., Mayer, L., Mamon, G.A., 2007, Mass modelling of dwarf spheroidal galaxies: the effect of unbound stars from tidal tails and the Milky Way, *MNRAS* 378, 353
- Klypin, A., Prada, F., 2009, Testing Gravity With Motion of Satellites Around Galaxies: Newtonian Gravity Against Modified Newtonian Dynamics, *ApJ* 690, 1488
- Klypin, A., Zhao, H., Somerville, R.S., 2002,  $\Lambda$ CDM-based Models for the Milky Way and M31. I. Dynamical Models, *ApJ* 573, 597
- Knapp, G.R., Turner, E.L., Cunniffe, P.E., 1985, The statistical distribution of the neutral-hydrogen content of elliptical galaxies, *AJ* 90, 454
- Kochanek, C.S., 1991, The implications of lenses for galaxy structure, *ApJ* 373, 354
- Kochanek, C.S., 1996, The Mass of the Milky Way, *ApJ* 457, 228
- Kochanek, C.S., 2006, Strong Gravitational Lensing, p. 91
- Kochanek, C.S., Dalal, N., 2004, Tests for Substructure in Gravitational Lenses, *ApJ* 610, 69
- Koopmans, L., 2004, Dark-Matter and Baryons in Early-type Lens Galaxies, in: Dettmar, R., Klein, U., Salucci, P. (eds.), *Baryons in Dark Matter Halos*
- Koopmans, L.V.E., 2005, Gravitational imaging of cold dark matter substructures, *MNRAS* 363, 1136
- Koopmans, L.V.E., Biggs, A., Blandford, R.D., Browne, I.W.A., Jackson, N.J., Mao, S., Wilkinson, P.N., de Bruyn, A.G., Wambsganss, J., 2003, Extrinsic Radio Variability of JVAs/CLASS Gravitational Lenses, *ApJ* 595, 712
- Koopmans, L.V.E., Bolton, A., Treu, T., Czoske, O., Auger, M.W., Barnabè, M., Vegetti, S., Gavazzi, R., Moustakas, L.A., Burles, S., 2009, The Structure and Dynamics of Massive Early-Type Galaxies: On Homology, Isothermality, and Isotropy Inside One Effective Radius, *ApJ* 703, L51
- Koopmans, L.V.E., de Bruyn, A.G., Jackson, N., 1998, The edge-on spiral gravitational lens B1600+434, *MNRAS* 295, 534
- Koopmans, L.V.E., Treu, T., 2002, The Stellar Velocity Dispersion of the Lens Galaxy in MG 2016+112 at  $z=1.004$ , *ApJ* 568, L5

- Koopmans, L.V.E., Treu, T., 2003, The Structure and Dynamics of Luminous and Dark Matter in the Early-Type Lens Galaxy of 0047-281 at  $z = 0.485$ , ApJ 583, 606
- Koopmans, L.V.E., Treu, T., Bolton, A.S., Burles, S., Moustakas, L.A., 2006, The Sloan Lens ACS Survey. III. The Structure and Formation of Early-Type Galaxies and Their Evolution since  $z \sim 1$ , ApJ 649, 599
- Koposov, S.E., Rix, H.W., Hogg, D.W., 2010, Constraining the Milky Way Potential with a Six-Dimensional Phase-Space Map of the GD-1 Stellar Stream, ApJ 712, 260
- Kormendy, J., Fisher, D.B., Cornell, M.E., Bender, R., 2009, Structure and Formation of Elliptical and Spheroidal Galaxies, ApJS 182, 216
- Kormendy, J., Ho, L.C., 2013, Coevolution (Or Not) of Supermassive Black Holes and Host Galaxies, ARA&A 51, 511
- Krajnović, D., Cappellari, M., Emsellem, E., McDermid, R.M., de Zeeuw, P.T., 2005, Dynamical modelling of stars and gas in NGC 2974: determination of mass-to-light ratio, inclination and orbital structure using the Schwarzschild method, MNRAS 357, 1113
- Krajnović, D., Emsellem, E., Cappellari, M., Alatalo, K., Blitz, L., Bois, M., Bournaud, F., Bureau, M., Davies, R.L., Davis, T.A., de Zeeuw, P.T., Khochfar, S., Kuntschner, H., Lablanche, P.Y., McDermid, R.M., Morganti, R., Naab, T., Oosterloo, T., Sarzi, M., Scott, N., Serra, P., Weijmans, A.M., Young, L.M., 2011, The ATLAS<sup>3D</sup> project - II. Morphologies, kinematic features and alignment between photometric and kinematic axes of early-type galaxies, MNRAS 414, 2923
- Krancz, T., Slyz, A., Rix, H.W., 2003, Dark Matter within High Surface Brightness Spiral Galaxies, ApJ 586, 143
- Kravtsov, A.V., Klypin, A.A., Bullock, J.S., Primack, J.R., 1998, The Cores of Dark Matter-dominated Galaxies: Theory versus Observations, ApJ 502, 48
- Kregel, M., van der Kruit, P.C., Freeman, K.C., 2005, Structure and kinematics of edge-on galaxy discs - V. The dynamics of stellar discs, MNRAS 358, 503
- Kronawitter, A., Saglia, R.P., Gerhard, O., Bender, R., 2000, Orbital structure and mass distribution in elliptical galaxies, A&AS 144, 53
- Kroupa, P., 2001, On the variation of the initial mass function, MNRAS 322, 231
- Kuijken, K., 1995, An Axisymmetric Distribution Function for the Galactic Bulge, ApJ 446, 194
- Kuijken, K., Gilmore, G., 1989, The Mass Distribution in the Galactic Disc - II - Determination of the Surface Mass Density of the Galactic Disc Near the Sun, MNRAS 239, 605
- Kuzio de Naray, R., Arsenault, C.A., Spekkens, K., Sellwood, J.A., McDonald, M., Simon, J.D., Teuben, P., 2012, Searching for non-axisymmetries in NGC 6503: a weak end-on bar, MNRAS 427, 2523

- Lablanche, P.Y., Cappellari, M., Emsellem, E., Bournaud, F., Michel-Dansac, L., Alatalo, K., Blitz, L., Bois, M., Bureau, M., Davies, R.L., Davis, T.A., de Zeeuw, P.T., Duc, P.A., Khochfar, S., Krajnović, D., Kuntschner, H., Morganti, R., McDermid, R.M., Naab, T., Oosterloo, T., Sarzi, M., Scott, N., Serra, P., Weijmans, A.M., Young, L.M., 2012, The ATLAS 3D project - XII. Recovery of the mass-to-light ratio of simulated early-type barred galaxies with axisymmetric dynamical models, MNRAS 424, 1495
- Lacy, J.H., Townes, C.H., Hollenbach, D.J., 1982, The nature of the central parsec of the Galaxy, ApJ 262, 120
- Lagattuta, D.J., Fassnacht, C.D., Auger, M.W., Marshall, P.J., Bradač, M., Treu, T., Gavazzi, R., Schrabbach, T., Faure, C., Anguita, T., 2010, Cosmic Evolution of Virial and Stellar Mass in Massive Early-type Galaxies, ApJ 716, 1579
- Laureijs, R., Amiaux, J., Arduini, S., Auguères, J., Brinchmann, J., Cole, R., Cropper, M., Dabin, C., Duvet, L., Ealet, A., et al., 2011, Euclid Definition Study Report, arXiv:1110.3193
- Leauthaud, A., Tinker, J., Behroozi, P.S., Busha, M.T., Wechsler, R.H., 2011, A Theoretical Framework for Combining Techniques that Probe the Link Between Galaxies and Dark Matter, ApJ 738, 45
- Leauthaud, A., Tinker, J., Bundy, K., Behroozi, P.S., Massey, R., Rhodes, J., George, M.R., Kneib, J.P., Benson, A., Wechsler, R.H., Busha, M.T., Capak, P., Cortés, M., Ilbert, O., Koekemoer, A.M., Le Fèvre, O., Lilly, S., McCracken, H.J., Salvato, M., Schrabbach, T., Scoville, N., Smith, T., Taylor, J.E., 2012, New Constraints on the Evolution of the Stellar-to-dark Matter Connection: A Combined Analysis of Galaxy-Galaxy Lensing, Clustering, and Stellar Mass Functions from  $z = 0.2$  to  $z = 1$ , ApJ 744, 159
- Lee, M.G., Park, H.S., Hwang, H.S., Arimoto, N., Tamura, N., Onodera, M., 2010, The Globular Cluster System of the Virgo Giant Elliptical Galaxy NGC 4636. II. Kinematics of the Globular Cluster System, ApJ 709, 1083
- Leitherer, C., Ekström, S., 2012, Population synthesis at the crossroads, in: Tuffs, R.J., Popescu, C.C. (eds.), IAU Symposium, vol. 284 of IAU Symposium, p. 2
- Leonard, P.J.T., Merritt, D., 1989, The mass of the open star cluster M35 as derived from proper motions, ApJ 339, 195
- Lewin, J.D., Smith, P.F., 1996, Review of mathematics, numerical factors, and corrections for dark matter experiments based on elastic nuclear recoil, Astroparticle Physics 6, 87
- Limousin, M., Kneib, J.P., Bardeau, S., Natarajan, P., Czoske, O., Smail, I., Ebeling, H., Smith, G.P., 2007, Truncation of galaxy dark matter halos in high density environments, Astron. Astrophys. 461, 881
- Lin, H., Buckley-Geer, E., Allam, S.S., Tucker, D.L., Diehl, H.T., Kubik, D., Kubo, J.M., Annis, J., Frieman, J.A., Oguri, M., Inada, N., 2009, Discovery of a Very Bright, Strongly Lensed  $z = 2$  Galaxy in the SDSS DR5, ApJ 699, 1242
- Lindblad, P.A.B., Lindblad, P.O., Athanassoula, E., 1996, Hydrodynamical simulations of the barred spiral galaxy NGC 1365. Dynamical interpretation of observations., A&A 313, 65

- Little, B., Tremaine, S., 1987, Distant satellites as probes of our Galaxy's mass distribution, *ApJ* 320, 493
- Loewenstein, M., White, III, R.E., 1999, Prevalence and Properties of Dark Matter in Elliptical Galaxies, *ApJ* 518, 50
- Lokas, E.L., 2002, Dark matter distribution in dwarf spheroidal galaxies, *MNRAS* 333, 697
- Lokas, E.L., Mamon, G.A., 2003, Dark matter distribution in the Coma cluster from galaxy kinematics: breaking the mass-anisotropy degeneracy, *MNRAS* 343, 401
- Lokas, E.L., Mamon, G.A., Prada, F., 2005, Dark matter distribution in the Draco dwarf from velocity moments, *MNRAS* 363, 918
- Long, R.J., Mao, S., 2010, Made-to-measure galaxy models - I. Methodology, *MNRAS* 405, 301
- Lynden-Bell, D., Cannon, R.D., Godwin, P.J., 1983, Slippery evidence on the Galaxy's invisible heavy halo, *MNRAS* 204, 87P
- Lyubenova, M., Kuntschner, H., Rejkuba, M., Silva, D.R., Kissler-Patig, M., Tacconi-Garman, L.E., 2012, Integrated J- and H-band spectra of globular clusters in the LMC: implications for stellar population models and galaxy age dating, *A&A* 543, A75
- MacArthur, L.A., 2005, Dust Sensitivity of Absorption-Line Indices, *ApJ* 623, 795
- MacArthur, L.A., Courteau, S., Bell, E., Holtzman, J.A., 2004, Structure of Disk-dominated Galaxies. II. Color Gradients and Stellar Population Models, *ApJS* 152, 175
- MacArthur, L.A., González, J.J., Courteau, S., 2009, Stellar population and kinematic profiles in spiral bulges and discs: population synthesis of integrated spectra, *MNRAS* 395, 28
- MacArthur, L.A., McDonald, M., Courteau, S., Jesús González, J., 2010, Integrated Stellar Populations: Confronting Photometry with Spectroscopy, *ApJ* 718, 768
- Macciò, A.V., Dutton, A.A., van den Bosch, F.C., 2008, Concentration, spin and shape of dark matter haloes as a function of the cosmological model: WMAP1, WMAP3 and WMAP5 results, *MNRAS* 391, 1940
- Macciò, A.V., Moore, B., Stadel, J., Diemand, J., 2006, Radial distribution and strong lensing statistics of satellite galaxies and substructure using high-resolution  $\Lambda$ CDM hydrodynamical simulations, *MNRAS* 366, 1529
- Macciò, A.V., Stinson, G., Brook, C.B., Wadsley, J., Couchman, H.M.P., Shen, S., Gibson, B.K., Quinn, T., 2012, Halo Expansion in Cosmological Hydro Simulations: Toward a Baryonic Solution of the Cusp/Core Problem in Massive Spirals, *ApJ* 744, L9
- Magorrian, J., 1995, Reconstructing Two-Integral Distribution Functions from Moments, *MNRAS* 277, 1185
- Magorrian, J., 2013, Bayes versus the virial theorem: inferring the potential of a galaxy from a kinematical snapshot, arXiv:1303.6099

- Magorrian, J., Ballantyne, D., 2001, Mass profiles and anisotropies of early-type galaxies, MNRAS 322, 702
- Magorrian, J., Binney, J., 1994, Predicting line-of-sight velocity distributions of elliptical galaxies, MNRAS 271, 949
- Malhotra, S., 1995, The Vertical Distribution and Kinematics of H i and Mass Models of the Galactic Disk, ApJ 448, 138
- Maller, A.H., Simard, L., Guhathakurta, P., Hjorth, J., Jaunsen, A.O., Flores, R.A., Primack, J.R., 2000, Breaking the Disk/Halo Degeneracy with Gravitational Lensing, ApJ 533, 194
- Mamon, G.A., Biviano, A., Boué, G., 2013, MAMPOSSt: Modelling Anisotropy and Mass Profiles of Observed Spherical Systems - I. Gaussian 3D velocities, MNRAS 429, 3079
- Mamon, G.A., Boué, G., 2010, Kinematic deprojection and mass inversion of spherical systems of known velocity anisotropy, MNRAS 401, 2433
- Mamon, G.A., Łokas, E., Dekel, A., Stoehr, F., Cox, T.J., 2006, Kinematical and Dynamical Modeling of Elliptical Galaxies, in: Mamon, G.A., Combes, F., Deffayet, C., Fort, B. (eds.), , EAS Publications Series, vol. 20 of EAS Publications Series, p. 139
- Mamon, G.A., Łokas, E.L., 2005a, Dark matter in elliptical galaxies - I. Is the total mass density profile of the NFW form or even steeper?, MNRAS 362, 95
- Mamon, G.A., Łokas, E.L., 2005b, Dark matter in elliptical galaxies: II. Estimating the mass within the virial radius, MNRAS 363, 705
- Mamon, G.A., Łokas, E.L., 2006, Erratum: Dark matter in elliptical galaxies - I. Is the total mass density profile of the NFW form or even steeper?, MNRAS 370, 1581
- Mandelbaum, R., Hirata, C.M., Broderick, T., Seljak, U., Brinkmann, J., 2006a, Ellipticity of dark matter haloes with galaxy-galaxy weak lensing, MNRAS 370, 1008
- Mandelbaum, R., Seljak, U., Kauffmann, G., Hirata, C.M., Brinkmann, J., 2006b, Galaxy halo masses and satellite fractions from galaxy-galaxy lensing in the Sloan Digital Sky Survey: stellar mass, luminosity, morphology and environment dependencies, MNRAS 368, 715
- Mao, S., Jing, Y., Ostriker, J.P., Weller, J., 2004, Anomalous Flux Ratios in Gravitational Lenses: For or against Cold Dark Matter?, ApJ 604, L5
- Mao, S., Schneider, P., 1998, Evidence for substructure in lens galaxies?, MNRAS 295, 587
- Maraston, C., 1998, Evolutionary synthesis of stellar populations: a modular tool, MNRAS 300, 872
- Maraston, C., 2005, Evolutionary population synthesis: models, analysis of the ingredients and application to high-z galaxies, MNRAS 362, 799
- Maraston, C., Daddi, E., Renzini, A., et al., 2006, Evidence for TP-AGB Stars in High-Redshift Galaxies, and Their Effect on Deriving Stellar Population Parameters, ApJ 652, 85

- Maraston, C., Greggio, L., Renzini, A., Ortolani, S., Saglia, R.P., Puzia, T.H., Kissler-Patig, M., 2003, Integrated spectroscopy of bulge globular clusters and fields. II. Implications for population synthesis models and elliptical galaxies, *A&A* 400, 823
- Maraston, C., Kissler-Patig, M., Brodie, J.P., Barmby, P., Huchra, J.P., 2001, The AGB phase-transition outside the local group: K-band observations of young star clusters in NGC 7252, *A&A* 370, 176
- Maraston, C., Pforr, J., Henriques, B.M., Thomas, D., Wake, D., Brownstein, J.R., Capozzi, D., Bundy, K., Skibba, R.A., Beifiori, A., Nichol, R.C., Edmondson, E., Schneider, D.P., Chen, Y., Masters, K.L., Steele, O., Bolton, A.S., York, D.G., Bizyaev, D., Brewington, H., Malanushenko, E., Malanushenko, V., Snedden, S., Oravetz, D., Pan, K., Shelden, A., Simmons, A., 2012, Stellar masses of SDSS-III BOSS galaxies at  $z \sim 0.5$  and constraints to galaxy formation models, *MNRAS*, in press (arXiv:1207.6114)
- Maraston, C., Pforr, J., Renzini, A., Daddi, E., Dickinson, M., Cimatti, A., Tonini, C., 2010, Star formation rates and masses of  $z \sim 2$  galaxies from multicolour photometry, *MNRAS* 407, 830
- Maraston, C., Thomas, D., 2000, Strong Balmer Lines in Old Stellar Populations: No Need for Young Ages in Ellipticals?, *ApJ* 541, 126
- Marigo, P., Girardi, L., Bressan, A., Groenewegen, M.A.T., Silva, L., Granato, G.L., 2008, Evolution of asymptotic giant branch stars. II. Optical to far-infrared isochrones with improved TP-AGB models, *A&A* 482, 883
- Martinez, G.D., Minor, Q.E., Bullock, J., Kaplinghat, M., Simon, J.D., Geha, M., 2011, A Complete Spectroscopic Survey of the Milky Way Satellite Segue 1: Dark Matter Content, Stellar Membership, and Binary Properties from a Bayesian Analysis, *ApJ* 738, 55
- Martizzi, D., Teyssier, R., Moore, B., Wentz, T., 2012, The effects of baryon physics, black holes and active galactic nucleus feedback on the mass distribution in clusters of galaxies, *MNRAS* 422, 3081
- Mateo, M.L., 1998, Dwarf Galaxies of the Local Group, *ARA&A* 36, 435
- Mathewson, D.S., Ford, V.L., Buchhorn, M., 1992, A southern sky survey of the peculiar velocities of 1355 spiral galaxies, *ApJS* 81, 413
- McDonald, M., Courteau, S., Tully, R.B., Roediger, J., 2011, A survey of 286 Virgo cluster galaxies at optical griz and near-IR H band: surface brightness profiles and bulge-disc decompositions, *MNRAS* 414, 2055
- McKay, T.A., Sheldon, E.S., Johnston, D., Grebel, E.K., Prada, F., Rix, H., Bahcall, N.A., Brinkmann, J., Csabai, I., Fukugita, M., Lamb, D.Q., York, D.G., 2002, Dynamical Confirmation of Sloan Digital Sky Survey Weak-lensing Scaling Laws, *ApJ* 571, L85
- McKay, T.A., Sheldon, E.S., Racusin, J., Fischer, P., Seljak, U., Stebbins, A., Johnston, D., Frieman, J.A., Bahcall, N., Brinkmann, J., Csabai, I., Fukugita, M., Hennessy, G.S., Ivezić, Z., Lamb, D.Q., Loveday, J., Lupton, R.H., Munn, J.A., Nichol, R.C., Pier, J.R., York, D.G., 2001, Galaxy Mass and Luminosity Scaling Laws Determined by Weak Gravitational Lensing, arXiv:astro-ph/0108013

- McMillan, P.J., Binney, J., 2012, Analysing surveys of our Galaxy - I. Basic astrometric data, MNRAS 419, 2251
- McMillan, P.J., Binney, J.J., 2013, Analysing surveys of our Galaxy - II. Determining the potential, MNRAS 433, 1411
- McNeil, E.K., Arnaboldi, M., Freeman, K.C., Gerhard, O.E., Coccato, L., Das, P., 2010, Counter-dispersed slitless-spectroscopy technique: planetary nebula velocities in the halo of NGC 1399, A&A 518, A44
- Ménard, B., Nestor, D., Turnshek, D., Quider, A., Richards, G., Chelouche, D., Rao, S., 2008, Lensing, reddening and extinction effects of MgII absorbers from  $z = 0.4$  to 2, MNRAS 385, 1053
- Méndez, R.H., Riffeser, A., Kudritzki, R.P., Matthias, M., Freeman, K.C., Arnaboldi, M., Capaccioli, M., Gerhard, O.E., 2001, Detection, Photometry, and Slitless Radial Velocities of 535 Planetary Nebulae in the Flattened Elliptical Galaxy NGC 4697, ApJ 563, 135
- Metcalf, R.B., Amara, A., 2012, Small-scale structures of dark matter and flux anomalies in quasar gravitational lenses, MNRAS 419, 3414
- Metcalf, R.B., Madau, P., 2001, Compound Gravitational Lensing as a Probe of Dark Matter Substructure within Galaxy Halos, ApJ 563, 9
- Michard, R., 1980, On the M/L ratios in elliptical galaxies, A&A 91, 122
- Milgrom, M., 1983, A modification of the Newtonian dynamics as a possible alternative to the hidden mass hypothesis, ApJ 270, 365
- Miyamoto, M., Nagai, R., 1975, Three-dimensional models for the distribution of mass in galaxies, PASJ 27, 533
- Mo, H., van den Bosch, F.C., White, S., 2010, Galaxy Formation and Evolution
- Moni Bidin, C., Carraro, G., Méndez, R.A., Smith, R., 2012, Kinematical and Chemical Vertical Structure of the Galactic Thick Disk. II. A Lack of Dark Matter in the Solar Neighborhood, ApJ 751, 30
- More, A., McKean, J.P., More, S., Porcas, R.W., Koopmans, L.V.E., Garrett, M.A., 2009, The role of luminous substructure in the gravitational lens system MG 2016+112, MNRAS 394, 174
- More, A., McKean, J.P., Muxlow, T.W.B., Porcas, R.W., Fassnacht, C.D., Koopmans, L.V.E., 2008, Probing a massive radio galaxy with gravitational lensing, MNRAS 384, 1701
- More, S., van den Bosch, F.C., Cacciato, M., Skibba, R., Mo, H.J., Yang, X., 2011a, Satellite kinematics - III. Halo masses of central galaxies in SDSS, MNRAS 410, 210
- More, S., van den Bosch, F.C., Cacciato, M., Skibba, R., Mo, H.J., Yang, X., 2011b, Satellite kinematics - III. Halo masses of central galaxies in SDSS, MNRAS 410, 210
- Morganti, L., Gerhard, O., 2012, Regularizing made-to-measure particle models of galaxies, MNRAS 422, 1571

- Morganti, R., de Zeeuw, P.T., Oosterloo, T.A., McDermid, R.M., Krajnović, D., Cappellari, M., Kenn, F., Weijmans, A., Sarzi, M., 2006, Neutral hydrogen in nearby elliptical and lenticular galaxies: the continuing formation of early-type galaxies, MNRAS 371, 157
- Murphy, J.D., Gebhardt, K., Adams, J.J., 2011, Galaxy Kinematics with VIRUS-P: The Dark Matter Halo of M87, ApJ 729, 129
- Nagai, R., Miyamoto, M., 1976, A family of self-gravitating stellar systems with axial symmetry, PASJ 28, 1
- Nagino, R., Matsushita, K., 2009, Gravitational potential and X-ray luminosities of early-type galaxies observed with XMM-Newton and Chandra, A&A 501, 157
- Napolitano, N.R., Romanowsky, A.J., Capaccioli, M., Douglas, N.G., Arnaboldi, M., Coccato, L., Gerhard, O., Kuijken, K., Merrifield, M.R., Bamford, S.P., Cortesi, A., Das, P., Freeman, K.C., 2011, The PN.S Elliptical Galaxy Survey: a standard  $\Lambda$ CDM halo around NGC 4374?, MNRAS 411, 2035
- Napolitano, N.R., Romanowsky, A.J., Coccato, L., Capaccioli, M., Douglas, N.G., Noordermeer, E., Gerhard, O., Arnaboldi, M., de Lorenzi, F., Kuijken, K., Merrifield, M.R., O'Sullivan, E., Cortesi, A., Das, P., Freeman, K.C., 2009, The Planetary Nebula Spectrograph elliptical galaxy survey: the dark matter in NGC 4494, MNRAS 393, 329
- Napolitano, N.R., Romanowsky, A.J., Tortora, C., 2010, The central dark matter content of early-type galaxies: scaling relations and connections with star formation histories, MNRAS 405, 2351
- Natarajan, P., Kneib, J., 1997, Lensing by galaxy haloes in clusters of galaxies, MNRAS 287, 833
- Natarajan, P., Kneib, J., Smail, I., Ellis, R.S., 1998, The Mass-to-Light Ratio of Early-Type Galaxies: Constraints from Gravitational Lensing in the Rich Cluster AC 114, ApJ 499, 600
- Natarajan, P., Kneib, J., Smail, I., Treu, T., Ellis, R., Moran, S., Limousin, M., Czoske, O., 2009, The Survival of Dark Matter Halos in the Cluster Cl 0024+16, ApJ 693, 970
- Navarro, J.F., Eke, V.R., Frenk, C.S., 1996a, The cores of dwarf galaxy haloes, MNRAS 283, L72
- Navarro, J.F., Frenk, C.S., White, S.D.M., 1996b, The Structure of Cold Dark Matter Halos, ApJ 462, 563
- Navarro, J.F., Frenk, C.S., White, S.D.M., 1997, A Universal Density Profile from Hierarchical Clustering, ApJ 490, 493
- Navarro, J.F., Hayashi, E., Power, C., Jenkins, A.R., Frenk, C.S., White, S.D.M., Springel, V., Stadel, J., Quinn, T.R., 2004, The inner structure of  $\Lambda$ CDM haloes - III. Universality and asymptotic slopes, MNRAS 349, 1039
- Navarro, J.F., Ludlow, A., Springel, V., Wang, J., Vogelsberger, M., White, S.D.M., Jenkins, A., Frenk, C.S., Helmi, A., 2010, The diversity and similarity of simulated cold dark matter haloes, MNRAS 402, 21
- Neto, A.F., Gao, L., Bett, P., Cole, S., Navarro, J.F., Frenk, C.S., White, S.D.M., Springel, V., Jenkins, A., 2007, The statistics of  $\Lambda$  CDM halo concentrations, MNRAS 381, 1450

- Neumayer, N., 2010, The Supermassive Black Hole at the Heart of Centaurus A: Revealed by the Kinematics of Gas and Stars, PASA 27, 449
- Newton, A.J., Binney, J., 1984, Constructing distribution functions for spherical galaxies, MNRAS 210, 711
- Newton, E.R., Marshall, P.J., Treu, T., Auger, M.W., Gavazzi, R., Bolton, A.S., Koopmans, L.V.E., Moustakas, L.A., 2011, The Sloan Lens ACS Survey. XI. Beyond Hubble Resolution: Size, Luminosity, and Stellar Mass of Compact Lensed Galaxies at Intermediate Redshift, ApJ 734, 104
- Nierenberg, A.M., Auger, M.W., Treu, T., Marshall, P.J., Fassnacht, C.D., Busha, M.T., 2012, Luminous Satellites. II. Spatial Distribution, Luminosity Function, and Cosmic Evolution, ApJ 752, 99
- Noordermeer, E., Merrifield, M.R., Aragón-Salamanca, A., 2008, Exploring disc galaxy dynamics using integral field unit data, MNRAS 388, 1381
- Noordermeer, E., van der Hulst, J.M., Sancisi, R., Swaters, R.S., van Albada, T.S., 2007, The mass distribution in early-type disc galaxies: declining rotation curves and correlations with optical properties, MNRAS 376, 1513
- Nordsieck, K.H., 1973, The Angular Momentum of Spiral Galaxies. Methods of Rotation-Curve Analysis, ApJ 184, 719
- O'Connell, R.W., 1976, Galaxy spectral synthesis. I - Stellar populations in the nuclei of giant ellipticals, ApJ 206, 370
- Oort, J.H., 1926, Asymmetry in the distribution of stellar velocities, The Observatory, Vol. 49, p. 302-304 (1926) 49, 302
- Oort, J.H., 1932, The force exerted by the stellar system in the direction perpendicular to the galactic plane and some related problems, Bull. Astron. Inst. Netherlands 6, 249
- Oort, J.H., 1940, Some Problems Concerning the Structure and Dynamics of the Galactic System and the Elliptical Nebulae NGC 3115 and 4494., ApJ 91, 273
- Oort, J.H., 1965, Stellar Dynamics, in: Blaauw, A., Schmidt, M. (eds.), Galactic Structure, p. 455
- Opik, E., 1922, An estimate of the distance of the Andromeda Nebula., ApJ 55, 406
- Ostriker, J.P., Peebles, P.J.E., 1973, A Numerical Study of the Stability of Flattened Galaxies: or, can Cold Galaxies Survive?, ApJ 186, 467
- Padmanabhan, N., Seljak, U., Strauss, M.A., Blanton, M.R., Kauffmann, G., Schlegel, D.J., Tremonti, C., Bahcall, N.A., Bernardi, M., Brinkmann, J., Fukugita, M., Ivezić, Ž., 2004, Stellar and dynamical masses of ellipticals in the Sloan Digital Sky Survey, New Astronomy 9, 329
- Panter, B., Jimenez, R., Heavens, A.F., Charlot, S., 2007, The star formation histories of galaxies in the Sloan Digital Sky Survey, MNRAS 378, 1550
- Papastergis, E., Cattaneo, A., Huang, S., Giovanelli, R., Haynes, M.P., 2012, A Direct Measurement of the Baryonic Mass Function of Galaxies and Implications for the Galactic Baryon Fraction, ApJ 759, 138

- Papastergis, E., Martin, A.M., Giovanelli, R., Haynes, M.P., 2011, The Velocity Width Function of Galaxies from the 40% ALFALFA Survey: Shedding Light on the Cold Dark Matter Overabundance Problem, *ApJ* 739, 38
- Parker, L.C., Hoekstra, H., Hudson, M.J., van Waerbeke, L., Mellier, Y., 2007, The Masses and Shapes of Dark Matter Halos from Galaxy-Galaxy Lensing in the CFHT Legacy Survey, *ApJ* 669, 21
- Pease, F.G., 1918, The Rotation and Radial Velocity of the Central Part of the Andromeda nebula, *Proceedings of the National Academy of Science* 4, 21
- Peebles, P.J.E., 1989, Tracing galaxy orbits back in time, *ApJ* 344, L53
- Pen, U., 1998, Reconstructing Nonlinear Stochastic Bias from Velocity Space Distortions, *ApJ* 504, 601
- Perryman, M.A.C., de Boer, K.S., Gilmore, G., et al., 2001, GAIA: Composition, formation and evolution of the Galaxy, *A&A* 369, 339
- Pforr, J., Maraston, C., Tonini, C., 2012, Recovering galaxy stellar population properties from broadband spectral energy distribution fitting, *MNRAS* 422, 3285
- Phelps, S., Nusser, A., Desjacques, V., 2013, The mass of the Milky Way and M31 using the method of least action, *arXiv:1306.4013*
- Pickles, A.J., 1985, Differential population synthesis of early-type galaxies. III - Synthesis results, *ApJ* 296, 340
- Pierce, M., Beasley, M.A., Forbes, D.A., et al., 2006, Gemini/GMOS spectra of globular clusters in the Leo group elliptical NGC 3379, *MNRAS* 366, 1253
- Pizzella, A., Corsini, E.M., Vega Beltrán, J.C., Bertola, F., 2004, Ionized gas and stellar kinematics of seventeen nearby spiral galaxies, *A&A* 424, 447
- Pontzen, A., Governato, F., 2012, How supernova feedback turns dark matter cusps into cores, *MNRAS* 421, 3464
- Poveda, A., 1958, The Masses of Spherical Galaxies M32. A likely application, *Boletin de los Observatorios Tonantzintla y Tacubaya* 2, 3
- Pozzetti, L., Bolzonella, M., Zucca, E., Zamorani, G., Lilly, S., Renzini, A., Moresco, M., Mignoli, M., Cassata, P., Tasca, L., Lamareille, F., Maier, C., Meneux, B., Halliday, C., Oesch, P., Vergani, D., Caputi, K., Kovač, K., Cimatti, A., Cucciati, O., Iovino, A., Peng, Y., Carollo, M., Contini, T., Kneib, J.P., Le Févre, O., Mainieri, V., Scudeggio, M., Bardelli, S., Bongiorno, A., Coppa, G., de la Torre, S., de Ravel, L., Franzetti, P., Garilli, B., Kampczyk, P., Knobel, C., Le Borgne, J.F., Le Brun, V., Pellò, R., Perez Montero, E., Ricciardelli, E., Silverman, J.D., Tanaka, M., Tresse, L., Abbas, U., Bottini, D., Cappi, A., Guzzo, L., Koekemoer, A.M., Leauthaud, A., Maccagni, D., Marinoni, C., McCracken, H.J., Memeo, P., Porciani, C., Scaramella, R., Scarlata, C., Scoville, N., 2010, zCOSMOS - 10k-bright spectroscopic sample. The bimodality in the galaxy stellar mass function: exploring its evolution with redshift, *A&A* 523, A13
- Prada, F., Klypin, A.A., Simonneau, E., Betancort-Rijo, J., Patiri, S., Gottlöber, S., Sanchez-Conde, M.A., 2006, How Far Do They Go? The Outer Structure of Galactic Dark Matter Halos, *ApJ* 645, 1001

- Prada, F., Vitvitska, M., Klypin, A., Holtzman, J.A., Schlegel, D.J., Grebel, E.K., Rix, H.W., Brinkmann, J., McKay, T.A., Csabai, I., 2003, Observing the Dark Matter Density Profile of Isolated Galaxies, *ApJ* 598, 260
- Press, W.H., Schechter, P., 1974, Formation of Galaxies and Clusters of Galaxies by Self-Similar Gravitational Condensation, *ApJ* 187, 425
- Proctor, R.N., Forbes, D.A., Romanowsky, A.J., Brodie, J.P., Strader, J., Spolaor, M., Mendel, J.T., Spitler, L., 2009, Probing the 2D kinematic structure of early-type galaxies out to three effective radii, *MNRAS* 398, 91
- Prugniel, P., Simien, F., 1997, The fundamental plane of early-type galaxies: non-homology of the spatial structure., *A&A* 321, 111
- Read, J.I., Lake, G., Agertz, O., Debattista, V.P., 2008, Thin, thick and dark discs in  $\Lambda$ CDM, *MNRAS* 389, 1041
- Reid, M.J., Menten, K.M., Zheng, X.W., et al., 2009, Trigonometric Parallaxes of Massive Star-Forming Regions. VI. Galactic Structure, Fundamental Parameters, and Noncircular Motions, *ApJ* 700, 137
- Remus, R.S., Burkert, A., Dolag, K., Johansson, P.H., Naab, T., Oser, L., Thomas, J., 2013, The Dark Halo—Spheroid Conspiracy and the Origin of Elliptical Galaxies, *ApJ* 766, 71
- Renzini, A., 1981, Energetics of stellar populations., *Annales de Physique* 6, 87
- Renzini, A., Buzzoni, A., 1986, Global properties of stellar populations and the spectral evolution of galaxies, Spectral evolution of galaxies; Proceedings of the Fourth Workshop, Erice, Italy, March 12-22, 1985 (A87-20001 07-90). Dordrecht, D. Reidel Publishing Co., 1986, p. 195-231; Discussion, p. 232-235. 122, 195
- Renzini, A., Ciotti, L., 1993, Transverse Dissections of the Fundamental Planes of Elliptical Galaxies and Clusters of Galaxies, *ApJ* 416, L49
- Renzini, A., Voli, M., 1981, Advanced evolutionary stages of intermediate-mass stars. I - Evolution of surface compositions, *A&A* 94, 175
- Reyes, R., Mandelbaum, R., Gunn, J.E., Pizagno, J., Lackner, C.N., 2011, Calibrated Tully-Fisher relations for improved estimates of disc rotation velocities, *MNRAS* 417, 2347
- Reyes, R., Mandelbaum, R., Seljak, U., Baldauf, T., Gunn, J.E., Lombriser, L., Smith, R.E., 2010, Confirmation of general relativity on large scales from weak lensing and galaxy velocities, *Nature* 464, 256
- Rhee, G., Valenzuela, O., Klypin, A., Holtzman, J., Moorthy, B., 2004, The Rotation Curves of Dwarf Galaxies: A Problem for Cold Dark Matter?, *ApJ* 617, 1059
- Richardson, T., Fairbairn, M., 2013a, Analytical solutions to the mass-anisotropy degeneracy with higher order Jeans analysis: a general method, *MNRAS* 432, 3361

- Richardson, T., Fairbairn, M., 2013b, Cores in Classical Dwarf Spheroidal Galaxies? A Dispersion-Kurtosis Jeans Analysis Without Restricted Anisotropy, MNRAS , submitted (arXiv:1305.0670 , submitted, arXiv:1305.0670
- Richstone, D.O., 1984, Scale-free models of galaxies. III - A survey of the oblate E6 solution set, ApJ 281, 100
- Richstone, D.O., Tremaine, S., 1984, A general method for constructing spherical galaxy models, ApJ 286, 27
- Roberts, M.S., Whitehurst, R.N., 1975, The rotation curve and geometry of M31 at large galactocentric distances., ApJ 201, 327
- Roediger, J.C., Courteau, S., MacArthur, L.A., McDonald, M., 2011, The formation and evolution of Virgo cluster galaxies - II. Stellar populations, MNRAS 416, 1996
- Rogstad, D.H., Shostak, G.S., 1972, Gross Properties of Five Scd Galaxies as Determined from 21-CENTIMETER Observations, ApJ 176, 315
- Romanowsky, A.J., Douglas, N.G., Arnaboldi, M., Kuijken, K., Merrifield, M.R., Napolitano, N.R., Capaccioli, M., Freeman, K.C., 2003, A Dearth of Dark Matter in Ordinary Elliptical Galaxies, Science 301, 1696
- Romanowsky, A.J., Strader, J., Spitler, L.R., Johnson, R., Brodie, J.P., Forbes, D.A., Ponman, T., 2009, Mapping The Dark Side with DEIMOS: Globular Clusters, X-Ray Gas, and Dark Matter in the NGC 1407 Group, AJ 137, 4956
- Rubin, V.C., Burley, J., Kiasatpoor, A., Klock, B., Pease, G., Rutscheidt, E., Smith, C., 1962, Kinematic studies of early-type stars. I. Photometric survey, space motions, and comparison with radio observations., AJ 67, 491
- Rubin, V.C., Burstein, D., Ford, Jr., W.K., Thonnard, N., 1985, Rotation velocities of 16 SA galaxies and a comparison of Sa, Sb, and SC rotation properties, ApJ 289, 81
- Rubin, V.C., Ford, Jr., W.K., 1970, Rotation of the Andromeda Nebula from a Spectroscopic Survey of Emission Regions, ApJ 159, 379
- Ruff, A.J., Gavazzi, R., Marshall, P.J., Treu, T., Auger, M.W., Brault, F., 2011, The SL2S Galaxy-scale Lens Sample. II. Cosmic Evolution of Dark and Luminous Mass in Early-type Galaxies, ApJ 727, 96
- Rupen, M.P., 1991, Neutral hydrogen observations of NGC 4565 and NGC 891, AJ 102, 48
- Sackett, P.D., 1997, Does the Milky Way Have a Maximal Disk?, ApJ 483, 103
- Sage, L.J., Welch, G.A., Young, L.M., 2007, The Cool ISM in Elliptical Galaxies. I. A Survey of Molecular Gas, ApJ 657, 232
- Saglia, R.P., Bertin, G., Stiavelli, M., 1992, Elliptical Galaxies with Dark Matter. II. Optimal Luminous-Dark Matter Decomposition for a Sample of Bright Objects, ApJ 384, 433

- Saha, P., Coles, J., Macciò, A.V., Williams, L.L.R., 2006, The Hubble Time Inferred from 10 Time Delay Lenses, *ApJ* 650, L17
- Salpeter, E.E., 1955, The Luminosity Function and Stellar Evolution., *ApJ* 121, 161
- Sambhus, N., Gerhard, O., Méndez, R.H., 2006, Kinematic Evidence for Different Planetary Nebula Populations in the Elliptical Galaxy NGC 4697, *AJ* 131, 837
- Sánchez, S.F., Kennicutt, R.C., Gil de Paz, A., van de Ven, G., Vílchez, J.M., Wisotzki, L., Walcher, C.J., Mast, D., Aguerri, J.A.L., Albiol-Pérez, S., Alonso-Herrero, A., Alves, J., Bakos, J., Bartáková, T., Bland-Hawthorn, J., Boselli, A., Bomans, D.J., Castillo-Morales, A., Cortijo-Ferrero, C., de Lorenzo-Cáceres, A., Del Olmo, A., Dettmar, R.J., Díaz, A., Ellis, S., Falcón-Barroso, J., Flores, H., Gallazzi, A., García-Lorenzo, B., González Delgado, R., Gruel, N., Haines, T., Hao, C., Husemann, B., Iglésias-Páramo, J., Jahnke, K., Johnson, B., Jungwiert, B., Kalinova, V., Kehrig, C., Kupko, D., López-Sánchez, Á.R., Lyubenova, M., Marino, R.A., Mármlor-Queraltó, E., Márquez, I., Masegosa, J., Meidt, S., Mendez-Abreu, J., Monreal-Ibero, A., Montijo, C., Mourão, A.M., Palacios-Navarro, G., Papaderos, P., Pasquali, A., Peletier, R., Pérez, E., Pérez, I., Quirrenbach, A., Relaño, M., Rosales-Ortega, F.F., Roth, M.M., Ruiz-Lara, T., Sánchez-Blázquez, P., Sengupta, C., Singh, R., Stanishev, V., Trager, S.C., Vazdekis, A., Viironen, K., Wild, V., Zibetti, S., Ziegler, B., 2012, CALIFA, the Calar Alto Legacy Integral Field Area survey. I. Survey presentation, *A&A* 538, A8
- Sanchis, T., Łokas, E.L., Mamon, G.A., 2004, The reliability of the kinematical evidence for dark matter: the effects of non-sphericity, substructure and streaming motions, *MNRAS* 347, 1198
- Sandage, A., 1986a, Star formation rates, galaxy morphology, and the Hubble sequence, *A&A* 161, 89
- Sandage, A., 1986b, The redshift-distance relation. IX - Perturbation of the very nearby velocity field by the mass of the Local Group, *ApJ* 307, 1
- Sarzi, M., Falcón-Barroso, J., Davies, R.L., Bacon, R., Bureau, M., Cappellari, M., de Zeeuw, P.T., Emsellem, E., Fathi, K., Krajnović, D., Kuntschner, H., McDermid, R.M., Peletier, R.F., 2006, The SAURON project - V. Integral-field emission-line kinematics of 48 elliptical and lenticular galaxies, *MNRAS* 366, 1151
- Satoh, C., 1980, Dynamical Models of Axisymmetric Galaxies and Their Applications to the Elliptical Galaxy NGC4697, *PASJ* 32, 41
- Scalo, J.M., 1986, The stellar initial mass function, *Fund. Cosmic Phys.* 11, 1
- Scheiner, J., 1899, On the spectrum of the great nebula in Andromeda., *ApJ* 9, 149
- Schneider, P., 1985, A new formulation of gravitational lens theory, time-delay, and Fermat's principle, *A&A* 143, 413
- Schneider, P., 2006a, Part 1: Introduction to gravitational lensing and cosmology, in: Meylan, G., Jetzer, P., North, P., Schneider, P., Kochanek, C.S., Wambsganss, J. (eds.), Saas-Fee Advanced Course 33: Gravitational Lensing: Strong, Weak and Micro, p. 1
- Schneider, P., 2006b, Part 3: Weak gravitational lensing, in: G. Meylan, P. Jetzer, P. North, P. Schneider, C. S. Kochanek, & J. Wambsganss (ed.), Saas-Fee Advanced Course 33: Gravitational Lensing: Strong, Weak and Micro, p. 269

- Schneider, P., Ehlers, J., Falco, E.E., 1992, *Gravitational Lenses*
- Schönrich, R., 2012, Galactic rotation and solar motion from stellar kinematics, MNRAS 427, 274
- Schuberth, Y., Richtler, T., Hilker, M., Dirsch, B., Bassino, L.P., Romanowsky, A.J., Infante, L., 2010, The globular cluster system of NGC 1399. V. dynamics of the cluster system out to 80 kpc, A&A 513, A52
- Schwarzchild, M., 1979, A numerical model for a triaxial stellar system in dynamical equilibrium, ApJ 232, 236
- Scott, N., Cappellari, M., Davies, R.L., Bacon, R., de Zeeuw, P.T., Emsellem, E., Falcón-Barroso, J., Krajnović, D., Kuntschner, H., McDermid, R.M., Peletier, R.F., Pipino, A., Sarzi, M., van den Bosch, R.C.E., van de Ven, G., van Scherpenzeel, E., 2009, The SAURON Project - XIV. No escape from  $V_{\text{esc}}$ : a global and local parameter in early-type galaxy evolution, MNRAS 398, 1835
- Scranton, R., Ménard, B., Richards, G.T., Nichol, R.C., Myers, A.D., Jain, B., Gray, A., Bartelmann, M., Brunner, R.J., Connolly, A.J., Gunn, J.E., Sheth, R.K., Bahcall, N.A., Brinkman, J., Loveday, J., Schneider, D.P., Thakar, A., York, D.G., 2005, Detection of Cosmic Magnification with the Sloan Digital Sky Survey, ApJ 633, 589
- Seljak, U., 2000, Analytic model for galaxy and dark matter clustering, MNRAS 318, 203
- Sellwood, J.A., 1985, The global stability of our Galaxy, MNRAS 217, 127
- Sellwood, J.A., McGaugh, S.S., 2005, The Compression of Dark Matter Halos by Baryonic Infall, ApJ 634, 70
- Sellwood, J.A., Sánchez, R.Z., 2010, Quantifying non-circular streaming motions in disc galaxies, MNRAS 404, 1733
- Sersic, J.L., 1968, *Atlas de galaxias australes*, Cordoba, Argentina: Observatorio Astronomico, 1968
- Shapiro, K.L., Gerssen, J., van der Marel, R.P., 2003, Observational Constraints on Disk Heating as a Function of Hubble Type, AJ 126, 2707
- Shapley, A.E., Steidel, C.C., Erb, D.K., Reddy, N.A., Adelberger, K.L., Pettini, M., Barmby, P., Huang, J., 2005, Ultraviolet to Mid-Infrared Observations of Star-forming Galaxies at  $z \sim 2$ : Stellar Masses and Stellar Populations, ApJ 626, 698
- Sharma, S., Bland-Hawthorn, J., Johnston, K.V., Binney, J., 2011, Galaxia: A Code to Generate a Synthetic Survey of the Milky Way, ApJ 730, 3
- Sheldon, E.S., Johnston, D.E., Frieman, J.A., Scranton, R., McKay, T.A., Connolly, A.J., Budavári, T., Zehavi, I., Bahcall, N.A., Brinkmann, J., Fukugita, M., 2004, The Galaxy-Mass Correlation Function Measured from Weak Lensing in the Sloan Digital Sky Survey, AJ 127, 2544
- Sheth, K., Melbourne, J., Elmegreen, D.M., Elmegreen, B.G., Athanassoula, E., Abraham, R.G., Weiner, B.J., 2012, Hot Disks and Delayed Bar Formation, ApJ 758, 136
- Shin, E.M., Evans, N.W., 2008, The effect of satellite galaxies on gravitational lensing flux ratios, MNRAS 385, 2107

- Shu, F.H., Stachnik, R.V., Yost, J.C., 1971, On the Density-Wave Theory of Galactic Spirals. III. Comparisons with External Galaxies, *ApJ* 166, 465
- Simon, J.D., Bolatto, A.D., Leroy, A., Blitz, L., 2003, High-Resolution Measurements of the Dark Matter Halo of NGC 2976: Evidence for a Shallow Density Profile, *ApJ* 596, 957
- Simon, J.D., Bolatto, A.D., Leroy, A., Blitz, L., Gates, E.L., 2005, High-Resolution Measurements of the Halos of Four Dark Matter-Dominated Galaxies: Deviations from a Universal Density Profile, *ApJ* 621, 757
- Simon, J.D., Geha, M., 2007, The Kinematics of the Ultra-faint Milky Way Satellites: Solving the Missing Satellite Problem, *ApJ* 670, 313
- Simon, J.D., Geha, M., Minor, Q.E., Martinez, G.D., Kirby, E.N., Bullock, J.S., Kaplinghat, M., Strigari, L.E., Willman, B., Choi, P.I., Tollerud, E.J., Wolf, J., 2011, A Complete Spectroscopic Survey of the Milky Way Satellite Segue 1: The Darkest Galaxy, *ApJ* 733, 46
- Skrutskie, M.F., Cutri, R.M., Stiening, R., et al., 2006, The Two Micron All Sky Survey (2MASS), *AJ* 131, 1163
- Slipher, V.M., 1914, The Radial Velocity of the Andromeda Nebula, *Popular Astronomy* 22, 19
- Smith, M.C., Ruchti, G.R., Helmi, A., et al., 2007, The RAVE survey: constraining the local Galactic escape speed, *MNRAS* 379, 755
- Smith, R.J., Lucey, J.R., 2013, A giant elliptical galaxy with a lightweight initial mass function, *MNRAS* 434, 1964
- Sofue, Y., Rubin, V., 2001, Rotation Curves of Spiral Galaxies, *ARA&A* 39, 137
- Solanes, J.M., Salvador-Solé, E., 1990, Analytical anisotropic models of clusters of galaxies, *A&A* 234, 93
- Sonnenfeld, A., Treu, T., Gavazzi, R., Marshall, P.J., Auger, M.W., Suyu, S.H., Koopmans, L.V.E., Bolton, A.S., 2012, Evidence for Dark Matter Contraction and a Salpeter Initial Mass Function in a Massive Early-type Galaxy, *ApJ* 752, 163
- Spekkens, K., Giovanelli, R., Haynes, M.P., 2005, The Cusp/Core Problem in Galactic Halos: Long-Slit Spectra for a Large Dwarf Galaxy Sample, *AJ* 129, 2119
- Spekkens, K., Sellwood, J.A., 2007, Modeling Noncircular Motions in Disk Galaxies: Application to NGC 2976, *ApJ* 664, 204
- Spinello, C., Koopmans, L.V.E., Trager, S.C., Czoske, O., Treu, T., 2011, The X-Shooter Lens Survey - I. Dark matter domination and a Salpeter-type initial mass function in a massive early-type galaxy, *MNRAS* 417, 3000
- Spinello, C., Trager, S., Koopmans, L.V.E., Conroy, C., 2013, The stellar IMF determined in early-type galaxies from a non-degenerate set of optical line indices, arXiv:1305.2873
- Spinello, C., Trager, S.C., Koopmans, L.V.E., Chen, Y.P., 2012, Evidence for a Mild Steepening and Bottom-heavy Initial Mass Function in Massive Galaxies from Sodium and Titanium-oxide Indicators, *ApJ* 753, L32

- Spinrad, H., Taylor, B.J., 1971, The Stellar Content of the Nuclei of Nearby Galaxies. I. M31, M32, and M81, ApJS 22, 445
- Spitzer, L., 1969, Equipartition and the formation of compact nuclei in spherical stellar systems, ApJ 158, L139
- Springel, V., Wang, J., Vogelsberger, M., Ludlow, A., Jenkins, A., Helmi, A., Navarro, J.F., Frenk, C.S., White, S.D.M., 2008, The Aquarius Project: the subhaloes of galactic haloes, MNRAS 391, 1685
- Springob, C.M., Haynes, M.P., Giovanelli, R., Kent, B.R., 2005, A Digital Archive of H I 21 Centimeter Line Spectra of Optically Targeted Galaxies, ApJS 160, 149
- Statler, T.S., 1989, Problems in determining the surface density of the Galactic disk, ApJ 344, 217
- Statler, T.S., 2001, The Shape and Orientation of NGC 3379: Implications for Nuclear Decoupling, AJ 121, 244
- Steinmetz, M., Zwitter, T., Siebert, A., Watson, F.G., Freeman, K.C., Munari, U., Campbell, R., Williams, M., Seabroke, G.M., Wyse, R.F.G., Parker, Q.A., Bienaymé, O., Roeser, S., Gibson, B.K., Gilmore, G., Grebel, E.K., Helmi, A., Navarro, J.F., Burton, D., Cass, C.J.P., Dawe, J.A., Fiegert, K., Hartley, M., Russell, K.S., Saunders, W., Enke, H., Bailin, J., Binney, J., Bland-Hawthorn, J., Boeche, C., Dehnen, W., Eisenstein, D.J., Evans, N.W., Fiorucci, M., Fulbright, J.P., Gerhard, O., Jauregi, U., Kelz, A., Mijović, L., Minchev, I., Parmentier, G., Peñarrubia, J., Quillen, A.C., Read, M.A., Ruchti, G., Scholz, R.D., Siviero, A., Smith, M.C., Sordo, R., Veltz, L., Vidrih, S., von Berlepsch, R., Boyle, B.J., Schilbach, E., 2006, The Radial Velocity Experiment (RAVE): First Data Release, AJ 132, 1645
- Strauss, M.A., Weinberg, D.H., Lupton, R.H., Narayanan, V.K., Annis, J., Bernardi, M., Blanton, M., Burles, S., Connolly, A.J., Dalcanton, J., Doi, M., Eisenstein, D., Frieman, J.A., Fukugita, M., Gunn, J.E., Ivezić, Ž., Kent, S., Kim, R.S.J., Knapp, G.R., Kron, R.G., Munn, J.A., Newberg, H.J., Nichol, R.C., Okamura, S., Quinn, T.R., Richmond, M.W., Schlegel, D.J., Shimasaku, K., SubbaRao, M., Szalay, A.S., Vanden Berk, D., Vogeley, M.S., Yanny, B., Yasuda, N., York, D.G., Zehavi, I., 2002, Spectroscopic Target Selection in the Sloan Digital Sky Survey: The Main Galaxy Sample, AJ 124, 1810
- Strigari, L.E., Bullock, J.S., Kaplinghat, M., Simon, J.D., Geha, M., Willman, B., Walker, M.G., 2008, A common mass scale for satellite galaxies of the Milky Way, Nature 454, 1096
- Strigari, L.E., Frenk, C.S., White, S.D.M., 2010, Kinematics of Milky Way satellites in a Lambda cold dark matter universe, MNRAS 408, 2364
- Suyu, S.H., Auger, M.W., Hilbert, S., Marshall, P.J., Tewes, M., Treu, T., Fassnacht, C.D., Koopmans, L.V.E., Sluse, D., Blandford, R.D., Courbin, F., Meylan, G., 2013, Two Accurate Time-delay Distances from Strong Lensing: Implications for Cosmology, ApJ 766, 70
- Suyu, S.H., Halkola, A., 2010, The halos of satellite galaxies: the companion of the massive elliptical lens SL2S J08544-0121, A&A 524, A94

- Suyu, S.H., Marshall, P.J., Auger, M.W., Hilbert, S., Blandford, R.D., Koopmans, L.V.E., Fassnacht, C.D., Treu, T., 2010, Dissecting the Gravitational lens B1608+656. II. Precision Measurements of the Hubble Constant, Spatial Curvature, and the Dark Energy Equation of State, *ApJ* 711, 201
- Suyu, S.H., Marshall, P.J., Blandford, R.D., Fassnacht, C.D., Koopmans, L.V.E., McKean, J.P., Treu, T., 2009, Dissecting the Gravitational Lens B1608+656. I. Lens Potential Reconstruction, *ApJ* 691, 277
- Swaters, R.A., Sancisi, R., van Albada, T.S., van der Hulst, J.M., 2011, Are Dwarf Galaxies Dominated by Dark Matter?, *ApJ* 729, 118
- Syer, D., Tremaine, S., 1996, Made-to-measure N-body systems, *MNRAS* 282, 223
- Sygnat, J.F., Tu, H., Fort, B., Gavazzi, R., 2010, A search for edge-on galaxy lenses in the CFHT Legacy Survey, *A&A* 517, A25
- Tamm, A., Tempel, E., Tenjes, P., Tikhonova, O., Tuvikene, T., 2012, Stellar mass map and dark matter distribution in M 31, *A&A* 546, A4
- Taylor, E.N., Franx, M., Brinchmann, J., van der Wel, A., van Dokkum, P.G., 2010, On the Masses of Galaxies in the Local Universe, *ApJ* 722, 1
- Taylor, E.N., Hopkins, A.M., Baldry, I.K., Brown, M.J.I., Driver, S.P., Kelvin, L.S., Hill, D.T., Robotham, A.S.G., Bland-Hawthorn, J., Jones, D.H., Sharp, R.G., Thomas, D., Liske, J., Loveday, J., Norberg, P., Peacock, J.A., Bamford, S.P., Brough, S., Colless, M., Cameron, E., Conselice, C.J., Croom, S.M., Frenk, C.S., Gunawardhana, M., Kuijken, K., Nichol, R.C., Parkinson, H.R., Phillipps, S., Pimbblet, K.A., Popescu, C.C., Prescott, M., Sutherland, W.J., Tuffs, R.J., van Kampen, E., Wijesinghe, D., 2011, Galaxy And Mass Assembly (GAMA): stellar mass estimates, *MNRAS* 418, 1587
- Teodorescu, A.M., Méndez, R.H., Bernardi, F., Thomas, J., Das, P., Gerhard, O., 2011, Planetary Nebulae in the Elliptical Galaxy NGC 4649 (M60): Kinematics and Distance Redetermination, *ApJ* 736, 65
- Teuben, P.J., 2002, Velocity Fields of Disk Galaxies, in: Athanassoula, E., Bosma, A., Mujica, R. (eds.), , Disks of Galaxies: Kinematics, Dynamics and Perturbations, vol. 275 of Astronomical Society of the Pacific Conference Series, p. 217
- The, L.S., White, S.D.M., 1986, The mass of the Coma cluster, *AJ* 92, 1248
- Thomas, D., Maraston, C., Johansson, J., 2011a, Flux-calibrated stellar population models of Lick absorption-line indices with variable element abundance ratios, *MNRAS* 412, 2183
- Thomas, D., Maraston, C., Korn, A., 2004a, Higher-order Balmer line indices in  $\alpha/\text{Fe}$ -enhanced stellar population models, *MNRAS* 351, L19
- Thomas, J., Jesseit, R., Saglia, R.P., Bender, R., Burkert, A., Corsini, E.M., Gebhardt, K., Magorrian, J., Naab, T., Thomas, D., Wegner, G., 2009, The flattening and the orbital structure of early-type galaxies and collisionless N-body binary disc mergers, *MNRAS* 393, 641

- Thomas, J., Saglia, R.P., Bender, R., Thomas, D., Gebhardt, K., Magorrian, J., Corsini, E.M., Wegner, G., 2007, Dynamical modelling of luminous and dark matter in 17 Coma early-type galaxies, MNRAS 382, 657
- Thomas, J., Saglia, R.P., Bender, R., Thomas, D., Gebhardt, K., Magorrian, J., Corsini, E.M., Wegner, G., Seitz, S., 2011b, Dynamical masses of early-type galaxies: a comparison to lensing results and implications for the stellar initial mass function and the distribution of dark matter, MNRAS 415, 545
- Thomas, J., Saglia, R.P., Bender, R., Thomas, D., Gebhardt, K., Magorrian, J., Richstone, D., 2004b, Mapping stationary axisymmetric phase-space distribution functions by orbit libraries, MNRAS 353, 391
- Tinker, J., Kravtsov, A.V., Klypin, A., Abazajian, K., Warren, M., Yepes, G., Gottlöber, S., Holz, D.E., 2008, Toward a Halo Mass Function for Precision Cosmology: The Limits of Universality, ApJ 688, 709
- Tinsley, B.M., 1972, Galactic Evolution, A&A 20, 383
- Tinsley, B.M., Gunn, J.E., 1976, Evolutionary synthesis of the stellar population in elliptical galaxies. I - Ingredients, broad-band colors, and infrared features, ApJ 203, 52
- Tojeiro, R., Heavens, A.F., Jimenez, R., Panter, B., 2007, Recovering galaxy star formation and metallicity histories from spectra using VESPA, MNRAS 381, 1252
- Tojeiro, R., Wilkins, S., Heavens, A.F., Panter, B. and Jimenez, R., 2009, A Public Catalog of Stellar Masses, Star Formation and Metallicity Histories, and Dust Content from the Sloan Digital Sky Survey using VESPA, ApJS 185, 1
- Tolstoy, E., Irwin, M.J., Helmi, A., Battaglia, G., Jablonka, P., Hill, V., Venn, K.A., Shetrone, M.D., Letarte, B., Cole, A.A., Primas, F., Francois, P., Arimoto, N., Sadakane, K., Kaufer, A., Szeifert, T., Abel, T., 2004, Two Distinct Ancient Components in the Sculptor Dwarf Spheroidal Galaxy: First Results from the Dwarf Abundances and Radial Velocities Team, ApJ 617, L119
- Tonry, J.L., 1983, Anisotropic velocity dispersions in spherical galaxies, ApJ 266, 58
- Toomre, A., 1963, On the Distribution of Matter Within Highly Flattened Galaxies., ApJ 138, 385
- Tormen, G., Bouchet, F.R., White, S.D.M., 1997, The structure and dynamical evolution of dark matter haloes, MNRAS 286, 865
- Tortora, C., Romanowsky, A.J., Napolitano, N.R., 2013, An Inventory of the Stellar Initial Mass Function in Early-type Galaxies, ApJ 765, 8
- Trager, S.C., Faber, S.M., Worthey, G., González, J.J., 2000, The Stellar Population Histories of Early-Type Galaxies. II. Controlling Parameters of the Stellar Populations, AJ 120, 165
- Tremaine, S., Richstone, D.O., Byun, Y.I., Dressler, A., Faber, S.M., Grillmair, C., Kormendy, J., Lauer, T.R., 1994, A family of models for spherical stellar systems, AJ 107, 634
- Treu, T., 2010, Strong Lensing by Galaxies, ARA&A 48, 87

- Treu, T., Auger, M.W., Koopmans, L.V.E., Gavazzi, R., Marshall, P.J., Bolton, A.S., 2010, The Initial Mass Function of Early-Type Galaxies, *ApJ* 709, 1195
- Treu, T., Dutton, A.A., Auger, M.W., Marshall, P.J., Bolton, A.S., Brewer, B.J., Koo, D.C., Koopmans, L.V.E., 2011, The SWELLS survey - I. A large spectroscopically selected sample of edge-on late-type lens galaxies, *MNRAS* 417, 1601
- Treu, T., Gavazzi, R., Gorecki, A., Marshall, P.J., Koopmans, L.V.E., Bolton, A.S., Moustakas, L.A., Burles, S., 2009, The SLACS Survey. VIII. The Relation between Environment and Internal Structure of Early-Type Galaxies, *ApJ* 690, 670
- Treu, T., Koopmans, L.V., Bolton, A.S., Burles, S., Moustakas, L.A., 2006, The Sloan Lens ACS Survey. II. Stellar Populations and Internal Structure of Early-Type Lens Galaxies, *ApJ* 640, 662
- Treu, T., Koopmans, L.V.E., 2002a, The Internal Structure and Formation of Early-Type Galaxies: The Gravitational Lens System MG 2016+112 at  $z = 1.004$ , *ApJ* 575, 87
- Treu, T., Koopmans, L.V.E., 2002b, The internal structure of the lens PG1115+080: breaking degeneracies in the value of the Hubble constant, *MNRAS* 337, L6
- Treu, T., Koopmans, L.V.E., 2004, Massive Dark Matter Halos and Evolution of Early-Type Galaxies to  $z \approx 1$ , *ApJ* 611, 739
- Trott, C.M., Treu, T., Koopmans, L.V.E., Webster, R.L., 2010, Stars and dark matter in the spiral gravitational lens 2237+0305, *MNRAS* 401, 1540
- Trott, C.M., Webster, R.L., 2002, Dissecting a galaxy: mass distribution of 2237+0305, *MNRAS* 334, 621
- Trujillo, I., Burkert, A., Bell, E.F., 2004, The Tilt of the Fundamental Plane: Three-Quarters Structural Nonhomology, One-Quarter Stellar Population, *ApJ* 600, L39
- Trujillo-Gomez, S., Klypin, A., Primack, J., Romanowsky, A.J., 2011, Galaxies in  $\Lambda$ CDM with Halo Abundance Matching: Luminosity-Velocity Relation, Baryonic Mass-Velocity Relation, Velocity Function, and Clustering, *ApJ* 742, 16
- Tyson, J.A., Valdes, F., Jarvis, J.F., Mills, Jr., A.P., 1984, Galaxy mass distribution from gravitational light deflection, *ApJ* 281, L59
- Tyson, J.A., Wenk, R.A., Valdes, F., 1990, Detection of systematic gravitational lens galaxy image alignments - Mapping dark matter in galaxy clusters, *ApJ* 349, L1
- Valenzuela, O., Klypin, A., 2003, Secular bar formation in galaxies with a significant amount of dark matter, *MNRAS* 345, 406
- Valenzuela, O., Rhee, G., Klypin, A., Governato, F., Stinson, G., Quinn, T., Wadsley, J., 2007, Is There Evidence for Flat Cores in the Halos of Dwarf Galaxies? The Case of NGC 3109 and NGC 6822, *ApJ* 657, 773
- Valluri, M., Merritt, D., Emsellem, E., 2004, Difficulties with Recovering the Masses of Supermassive Black Holes from Stellar Kinematical Data, *ApJ* 602, 66

- van Albada, T.S., Bahcall, J.N., Begeman, K., Sancisi, R., 1985, Distribution of dark matter in the spiral galaxy NGC 3198, *ApJ* 295, 305
- van de Ven, G., de Zeeuw, P.T., van den Bosch, R.C.E., 2008, Recovery of the internal orbital structure of galaxies, *MNRAS* 385, 614
- van de Ven, G., Hunter, C., Verolme, E.K., de Zeeuw, P.T., 2003, General solution of the Jeans equations for triaxial galaxies with separable potentials, *MNRAS* 342, 1056
- van de Ven, G., van den Bosch, R.C.E., Verolme, E.K., de Zeeuw, P.T., 2006, The dynamical distance and intrinsic structure of the globular cluster  $\omega$  Centauri, *A&A* 445, 513
- van den Bosch, F.C., Swaters, R.A., 2001, Dwarf galaxy rotation curves and the core problem of dark matter haloes, *MNRAS* 325, 1017
- van den Bosch, R., de Zeeuw, T., Gebhardt, K., Noyola, E., van de Ven, G., 2006, The Dynamical Mass-to-Light Ratio Profile and Distance of the Globular Cluster M15, *ApJ* 641, 852
- van den Bosch, R.C.E., van de Ven, G., 2009, Recovering the intrinsic shape of early-type galaxies, *MNRAS* 398, 1117
- van den Bosch, R.C.E., van de Ven, G., Verolme, E.K., Cappellari, M., de Zeeuw, P.T., 2008, Triaxial orbit based galaxy models with an application to the (apparent) decoupled core galaxy NGC 4365, *MNRAS* 385, 647
- van der Kruit, P.C., 1988, The three-dimensional distribution of light and mass in disks of spiral galaxies, *A&A* 192, 117
- van der Kruit, P.C., Allen, R.J., 1978, The kinematics of spiral and irregular galaxies, *ARA&A* 16, 103
- van der Kruit, P.C., Freeman, K.C., 2011, Galaxy Disks, *ARA&A* 49, 301
- van der Marel, R.P., Anderson, J., 2010, New Limits on an Intermediate-Mass Black Hole in Omega Centauri. II. Dynamical Models, *ApJ* 710, 1063
- van der Marel, R.P., Binney, J., Davies, R.L., 1990, Models of Elliptical Galaxies - NGC3379, NGC4261, NGC4278 and NGC4472, *MNRAS* 245, 582
- van der Marel, R.P., Cretton, N., de Zeeuw, P.T., Rix, H.W., 1998, Improved Evidence for a Black Hole in M32 from HST/FOS Spectra. II. Axisymmetric Dynamical Models, *ApJ* 493, 613
- van der Marel, R.P., Fardal, M., Besla, G., Beaton, R.L., Sohn, S.T., Anderson, J., Brown, T., Guhathakurta, P., 2012, The M31 Velocity Vector. II. Radial Orbit toward the Milky Way and Implied Local Group Mass, *ApJ* 753, 8
- van der Marel, R.P., Guhathakurta, P., 2008, M31 Transverse Velocity and Local Group Mass from Satellite Kinematics, *ApJ* 678, 187
- van der Marel, R.P., Rix, H.W., Carter, D., Franx, M., White, S.D.M., de Zeeuw, T., 1994, Velocity Profiles of Galaxies with Claimed Black-Holes - Part One - Observations of M31 M32 NGC3115 and NGC4594, *MNRAS* 268, 521

- van Dokkum, P.G., 2008, Evidence of Cosmic Evolution of the Stellar Initial Mass Function, *ApJ* 674, 29
- van Dokkum, P.G., Conroy, C., 2010, A substantial population of low-mass stars in luminous elliptical galaxies, *Nature* 468, 940
- van Dokkum, P.G., Conroy, C., 2012, The Stellar Initial Mass Function in Early-type Galaxies from Absorption Line Spectroscopy. I. Data and Empirical Trends, *ApJ* 760, 70
- van Uitert, E., Hoekstra, H., Schrabback, T., Gilbank, D.G., Gladders, M.D., Yee, H.K.C., 2012, Constraints on the shapes of galaxy dark matter haloes from weak gravitational lensing, *A&A* 545, A71
- van Uitert, E., Hoekstra, H., Velander, M., Gilbank, D.G., Gladders, M.D., Yee, H.K.C., 2011, Galaxy-galaxy lensing constraints on the relation between baryons and dark matter in galaxies in the Red Sequence Cluster Survey 2, *A&A* 534, A14
- van Waerbeke, L., 1998, Scale dependence of the bias investigated by weak lensing, *Astron. Astrophys.* 334, 1
- Van Waerbeke, L., Mellier, Y., Hoekstra, H., 2005, Dealing with systematics in cosmic shear studies: New results from the VIRMOS-Descart survey, *Astron. Astrophys.* 429, 75
- Van Waerbeke, L., Mellier, Y., Pelló, R., Pen, U., McCracken, H.J., Jain, B., 2002, Likelihood analysis of cosmic shear on simulated and VIRMOS-DESCART data, *Astron. Astrophys.* 393, 369
- Vazdekis, A., Casuso, E., Peletier, R.F., Beckman, J.E., 1996, A New Chemo-evolutionary Population Synthesis Model for Early-Type Galaxies. I. Theoretical Basis, *ApJS* 106, 307
- Vega Beltrán, J.C., Pizzella, A., Corsini, E.M., Funes, J.G., Zeilinger, W.W., Beckman, J.E., Bertola, F., 2001, Kinematic properties of gas and stars in 20 disc galaxies, *A&A* 374, 394
- Vegetti, S., Czoske, O., Koopmans, L.V.E., 2010a, Quantifying dwarf satellites through gravitational imaging: the case of SDSSJ120602.09+514229.5, *MNRAS* 407, 225
- Vegetti, S., Koopmans, L.V.E., 2009, Bayesian strong gravitational-lens modelling on adaptive grids: objective detection of mass substructure in Galaxies, *MNRAS* 392, 945
- Vegetti, S., Koopmans, L.V.E., Bolton, A., Treu, T., Gavazzi, R., 2010b, Detection of a dark substructure through gravitational imaging, *MNRAS* 408, 1969
- Vegetti, S., Lagattuta, D.J., McKean, J.P., Auger, M.W., Fassnacht, C.D., Koopmans, L.V.E., 2012, Gravitational detection of a low-mass dark satellite galaxy at cosmological distance, *Nature* 481, 341
- Verolme, E.K., Cappellari, M., Copin, Y., van der Marel, R.P., Bacon, R., Bureau, M., Davies, R.L., Miller, B.M., de Zeeuw, P.T., 2002, A SAURON study of M32: measuring the intrinsic flattening and the central black hole mass, *MNRAS* 335, 517
- Walcher, J., Groves, B., Budavári, T., Dale, D., 2011, Fitting the integrated spectral energy distributions of galaxies, *Ap&SS* 331, 1

- Walker, M.G., Mateo, M., Olszewski, E.W., 2009a, Stellar Velocities in the Carina, Fornax, Sculptor, and Sextans dSph Galaxies: Data From the Magellan/MMFS Survey, AJ 137, 3100
- Walker, M.G., Mateo, M., Olszewski, E.W., Peñarrubia, J., Wyn Evans, N., Gilmore, G., 2009b, A Universal Mass Profile for Dwarf Spheroidal Galaxies?, ApJ 704, 1274
- Walker, M.G., Peñarrubia, J., 2011, A Method for Measuring (Slopes of) the Mass Profiles of Dwarf Spheroidal Galaxies, ApJ 742, 20
- Warren, S.J., Iovino, A., Hewett, P.C., Shaver, P.A., 1998, Spectroscopy of the optical Einstein ring 0047-2808, MNRAS 299, 1215
- Watkins, L.L., Evans, N.W., An, J.H., 2010, The masses of the Milky Way and Andromeda galaxies, MNRAS 406, 264
- Weaver, H., Williams, D.R.W., 1973, The Berkeley low-latitude survey of neutral hydrogen Part I. Profiles, A&AS 8, 1
- Wegner, G.A., Corsini, E.M., Thomas, J., Saglia, R.P., Bender, R., Pu, S.B., 2012, Further Evidence for Large Central Mass-to-light Ratios in Early-type Galaxies: The Case of Ellipticals and Lenticulars in the A262 Cluster, AJ 144, 78
- Weijmans, A., Cappellari, M., Bacon, R., de Zeeuw, P.T., Emsellem, E., Falcón-Barroso, J., Kuntschner, H., McDermid, R.M., van den Bosch, R.C.E., van de Ven, G., 2009, Stellar velocity profiles and line strengths out to four effective radii in the early-type galaxies NGC3379 and 821, MNRAS 398, 561
- Weijmans, A.M., Krajnović, D., van de Ven, G., Oosterloo, T.A., Morganti, R., de Zeeuw, P.T., 2008, The shape of the dark matter halo in the early-type galaxy NGC 2974, MNRAS 383, 1343
- Weinberg, M.D., 1985, Evolution of barred galaxies by dynamical friction, MNRAS 213, 451
- Weiner, B.J., Sellwood, J.A., Williams, T.B., 2001, The Disk and Dark Halo Mass of the Barred Galaxy NGC 4123. II. Fluid-Dynamical Models, ApJ 546, 931
- Westfall, K.B., Bershady, M.A., Verheijen, M.A.W., Andersen, D.R., Martinsson, T.P.K., Swaters, R.A., Schechtman-Rook, A., 2011, The DiskMass Survey. IV. The Dark-matter-dominated Galaxy UGC 463, ApJ 742, 18
- Wevers, B.M.H.R., 1984, A study of spiral galaxies using HI synthesis observations and photographic surface photometry
- White, S.D.M., Rees, M.J., 1978, Core condensation in heavy halos - A two-stage theory for galaxy formation and clustering, MNRAS 183, 341
- Widrow, L.M., Dubinski, J., 2005, Equilibrium Disk-Bulge-Halo Models for the Milky Way and Andromeda Galaxies, ApJ 631, 838
- Widrow, L.M., Gardner, S., Yanny, B., Dodelson, S., Chen, H.Y., 2012, Galactoseismology: Discovery of Vertical Waves in the Galactic Disk, ApJ 750, L41
- Widrow, L.M., Pym, B., Dubinski, J., 2008, Dynamical Blueprints for Galaxies, ApJ 679, 1239

- Wilkins, S.M., Gonzalez-Perez, V., Baugh, C.M., Lacey, C.G., Zuntz, J., 2013, Single-colour diagnostics of the mass-to-light ratio - I. Predictions from galaxy formation models, MNRAS 431, 430
- Wilkinson, M.I., Evans, N.W., 1999, The present and future mass of the Milky Way halo, MNRAS 310, 645
- Wilkinson, M.I., Vallenari, A., Turon, C., et al., 2005, Spectroscopic survey of the Galaxy with Gaia-II. The expected science yield from the Radial Velocity Spectrometer, MNRAS 359, 1306
- Williams, M.E.K., Steinmetz, M., Binney, J., Siebert, A., Enke, H., Famaey, B., Minchev, I., de Jong, R., Boeche, C., Freeman, K.C., Bienayme, O., Bland-Hawthorn, J., Gibson, B.K., Gilmore, G.F., Helmi, A., Kordopatis, G., Munari, U., Navarro, J.F., Parker, Q.A., Reid, W., Seabroke, G.M., Sharma, S., Siviero, A., Watson, F.G., Wyse, R.F.G., Zwitter, T., 2013, The wobbly Galaxy: kinematics north and south with RAVE red clump giants, arXiv:1302.2468
- Wojtak, R., Lokas, E.L., Mamon, G.A., Gottlöber, S., 2009, The mass and anisotropy profiles of galaxy clusters from the projected phase-space density: testing the method on simulated data, MNRAS 399, 812
- Wojtak, R., Lokas, E.L., Mamon, G.A., Gottlöber, S., Klypin, A., Hoffman, Y., 2008, The distribution function of dark matter particles in massive haloes, MNRAS 388, 815
- Wojtak, R., Mamon, G.A., 2013, Physical properties underlying observed kinematics of satellite galaxies, MNRAS 428, 2407
- Wolf, J., Martinez, G.D., Bullock, J.S., Kaplinghat, M., Geha, M., Muñoz, R.R., Simon, J.D., Avedo, F.F., 2010, Accurate masses for dispersion-supported galaxies, MNRAS 406, 1220
- Woodley, K.A., Gómez, M., Harris, W.E., Geisler, D., Harris, G.L.H., 2010, The Kinematics of the Globular Cluster System of NGC 5128 with a New Large Sample of Radial Velocity Measurements, AJ 139, 1871
- Worthey, G., 1994, Comprehensive stellar population models and the disentanglement of age and metallicity effects, ApJS 95, 107
- Worthey, G., Ottaviani, D.L., 1997, H gamma and H delta Absorption Features in Stars and Stellar Populations, ApJS 111, 377
- Xu, D.D., Mao, S., Cooper, A.P., Gao, L., Frenk, C.S., Angulo, R.E., Helly, J., 2012, On the effects of line-of-sight structures on lensing flux-ratio anomalies in a  $\Lambda$ CDM universe, MNRAS 421, 2553
- Xu, D.D., Mao, S., Wang, J., Springel, V., Gao, L., White, S.D.M., Frenk, C.S., Jenkins, A., Li, G., Navarro, J.F., 2009, Effects of dark matter substructures on gravitational lensing: results from the Aquarius simulations, MNRAS 398, 1235
- Xue, X.X., Rix, H.W., Yanny, B., et al., 2011, Quantifying Kinematic Substructure in the Milky Way's Stellar Halo, ApJ 738, 79
- Xue, X.X., Rix, H.W., Zhao, G., et al., 2008, The Milky Way's Circular Velocity Curve to 60 kpc and an Estimate of the Dark Matter Halo Mass from the Kinematics of  $\sim$ 2400 SDSS Blue Horizontal-Branch Stars, ApJ 684, 1143

- Yang, X., Mo, H.J., van den Bosch, F.C., 2009, Galaxy Groups in the SDSS DR4. III. The Luminosity and Stellar Mass Functions, *ApJ* 695, 900
- Yanny, B., Rockosi, C., Newberg, H.J., et al., 2009, SEGUE: A Spectroscopic Survey of 240,000 Stars with  $g = 14\text{--}20$ , *AJ* 137, 4377
- Yegorova, I.A., Pizzella, A., Salucci, P., 2011, Probing dark matter haloes of spiral galaxies at poorly explored distances using satellite kinematics, *A&A* 532, A105
- Young, L.M., Bureau, M., Davis, T.A., Combes, F., McDermid, R.M., Alatalo, K., Blitz, L., Bois, M., Bournaud, F., Cappellari, M., Davies, R.L., de Zeeuw, P.T., Emsellem, E., Khochfar, S., Krajnović, D., Kuntschner, H., Lablanche, P.Y., Morganti, R., Naab, T., Oosterloo, T., Sarzi, M., Scott, N., Serra, P., Weijmans, A.M., 2011, The ATLAS<sup>3D</sup> project - IV. The molecular gas content of early-type galaxies, *MNRAS* 414, 940
- Zaritsky, D., Colucci, J.E., Pescev, P.M., Bernstein, R.A., Chandar, R., 2012, Evidence for Two Distinct Stellar Initial Mass Functions, *ApJ* 761, 93
- Zibetti, S., Charlot, S., Rix, H.W., 2009, Resolved stellar mass maps of galaxies - I. Method and implications for global mass estimates, *MNRAS* 400, 1181
- Zwaan, M.A., van der Hulst, J.M., de Blok, W.J.G., McGaugh, S.S., 1995, The Tully-Fisher relation for low surface brightness galaxies: implications for galaxy evolution, *MNRAS* 273, L35
- Zwicky, F., 1933, Die Rotverschiebung von extragalaktischen Nebeln, *Helvetica Physica Acta* 6, 110